Investigations into the Molecular Origin of Mechanisms in Supramolecular Polymerization

A Thesis

Submitted For the Degree of

DOCTOR OF PHILOSOPHY

in the Faculty of Science

by

Chidambar Kulkarni

CHEMISTRY AND PHYSICS OF MATERIALS UNIT
JAWAHARLAL NEHRU CENTRE FOR ADVANCED SCIENTIFIC RESEARCH
Bangalore – 560 064, India

JUNE 2015

Dedicated to Ma, Pa and Anya

DECLARATION

I hereby declare that the matter embodied in the thesis entitled "**Investigations into the Molecular Origin of Mechanisms in Supramolecular Polymerization**" is the result of investigations carried out by me at the Chemistry and Physics of Materials Unit, Jawaharlal Nehru Centre for Advanced Scientific Research, Bangalore, India under the supervision of Prof. S. Balasubramanian and Prof. Subi Jacob George and that it has not been submitted elsewhere for the award of any degree or diploma.

In keeping with the general practice in reporting scientific observations, due acknowledgement has been made whenever the work described is based on the findings of other investigators. Any omission that might have occurred by oversight or error of judgement is regretted.

Chidambar Kulkarni

CERTIFICATE

I hereby certify that the matter embodied in this thesis entitled "**Investigations into the Molecular Origin of Mechanisms in Supramolecular Polymerization**" has been carried out by Mr. Chidambar Kulkarni at the Chemistry and Physics of Materials Unit, Jawaharlal Nehru Centre for Advanced Scientific Research, Bangalore, India under my supervision and that it has not been submitted elsewhere for the award of any degree or diploma.

Prof. S. Balasubramanian and Prof. Subi Jacob George
(Research Supervisors)

Acknowledgements

First and foremost, I would like to thank my research supervisors, Prof. S. Balasubramanian and Prof. Subi J. George for the enormous freedom, encouragement and constant support provided to me throughout the course of work. From the summer of 2009 when I was a summer intern in Bala sir lab to the present day, I have immensely enjoyed his perfectionist approach to research and teaching. I thank him for inspiring me to achieve similar or better standards. I greatly appreciate the openness of Subi sir in pursuing varied kinds of problems and his unending passion towards science. I am thankful to Subi and Bala sir for their valuable suggestions and inputs during the course of this work. I am greatly thankful to them for the excellent computational and experimental resources they have provided for the group and for their help during writing of this thesis.

I thank Prof. C. N. R. Rao, FRS for inspiring tales on the history of chemistry and chemists.

My special thanks to Prof. C. N. R. Rao, Prof. G. U. Kulkarni and Prof. S. Balasubramanian for allowing me to work as a combined student and for providing excellent research facilities as head of the departments.

I express my gratitude to faculties from JNCASR and IISc for the various course; Prof. S. Balasubramanian, Prof. T. K. Maji, Prof. A. Sundaresan, Prof. M. Eswaramoorthy, Prof. N. Chandrabhas, Prof. K. S. Narayan, Prof. N. S. Vidhyadhiraja, Prof. S. J. George, Prof. T. Govindaraju, Prof. R. Datta, Prof. S. Pati, Prof. U. V. Waghmare, Prof. S. Narasimhan, Prof. S. M. Shivaprasad, Prof. P. Balaram, Prof. S. Sharma, Shobha Madam.

I thank my collaborators Prof. K. S. Narayan, Dr. Satysprasad, Prof. E. W. Meijer, Dr. Peter Korevaar and Karteek Kumar for fruitful collaborations and insightful discussions.

I am thankful to open source community for their service in providing the useful softwares and operating systems. I particularly acknowledge the developers of CPMD, CP2K, JMOL and VMD softwares.

I owe my sincere thanks to my lab mates, Dr. Mohit Kumar, Ankit Jain and Dr. Sandeep Kumar Reddy for their help and guidance during my first couple of years of Ph.D. I thank all past and present lab mates; Dr. Venkat, Bhawani, Krishnendu, Ananya, Suman, Anjali, Dr. Raju, Dr. Saswati, Karteek, Dr. Rajdeep, Satya, Anirban, Tarak, Dr. Kanchan, Dr. Ganga, Sudip, Pallabi, Dr. Anurag, Bharat, Promit, Divya and POCE and SRFP students who worked with me.

Special thanks to Dr. Sridhar Rajaram and his group for helping me at various stages of synthesis.

I thank a wonderful bunch of Int. Ph. D. batachmates: Arpan, Dileep, Gayatri, Sharma, Rana, Pandu, Varun and Sudeshna, for making my stay here memorable. I would also like to thank other friends from JNC; Mohit, Ankit, Amrit, Pawan, Satya, Nitesh, Urmi, Piyush, Anand, Chandan, Ritesh, Jayaram, Avinash, Umesha, Swamynathan (from RRI)... Thank you guys for the wonderful time we had together.

I would like to thank Prof G. U. Kulkarni and Dr. Basavaraj for AFM and Dr. Ranjani Vishwanatha for TCSPC facilities.

I am grateful to Dr. Ralf Bovee, Dr. Lou and Hitesh Khandelwal from TU/e Eindhoven, Netherlands for timely measurement of MALDI-TOF spectra.

I am extemely thankful to the technical staff of JNC; Dr. Usha Tumkurar for TEM, Vasu for UV&PL, Shivakumar for HRMS, Mahesh for NMR, Selvi for FE-SEM, Vijya Amurthraj, Anand Raman and Amit Patel for maintaining the computational resources.

My sincere thanks to Subi sir and family for the wonderful hospitality.

I would like to express my thanks to Dr. Manohar Kulkarni and Late Ms. Dr. G. M. Kulkarni from Dharwad for encouraging me from the BSc days.

All these would not have been possible without the support of my family and I thank them for being with me through my ups and downs.

I thank all those who have helped me directly or indirectly.

Preface

Supramolecular polymers are extensively studied in the past few decades not only for their role as model systems to study polymerization processess in biology, but also for optoelectronic applications. This thesis is aimed at gaining a molecular level understanding of mechanisms operating in supramolecular polymers through experimental and computational studies.

In Chapter 1, a brief introduction to supramolecular polymers, the various mechanisms of formation of one-dimensional assemblies and their importance is provided. Different experimental and computational techniques used to study the polymerization mechanisms are reviewed.

In Chapter 2, quantum chemical calculations are performed on oligomers of benzene-1,3,5-tricarboxamide, a prototypical example of supramolecular polymer known to exhibit a cooperative mechanism of self-assembly. The origin of cooperativity is attributed to the formation of triple-helical intermolecular hydrogen bonding network in the stacks as evidenced from the non-linear changes in stabilization energy, various structural parameters of the assembly and the macrodipole moment. Also, a significant amount of stabilization of the stacks is observed to arise from dipersive forces.

In Chapter 3, four families of molecules are chosen in which both isodesmic and cooperative mechanisms of self-assembly are observed. The molecular features governing the mechanisms in each family are outlined. In addition, other systems which possess intermolecular hydrogen-bonding and show a cooperative mechanism have been examined. Based on these case studies, we conjecture that the presence of long-range intermolecular interaction along the stacking direction leads to a cooperative mechanism and the lack of it to isodesmic polymerization.

In Chapter 4, a cooperative mechanism of polymerization is observed for perylene bisimide derivatives possessing dipolar carbonate linkers and rigid steroidal moieties. Lack of either the dipolar linkers or rigid self-assembling groups results in isodesmic polymerization. Molecular dynamic simulations and bulk dielectric measurements show significant macrodipole moment (or polarization) for systems following a cooperative mechanism. Thus we provide an example of long-range interaction (dipole moment) driven cooperativity.

In Chapter 5, we apply similar design principles as in Chapter 3.1 to other chromophores to examine the generality of the conclusions. A cooperative mechanism is observed for perylene-3,4-dicarboximide and oligo(*p*-phenylenevinylene) derivatives possessing dipolar linkers and rigid steroidal moiety. In addition, ester groups are shown to contribute significantly to the molecular dipole moment to result in a cooperative mechanism mechanism of self-assembly.

In Chapter 6, naphthalene diimides appended with dipolar carbonates and steroids are shown to follow a cooperative mechanism of self-assembly, again reaffirming the conclusions of Chapter 3.1. Interestingly the inclusion of carbonate groups lead to highly red-shifted (560 nm) excimer formation in both solution and solid states. This observation is attributed to intermolecular packing enforced by the carbonate groups. Thus, the dipolar linkers can affect not only the mechanism of polymerization but also the photophysical properties of the assemblies.

In Chapter 7, naphthalene diimides without bay substitution are shown to form ground-state charge-transfer complexes with various electron rich aromatic solvents as evidenced from experiments and TD-DFT computational studies.

In Chapter 8, coronene bisimide derivatives possessing chiral and achiral gallic wedges are seen to follow an isodesmic mechanism of self-assembly. The lack of long-range interaction in an assembly of these molecules leads to isodesmic mechanism. Co-assembly of chiral and achiral derivatives results in chiral amplification through a sergeant-soldiers experiment. The observation suggests that systems following isodesmic mechanism too can exhibit chiral amplification.

In Chapter 9, temperature-dependent reversal of supramolecular chirality is observed for a coronene bisimide derivative (CBI-35CH, containing 3,5-di((*s*)-3,7-dimethyloctyl)phenoxy groups on the imide position) in various cyclic and linear

solvents. An isodesmic mechanism of self-assembly is observed for this derivative. Through detailed experiments in various cyclic solvents and MD simultations, we hypothesize that at low temperature the solvent molecules reside in the pocket of CBI-35CH, correlated with the change in supramolecular chirality.

In Chapter 10, brief conclusions derived from the work and outlook for the future work are provided.

Contents

Acknowledgements **v**

Preface **vii**

List of Figures **xvii**

List of Tables **xxxi**

1 Introduction to Supramolecular Polymers and the Mechanisms of Self-Assembly **1**

1.1 Supramolecular polymers 1

1.2 Mechanisms of Supramolecular Polymerization 3

1.2.1 Isodesmic Polymerization 3

1.2.2 Cooperative Polymerization 3

1.3 Theories of Supramolecular Polymerization 5

1.4 Methods to Study the Mechanisms of Supramolecular Polymerization 6

1.4.1 Experimental Techniques 6

1.4.2 Computational Techniques 8

1.5 Aim of the thesis 9

Bibliography 9

2 Cooperativity in the Stacking of Benzene-1,3,5-tricarboxamide: The Role of Dispersion **13**

2.1 Introduction 13

2.2 Computational details 14

2.3 Results and discussion 15

2.3.1 Molecular assembly 15

2.3.2 The dimer of BTA 16

2.3.3 Higher oligomers of BTA 18

2.3.4 Cooperativity 20
2.3.5 Dipole moment 22
2.4 Conclusions 23
Bibliography 24

3 What Molecular Features Govern the Mechanism of Supramolecular Polymerization? 27
3.1 Introduction 27
3.2 Discussion 28
3.2.1 Benzene-1,3,5-tricarboxamide (BTA) Family 28
3.2.2 Perylene-3,4,9,10-tetracarboxylic acid bisimide (PBI) Family . 30
3.2.3 Squaraine Family 33
3.2.4 Oligo(phenylene ethynylene) Family 36
3.2.5 Miscellaneous Examples 38
3.2.6 The case of Oligo(*p*-phenylenevinylene)s 39
3.3 Perspective on the Mechanism of Supramolecular Polymerization . . . 41
3.4 Conclusions and outlook 43
3.5 Computational details 45
Bibliography 45

4 Dipole-Moment-Driven Cooperativity in Perylene Bisimides 51
4.1 Introduction 51
4.2 Results 53
4.2.1 Molecular design 53
4.2.2 Self-assembly studies 54
4.2.3 Mechanism of self-assembly 59
4.2.4 Molecular Dynamics (MD) Simulations 65
4.2.5 Dielectric Measurements 67
4.3 Discussion 69
4.4 Conclusions 69
4.5 Experimental section 70
4.5.1 General Methods 70
4.5.2 Synthetic details 72
4.5.3 Capacitance fabrication and measurement 85
Bibliography 85

5 Generality of Dipole-Moment-Driven Cooperativity and the Role of Linker **93**
5.1 Introduction . . . 93
5.2 Results and discussion . . . 94
5.2.1 Perylene-3,4-dicarboximide . . . 94
5.2.2 Oligo-(*p*-phenylenevinylene) (OPV) . . . 97
5.2.3 Esters as source of dipole-moment . . . 99
5.3 Conclusions . . . 101
5.4 Experimental details . . . 101
5.4.1 General Methods . . . 101
5.4.2 Synthetic details . . . 102
Bibliography . . . 104

6 Carbonate Linkage Bearing Naphthalenediimides: Self-Assembly and Photophysical Properties **107**
6.1 Introduction . . . 107
6.2 Results . . . 108
6.2.1 Molecular design . . . 108
6.2.2 Self-assembly studies . . . 109
6.2.3 Morphological and structural studies . . . 114
6.2.4 Computational studies . . . 116
6.2.5 Chiroptical studies . . . 117
6.3 Conclusion . . . 118
6.4 Experimental section . . . 119
6.4.1 General methods . . . 119
6.4.2 Computational details . . . 120
6.4.3 Synthetic details . . . 120
Bibliography . . . 124

7 Charge-transfer Complexation between Naphthalene Diimides and Aromatic Solvents **129**
7.1 Introduction . . . 129
7.2 Results and discussion . . . 131
7.2.1 Interaction of **1** and **2** with aromatic solvents . . . 131
7.2.2 Role of aggregation . . . 132
7.2.3 Effect of imide substitution . . . 134
7.2.4 Computational studies . . . 136

7.3 Conclusions . . . 138
7.4 Experimental details . . . 138
7.5 Computational details . . . 139
Bibliography . . . 139

8 Self-Assembly of Coronene Bisimides: Mechanistic Insight and Chiral Amplification 145
8.1 Introduction . . . 145
8.2 Results and Discussion . . . 147
8.2.1 Molecules under study . . . 147
8.2.2 Self-assembly of **CBI-GCH** . . . 147
8.2.3 Mechanism of self-assembly of **CBI-GCH** . . . 149
8.2.4 Morphological studies of **CBI-GCH** . . . 151
8.2.5 Self-assembly of **CBI-GACH** . . . 154
8.2.6 CBI co-assembly: sergeant-and-soldiers experiment . . . 156
8.3 Conclusion . . . 159
8.4 Experimental section . . . 159
8.4.1 General methods . . . 159
8.4.2 Computational details . . . 161
8.4.3 Synthetic details . . . 162
Bibliography . . . 164

9 Mechanism of Self-Assembly and Temperature-dependent Reversal of Supramolecular Chirality in a CBI derivative 171
9.1 Introduction . . . 171
9.2 Results and discussion . . . 172
9.2.1 Mechanisms of self-assembly and morphology . . . 172
9.2.2 Reversal of supramolecular chirality in cyclic solvents . . . 175
9.2.3 Reversal of supramolecular chirality in *n*-heptane . . . 177
9.2.4 Role of molecular structure in chirality reversal . . . 178
9.2.5 Molecular dynamics simulations . . . 179
9.3 Conclusions . . . 180
9.4 Experimental details . . . 181
9.4.1 General methods . . . 181
9.4.2 Synthetic details . . . 182
Bibliography . . . 185

10 Conclusions and Future Outlook **189**

List of Publications **191**

List of Figures

1.1 A schematic showing the difference between covalent and supramolecular polymers. The blue filled circles indicate the monomers. The distance between the monomers is depicted smaller in conventional polymers to show the covalent bonds, whereas in supramolecular polymers, this distance is larger indicating the non-covalent, weaker nature of bonding between monomers. The reversible arrow for supramolecular polymer indicates the equilibrium between monomers and polymers. This equilibrium is lacking in the formation of covalent polymers. . . 2

1.2 a) and c) The standard Gibbs free energy (ΔG^0) profile for an isodesmic and a cooperative supramolecular polymerization respectively. The abscissa represents the oligomer number (n). ΔG^0 remains negative with a constant slope throughout the course of polymerization for an isodesmic pathway, whereas a change in slope is observed for the cooperative counter-part. The oligomer number for which the ΔG^0 is highest is termed as the nucleus. b) and d) Fraction of aggregates (α) versus the concentration or temperature for an isodesmic and a cooperative mechanism respectively. A smooth transition from monomers ($\alpha = 0$) to aggregates ($\alpha = 1$) with a sigmoidal shape is observed for an isodesmic mechanism, whereas the cooperative pathway is characterized by a kink. The temperature or concentration at which kink is observed corresponds to the nucleation step. 4

1.3 The fraction of aggregates (α) versus the reduced temperature (T/T_e) at different values of σ. The lower the value of σ, higher the extent of cooperativity and more steeper the transition from monomers to aggregates. $\sigma = 1$ indicates $K_n = K_e$ and an isodesmic mechanism of self-assembly. 7

2.1 Structure of benzene-1,3,5-tricarboxamide (**1**) used for computational studies. 16

2.2 Optimized geometry of a dimer of **1**. The intermolecular hydrogen-bonds are shown in bold-dotted green lines. 16

2.3 Stabilisation energy of oligomers of **1** obtained using B3LYP/6-31+G(d,p) and PBE/85 Ry levels of theory. 18

2.4 Stabilisation energy of oligomers of **1** as a function of their size, n using PBE/ 85 Ry level of theory including empirical vdW corrections. 19

2.5 Variation of a) hydrogen bond length, b) π-π stacking distance, c) dihedral angle H-N-C_{Ar}-C_{Ar} (ϕ_1) and d) dihedral angle O-$C_{carbonyl}$-C_{Ar}-C_{Ar} (ϕ_2) in the core region of the oligomers as a function of its size, n using PBE/85 Ry + vdW level of theory. The inset of each sub-figure shows the pictorial representation of the corresponding parameter from the core an oligomer. 21

2.6 a) Mean dipole moment per molecule as a function of oligomer size, n calculated at two different levels of theory. b) Electrostatic potential isosurfaces plotted on electronic density isosurfaces of 4×10^{-4} e/bohr^3 for different oligomers of **1** calculated from the optimized geometries obtained at B3LYP/6-31+G(d,p) level of theory. The total dipole moment of oligomers is mentioned in blue color below the respective oligomers. 22

3.1 A schematic illustrating the various intermolecular interactions which aid in the supramolecular polymerization of a small molecule (represented by disc). 28

3.2 Molecular structures of BTA derivatives **1** along with a schematic of its assembly and **2**. a) Fraction of aggregates (α) versus reduced temperature for molecule **1** at different concentrations in heptane with a 0.25 offset for each concentration. Reproduced with permission from reference [4]. Copyright 2008 American Chemical Society. b) α as a function of temperature for different concentrations of **2** in methylcyclohexane. Reproduced with permission from reference [5]. Copyright 2011 Royal Society of Chemistry. 29

3.3 Structure of the PBI molecule under consideration with a schematic representation of self-assembly of **3**. a) Fraction of aggregates (α) versus dimensionless concentration at different σ values according to the cooperative nucleation model. The hollow blue circles represent experimental data points obtained at different concentrations of **3**. Reproduced with permission from reference [14]. Copyright 2009 American Chemical Society. b) Fraction of aggregates (α) of **4** versus concentration (2.1×10^{-7} to 1.1×10^{-3} M) in MCH. c) Cooling curve of **4** in MCH (c = 5.0×10^{-4} M). The solid blue circles represent experimental data points in b) and c) and the solid black line represents the isodesmic fit to the data points. Reproduced with permission from reference [15]. Copyright 2007 Wiley-VCH 31

3.4 Molecular structure of squaraine derivatives **5** and **6**. a) Fraction of aggregates (α) versus dimensionless concentration at different σ values according to the cooperative-nucleation model. Solid blue circles correspond to experimental data of **5** at different concentrations. Reproduced with permission from reference [22]. Copyright 2012 Royal Society of Chemistry. b) Solid blue circles represent the experimental data for the fraction of aggregates (α) plotted against the concentration for molecule **6** with R = Cl. The black line shows an isodesmic fit to the data points. Reproduced with permission from reference [23]. Copyright 2012 Wiley-VCH. 34

3.5 Molecular structures of OPE derivatives **7** and **8**. a) Fraction of aggregates (α) as a function of temperature for different derivatives of **7** in MCH at 1×10^{-5} M with an offset of 0.3 (Black solid lines are the corresponding fits to the nucleation-growth model). Reproduced with permission from reference [25]. Copyright 2011 Wiley-VCH. b) Fraction of aggregates (α) versus concentration for **8** in different solvents. Reproduced with permission from reference [26]. Copyright 2009 Wiley-VCH. 37

3.6 Structures of various molecules studied for their self-assembly mechanisms in the literature. [31–35] 39

3.7 Structure of OPV UT (**14**) with a schematic of its self-assembly and hexa-OPV-substituted benzene (**15**). a) Normalized cooling curve for **14** with y=2 in dodecane at different concentrations (5.4×10^{-6} to 4.8×10^{-5} M). Reproduced with permission from ref. [6]. Copyright 2006 American Association for the Advancement of Science. b) Fraction of aggregates (α) versus temperature for **15** in MCH at 2.5×10^{-6} M fitted to the nucleation-elongation model. Reproduced with permission from ref. [36]. Copyright 2007 American Chemical Society. . . 40

3.8 Structure of molecules (**16-18**) studied computationally. Electrostatic potential isosurfaces plotted on electronic density isosurfaces of 4×10^{-4} e/bohr^3 for the tetramer of all three classes of molecules. The dipole moments in the stacking direction for the tetramers of different molecules as obtained from the BLYP/DZVP//B97D/cc-PVDZ level of theory are mentioned below respective oligomers. 42

4.1 Molecules under study. (a) PBI is functionalized on both imide nitrogens with either carbonate or ether linker (marked in red). Cholesterol (**1** and **3**), dihydrocholesterol (**2**), and chiral swallowtail (**4**) are used as the self-assembling motifs. (b) Schematic representation of the assembly of different PBI derivatives. PBIs are depicted by red blocks. Blue and cyan cylinders represent carbonate and ether linkers, respectively. Self-assembling moieties are shown in green. Small yellow arrows indicate molecular dipoles along the carbonate C=O axis. Macro-dipole moment is shown as a large yellow arrow along the stacking direction. 53

4.2 a) and b) UV/Vis absorption and fluorescence spectra respectively of **1** in chloroform and MCH (λ_{exc} = 450 nm). Inset of a) shows the schematic arrangement of **1** in chloroform and MCH. Inset of b) displays the normalized fluorescence spectra in different solvents. These spectra are recorded at room temperature. 54

4.3 Normalized fluorescence excitation (by monitoring fluorescence intensity at 650 nm and 565 nm) and absorption spectrum of **1** in MCH (c = 1×10^{-5} M). 55

4.4 a) UV/Vis absorption (black curve) and fluorescence spectra (red curve) of **2** in chloroform (solid curve) and MCH (dashed curve) (c = 1×10^{-5}M, λ_{exc} = 450 nm). Studies were performed in a 10 mm cuvette. b) Excitation spectra of **2** in MCH (c = 1×10^{-5}M) overlaid with the corresponding absorption spectra. These studies were performed in 1 mm cuvette to minimize self-absorption. 55

4.5 a) and b) UV/Vis absorption and fluorescence spectra respectively of **3** in chloroform (black curve) and MCH (red curve) (c = 5.21×10^{-6}M). Studies were performed in a 10 mm cuvette. Emission spectra of **3** in $CHCl_3$ was recorded in a 1 mm cuvette to reduce the self-absorption. 56

4.6 a) and b) UV/Vis absorption and fluorescence spectra respectively of **4** in different solvents. Concentration in different solvents are as follows, $CHCl_3$; c= 9.52×10^{-6} M, MCH; c = 2.45×10^{-5} M, *n*-dodecane; c = 3.6×10^{-5} M. Spectra were recorded in a 10 mm cuvette. 56

4.7 a) DLS size distribution of **1** in solution state (c = 1×10^{-5} M in 95:5 MCH:TCE (v/v)). b) AFM height profile of a film of **1** on a glass slide. 57

4.8 a) DLS size distribution of **3** in solution state. b) AFM height profile of a film of **3** on a glass slide. b) TEM micrograph of **3** obtained by drop-casting a solution on a copper grid. All these studies were performed in 80:20 MCH:TCE (v/v) at a concentration of 2×10^{-5} M. 57

4.9 Temperature-dependent CD (a) and UV/vis absorption spectra (b) of **1** in MCH/TCE (95:5, v/v) at every 10 °C. All studies were done at a concentration of 1×10^{-5} M in a 10 mm cuvette. Inset of (a) shows a schematic representation of the assembly at high and low temperatures. Arrows indicate spectral changes with an increase in temperature. 58

4.10 a)Temperature-dependent CD of **2** (c = 8×10^{-6} M) in MCH/TCE (95:5, v/v). b) CD spectra of **3** in MCH/TCE (80:20, v/v, c = 2×10^{-5} M). The spectra were recorded in a 10 mm cuvette. 59

4.11 Mechanism of self-assembly of **1**-**4**. a) and b) Degree of aggregation (α) as a function of temperature (cooling curve) for a solution (95%MCH and 5% TCE) of **1** and **2**, respectively, by monitoring the CD effect at 480 nm (for **1**) and 485 nm (for **2**) at a cooling rate of 2 K/min (c = 8.0×10^{-6} M). c) Cooling curve obtained by monitoring changes in UV/vis absorbance of **3** at 570 nm at a cooling rate of 1 K/min (c = 2×10^{-5} M in 80% MCH and 20% TCE). d) Normalized change in UV/vis absorbance of **4** as a function of temperature, monitoring the absorbance at 570 nm (cooling rate 2 K/min, c = 4.69×10^{-4} M, in MCH). The solid blue and red lines are the fits obtained from nucleation-elongation and isodesmic models, respectively. The structures of linker and self-assembling group corresponding to each of the molecules are shown as insets. 60

4.12 UV/Vis absorption cooling curves of **1** in 95% MCH and 5% TCE at different concentrations. Cooling rate of 1 K/minute was used. The red solid lines represent the fits obtained by the nucleation-elongation model. 61

4.13 a) UV/Vis absorption cooling curves of **2** (c = 1×10^{-5}). b) Temperature-dependent UV/Vis cooling curves of **2** (c = 8×10^{-6} M) obtained by monitoring absorption at two different wavelengths with a cooling rate of 1 dpm. These studies were carried out in 95% MCH and 5% TCE solvent composition. 62

4.14 a) UV/Vis absorption spectra of **2** in 95:5 (MCH:TCE, v/v) at different concentrations. b) Molar extinction coefficient (ϵ) versus the concentration monitored at two different wavelengths (The value of ϵ are obtained from figure a). 62

4.15 Molecular structure of **PBI_carb_dd**. 63

4.16 a) UV/Vis absorption cooling curve of **PBI_carb_dd**. b) Fluorescence spectra of **PBI_carb_dd** in 95:5 MCH:TCE (v/v) (c = 1.3×10^{-5} M). These studies are performed in a 1 mm cuvette at 20 °C. 64

4.17 UV/Vis cooling curve of **PBI_carb_dd** (c = 2.6×10^{-5} M in 95:5 MCH:TCE (v/v)) with a cooling rate of 1 dpm. The spectra was recorded in a 10 mm cuvette. 64

4.18 MD simulations of the assemblies of **1**, **3** and **4**. a) Snapshot illustrating the arrangement of molecules in the assembled state. Linkers are highlighted in yellow and magenta to aid in the visualization of the helical packing. Self-assembling groups are represented with thin sticks, and hydrogens are omitted for clarity. b) Distance distribution between the linkers of neighboring molecules. c) Macro-dipole along the stacking direction as a function of time. Solid horizontal lines (yellow for **1**, blue for **3**, and maroon for **4**) are drawn to represent the mean dipole moment value for each system. d) Weighted probability distribution of macro-dipole obtained from (c). All the analysis was performed on the last 12 ns of the MD trajectory. 65

4.19 Bulk dielectric measurements. a) ϵ_r measurement as a function of frequency. b) ϵ_r variation with temperature for molecule **2** at 10 kHz. Inset in b) shows a schematic of the device and the dipole alignment at different temperatures. The oval-shaped dipoles represent the polarization of an aggregate and not that of individual molecules. 68

4.20 Synthetic route for **1**. 72

4.21 Synthetic route for **2**. 75

4.22 Synthetic route for **3**. 78

4.23 Synthetic route for **4**. 79

4.24 Synthetic route for **PBI_carb_dd**. 83

5.1 Structure of **PMI_carb_chol**. 94

5.2 a) and b) UV/vis absorption and emission spectra respectively of **PMI_carb_chol** in chloroform (c = 1.15×10^{-5} M). Emission spectra were recorded in a 1 mm pathlength cuvette to minimize self-absorption. 94

5.3 a) and b) Temperature-dependent UV/vis absorption and emission spectra respectively of **PMI_carb_chol** in MCH (c = 7.5×10^{-5} M). These studies were carried out in a 10 mm path length cuvette. Arrows indicate spectral changes with increase in temperature. The intensity of the emission peak at 524 nm is lower than the one at 557 nm at high temperature. At elevated temperature, the monomer concentration and the emission from them increases, since the studies are performed in a 10 mm cuvette a significant amount of self-absorption takes place leading to the lowering in the intensity of the first emission band. 95

5.4 a) TEM micrographs of **PMI_carb_chol** obtained by drop-casting a solution (in MCH, c = 5×10^{-5} M) on a copper-grid without any staining. 96

5.5 a) CD spectra of **PMI_carb_chol** in MCH (c = 5×10^{-5} M) at different temperatures. b) Cooling curves obtained from CD studies at two different concentrations. 96

5.6 Structure of **OPV_carb_chol**. 98

5.7 a) Temperature-dependent CD spectra of **OPV_carb_chol** in *n*-dodecane every 10 °C (c = 1×10^{-3} M). Spectra were recorded in a 10 mm cuvette. b) Heating curve obtained from CD studies with a ramp rate of 3 °C/minute. 98

5.8 Structure of **PBI_est_chol**. 99

5.9 a) and b) UV/vis absorption and emission spectra of **PBI_est_chol** respectively in different solvents (c = 1×10^{-5} M). The emission spectra are recorded in 1 mm cuvette to minimize self-absorption. 100

5.10 a) Temperature-dependent CD spectra of **PBI_est_chol** in MCH:TCE (8:2, v/v) every 10 °C (c = 1.2×10^{-5} M). Spectra were recorded in a 10 mm cuvette. Arrow indicates spectral changes with decrease in temperature. b) Cooling curve obtained from CD studies at different concentrations with a cooling rate of 2 °C/minute. Solid blue lines indicate the nucleation-elongation fits to the data. 100

5.11 Synthetic route to **PMI_carb_chol**. 103

5.12 Synthetic route to **PBI_est_chol**. 104

6.1 a) Structure of molecules under study. b)-d) Different emissive states of **1**. Photographs show the emission in different states along with the schematic of corresponding photophysical states. 109

6.2 Self-assembly of **1**. a) UV/vis absorption and b) emission (λ_{exc} = 350 nm) spectra of **1** in ACN/DCE solvent mixture (path length, l = 10 mm). Notations 0-0 and 0-1 indicate the vibrionic transitions of NDI. Emission spectra were normalized at 407 nm. c) Life-time decay profiles of **1** in DCE/ACN solvent mixture and film state (λ_{exc} = 380 nm; $\lambda_{monitored}$ = 550 nm). Inset: the solid-state emission spectrum of **1** along with a photograph of the sample under 365 nm UV lamp. d) Excitation and UV/vis absorption spectra of **1** in 1:1 DCE/ACN. All solution-state studies were carried out at a concentration of 5×10^{-5} M. Arrows indicate the spectral changes with increasing percentage of ACN in DCE. 110

6.3 a) UV/vis absorption and emission spectra of **2** in chloroform (c = 1×10^{-4} M, λ_{exc} = 350 nm) b) UV/vis absorption and emission (λ_{exc} = 350 nm) spectra of **2** in 90% DMSO and 10% chloroform. c) TCSPC decay profiles of **2** monitored at two different wavelengths with a 380 nm excitation. The average life-time values are given in the graph. d) Absorption and excitation spectra of **2**. Spectra b) to d) were recorded with a concentration of 1×10^{-4} M in 90% DMSO and 10% Chloroform. All studies were performed in a 10 mm cuvette. 112

6.4 a) UV/vis absorption b) emission spectra of **3** in DCE/ACN solvent mixtures (λ_{exc} = 350 nm). Emission spectra are normalized at 408 nm. c) TCSPC decay profile of **3** in 90% ACN and 10% DCE with an λ_{exc} of 380 nm and $\lambda_{monitoring}$ of 520 nm. All studied were performed in a 10 mm cuvette with a concentration of 5×10^{-5} M. 113

6.5 Normalized emission spectra of **1** (c = 5×10^{-5} M in 60:40 ACN to DCE), **3** (c = 5×10^{-5} M in 90:10 ACN:DCE) and **NDI_Bola** (c = 1×10^{-3} M in 85:15 Water:Methanol). λ_{exc} = 350 nm. Structure of **NDI_Bola** is shown on the right side of the graph. 114

6.6 a) AFM height image of **1** obtained in the film state. b) DLS particle size distribution of **1**. c) Confocal microscopy image of the nanoparticles of **1**. The inset shows the fluorescence spectrum recorded at the plus sign shown on the Figure. A 6:4 (ACN:DCE) solution of **1** with a concentration of 5×10^{-5} M was for a) to c) studies. d) TEM micrograph of **2** (c = 1×10^{-4} M in 90% DMSO and 10% $CHCl_3$) obtained by dropcasting on a copper grid. Uranyl acetate (1% aqueous) was used for staining. 115

6.7 Powder XRD pattern of **1** and **2**. Inset: the zoom-in of the wide-angle region corresponding to the stacking distances. 116

6.8 Structure of the model compound used for computational studies is shown on the left. Right hand side figure shows the geometry-optimized structure of the trimer of model compound. The solid lines indicate the C-H$\cdots$O and π-stacking interactions along with the corresponding distances. 116

6.9 a) and b) Temperature-dependent CD and UV/vis spectra respectively of **1** in 95% MCH and 5% TCE (c = 5×10^{-5} M). Spectra are recorded every 10 °C while cooling down from high temperature in a 10 mm cuvette. c) and d) Cooling curves obtained from CD and UV/vis studies respectively by monitoring spectral changes at 366 nm with a cooling rate of 2 K/minute at different concentrations. . . 117

6.10 Synthetic route to molecules **1-3** 121

7.1 a) Structure of molecules studied. b) Photographs of tunable emission of **1** in different solvents excited at 365 nm. c) Schematic showing the interaction between NDIs and an aromatic solvent molecule. . . 130

7.2 a) and b) UV/vis and fluorescence spectra of **1** (c = 5×10^{-5} M) in different aromatic solvents, respectively. Arrows indicate spectral changes from *o*-DCB to mesitylene. c) TCSPC decay profiles of **1** in benzene ($\lambda_{monitored}$ = 445 nm) and mesitylene ($\lambda_{monitored}$ = 528 nm) for an excitation at 380 nm (c = 5×10^{-5} M). d) A plot of emission maximum (obtained from b)) versus the ionization potential [30] of aromatic solvent molecules. Error bars correspond to the spread in the emission maxima. 131

7.3 a) and b) Normalized UV/vis absorption and emission spectra (λ_{exc} = 350 nm) respectively of **1** in toluene at different concentrations. c) Excitation spectra of **1** in toluene overlapped with the corresponding UV/vis absorption spectra (c = 3.3×10^{-6} M). d) CD spectra of **1** in different aromatic solvents (c = 5×10^{-5} M). 133

7.4 Temperature-dependent UV/Vis absorption (a) and emission spectra (b) of **2** in mesitylene at every 10 °C (c = 5×10^{-5} M). Arrows indicates spectral changes with increase in temperature. 133

7.5 Partial ^{1}H-NMR spectra of **2** in different deuterated solvents (c = 2.5×10^{-3} M) 134

7.6 a) and b) UV/Vis absorption and emission spectra respectively of **NDI-Amph** (c = 5×10^{-5} M). 135

7.7 a) and b) UV/Vis absorption and emission spectra respectively of **NDI-Bolaamph** (c = 5×10^{-5} M). 135

7.8 Calculated vertical transitions of **1′**-solvent complexes using BLYP-D3/DZVP//B3LYP/6-31+G(d,p) level of theory (fwhm = 1000 cm^{-1}). Four aromatic molecules were considered in each complex. The black dashed arrow indicates the changes in the CT transition with increasing electron donating capacity of the solvent molecule. [36] 136

7.9 a) Computed energy level diagram of **1′**+four molecules of mesitylene. b) Frontier molecular orbtials of **1′**+four molecules of mesitylene. H and L stand for HOMO and LUMO respectively. Isovalue of 0.02 e(bhor)$^{-3}$ was used for molecular orbital plots. 137

8.1 Coronene bisimide molecules **CBI-GCH** and **CBI-GACH** under study. 147

8.2 Self-assembly of **CBI-GCH**. a) Normalized UV/vis spectra in two different solvents at 20 °C. b) Top view of the optimized geometry of the CBI dimer (with 3,4,5-triethoxyphenyl groups) by using DFT-based calculations. Carbon: gray, hydrogen: white, oxygen: red and nitrogen: blue. Temperature-dependent c) CD and d) UV/vis spectra (c = 5×10^{-5} M in MCH, 1 cm cuvette). The arrows indicate the spectral changes with decrease in temperature. 148

8.3 Mechanism of self-assembly of **CBI-GCH**. Fraction of aggregates (α) monitored at λ = 322 nm versus temperature at four different concentrations in MCH, with a cooling rate of 2 K/min. The solid line for each curve shows the fit to the temperature-dependent isodesmic model. Each curve is displaced vertically by 0.20 from each other for clarity. 150

8.4 van't Hoff plot for **CBI-GCH** in MCH (c = 5×10^{-5} M). 151

8.5 Morphological studies of **CBI-GCH** (c = 5×10^{-5} M in MCH). a) FESEM image of the film recorded on a glass substrate in the low-vacuum mode. b) AFM height image of a film obtained by drop-casting a solution of in MCH on a freshly cleaved mica surface. c) Cross-sectional analysis along the lines shown in (b). The inset shows the presence of individual fibers with a typical height of 4 nm. d) Histogram of fiber heights obtained from the analysis of four or five independent images with areas of 20×20 μm and 10×10 μm. 152

8.6 Dynamic Light Scattering (DLS) of **CBI-GCH** in MCH (c = 5×10^{-5} M). 153

8.7 a) XRD pattern of **CBI-GCH** on a glass substrate. The inset shows the hexagonal columnar arrangement with lattice parameter (a). b) Low-angle reflections of the XRD pattern that show the peak indexing and d-spacing. 153

8.8 Self-assembly of **CBI-GACH**. a) Normalized UV/vis spectra in chloroform and MCH in a 1 cm cuvette. b) Temperature-dependent UV/vis spectra of in MCH (c = 2.5×10^{-5} M). Arrow indicates spectral changes with decrease in temperature. c) Cooling curves obtained by monitored the absorbance at 472 nm from temperature-dependent UV/vis absorption studies. The solid black line indicates the corresponding fit to the temperature-dependent isodesmic model. [79] d) FESEM image of a film obtained by drop-casting a solution (c = 5×10^{-5} M in MCH) on a glass substrate. 155

8.9 a) AFM height profile of **CBI-GACH** film on mica surface. b) Height analysis along the lines shown in Figure a). 156

8.10 Coassembly of **CBI-GCH** and **CBI-GACH** and resultant chiral amplification. All the experiments were done in MCH (c = 2.5×10^{-5} M). a) and b) CD and UV/vis absorption spectra of the coassembly at different percentages of **CBI-GCH** in a 1 cm cuvette at 20 °C. The arrow indicates the spectral change with an increase in the percentage of the sergeant. c) Anisotropy (g) value monitored at λ = 320 nm as a function of the percentage of **CBI-GCH**. The dashed line that connects the fraction of **CBI-GCH** indicates the linear variation of the g value in the absence of any chiral amplification. d) The kinetics of the assembly seen by monitoring the time taken to reach the CD effect at $\lambda = 320$ nm when preassembled **CBI-GCH** (35%) was added to CBI-GACH at a constant concentration. 157

8.11 Normalized g ($\Delta\epsilon/\epsilon$) value at different concentrations (in MCH) for the co-assembly of **CBI-GCH** and **CBI-GACH**. 158

8.12 a) FESEM and b) AFM images of a film obtained by drop-casting a solution (c = 2.5×10^{-5} M in MCH) containing 40% **CBI-GCH** on glass and freshly cleaved mica surface, respectively. c) AFM cross-sectional analysis of fibers in (b) along the line 1-1′ showing the presence of individual fibers. 158

8.13 Energy as a function of angle between the molecules of a dimer of CBI with 3,4,5-triethoxy phenyl substitution on the imide position studied at BLYP/DZVP using CP2K package. 162

8.14 Synthetic routes to obtain **CBI-GCH** and **CBI-GACH**. 162

9.1 Structure of **CBI-35CH**. 172

9.2 a) and b) Temperature-dependent UV/vis absorption and CD spectra respectively of **CBI-35CH** in MCH (c = 5×10^{-5} M). c) Cooling curves of **CBI-35CH** obtained from CD studies at different concentrations with a cooling rate of 2 K/minute. 173

9.3 a) AFM height image of a film obtained by drop-casting a solution of **CBI-35CH** in MCH (c = 1×10^{-4} M) on a freshly cleaned glass surface. b) Height profile along the lines indicated in Figure a). . . . 174

9.4 a) and b) Full cooling curves of **CBI-35CH** at different concentrations by monitoring CD spectral changes at 320 and 265 nm respectively. c) and d) Temperature-dependent CD spectra in "state A" and "state B" respectively. In c) and d) CD spectra are recorded every 5 °C and 1 °C respectively (c = 5×10^{-5} M). Green arrows indicate spectral changes with decrease in temperature. All studies were performed in MCH. 175
9.5 a) Temperature-dependent CD spectra of **CBI-35CH** in "state B" (MCH, c = 5.9×10^{-5} M). b) Comparison of the CD spectra after 5 days at 0 °C ("state A") and -5 °C ("state B") of **CBI-35CH** (MCH, c = 5×10^{-5} M). 176
9.6 a) Full cooling curves of **CBI-35CH** in different cyclic solvents (c = 7×10^{-5} M for cis-1,2-dimethylcyclohexane and for the rest of the solvents, c = 5×10^{-5} M). The structure of the solvents is shown in the inset of the graph. b) Full cooling curve of **CBI-35CH** in a mixture of cis-trans decalin (c = 3×10^{-5} M). All cooling curves were recorded with a rate of 2 K/minute cooling. 177
9.7 a) Temperature-dependent CD spectra of **CBI-35CH** in *n*-heptane (c = 6.5×10^{-5} M). 178
9.8 a) Structure of **CBI-GCH**. b) and c) Temperature-dependent CD spectra of **CBI-GCH** in MCH and *n*-heptane respectively (c = 5×10^{-5} M). The structure of solvent is shown in the inset of graphs. . 179
9.9 a) Pair correlation function (g(r)) as a function of distance between the center of alkyl tails on the phenoxy wedge to the solvent molecules at different temperatures. b) Probability distribution of **CBI-GCH** as a function of dihedral angle. The scanned dihedral angle is shown in the inset. 180
9.10 Synthetic route to **CBI-35CH** 182

List of Tables

2.1 Stabilization energy for dimer of **1** at different levels of theory. The methods shown in blue color exhibit comparable SE. 17

4.1 Thermodynamic parameters of **1** at different concentrations in MCH/TCE (95:5, v/v) obtained from temperature-dependent CD measurements. ΔG^0 was calculated at 298.15 K. 61

4.2 Comparison of Thermodynamic Parameters for the Assembly of **1** and **2** (in 95% MCH and 5% TCE). Values presented are average of those obtained by fitting to the EMM model [59, 60] for **1** and **2** (from CD and UV/vis studies at different concentrations). The values for **1** are averages of those presented in Table 4.1 and the ones obtained from UV/vis studies. ΔG^0 was calculated at 298.15 K. 63

5.1 Thermodynamic parameters of **PMI_carb_chol** at different concentrations in MCH obtained from temperature-dependent CD measurements. ΔG^0 was calculated at 298.15 K. 97

5.2 Thermodynamic parameters of **PBI_est_chol** at different concentrations in MCH:TCE (8:2, v/v) obtained from temperature-dependent CD measurements. ΔG^0 was calculated at 298.15 K. 101

6.1 Thermodynamic parameters of **1** at different concentrations in MCH/TCE (95:5, v/v) obtained from temperature-dependent CD measurements. ΔG^0 was calculated at 298.15 K. 118

7.1 Fluorescence quantum yield (Φ_f) of different molecules in various aromatic solvents (c = 5×10^{-5} M) 135

8.1 Thermodynamic parameters for the self-assembly of **CBI-GCH** in MCH. DP_N was calculated at 298.15 K. 151

8.2 Assingment of Miller indices to XRD peaks of **CBI-GCH**. 154

9.1 Thermodynamic parameters for the self-assembly of **CBI-35CH** in MCH. ΔH values in paranthesis and the ΔS values are obtained from van't Hoff plot (ln(K_e) vs 1/T) at different concentrations. ΔH values in the column three are obtained from isodesmic fit to the experimental data. Average ΔH values were used to calculate the ΔG at 298.15 K. 174
9.2 Comparison of the transition temperature (CD effect = 0, T_{cross}) of **CBI-35CH** with crystallization temperature for different cyclic solvents (c = 5×10^{-5} M). 177
9.3 Percentage of defects in an assembly of **CBI-35CH** at different temperatures. 180

Chapter 1

Introduction to Supramolecular Polymers and the Mechanisms of Self-Assembly

1.1 Supramolecular polymers

The process of organizing molecules into well-defined structures by using non-covalent and reversible interactions, such as hydrogen-bonding, π-stacking, hydrophobic, electrostatic and van der Waals interactions, is called molecular self-assembly. [1, 2] Self-assembly of small molecules into large, complex and functional architectures has attracted the attention of researchers for the past two decades. This increased interest in self-assembly is due to two factors: firstly, to build functional nanostructures from a bottom-up approach for practical applications, such as in organic electronics; [3–5] and secondly, to understand the process of self-assembly in biological macromolecules, that is, synthetic mimics. [6] This process of formation of large, one-dimensional aggregates from their monomers by using non-covalent interactions is termed supramolecular polymerization and the obtained assembly a supramolecular polymer (Figure 1.1). [7–11] The reversible nature of non-covalent intermolecular interactions manifests in properties like self-healability and stimuli responsiveness which are uncommon in most conventional polymers. [12, 13] Meijer and coworkers

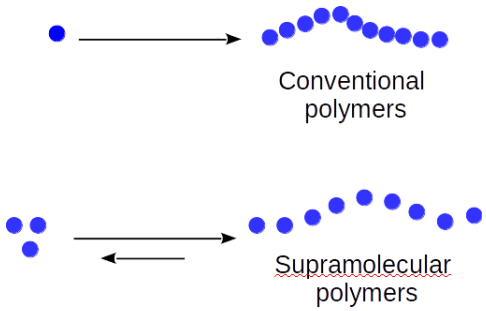

Figure 1.1: A schematic showing the difference between covalent and supramolecular polymers. The blue filled circles indicate the monomers. The distance between the monomers is depicted smaller in conventional polymers to show the covalent bonds, whereas in supramolecular polymers, this distance is larger indicating the non-covalent, weaker nature of bonding between monomers. The reversible arrow for supramolecular polymer indicates the equilibrium between monomers and polymers. This equilibrium is lacking in the formation of covalent polymers.

have utilized quadruple hydrogen-bonding strategy to create functional supramolecular polymers with mechanical and material properties comparable to that of their conventional counter-part. [14] Supramolecular polymers are being explored for applications ranging from biomedicine to electronics. [14, 15]

In spite of the great interest in supramolecular polymers, the control of monodispersity and understanding the dynamics of these polymers is lacking. Recently, Takeuchi and coworkers [16] have utilized the understanding derived from mechanisms of self-assembly of a porphyrin derivative to realize living supramolecular polymers with controlled length and polydispersity. It is thus imperative to study the mechanisms of supramolecular polymerization to address these issues which have received recent attention. The mechanisms underlying supramolecular polymerization are classified into three main types-cooperative, isodesmic and ring-chain polymerization. [17] For ring-chain polymerization, the monomer has to be ditopic, that is, with two end groups connected through a flexible chain or directly attached. This criterion is most often not met in many molecules. The cooperative and isodesmic polymerization mechanisms, which impose no such constraint on the form of the monomer, are thus prevalent.

Herein, we first provide a brief introduction to isodesmic and cooperative mechanisms of self-assembly, along with the different models employed to understand them. In the next section, experimental and computational methods of studying these mechanisms are presented. Finally we conclude the chapter with a section on the aim of the thesis.

1.2 Mechanisms of Supramolecular Polymerization

The mechanisms of supramolecular polymerization have been classified by Meijer and co-workers [17] and a detailed discussion is beyond the scope of this chapter. Herein, the two most important mechanisms of polymerization are briefly discussed.

1.2.1 Isodesmic Polymerization

$$
\begin{aligned}
M + M &\leftrightarrows M_1 \cdots K_e \\
M_1 + M &\leftrightarrows M_2 \cdots K_e \\
M_2 + M &\leftrightarrows M_3 \cdots K_e \\
&\cdots \\
M_{n-1} + M &\leftrightarrows M_n \cdots K_e
\end{aligned}
\tag{1.1}
$$

The isodesmic pathway of polymerization [18] is similar to step-growth polymerization in conventional polymers. Each monomer adds to the short oligomers or to other monomers to form a larger assembly. The strength of such association between two monomers in an oligomer is nearly independent of the length of the stack. This is reflected in a single equilibrium constant (K_e) describing the whole polymerization process (Equation 1.1). Also, the standard Gibbs free energy (ΔG^0) of polymerization decreases with a constant slope (Figure 1.2a). The change in ΔG^0 is constant throughout the course of polymerization. The fraction of aggregated species (denoted by α) versus temperature or concentration is sigmoidal for the isodesmic process, as shown in Figure 1.2b.

1.2.2 Cooperative Polymerization

$$
\begin{aligned}
M + M &\leftrightarrows M^* \cdots K_n \\
M + M^* &\leftrightarrows M^*M \cdots K_e \\
M^*M + M &\leftrightarrows M^*M_2 \cdots K_e \\
&\cdots \\
M^*M_{n-1} + M &\leftrightarrows M^*M_n \cdots K_e
\end{aligned}
\tag{1.2}
$$

Cooperative polymerization is similar to chain-growth or radical polymerization in conventional polymers. It is also called nucleation-growth polymerization. [17]

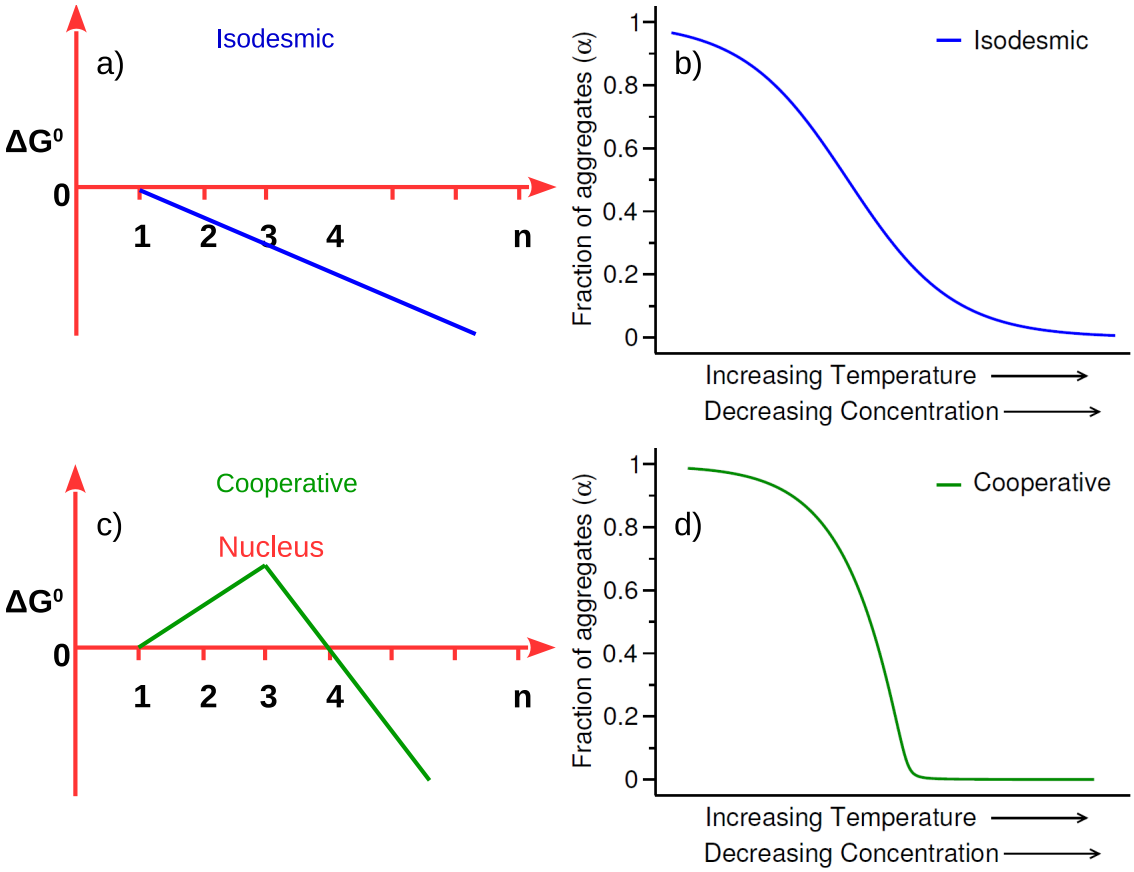

Figure 1.2: a) and c) The standard Gibbs free energy (ΔG^0) profile for an isodesmic and a cooperative supramolecular polymerization respectively. The abscissa represents the oligomer number (n). ΔG^0 remains negative with a constant slope throughout the course of polymerization for an isodesmic pathway, whereas a change in slope is observed for the cooperative counter-part. The oligomer number for which the ΔG^0 is highest is termed as the nucleus. b) and d) Fraction of aggregates (α) versus the concentration or temperature for an isodesmic and a cooperative mechanism respectively. A smooth transition from monomers ($\alpha = 0$) to aggregates ($\alpha = 1$) with a sigmoidal shape is observed for an isodesmic mechanism, whereas the cooperative pathway is characterized by a kink. The temperature or concentration at which kink is observed corresponds to the nucleation step.

The nucleation-elongation or nucleation-growth mechanism was reviewed in great detail by Moore and co-workers. [19] There are three sub-classes of cooperative polymerization, namely nucleated, downhill and anti-cooperative polymerization. [17] In nucleated polymerization, few molecules initially come together to form a small aggregate called a nucleus (M^* in the above equation), which is thermodynamically unfavourable ($\Delta G^0 > 0$) with respect to unassociated monomers; on further addition of a few more monomers (M), the polymerization becomes favourable ($\Delta G^0 < 0$)

leading to the spontaneous formation of one or more large polymers or aggregates (Figure 1.2c). This pathway is characterized by a specific point in temperature (T_e) or concentration at which the nucleus is generated. Thus, the fraction of aggregates (α) versus temperature or concentration is non-sigmoidal with a critical point, as shown in Figure 1.2d. Cooperative-nucleated polymerization is characterized by a parameter called the cooperativity factor, $\sigma = K_n/K_e$, where K_n is the equilibrium constant for nucleus formation and K_e is the equilibrium constant for elongation (Equation 1.2). The cooperativity factor for isodesmic polymerization is unity.

The cooperative-nucleated, downhill and anti-cooperative mechanisms have been reviewed in greater detail by Meijer and co-workers, [17] who described the thermodynamic classification and various properties exhibited by these polymers. In another critical review concerning the self-assembly of functional supramolecular dyes, Würthner and co-workers [20] provided an overview of the strengths of the association constants for a varied class of functional π-conjugated systems.

1.3 Theories of Supramolecular Polymerization

Early theories of supramolecular polymerization by van Gestel, van der Schoot and co-workers. [21–28] adopted the one-dimensional Ising model of conventional polymers and that of models of protein aggregation to supramolecular polymers. These models [27, 28] have been successful in analysing the experimental data leading to thermodynamic parameters of polymerization. However, in these models the equilibrium between the monomers and aggregates was not considered. Recently, another model was developed by Markvoort et al. in which the equilibrium between the monomers and supramolecular polymers is taken into account, [29, 30] an improvement over the previous work. In addition to the thermodynamic parameters one obtains from the above models, it has been recently shown that the kinetics of polymerization (through both experimental and modelling methods) can shed light on the subtle differences in the pathway of supramolecular polymerization. [31]

Many synthetic molecules form supramolecular polymers under given conditions such as solvent, concentration and temperature. Although most of them have been analysed through the model discussed above, [28] it is still unclear as to what molecular features determine the pathway taken by different molecules. A molecular feature based view on the mechanism of supramolecular polymerization can aid researchers to achieve the desired path through intelligent molecular design. Such an approach was pioneered by Meijer and co-workers in their seminal review. [17] It was shown

that electronic, structural and hydrophobic interactions are the sources of cooperativity. Post this work, many examples have been studied and a clearer picture seems to be emerging on the factors leading to cooperativity.

1.4 Methods to Study the Mechanisms of Supramolecular Polymerization

1.4.1 Experimental Techniques

The transformation of molecules from the molecularly dissolved state to the assembled or aggregated or supramolecular polymeric state can be driven through different means such as concentration and temperature.

As a function of either concentration or temperature, one measures quantities such as the ellipticity from circular dichroism (CD), optical density from UV/Vis spectroscopy and fluorescence intensity from photoluminescence spectroscopy at a particular wavelength that is a characteristic of aggregates. The change in the environment of the protons in a molecule as a result of aggregation can also be quantified by the change in the NMR chemical shift as a function of concentration or temperature. The data are typically normalized between zero and one: the value zero corresponds to the molecularly dissolved state whereas unity represents the completely aggregated state possible under the given conditions (Figure 1.3). This curve of the fraction of aggregates(α) versus temperature is termed the cooling curve or melting curve. Throughout the course of this thesis, we refer to such curves as cooling curves. The cooling curves are further fitted with either temperature-dependent cooperative [28–30] or isodesmic [32] models to obtain the various thermodynamic parameters of self-assembly.

Initial studies on the mechanism of self-assembly monitored the changes in ^{1}H NMR chemical shifts as a function of concentration. This method is general in the sense that it can be applied to a varied class of molecules. But the downside of this method is that while working with sufficiently high or low concentration of samples, the NMR peaks might broaden or the changes in chemical shifts can be negligible. In this method of analysis, the number of data points obtained is smaller, thus making a quantitative analysis of the data less accurate. Also, the initial studies using ^{1}H NMR spectroscopy were modelled mainly through the isodesmic mechanism. [33, 34]

Functional chromophores have been extensively studied from an optoelectronic application point of view in the last decade. The advantage of these chromophores

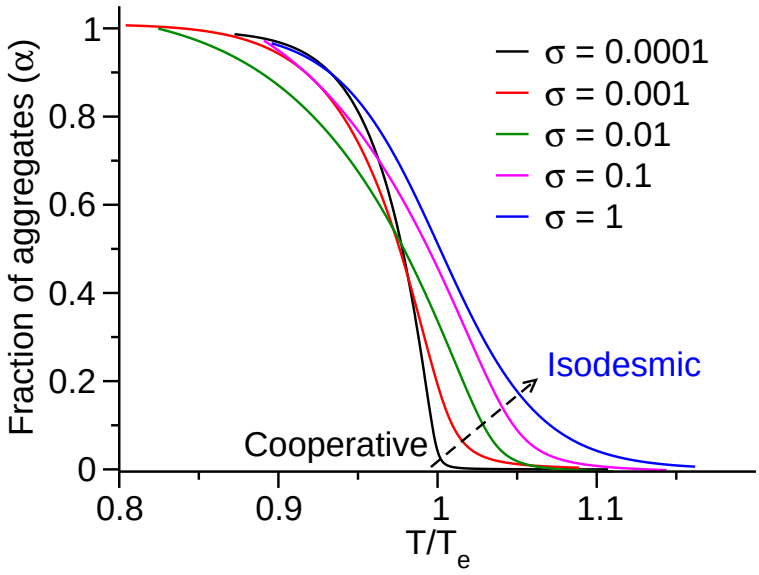

Figure 1.3: The fraction of aggregates (α) versus the reduced temperature (T/T_e) at different values of σ. The lower the value of σ, higher the extent of cooperativity and more steeper the transition from monomers to aggregates. $\sigma = 1$ indicates $K_n = K_e$ and an isodesmic mechanism of self-assembly.

is that their optical properties can be used as a probe for aggregation. [35] Thus, throughout this thesis, we have as such used them to study the mechanisms of self-assembly. In such studies, one needs to cover four orders of magnitude in concentration to examine the full range-from the molecularly dissolved state to the completely aggregated state. Because of the presence of clear signatures of aggregation such as a new absorption band (either hypsochromically or bathochromically shifted) in most cases, the changes recorded are more reliable. However, the number of data points obtained in concentration-dependent studies is smaller than what is required to obtain a good fit of the data to either of the two models discussed earlier. Lack of adequate data can even lead to wrong conclusions in borderline cases. [36] To circumvent these problems, van der Schoot and co-workers showed that temperature-dependent studies are the most appropriate as they provide a greater number of data points, which decreases the error in fitting to the desired model. [28] A recent article by Smulders et al. [32] compares concentration and temperature-dependent studies and demonstrates that the latter are the most appropriate for unambiguously assigning the mechanism of supramolecular polymerization. However, temperature-dependent studies are not suitable in cases where the molecule can show lower critical solution temperature (LCST) behaviour. In such systems, aggregates are formed at high temperature as opposed to the commonly observed

molecularly dissolved state. To overcome the difficulty of LCST when performing temperature-dependent measurements of amphiphilic molecules, a new way of controlling the extent of aggregation has been developed by Korevaar et al. [37] in which the mole fraction of the solvents is varied. This method could also be useful for highly stable assemblies that cannot be disassembled thermally. [38]

We envisage that the mechanism of supramolecular polymerization for non-chromophoric systems can also be monitored through other physical properties of supramolecular polymers, such as viscosity.

1.4.2 Computational Techniques

In contrast to the many experimental studies on the mechanism of supramolecular polymerization, surprisingly, very few computational investigations exist. [39] Atomistic simulations, although truthful to the interactions at play, are beset with issues in accessing length and time scales relevant to supramolecular aggregation. Density functional theory (DFT)-based calculations have been carried out for molecules or small molecular clusters in the gas phase. Grimme and co-workers have shown the significance of dispersion in describing such molecular clusters by using DFT calculations. [40, 41]

DFT calculations were performed on linear hydrogen bonded urea [42] and formamide [43] molecules by considering them as model systems to understand the cooperativity in peptides and proteins. The non-pairwise additive and polarization effects are shown to be the underlying cause of cooperativity in these cases. Recent DFT-based work on benzene-1,3,5-tricarboxamide (BTA) derivatives has shown that the high cooperativity in this system arises from triple helical intermolecular hydrogen bonds. [44] In all these cases, the stabilization energy gained on the addition of a monomer to an existing small oligomer changes rapidly for smaller oligomer sizes and saturates beyond a certain oligomer size. This non-additivity of the stabilization energy reflects the cooperativity (or many-body effects) in these systems, that is, the total energy of the oligomer is more than the sum of its parts, treated pairwise. As capturing these interactions is nontrivial, almost no report exists on the examination of cooperativity, through computation, arising from either hydrophobic interactions or structural effects. To our knowledge, no detailed quantum chemical calculations are available on isodesmic supramolecular systems. It is our thesis that DFT calculations carried out with an appropriate functional (capable of capturing the weak interactions fairly accurately) can be employed to differentiate the mechanism of supramolecular polymerization based on the nature of change in stabilization

energy during the course of polymerization. Polarizable empirical potentials are also potential candidates for capturing the electronic, structural and hydrophobic interactions. But because of the presence of a wide variety of molecular structures, it becomes difficult and laborious to build polarizable empirical models that capture the details of the structure and energetics of polymerization.

1.5 Aim of the thesis

The mechanism of self-assembly of a large number of supramolecular polymers is experimentally studied and most of them are seen to follow either an isodesmic or a cooperative mechanism. In most of the systems, the molecular level origin of mechanisms is unclear and also it is a challenging task to predict the mechanism of self-assembly of a system a priori. Thus the thesis is aimed at rationalizing the isodesmic and cooperative mechanisms of self-assembly based on the nature of intermolecular interaction between the monomers in a supramolecular polymer. To this end, we first perform a preliminary gas phase quantum chemical calculations (Chapter 2) and a thorough literature survey to come up with possible hypothesis on the molecular origin of mechanisms (Chapter 3). Further, this hypothesis is tested both experimentally and computationally in the subsequent Chapters.

Bibliography

[1] Whitesides, G. M.; Boncheva, M. *Proc. Natl. Acad. Sci. USA* **2002**, *99*, 4769–4774.

[2] Menger, F. M. *Proc. Natl. Acad. Sci. USA* **2002**, *99*, 4818–4822.

[3] Würthner, F.; Meerholz, K. *Chem. Eur. J.* **2010**, *16*, 9366–9373.

[4] Wasielewski, M. R. *Acc. Chem. Res.* **2009**, *42*, 1910–1921.

[5] Hoeben, F. J. M.; Jonkheijm, P.; Meijer, E. W.; Schenning, A. P. H. J. *Chem. Rev.* **2005**, *105*, 1491–1546.

[6] Uhlenheuer, D. A.; Petkau, K.; Brunsveld, L. *Chem. Soc. Rev.* **2010**, *39*, 2817–2826.

[7] Brunsveld, L.; Folmer, B. J. B.; Meijer, E. W.; Sijbesma, R. P. *Chem. Rev.* **2001**, *101*, 4071–4098.

[8] Moore, J. S. *Curr. Opin. Colloid Interface Sci.* **1999**, *4*, 108 – 116.

[9] Ciferri, A. *Macromol. Rapid Commun.* **2002**, *23*, 511–529.

[10] Aida, T.; Meijer, E. W.; Stupp, S. I. *Science* **2012**, *335*, 813–817.

[11] Fox, J. D.; Rowan, S. J. *Macromolecules* **2009**, *42*, 6823–6835.

[12] Rieth, S.; Baddeley, C.; Badjic, J. D. *Soft Matter* **2007**, *3*, 137–154.

[13] Yan, X.; Wang, F.; Zheng, B.; Huang, F. *Chem. Soc. Rev.* **2012**, *41*, 6042–6065.

[14] de Greef, T. F. A.; Meijer, E. W. *Nature* **2008**, *453*, 171–173.

[15] Bosman, A. W.; Sijbesma, R. P.; Meijer, E. *Mater. Today* **2004**, *7*, 34 – 39.

[16] Ogi, S.; Sugiyasu, K.; Manna, S.; Samitsu, S.; Takeuchi, M. *Nat. Chem.* **2014**, *6*, 188–195.

[17] De Greef, T. F. A.; Smulders, M. M. J.; Wolffs, M.; Schenning, A. P. H. J.; Sijbesma, R. P.; Meijer, E. W. *Chem. Rev.* **2009**, *109*, 5687–5754.

[18] Martin, R. B. *Chem. Rev.* **1996**, *96*, 3043–3064.

[19] Zhao, D.; Moore, J. S. *Org. Biomol. Chem.* **2003**, *1*, 3471–3491.

[20] Chen, Z.; Lohr, A.; Saha-Möller, C. R.; Würthner, F. *Chem. Soc. Rev.* **2009**, *38*, 564–584.

[21] van Gestel, J.; van der Schoot, P.; Michels, M. A. J. *J. Phys. Chem. B* **2001**, *105*, 10691–10699.

[22] van der Schoot, P.; Michels, M. A. J.; Brunsveld, L.; Sijbesma, R. P.; Ramzi, A. *Langmuir* **2000**, *16*, 10076–10083.

[23] van Gestel, J.; van der Schoot, P.; Michels, M. A. J. *Langmuir* **2003**, *19*, 1375–1383.

[24] van Gestel, J.; van der Schoot, P.; Michels, M. A. J. *Macromolecules* **2003**, *36*, 6668–6673.

[25] van Gestel, J.; van der Schoot, P. *Langmuir* **2006**, *22*, 446–452.

[26] Frieden, C. *Protein Sci.* **2007**, *16*, 2334–2344.

[27] Oosawa, F.; Kasai, M. *J. Mol. Biol.* **1962**, *4*, 10 – 21.

[28] Jonkheijm, P.; van der Schoot, P.; Schenning, A. P. H. J.; Meijer, E. W. *Science* **2006**, *313*, 80–83.

[29] Markvoort, A. J.; ten Eikelder, H. M. M.; Hilbers, P. A. J.; de Greef, T. F. A.; Meijer, E. W. *Nat. Commun.* **2011**, *2*, 509.

[30] ten Eikelder, H. M. M.; Markvoort, A. J.; de Greef, T. F. A.; Hilbers, P. A. J. *J. Phys. Chem. B* **2012**, *116*, 5291–5301.

[31] Korevaar, P. A.; George, S. J.; Markvoort, A. J.; Smulders, M. M. J.; Hilbers, P. A. J.; Schenning, A. P. H. J.; De Greef, T. F. A.; Meijer, E. W. *Nature* **2012**, *481*, 492–496.

[32] Smulders, M.; Nieuwenhuizen, M.; deGreef, T.; vanderSchoot, P.; Schenning, A.; Meijer, E. *Chem. Eur. J.* **2010**, *16*, 362–367.

[33] Tobe, Y.; Utsumi, N.; Kawabata, K.; Nagano, A.; Adachi, K.; Araki, S.; Sonoda, M.; Hirose, K.; Naemura, K. *J. Am. Chem. Soc.* **2002**, *124*, 5350–5364.

[34] Lahiri, S.; Thompson, J. L.; Moore, J. S. *J. Am. Chem. Soc.* **2000**, *122*, 11315–11319.

[35] Würthner, F.; Thalacker, C.; Diele, S.; Tschierske, C. *Chem. Eur. J.* **2001**, *7*, 2245–2253.

[36] Schenning, A. P. H. J.; Jonkheijm, P.; Peeters, E.; Meijer, E. W. *J. Am. Chem. Soc.* **2001**, *123*, 409–416.

[37] Korevaar, P. A.; Schaefer, C.; de Greef, T. F. A.; Meijer, E. W. *J. Am. Chem. Soc.* **2012**, *134*, 13482–13491.

[38] Narayan, B.; Kulkarni, C.; George, S. J. *J. Mater. Chem. C* **2013**, *1*, 626–629.

[39] Maiti, P. K.; Lansac, Y.; Glaser, M. A.; Clark, N. A. *Liquid Crystals* **2002**, *29*, 619–626.

[40] Grimme, S.; Antony, J.; Schwabe, T.; Muck-Lichtenfeld, C. *Org. Biomol. Chem.* **2007**, *5*, 741–758.

[41] Grimme, S. *Chem. Eur. J.* **2012**, *18*, 9955–9964.

[42] Dannenberg, J. J.; Haskamp, L.; Masunov, A. *J. Phys. Chem. A* **1999**, *103*, 7083–7086.

[43] Kobko, N.; Dannenberg, J. J. *J. Phys. Chem. A* **2003**, *107*, 10389–10395.

[44] Filot, I. A. W.; Palmans, A. R. A.; Hilbers, P. A. J.; van Santen, R. A.; Pidko, E. A.; de Greef, T. F. A. *J. Phys. Chem. B* **2010**, *114*, 13667–13674.

Chapter 2

Cooperativity in the Stacking of Benzene-1,3,5-tricarboxamide: The Role of Dispersion

2.1 Introduction

Benzene-1,3,5-tricarboxamides (BTA) are a versatile class of supramolecular polymers. [1] They self-assemble into one-dimensional fibers in solution, [2, 3] are known to exist in solid state, [4, 5] liquid crystalline phases, [6, 7] and also to form low molecular weight organogels [8, 9] depending on the nature of the substituents on the amide group. They have also been used to study concepts of chiral amplification such as the sergeant and soldiers principle [10, 11] and the majority rules [12, 13] in helical self-assembled systems. Due to the ease of synthesis, a wide variety of BTA derivatives are accessible. In addition, the presence of amide groups and the stacking of these molecules in solution render them as ideal model systems for the study of mechanisms of self-assembly that are operative in many biological systems.

In this Chapter, we have carried out quantum chemical calculations to study the stacking behaviour and cooperativity in BTA. In order to reduce the computational costs, molecule **1** which does not contain any substituents has been considered. Thus, it is the simplest member of the BTA family to exhibit features such as hydrogen

Reprinted with permission from "Cooperativity in the stacking of benzene-1,3,5-tricarboxamide: The role of dispersion" *Chem. Phys. Lett.* **2011**, *515*, 226. Copyright 2011, Elsevier. http://www.sciencedirect.com/science/article/pii/S0009261411011377

bonding (HB) and π-π interaction; one obvious omission is the van der Waals (vdW) interaction between the substituents on the amide nitrogen, had they been present. Yet, it is important to carry out these calculations to benchmark the energetics of these interactions and their effect on intermolecular structure.

Pioneering attempts to study the stacking of substituted benzene molecules focussed their attention on small oligomers. [14–17] de Greef and coworkers have examined cooperativity in supramolecular aggregates in the BTA family induced through intermolecular hydrogen bonding, using density functional theory. [18] They demonstrated that apart from electrostatic interactions non-additive effects play a role in the cooperative growth of the stack. Their calculations employing the PBE functional, were carried out for oligomers containing one to seven molecules in the stack. In the present work, we build on these observations, and specifically highlight the importance of dispersive interactions. Our reference calculations for a dimer include Møller-Plesset perturbation theory (MP2), [19] B97-D [20] and Spin-Component-Scaled MP2 (SCS-MP2) [21] levels of theory using Dunnings correlation-consistent, polarized valence triple-zeta basis sets. [22] Using these calculations as a benchmark, we report results from both B3LYP [23, 24] and PBE functional [25] based calculations for oligomers up to a decamer. Additional calculations have also been carried out by augmenting the PBE functional with empirical vdW corrections based on the parametrization of Williams and Malhotra. [26] These have been shown to be crucial in the accurate description of weakly bound complexes such as the ones described here. These results can in turn be used to build and refine atomistic force fields to enable the study of aggregation mechanisms in solution.

2.2 Computational details

Electronic structure calculations were performed within density functional theory (DFT) using the GAUSSIAN-03 [27] package. The geometry optimizations were carried out using the B3LYP hybrid functional and 6-31+G(d,p) basis set. These are shown in the literature to capture weak HB fairly well. [28, 29] Basis set superposition error (BSSE) in energy was calculated using the counterpoise method. [30] The Merz and Kollman (MK) method [31, 32] was used to calculate the atomic charges. Electrostatic potential surfaces were generated by mapping the total self-consistent field electron density onto a surface of constant molecular potential of 4×10^{-4} e/bohr^3. Further, geometry optimizations for the monomer and dimer of **1** were carried out using MP2/6-31+G(d,p), MP2/cc-PVTZ as well as SCS-MP2 (with

the same basis sets) levels of theory. As the study of larger oligomers with these methods and basis sets are prohibitively expensive, such calculations were carried out using the PBE functional [25] with a plane wave basis set as implemented in the CPMD code. [33] These calculations were performed with the plane wave code as it scaled well on distributed memory computing platforms. Since functionals such as PBE may not capture the van der Waals contribution adequately, empirical vdW corrections were employed. The use of PBE plus empirical vdW calculations for the higher oligomers was tested against results obtained from wave function based methods with Dunnings correlation-consistent, triple-zeta plus polarization basis set. [22] The empirical van der Waals corrections were based on the parameters derived by Williams and Malhotra. [26] In the plane wave calculations for the oligomers, the energy cutoff for the expansion of wave function was 85 Ry. The oligomers were studied under isolated conditions using a tetragonal box of linear dimensions of 40 Å, 14 Å, 14 Å along the x, y and z directions, respectively. Cluster boundary conditions [34] and the Hockney Poisson solver [35] consistent with calculations for an isolated system were empolyed. Initial configurations of the oligomers were in a stacked geometry with the stack axis oriented along the Cartesian x-axis. In the plane wave calculations, the effect of the nuclei and the core electrons on the valence shell was treated using norm conserving Troullier-Martins pseudopotentials. [36] At the optimized geometry, the maximum force component on any atom was below 4.5×10^{-4} a.u. Dipole moments of stacks were calculated using the Berry's phase formalism [37] as implemented in the CPMD code. [33] The structures were visualised using Visual Molecular Dynamics (VMD). [38]

2.3 Results and discussion

2.3.1 Molecular assembly

Weak hydrogen bonding has been treated with different ab initio methods and also using various basis sets. [39–41] The B3LYP hybrid functional along with diffuse and polarizable basis functions is expected to describe weak hydrogen bonding fairly well. [42] Also recently, results on formic acid using a plane wave basis set are shown to be in reasonably good agreement with those obtained from localised Gaussian basis sets. [43] Thus, in the current calculations, larger oligomers have been studied using a plane wave basis set with the PBE functional.

The molecule under study is shown in Figure 2.1. Different initial conformations

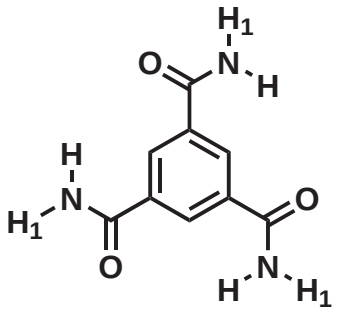

Figure 2.1: Structure of benzene-1,3,5-tricarboxamide (**1**) used for computational studies.

of **1** in optimization all led to a minimum energy planar structure. This planarity in geometry and the C_3-symmetry of the molecule is reflected in the small value of its dipole moment (0.149 D). The stability offered by oligomerization has been quantified through a "Stabilisation energy (SE)", defined as SE = (E_n - n×E_1)/(n-1) where n is the number of molecules in the oligomer. Factors contributing to the stability of the stacks include hydrogen bonding, π-π and van der Waals interactions . [44] A recent work has examined DFT and DFT-D methods to describe the distance dependence of hydrogen bonding interactions in bimolecular complexes. [45] Post Hartree-Fock methods such as the Møller-Plesset perturbation theory (MP2) as well as the SCS-MP2 method are expected to better capture these interactions.

2.3.2 The dimer of BTA

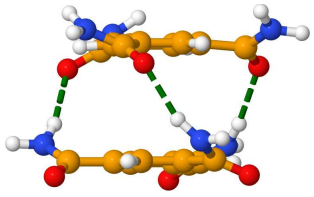

Figure 2.2: Optimized geometry of a dimer of **1**. The intermolecular hydrogen-bonds are shown in bold-dotted green lines.

The dimer of BTA is characterized by the formation of three intermolecular hydrogen bonds (Figure 2.2), leading to its stabilization. Geometry optimization at the MP2/6-31+G(d,p) level of theory for the BTA dimer yielded a counterpoise-corrected SE of -19.1 kcal/mol. This is in contrast to the value of -6.8 kcal/mol for the dimer at B3LYP/6-31+G(d,p) level of theory. At least a part of the energy deficit

Method	Basis set	Counterpoise corrected stabilization energy (SE) (kcal/mol)
B97-D	6-31+G(d,p)	-21.3
	cc-PVDZ	-19.3
	cc-PVTZ	-21.1
MP2	6-31+G(d,p)	-19.1
	cc-PVTZ	-22.8
SCS-MP2	6-31+G(d,p)	-13.4
SCS-MP2	cc-PVTZ	-14.6
PBE/85 Ry	Plane wave	-9.1 (no BSSE)
PBE/85 Ry + vdW	Plane wave	-16.0 (no BSSE)
B3LYP	6-31+G(d,p)	-6.8

Table 2.1: Stabilization energy for dimer of **1** at different levels of theory. The methods shown in blue color exhibit comparable SE.

in the DFT calculations could likely be due to the inadequate treatment of dispersive interactions. Incomplete basis sets too can cause large variations in stabilization energies. Hence, we have carried out geometry optimizations (with no constraints) of the monomer and dimer at MP2 level using Dunnings correlation -consistent polarized valence triple-zeta basis sets. [22] The counterpoise corrected SE are shown in Table 2.1. At MP2/cc-PVTZ level of theory, its value is -22.8 kcal/mol. Further, the stabilization energies of the dimer calculated using the Grimmes functional, B97-D [20] in various basis sets ranges between -19.3 and -21.3 kcal/mol (Table 2.1). These observations point out the significant amount of dispersion contribution to the stabilization of the BTA dimer among various levels of theory. However, it is also believed that the MP2 method may overestimate the dispersion contribution [46] and an alternative called the Spin-Component-Scaled MP2 (SCS-MP2) has been developed by Grimme and coworkers. [21] We have performed the scaling of spin components obtained from MP2 level of theory of the BTA monomer and dimer to obtain stabilization energies at the SCS-MP2 level using different basis sets. The counterpoise corrected SE obtained at SCS-MP2/cc-PVTZ level of theory is -14.6 kcal/mol, whereas the SE obtained at PBE/85 Ry + vdW level of theory is -16.0 kcal/mol. Thus, there is good agreement between the SE obtained at SCS-MP2/cc-PVTZ and PBE/85 Ry + vdW level of theory. The MP2 energies too are comparable to the van der Waals corrected stabilization energies than the uncorrected value. We can thus safely conclude that dispersion interactions contribute significantly to the stabilization of the BTA dimer and that PBE/85 Ry + vdW can be employed to

study higher oligomers. In marked contrast to the performance of PBE/85 Ry + vdW, the stabilization energies obtained through PBE/85 Ry as well as B3LYP/6-31+G(d,p) levels of theory are much below the values obtained through MP2 or SCS-MP2 calculations, as seen from Table 2.1.

2.3.3 Higher oligomers of BTA

Firstly, the geometries of BTA oligomers were optimized using B3LYP and PBE exchange and correlation functionals. The behaviour of the stabilization energy obtained by these methods is shown in Figure 2.3. The SE decreases with increasing oligomer size (n) and should eventually converge to a bulk value. On fitting the stabilization energies obtained from the PBE/85 Ry calculations to a polynomial, a "bulk" (i.e., converged) SE value of around -17.0 kcal/mol is obtained, which is comparable to the value of -17.7 kcal/mol obtained for an infinite chain of trimethyl substituted BTA using the same PBE functional by de Greef and coworkers. [18] The SE curve for the B3LYP functional exhibits a similar rate of convergence as the PBE curve; however its values are estimated to be lower by about 4 kcal/mol than the PBE result.

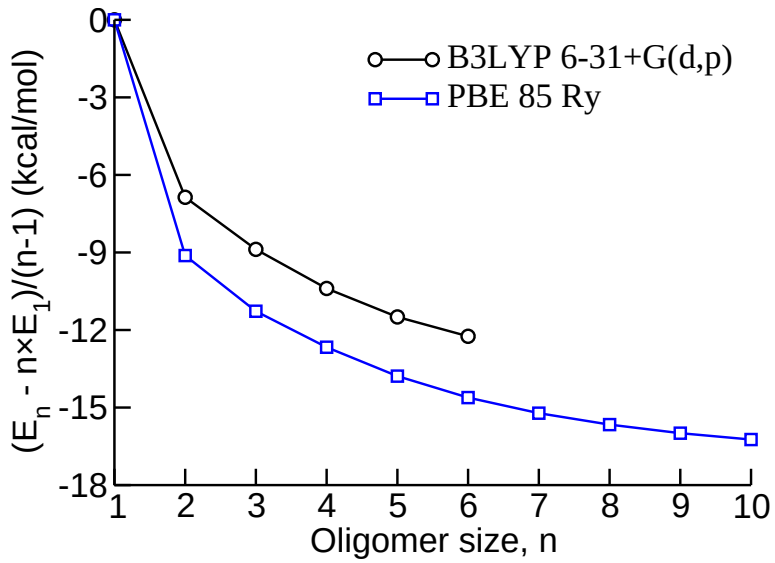

Figure 2.3: Stabilisation energy of oligomers of **1** obtained using B3LYP/6-31+G(d,p) and PBE/85 Ry levels of theory.

Having identified the significant contribution of the dispersion interaction towards the stabilization of the dimer (as discussed in the previous subsection), larger oligomers of BTA were optimized for their geometries with empirical vdW correction

added on top of the PBE functional using the CPMD code. [33] The resulting stabilization energies are shown in Figure 2.4. The dimerization energy for the PBE/85 Ry + vdW calculation is found to be -16.0 kcal/mol which is much closer to the SCS-MP2/cc-PVTZ estimate of -14.6 kcal/mol than those obtained from either the PBE/85 Ry or the B3LYP calculations. Thus, in the following, we discuss in detail, the results obtained from PBE/85 Ry + vdW level of theory. Independent self-consistent field calculations on the optimized configurations carried out without the van der Waals corrections yielded the contribution of DFT to the total SE. The difference between the SE with and without vdW corrections yielded the van der Waals contribution to stabilization. Figure 2.4 shows that the van der Waals contribution is quite large for small oligomers, however it decreases and plateaus off for higher oligomers. The intermolecular distance in small oligomers is short ($\approx$ 3.4 Å), resulting in a larger van der Waals stabilization energy. This distance increases to a value of around 3.7 Å for higher oligomers thus reducing the contribution of van der Waals interaction to the stabilization energy.

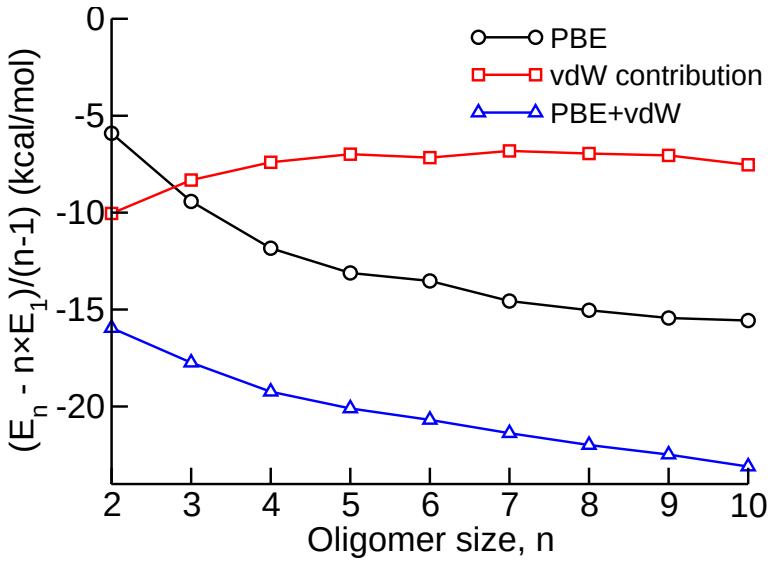

Figure 2.4: Stabilisation energy of oligomers of **1** as a function of their size, n using PBE/ 85 Ry level of theory including empirical vdW corrections.

Fitting the data in Figure 2.4 to polynomial functions, "bulk" SE values for the PBE energy is found to be about -18.9 kcal/mol and that of the total SE to be about -27.1 kcal/mol. Thus, around -8.2 kcal/mol of the SE in the bulk stack arises from vdW interaction.

From the optimized molecular geometries of the oligomers of **1**, different geometrical parameters can be studied. One such geometrical parameter is the $r_{N\cdots O}$

distance i.e., the distance between the nitrogen of one molecule and the corresponding hydrogen bonded oxygen of the neighbouring molecule. For the decamer, using PBE/85 Ry + vdW correction this value is 2.88 Å, which is comparable to the value of 2.95 Å obtained by de Greef and coworkers [18] using the same functionals for an infinite chain of trimethyl substituted BTA.

One way to characterize the intermolecular stacking is to observe the twist angles; these twist angles are defined as (1)the angle between the hydrogen bonded H-N plane (H-N-C_{Ar}) and the benzene plane (N-C_{Ar}-C_{Ar}) designated as dihedral angle (ϕ_1, H-N-C_{Ar}-C_{Ar}), (2) the angle between the amide carbonyl plane (O-$C_{carbonyl}$-C_{Ar}) and the benzene plane ($C_{carbonyl}$-C_{Ar}-C_{Ar}) designated as dihedral angle (ϕ_2, O-$C_{carbonyl}$-C_{Ar}-C_{Ar}) and (3) the angle between the non-hydrogen bonded H_1-N plane (H_1-N-C_{Ar}) and the benzene plane (N-C_{Ar}-C_{Ar}) designated as dihedral angle (ϕ_3, H_1-N-C_{Ar}-C_{Ar}). For the decamer, ϕ_1, ϕ_2 and ϕ_3 for the core region of the stack are found to be approximately 42.3° (36.8°), 46.0° (42.4°) and 40.8° (45.5°) respectively, using PBE/85 Ry + vdW level of theory. The values in the parentheses are the corresponding dihedral angles for the experimentally studied molecule, N,N′,N″-tris(2-methoxyethyl) benzene-1,3,5-tricarboxamide. [5] Also, the average of all the three dihedral angles is calculated to be 43.02° for the BTA decamer using PBE/85 Ry + vdW level of theory which is again comparable to the value of 40.5° obtained at the same level of theory for an infinite chain of trimethyl substituted BTA. [18]

2.3.4 Cooperativity

An important feature of supramolecular aggregates which emerges from these calculations is cooperativity. Cooperativity captures the influence that a third molecule exerts on the interaction between a pair of molecules. [47] Here we examine cooperativity in light of the subtle, but systematic changes observed in various geometrical parameters in the core region of the oligomers obtained using PBE/85 Ry + vdW level of theory.

The hydrogen bonding between the oxygen of the carbonyl of one molecule and the hydrogen of the amide group belonging to its neighbour is a key element in oligomerization. The length of the hydrogen bond between the molecules in the central (or, core) region of an oligomer is plotted as a function of oligomer size in Figure 2.5a. It decreases monotonically with increasing oligomer size, from an initial value of 1.93 Å to a converged value of 1.82 Å. This gradual change (albeit for small

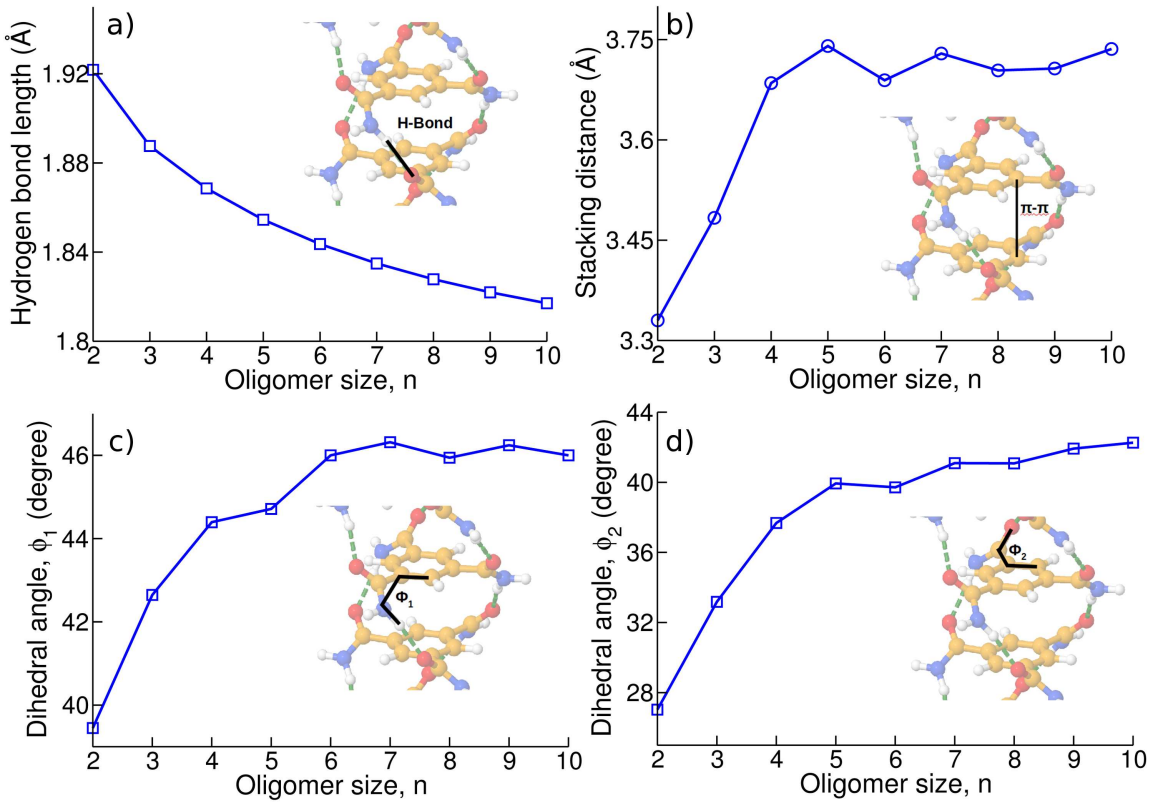

Figure 2.5: Variation of a) hydrogen bond length, b) π-π stacking distance, c) dihedral angle H-N-C_{Ar}-C_{Ar} (ϕ_1) and d) dihedral angle O-$C_{carbonyl}$-C_{Ar}-C_{Ar} (ϕ_2) in the core region of the oligomers as a function of its size, n using PBE/85 Ry + vdW level of theory. The inset of each sub-figure shows the pictorial representation of the corresponding parameter from the core an oligomer.

oligomer sizes) is a manifestation of cooperativity - as monomers are added, intermolecular distances in the core region of the oligomer shorten. The HB lengths obtained from B3LYP/6-31+G(d,p) and PBE/85 Ry + vdW level of theory follow similar trends and are comparable to the experimentally determined HB length of 2.09 Å in N,N′,N″-tris(2-methoxyethyl)benzene-1,3,5-tricarboxamide. [5] The HB lengths for another derivative, N,N′,N″-tris(3,3-dimethylbutyric acid methyl ester)benzene-1,3,5-tricarboxamide in the solid state is also around 2.06 Å. [2] The slight deviation of the calculated HB length from the experimental values can be attributed to the presence of alkyl substitutents in the experimentally studied molecules when compared to just hydrogen (H_1) in **1** studied here.

Steep increases of about 0.15 Å and 0.20 Å in the π-π stacking distance (Figure 2.5b) are observed between the dimer and the trimer and between the trimer and the tetramer respectively; however for larger oligomers, the rate of increase is

diminished. As the stacking distance increases, the hydrogen-bond angle (N-H$\cdots$O) approaches closer to the ideal value of 180°, contributing to the stabilization of the oligomer. PBE/85 Ry + vdW level of calculations yield a stacking distance of 3.72 Å which is comparable to the experimental stacking distance of 3.62 Å. [5]

It may be recalled that although the monomer is planar, a nonzero twist angle is set between the amide plane and the benzene ring plane in larger oligomers. Thus, the nature of the change of this twist angle is important from the point of view of cooperativity. From Figure 2.5c and d, we can see that these dihedral angles (ϕ_1 and ϕ_2) increase steeply as a function of oligomer size, similar to the behaviour exhibited by the stacking distance. The converged dihedral angles are also in good agreement with experimental values of 36.8°, and 42.4°. [5]

2.3.5 Dipole moment

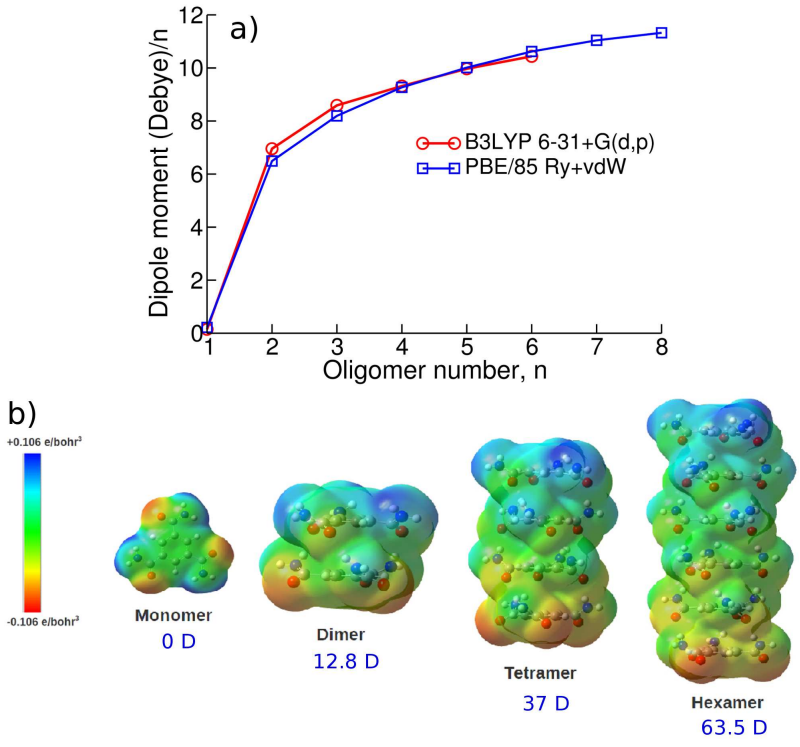

Figure 2.6: a) Mean dipole moment per molecule as a function of oligomer size, n calculated at two different levels of theory. b) Electrostatic potential isosurfaces plotted on electronic density isosurfaces of 4×10^{-4} e/bohr^3 for different oligomers of **1** calculated from the optimized geometries obtained at B3LYP/6-31+G(d,p) level of theory. The total dipole moment of oligomers is mentioned in blue color below the respective oligomers.

Another noteworthy feature of the stacks of **1** is the enormous increase in the dipole moment of the oligomer as its size increases, manifesting in high surface potentials observed experimentally using Kelvin probe microscopy. [6] Dipole moment arises from the directionality and alignment of the hydrogen bonds along the long axis of the stack. The dipole moment component along the long axis add up to give rise to a macrodipole for the oligomer. The plot of dipole-moment per molecule (DM/oligomer size,n) versus the oligomer size shows a non-linear behaviour (Figure 2.6a)). DM/n increases steeply for smaller oligomers and saturates to a value of 12.35 D for an infinitly long oligomer as obtained from the PBE/85 Ry + vdW calculations. These non-linear changes in the dipole moment per molecule reaffirm the cooperativity of aggregation in this system.

One can obtain insight into the macrodipole by mapping the total electron density on the surface of constant electrostatic potential. This approach was used to visualise the electron density distribution for different oligomers and Figure 2.6b shows such maps. It has been shown that, the charges derived from Merz and Kollman (MK) method reproduce the experimental dipole moments fairly accurately, given the level of theory and the optimized geometry. [48]

2.4 Conclusions

Quantum chemical calculations have been employed to study the supramolecular organization of benzene-1,3,5-tricarboxamide in the gas phase. Accurate MP2 and SCS-MP2 reference calculations using Dunning's correlation-consistent, polarized valence triple-zeta basis set have demonstrated the significant role played by dispersive forces in the stabilization of a dimer of BTA. Further, we have carried out DFT calculations of oligomers of sizes up to a decamer using the PBE functional augmented by empirical van der Waals corrections. These were performed in a plane wave basis set. The bulk stabilization energy of a stack of **1** is estimated to be -27.1 kcal/mol using PBE/85 Ry + vdW level of theory. vdW interactions contribute a significant amount (about -8.2 kcal/mol) to the total stabilization energy and the calculations reproduce the experimental value of intermolecular distance. The formation of threefold intermolecular hydrogen bonds is a crucial step in the oligomerization of BTA. However, pair-wise interactions are seen to be further stabilized by the presence of other molecules in the aggregate or stack - a feature termed, cooperativity. Cooperativity has been shown to reflect in different parameters of the central hydrogen bonding pair and also in the variation of dipole moment of the stacks of **1**. The

macrodipole-macrodipole interaction between neighbouring stacks in solution can be expected to result in the formation of fibers observed experimentally. [2]

Bibliography

[1] Cantekin, S.; de Greef, T. F. A.; Palmans, A. R. A. *Chem. Soc. Rev.* **2012**, *41*, 6125–6137.

[2] Bose, P. P.; Drew, M. G. B.; Das, A. K.; Banerjee, A. *Chem. Commun.* **2006**, 3196–3198.

[3] Mes, T.; Smulders, M. M. J.; Palmans, A. R. A.; Meijer, E. W. *Macromolecules* **2010**, *43*, 1981–1991.

[4] Jiménez, C. A.; Belmar, J. B.; Ort´iz, L.; Hidalgo, P.; Fabelo, O.; Pasán, J.; Ruiz-Pérez, C. *Cryst. Growth Des.* **2009**, *9*, 4987–4989.

[5] P. Lightfoot, M.; S. Mair, F.; G. Pritchard, R.; E. Warren, J. *Chem. Commun.* **1999**, 1945–1946.

[6] Fitié, C. F. C.; Roelofs, W. S. C.; Kemerink, M.; Sijbesma, R. P. *J. Am. Chem. Soc.* **2010**, *132*, 6892–6893.

[7] Stals, P.; Smulders, M.; Martn-Rapn, R.; Palmans, A.; Meijer, E. *Chem. Eur. J.* **2009**, *15*, 2071–2080.

[8] Danila, I.; Riobe, F.; Puigmarti-Luis, J.; Perez del Pino, A.; Wallis, J. D.; Amabilino, D. B.; Avarvari, N. *J. Mater. Chem.* **2009**, *19*, 4495–4504.

[9] Roosma, J.; Mes, T.; Leclère, P.; Palmans, A. R. A.; Meijer, E. W. *J. Am. Chem. Soc.* **2008**, *130*, 1120–1121.

[10] Smulders, M. M. J.; Schenning, A. P. H. J.; Meijer, E. W. *J. Am. Chem. Soc.* **2008**, *130*, 606–611.

[11] Smulders, M. M. J.; Filot, I. A. W.; Leenders, J. M. A.; van der Schoot, P.; Palmans, A. R. A.; Schenning, A. P. H. J.; Meijer, E. W. *J. Am. Chem. Soc.* **2010**, *132*, 611–619.

[12] van Gestel, J.; Palmans, A. R. A.; Titulaer, B.; Vekemans, J. A. J. M.; Meijer, E. W. *J. Am. Chem. Soc.* **2005**, *127*, 5490–5494.

[13] Smulders, M. M. J.; Stals, P. J. M.; Mes, T.; Paffen, T. F. E.; Schenning, A. P. H. J.; Palmans, A. R. A.; Meijer, E. W. *J. Am. Chem. Soc.* **2010**, *132*, 620–626.

[14] Bushey, M. L.; Hwang, A.; Stephens, P. W.; Nuckolls, C. *J. Am. Chem. Soc.* **2001**, *123*, 8157–8158.

[15] Rochefort, A.; Bayard, .; Hadj-Messaoud, S. *Adv. Mater.* **2007**, *19*, 1992–1995.

[16] Bushey, M. L.; Hwang, A.; Stephens, P. W.; Nuckolls, C. *Angew. Chem. Int. Ed.* **2002**, *41*, 2828–2831.

[17] Bayard, .; Hamel, S.; Rochefort, A. *Org. Electron.* **2006**, *7*, 144 – 154.

[18] Filot, I. A. W.; Palmans, A. R. A.; Hilbers, P. A. J.; van Santen, R. A.; Pidko, E. A.; de Greef, T. F. A. *J. Phys. Chem. B* **2010**, *114*, 13667–13674.

[19] Möller, C.; Plesset, M. S. *Phys. Rev.* **1934**, *46*, 618–622.

[20] Grimme, S. *J. Comput. Chem.* **2006**, *27*, 1787–1799.

[21] Grimme, S. *J. Chem. Phys.* **2003**, *118*, 9095–9102.

[22] Dunning, T. H. *J. Chem. Phys.* **1989**, *90*, 1007–1023.

[23] Becke, A. D. *J. Chem. Phys.* **1993**, *98*, 5648–5652.

[24] Lee, C.; Yang, W.; Parr, R. G. *Phys. Rev. B* **1988**, *37*, 785–789.

[25] Perdew, J. P.; Burke, K.; Ernzerhof, M. *Phys. Rev. Lett.* **1996**, *77*, 3865–3868.

[26] Williams, R. W.; Malhotra, D. *Chem. Phys.* **2006**, *327*, 54–62.

[27] Frisch, M. J. et al. Gaussian 09 Revision D.01. Gaussian Inc. Wallingford CT 2009.

[28] Sim, F.; St. Amant, A.; Papai, I.; Salahub, D. R. *J. Am. Chem. Soc.* **1992**, *114*, 4391–4400.

[29] Pudzianowski, A. T. *J. Phys. Chem.* **1996**, *100*, 4781–4789.

[30] Boys, S.; Bernardi, F. *Mol. Phys.* **1970**, *19*, 553–566.

[31] Singh, U. C.; Kollman, P. A. *J. Comput. Chem.* **1984**, *5*, 129–145.

[32] Besler, B. H.; Merz, K. M.; Kollman, P. A. *J. Comput. Chem.* **1990**, *11*, 431–439.

[33] Hutter, J.; Ballone, J. P.; Bernasconi, M.; Focher, P.; Fois, E.; Goedecker, S.; Marx, D.; Parrinello, M.; Tuckerman, M. E.; CPMD version 3.13.2, Max Planck Institut fuer Festkoerperforschung, Stuttgart, and IBM Zurich Research Laboratory, 1990.

[34] Barnett, R. N.; Landman, U. *Phys. Rev. B* **1993**, *48*, 2081–2097.

[35] Hockney, R. W. *Meth. Comput. Phys.* **1970**, *9*, 136.

[36] Troullier, N.; Martins, J. L. *Phys. Rev. B* **1991**, *43*, 1993–2006.

[37] King-Smith, R. D.; Vanderbilt, D. *Phys. Rev. B* **1993**, *47*, 1651–1654.

[38] Humphrey, W.; Dalke, A.; Schulten, K. *J. Mol. Graphics* **1996**, *14*, 33–38.

[39] Riley, K. E.; Pitoňák, M.; Jurečka, P.; Hobza, P. *Chem. Rev.* **2010**, *110*, 5023–5063.

[40] Dkhissi, A.; Ramaekers, R.; Houben, L.; Adamowicz, L.; Maes, G. *Chem. Phys. Lett.* **2000**, *331*, 553–560.

[41] Wojtulewski, S.; Grabowski, S. J. *Chem. Phys. Lett.* **2003**, *378*, 388–394.

[42] Lozynski, M.; Rusinska-Roszak, D.; Mack, H.-G. *J. Phys. Chem. A* **1998**, *102*, 2899–2903.

[43] Tosoni, S.; Tuma, C.; Sauer, J.; Civalleri, B.; Ugliengo, P. *J. Chem. Phys.* **2007**, *127*, 154102.

[44] Grimme, S. *Angew. Chem. Int. Ed.* **2008**, *47*, 3430–3434.

[45] Thanthiriwatte, K. S.; Hohenstein, E. G.; Burns, L. A.; Sherrill, C. D. *J. Chem. Theory Comput.* **2011**, *7*, 88–96.

[46] Bachorz, R. A.; Bischoff, F. A.; Hofener, S.; Klopper, W.; Ottiger, P.; Leist, R.; Frey, J. A.; Leutwyler, S. *Phys. Chem. Chem. Phys.* **2008**, *10*, 2758–2766.

[47] Hunter, C.; Anderson, H. *Angew. Chem. Int. Ed.* **2009**, *48*, 7488–7499.

[48] Maciel, G. S.; Garcia, E. *Chem. Phys. Lett.* **2005**, *409*, 29–33.

Chapter 3

What Molecular Features Govern the Mechanism of Supramolecular Polymerization?

3.1 Introduction

The mechanism of self-assembly of a large number of supramolecular polymers has been experimentally studied. These are seen to follow either an isodesmic or a cooperative mechanism. [1, 2] In most of the systems, the molecular level origin of mechanisms is unclear. Further, it is a challenging task to predict the mechanism of self-assembly a priori. Thus, to shed light on the molecular origin of mechanisms, here we undertake a critical survey of literature and come up with a rationale for the experimental observations.

Four different classes of molecules, within each of which specific examples of compounds exhibiting either an isodesmic or cooperative mechanism are discussed. We ascribe the observed differences in the polymerization mechanisms to characteristic molecular features. Common molecular motifs are identified across these four classes and are discussed in the antepenultimate section. This section also presents our computational results on three systems which strengthen our hypothesis. We conclude with a summary and discuss the challenges and possible future directions.

Reprinted with permission from "What Molecular Features Govern the Mechanism of Supramolecular Polymerization?" *ChemPhysChem.* **2013**, *14*, 661-673. Copyright 2013, Wiley-VCH. http://onlinelibrary.wiley.com/doi/10.1002/cphc.201200801/full

3.2 Discussion

We have chosen systems for which the mechanism is clearly elucidated by using either concentration- or temperature-dependent measurements. In the following discussion, we consider many classes of molecules and compare the mechanisms exhibited by them in each class in terms of intermolecular interactions (Figure 3.1).

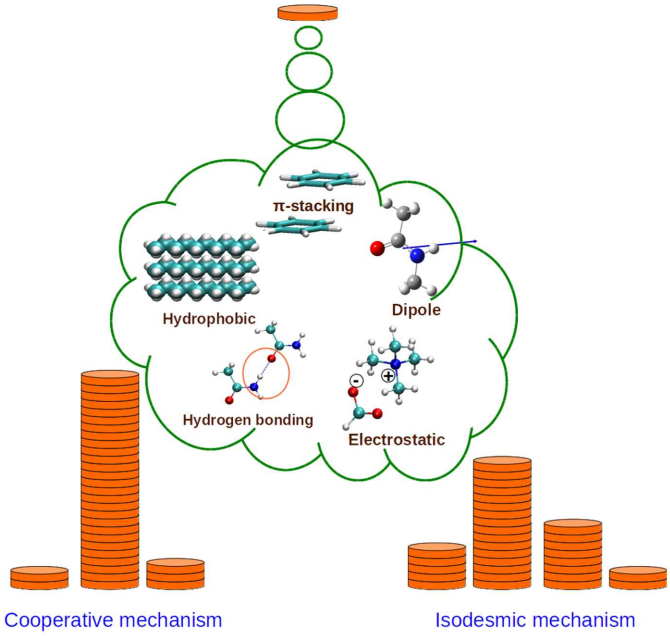

Figure 3.1: A schematic illustrating the various intermolecular interactions which aid in the supramolecular polymerization of a small molecule (represented by disc).

3.2.1 Benzene-1,3,5-tricarboxamide (BTA) Family

BTA derivatives are one of the most studied classes of molecules from a mechanistic point of view as well as for applications ranging from liquid-crystalline materials to biomedical areas. [3]

The N,N′,N″-trialkylbenzene-1,3,5-tricarboxamide (**1**, Figure 3.2) bearing chiral side chains on the amide nitrogen atoms was shown to form long, columnar and chiral aggregates in the presence of apolar solvents such as heptane and methylcyclohexane (MCH) at dilute concentrations. [4] The mechanism of supramolecular polymerization has been modelled using the modified theory of the nucleation-growth model, [6] originally proposed by Oosawa and Kasai. [7] The experimental data follow a cooperative behaviour, as shown in Figure 3.2a, and provide insights into the

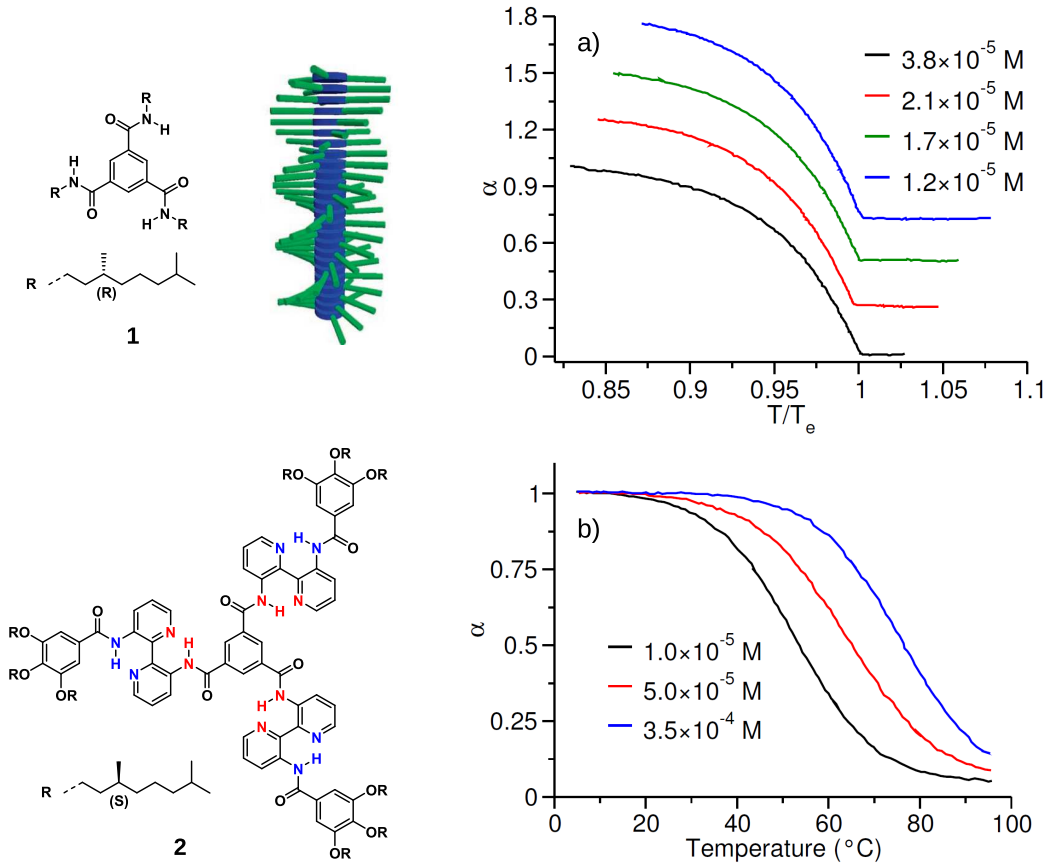

Figure 3.2: Molecular structures of BTA derivatives **1** along with a schematic of its assembly and **2**. a) Fraction of aggregates (α) versus reduced temperature for molecule **1** at different concentrations in heptane with a 0.25 offset for each concentration. Reproduced with permission from reference [4]. Copyright 2008 American Chemical Society. b) α as a function of temperature for different concentrations of **2** in methylcyclohexane. Reproduced with permission from reference [5]. Copyright 2011 Royal Society of Chemistry.

thermodynamics of the polymerization. The molecules self-assemble in a cooperative manner, that is, they follow the nucleation-elongation model of self-assembly, which is reflected in the low value of the cooperativity parameter, $\sigma = 10^{-6}$. The supramolecular polymerization is driven primarily by triple helical hydrogen bonding between the amide groups, thus leading to the formation of H-type aggregates. [4] Recent computational work has elucidated cooperativity in this class. [8, 9] In a BTA stack, the amide groups of the molecules are rotated out of the benzene plane by 45° to form triple helical hydrogen bonds, although the isolated molecule in the gas phase is planar. The dominant contributor to the stabilization of the stacks stems from these hydrogen bonds. Dispersion, calculated through the empirical correction

to DFT, [8] is found to contribute about 30% to the stabilization of the stack. As the hydrogen bonds are all directed along the long axis of the stack, the latter acquires a macrodipole. [8–10]

Another derivative of BTA, which possesses large 3,3′-bis(acylamino)- 2,2′-bipyridine groups on the amide nitrogen atoms (**2**, Figure 3.2), also self-assembles to form chiral aggregates in dilute MCH solution. [5] A detailed study of the superstructure of **2** has been carried out by using combined experiments and theory. In MCH, **2** aggregates through an isodesmic pathway, as shown in Figure 3.2b. Quantum chemical calculations [5] show no evidence of intermolecular hydrogen bonding. Moreover, the inter-disc distance of 3.4 Å does not allow for a pronounced twisting of the central amide groups. X-ray diffraction studies [5] and quantum chemical calculations suggest a rotation angle of 10-40° between neighbouring molecules in a stack, and this small angle does not allow for intermolecular hydrogen bonding. It has been shown [11] that this molecule exhibits intramolecular hydrogen bonding between the amide N-H and the nitrogen of the pyridine group (the colored atoms in Figure 3.2 engage in hydrogen bonds), thus leading to a total of six intramolecular hydrogen bonds per monomer. The striking difference between the trialkyl-substituted BTA (**1**) and this derivative of BTA (**2**) is the absence of intermolecular hydrogen bonding between the monomer units in the latter. The intramolecular hydrogen bonds present in **2** prevent the rotation of the amide bonds along one direction, which is reflected in a small dihedral angle of 7-13° between the central amide plane and the benzene plane. Thus, the molecule adopts a propeller kind of structure in the monomer and stacks further through π-stacking and hydrophobic interactions.

We envisage that the difference in mechanism of supramolecular polymerization of the two molecules most likely arises from a subtle difference in the hydrogen-bonding pattern between them. The trialkyl-substituted BTA (**1**), which forms strong intermolecular hydrogen bonds that are oriented along the stack direction, assembles through a cooperative mechanism whereas a very similar molecule **2**, which has intramolecular hydrogen bonds, self-assembles in an isodesmic pathway mainly through π-stacking and hydrophobic interactions.

3.2.2 Perylene-3,4,9,10-tetracarboxylic acid bisimide (PBI) Family

PBIs are one of the most studied classes of dyes and also n-type organic semiconductors. [12, 13] The initial interest in PBI was from a dye chemistry point of view. With

the advent of supramolecular chemistry, PBIs with tailored molecular features were explored for applications in organic electronics due to their n-type semiconducting properties. It has been a great challenge to control their aggregation features towards attaining desired properties. In the past decade, a plethora of PBI derivatives have been studied, but very few from a mechanistic point of view. Two such examples in which the mechanism of supramolecular polymerization has been studied are presented below.

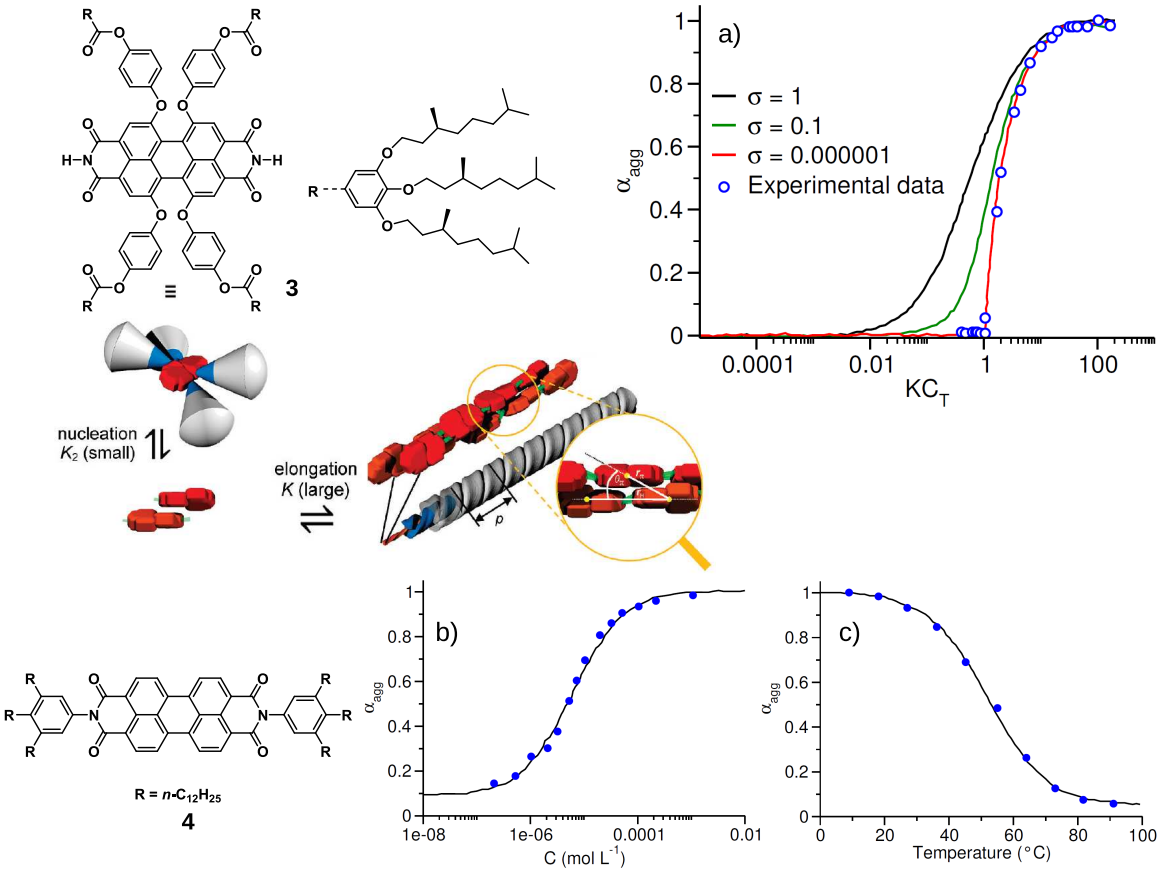

Figure 3.3: Structure of the PBI molecule under consideration with a schematic representation of self-assembly of **3**. a) Fraction of aggregates (α) versus dimensionless concentration at different σ values according to the cooperative nucleation model. The hollow blue circles represent experimental data points obtained at different concentrations of **3**. Reproduced with permission from reference [14]. Copyright 2009 American Chemical Society. b) Fraction of aggregates (α) of **4** versus concentration (2.1×10^{-7} to 1.1×10^{-3} M) in MCH. c) Cooling curve of **4** in MCH ($c = 5.0\times10^{-4}$ M). The solid blue circles represent experimental data points in b) and c) and the solid black line represents the isodesmic fit to the data points. Reproduced with permission from reference [15]. Copyright 2007 Wiley-VCH

PBIs, on aggregation, generally tend to form H-type or cofacial aggregates leading to the quenching of fluorescence. To avoid the quenching and yet obtain larger aggregates, Würthner and co-workers designed PBIs with bulky phenoxy ester groups on all four carbon atoms of the bay-region and N-H in the imide or peri-region (**3**, Figure 3.3). [14] Because of the presence of bulky groups on the bay region, the molecule has a twisted conformation in the monomer state itself, as shown in the schematic of Figure 3.3; this inhibits the classical H-type aggregation. This molecule was studied in detail by UV/vis, CD and linear dichroism (LD) spectroscopy, microscopic studies such as atomic force microscopy (AFM) and scanning tunnelling microscopy (STM) along with molecular modelling to reveal the structure of the aggregates. [14] These studies show that the peri-region imides form two lateral hydrogen bonds between two molecules. Further, they also form dimers, which are mainly stabilized by π-stacking. The hydrogen bonds extend laterally to form long one-dimensional twisted chains; two such one-dimensional chains π-stacked and slipped laterally constitute a J-type aggregate. The mechanism of supramolecular polymerization of these chromophores was studied by concentration-dependent UV/vis studies [14] in dilute nonpolar solvent such as MCH. The fraction of aggregates versus the dimensionless concentration was non-sigmoidal and did not fit the isodesmic model of polymerization ($\sigma = 1$). However, the experimental data could be fitted to the nucleation-elongation model with a nucleus of size two, as shown in Figure 3.3a. The cooperativity parameter σ was between 10^{-6} and 10^{-5}. [14] But it is still unclear whether the formation of a dimer (the nucleus) is through lateral hydrogen bonds or through J-type π-stacking. The equilibrium constant for nucleus formation is estimated to be similar in magnitude for both these dimerization processes. Remarkably, if the imide positions were substituted by butyl groups instead of hydrogen, no lateral polymerization was seen and only dimeric (J-type π-stacked) species were found at very high concentrations. [14] This exemplifies the role played by hydrogen bonding in the polymerization of this molecule.

Another molecule belonging to the PBI family containing trialkyl phenyl substitution on the imide positions (**4**) was studied by Chen et al (Figure 3.3b). [15] This molecule was shown to self-assemble in organic apolar solvents such as MCH by forming π-stacks between PBIs. The self-assembly in solution was studied through many techniques such as NMR spectroscopy, vapour pressure osmometry (VPO), and UV/vis and fluorescence spectroscopy. The PBIs were shown to self-assemble in a co-facial manner (H-type aggregate) with a slip of 55° between two neighbouring molecules. Both concentration- and temperature-dependent studies showed a

sigmoidal curve for the fraction of aggregates versus concentration or temperature. These curves were modelled using the isodesmic self-assembly model as shown in Figure 3.3b and c. [15] The equilibrium constant for the association of the molecules was found to be K = 9.7×10^4 L/mol; this value is two orders of magnitude smaller than the association constant of a similar molecule containing a trialkoxy phenyl derivative in the same solvent. This indicates that trialkoxy phenyl groups lead to stronger association as a result of weak interactions. NMR spectroscopy, VPO and UV/vis spectroscopy demonstrate that the aggregates of **4** at 10^{-3} mol/L concentration contain just ten molecules. This again emphasizes the finding that the self-assembly follows an isodesmic pathway.

From the above-mentioned two examples, it is evident that the presence of intermolecular in-plane hydrogen bonding (which is along the growth direction of assembly) in the former PBI molecule (**3**) drives the self-assembly through a cooperative pathway leading to large aggregates, whereas in the latter (**4**), the molecules self-assemble in an isodesmic pathway through π-stacking and hydrophobic interactions to form smaller aggregates.

Another derivative of PBI containing chiral gallic amide wedges at both the imide positions [16] has been shown to be an excellent super-gelator of various organic solvents. This molecule self-assembles through mainly intermolecular hydrogen bonding between the amide groups assisted by π-stacking. The mechanism of supramolecular polymerization of this molecule is not studied. But from the above arguments, we anticipate this molecule to self-assemble by a cooperative mechanism because of the presence of intermolecular hydrogen bonds.

3.2.3 Squaraine Family

Squaraines are zwitterionic dyes containing a four-membered aromatic core. Because of the zwitterionic character, they show intense absorption in the near-infrared region and also have typically high quantum yields. [17, 18] As a result of these properties, they are much sought after for use in optoelectronic devices, organic solar cells and sensors. The self-assembly of these dyes has been studied in solution, and they are also known to form both H- and J-types of excitonically coupled aggregates. [19–21] So far, very few reports exist on the mechanism of supramolecular polymerization of this class of dyes. Recently, Würthner et al. reported on the cooperative and isodesmic mechanism of supramolecular polymerization for two derivatives of squaraine dyes. Both the examples are examined in the following discussion with an emphasis on the possible molecular-level features driving the different self-assembly

mechanisms.

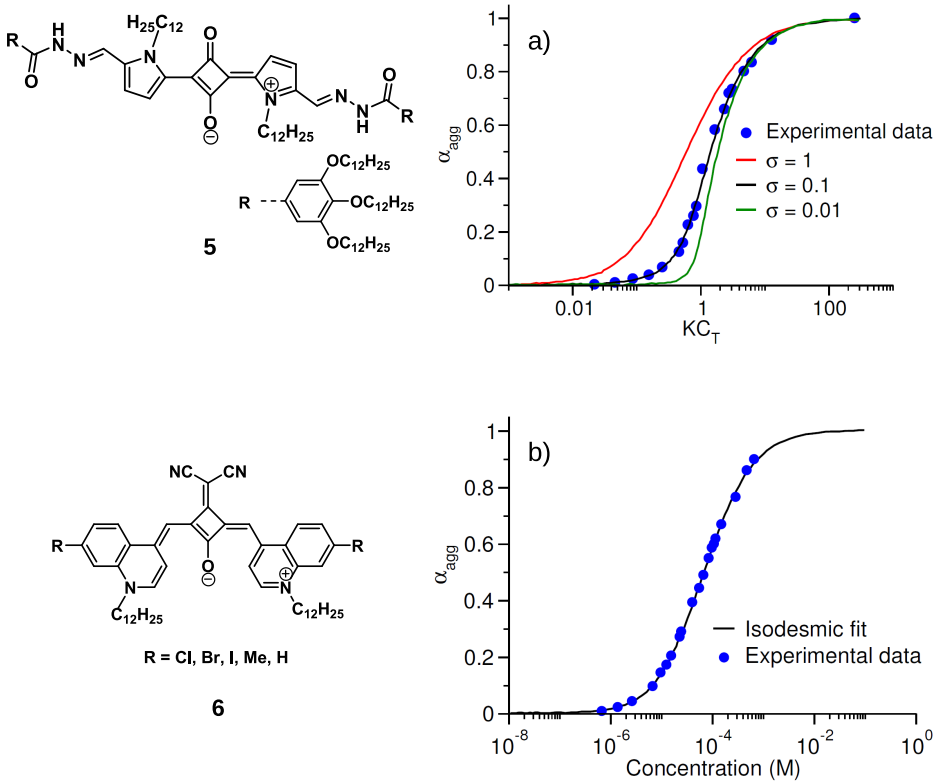

Figure 3.4: Molecular structure of squaraine derivatives **5** and **6**. a) Fraction of aggregates (α) versus dimensionless concentration at different σ values according to the cooperative-nucleation model. Solid blue circles correspond to experimental data of **5** at different concentrations. Reproduced with permission from reference [22]. Copyright 2012 Royal Society of Chemistry. b) Solid blue circles represent the experimental data for the fraction of aggregates (α) plotted against the concentration for molecule **6** with R = Cl. The black line shows an isodesmic fit to the data points. Reproduced with permission from reference [23]. Copyright 2012 Wiley-VCH.

The self-assembly of a squaraine dye containing amide groups between the four-membered aromatic core and the peripheral gallic wedge (**5**, Figure 3.4) was studied through solution-phase optical studies and by using AFM of its spin-cast samples on highly oriented pyrolytic graphite (HOPG). [22] Infrared spectroscopy revealed evidence of hydrogen bonding between molecules of **5** in MCH (c = 10^{-3} M). A hydrogen bond was formed between the N-H of the amide group and the oxygen atom of the carbonyl group of the neighbouring molecule. AFM of the spin-coated substrate showed extended one-dimensional aggregates. In a highly apolar solvent such as MCH, the molecule forms kinetically trapped aggregates, whereas in relatively apolar toluene they form thermodynamically stable assemblies.

The mechanism of supramolecular polymerization in toluene was studied by using both concentration- and temperature-dependent measurements. The fraction of aggregates versus the concentration showed a non-sigmoidal nature, which could not be explained through the isodesmic model. Thus the nucleation elongation model (K_2-K model) was employed to explain the observed experimental data as shown in Figure 3.4a. The cooperativity parameter (σ) was found to be 0.1. [22] A cooperativity parameter as high as 0.1 hints towards a weakly cooperative system. It is rather surprising to see such a weakly cooperative system despite the presence of intermolecular hydrogen bonds. This weak cooperativity can be rationalized based on the molecular modelling studies of Würthner et al. Molecular modelling studies carried out at the MM+AM1 level of theory showed the formation of dimers with a centre to-centre distance of 4.7 Å and a rotational displacement angle of 26° between the two monomers. [22] Also, it can be seen that O$\cdots$H hydrogen bond distance is about 3.6 Å, which indicates its weak character. Since the molecule possesses both negatively charged oxygen and positively charged nitrogen, the minimum-energy geometry for the dimer would be one that minimizes repulsions between like sites across molecules. This causes two neighbouring molecules to be rotated by an angle of 26°. The rotational displacement increases the hydrogen bond donor-acceptor distance and weakens the hydrogen bond.

In another interesting article by Würthner and co-workers, a squaraine dye containing two quinolinium groups (**6**) was shown to have pronounced halogen-arene interactions in self assembly in toluene solvent. [23] The authors synthesized five molecules in which the substituents on the quinolinium ring are: hydrogen, methyl, chlorine, bromine and iodine. The halogenated derivatives form H-type excitonically coupled aggregates in toluene, which is evidenced by the appearance of a new hypsochromically (blue) shifted band in the UV/vis spectra. The non-halogenated molecules do not aggregate in toluene. This behaviour is attributed to the dispersive interactions of halogen-arenes in the halogenated derivatives. Two-dimensional NMR spectroscopy and molecular modelling have shown that the molecules are arranged in an anti-parallel arrangement in the aggregates. The mechanism of supramolecular polymerization of the halogenated derivatives in toluene, studied through variation of both concentration and temperature, showed a sigmoidal curve. This curve fits well with the isodesmic model of self-assembly, as shown in Figure 3.4b. The authors attribute the isodesmic behaviour to the planarity and rigidity of the molecule; thus, no driving force is required to form a nucleus and the further addition of molecules to small aggregates is unlikely to be preferred. This

argument rules out the cooperative mechanism based on the absence of unfavourable entropic factors. In the example discussed above, the squaraine derivative **5** is fairly rigid, but yet it self-assembles through a cooperative mechanism. This observation suggests that not just rigidity but hydrogen bonding is necessary for the cooperative mechanism to be operative. The specific nature of arene-halide interactions, in contrast to that between the arene and the proton, is as yet unclear.

The above-mentioned two examples again re-emphasize the role of hydrogen bonding in determining the mechanism of polymerization.

3.2.4 Oligo(phenylene ethynylene) Family

Oligo(phenylene ethynylene)s (OPEs) are one of the potential candidates for use in organic electronics. [24] Tuning the architecture of this class of π-conjugated systems by using supramolecular chemistry can significantly impact device performance. It is thus crucial to obtain control of the morphology of these assemblies. OPEs with different shapes, such as rectangular, triangular and linear, have been studied for self-assembly in the solution phase. Very few examples of mechanistic insights are available in this family as well. Yet, we will discuss two such examples.

Sánchez and co-workers reported on the cooperative self-assembly of a triangular-shaped OPE trisamide (**7**, Figure 3.5). [25] X-ray diffraction and scanning electron microscopy showed that the molecules form columnar aggregates in bulk. Concentration-dependent ^{1}H NMR studies revealed the formation of hydrogen-bonded and π-stacked aggregates. Both variable-temperature UV/vis and CD spectroscopic measurements exhibited non-sigmoidal cooling curves. They were best explained by the nucleation-elongation model, as shown in Figure 3.5a, yielding a cooperativity parameter of $\sigma = 10^{-4}$. Also, quantum chemical calculations at the MPWB1K/6-31G** level of theory showed [25] a bi-exponential decay for the stabilization energy (SE) per monomer with a saturation value of -27.8 kcal/mol (beyond dodecamer). The SE of -27.8 kcal/mol for an infinitely long stack is coincidentally very close to the SE of -27.1 kcal/mol for an infinite stack of BTA. [8] One might argue that the levels of theory used in both the studies are different, but both methods, MPWB1K/6-31G** and PBE/85Ry+vdW, are shown to capture the dispersive interactions fairly well. Also, in both cases the central benzene unit is co-facial and the molecules form triple helical hydrogen bonds. The change in SE is more rapid for shorter oligomers and saturates beyond dodecamer, and this behaviour has been attributed to the cooperative process of polymerization. In another independent study, Meijer and

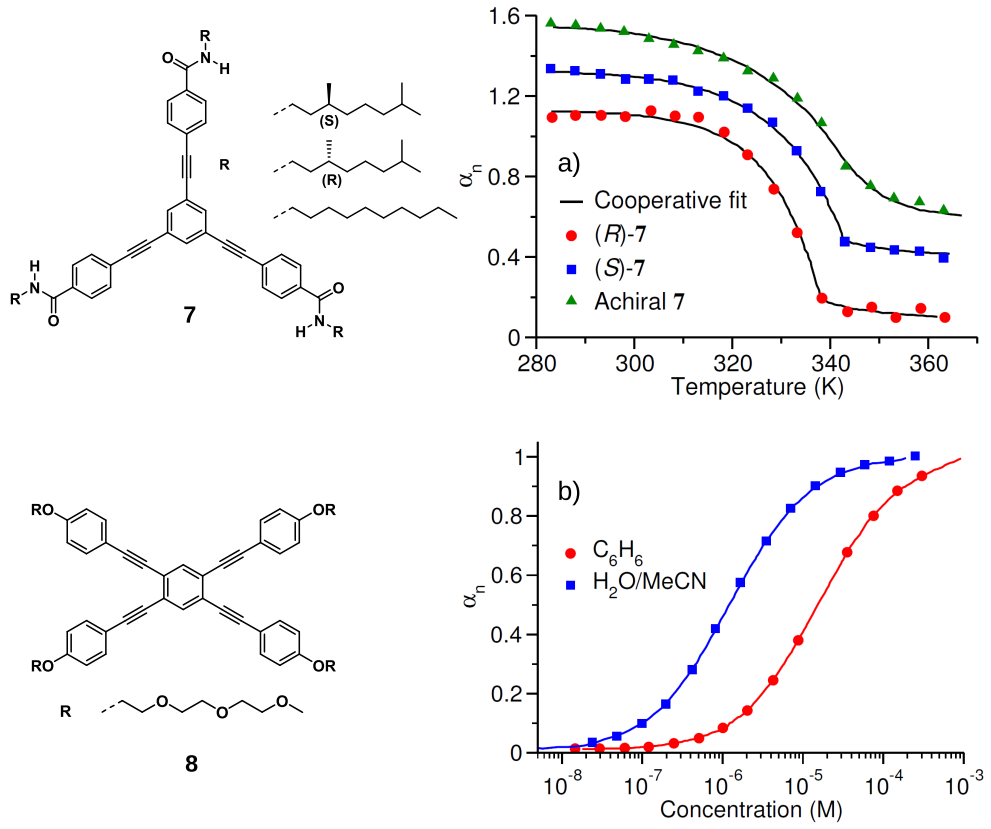

Figure 3.5: Molecular structures of OPE derivatives **7** and **8**. a) Fraction of aggregates (α) as a function of temperature for different derivatives of **7** in MCH at 1×10^{-5} M with an offset of 0.3 (Black solid lines are the corresponding fits to the nucleation-growth model). Reproduced with permission from reference [25]. Copyright 2011 Wiley-VCH. b) Fraction of aggregates (α) versus concentration for **8** in different solvents. Reproduced with permission from reference [26]. Copyright 2009 Wiley-VCH.

co-workers [27] studied the effect of core symmetry on the mechanism of supramolecular polymerization and chiral amplification in OPE trisamides containing both chiral and achiral gallic wedges. These molecules also show a cooperative mechanism of supramolecular polymerization in dilute MCH solution.

Amphiphilic, [28, 29] C_3 [30] and C_4 symmetric (**8**) [26] OPEs functionalized with oligo(ethylene oxide) units and alkyl chains have been studied in the solution phase as well as on different substrates. Temperature-dependent ^{1}H NMR spectroscopy in CD_3CN for C_4-symmetric OPE containing tetraethylene glycol (TEG) chains shows the formation of π-stacked molecules rotated with respect to each other in the aggregates. Concentration-dependent UV/vis studies also indicate the same in different solvents such as benzene, acetonitrile and acetonitrile/water mixture. In contrast to the OPE trisamide (**7**), molecule **8** exhibits a sigmoidal growth kinetics, which

can be explained by an isodesmic mechanism of polymerization, as can be seen from Figure 3.5b. This molecule shows different morphologies based on the nature of the solvent in which the self-assembly is carried out. As the studies are performed in polar solvents, the peripheral TEG groups are solvated by the polar solvent molecules. Since **8** possesses a non-polar core, the solvophobic interactions between the core of the molecule and the solvent enhance the π-stacking. This is corroborated by the fact that the equilibrium constant is 5.2×10^5 M^{-1} in acetonitrile/water mixture compared to a value of 3.8×10^5 M^{-1} in pure acetonitrile. Thus, molecule **8** is an example of isodesmic supramolecular polymerization driven mainly by π-stacking and solvophobic interactions.

3.2.5 Miscellaneous Examples

In addition to the above-mentioned examples, there are numerous other cases of self-assembly driven by hydrogen bonding and which show a cooperative mechanism of polymerization. These are shown in Figure 3.6. Meijer and co-workers reported on the cooperative self-assembly of tetraphenyl zinc-porphyrins (**9**) containing amide groups between the peripheral chiral gallic wedges and the central phenylporphyrins. [31] Solution-phase infrared spectroscopy provides evidence for the formation of intermolecular hydrogen bonds. A cooperativity parameter of $\sigma = 5\times10^{-5}$ is reported for this molecule in MCH. Bouteiller and co-workers showed the formation of supramolecular polymers of bis-urea-based small molecule **10**. [32] Although this molecule does not possess any larger chromophore than benzene, it is also shown to self-assemble cooperatively through the formation of intermolecular hydrogen bonds. Recently, Sánchez and co-workers have shown the cooperative self-assembly of a linear molecule containing two amide groups between the para positions of the benzene and the chiral gallic wedge (**11**) in MCH. [33] This molecule is also shown to form intermolecular hydrogen bonds in the solution phase, as evidenced from infrared spectroscopy. Ajayaghosh and co-workers have shown the cooperative self-assembly of linear OPE containing azobenzenes at the periphery connected by an amide group (**12**). [34]

Müllen and co-workers studied the self-association of hexa-peri-hexabenzocoronenes (HBCs) substituted with different alkyl chains (**13**) in the solution state by using primarily ^{1}H NMR spectroscopy. [35] In spite of the large aromatic core of HBC, this derivative substituted with a solubilizing branched alkyl chain self-assembles through an isodesmic process. This provides an example of an isodesmic mechanism

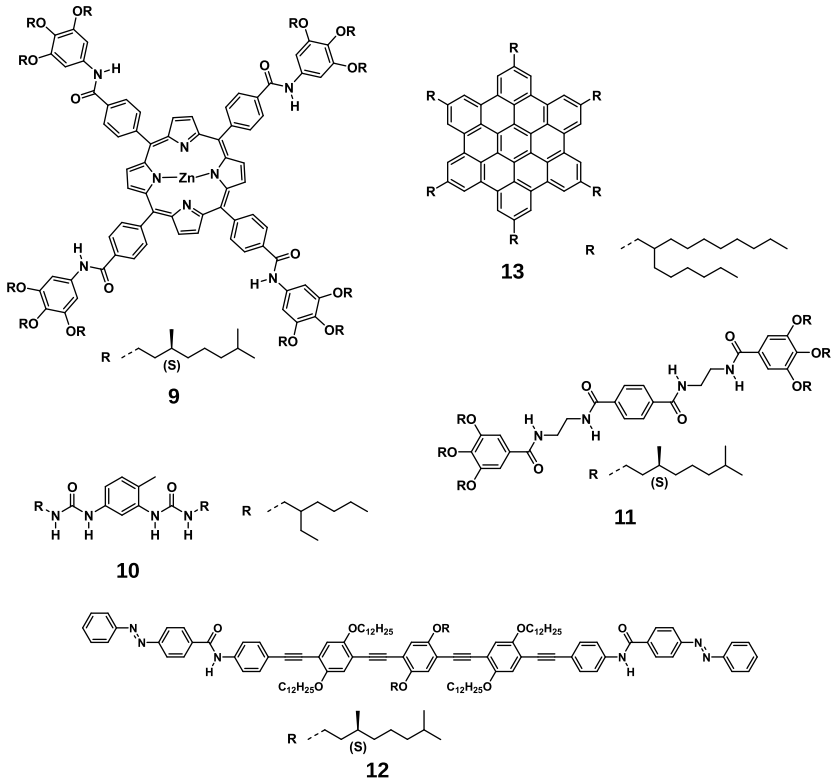

Figure 3.6: Structures of various molecules studied for their self-assembly mechanisms in the literature. [31–35]

of supramolecular polymerization mainly driven by π-stacking and hydrophobic interactions of the side chain.

3.2.6 The case of Oligo(*p*-phenylenevinylene)s

Apart from the above-mentioned examples of cooperative self-assembly, there are two more systems that are shown to be cooperative. Oligo(*p*-phenylenevinylene) (OPV) with ureidotriazine (UT) groups at the terminus (**14**) forms dimers through quadruple hydrogen bonds between two molecules. This in-plane dimer is the building block for further assembly, as shown in the schematic of Figure 3.7. The molecule self-assembles to chiral, ordered stacks in a highly cooperative manner (Figure 3.7a), as indicated by the cooperativity parameter of $\sigma = 10^{-4}$. [6] Further, this was the first detailed report of supramolecular polymerization to derive the thermodynamic parameters and to demonstrate the utility of temperature-dependent study to monitor the mechanism of supramolecular polymerization. In another example, self-assembly of an OPVsubstituted hexarylbenzene (**15**, Figure 3.7) led to the formation of ordered, columnar superstructures. This molecule possesses a tilt angle of

approximately 35° and a π-stacking distance of 4.5 Å in the superstructure. They self-assemble in MCH solution at low concentrations and the cooling curve shows a critical point around 331 K; this curve was shown to follow cooperative behaviour (Figure 3.7b) with a cooperativity parameter of $\sigma = 3\times10^{-5}$. [36]

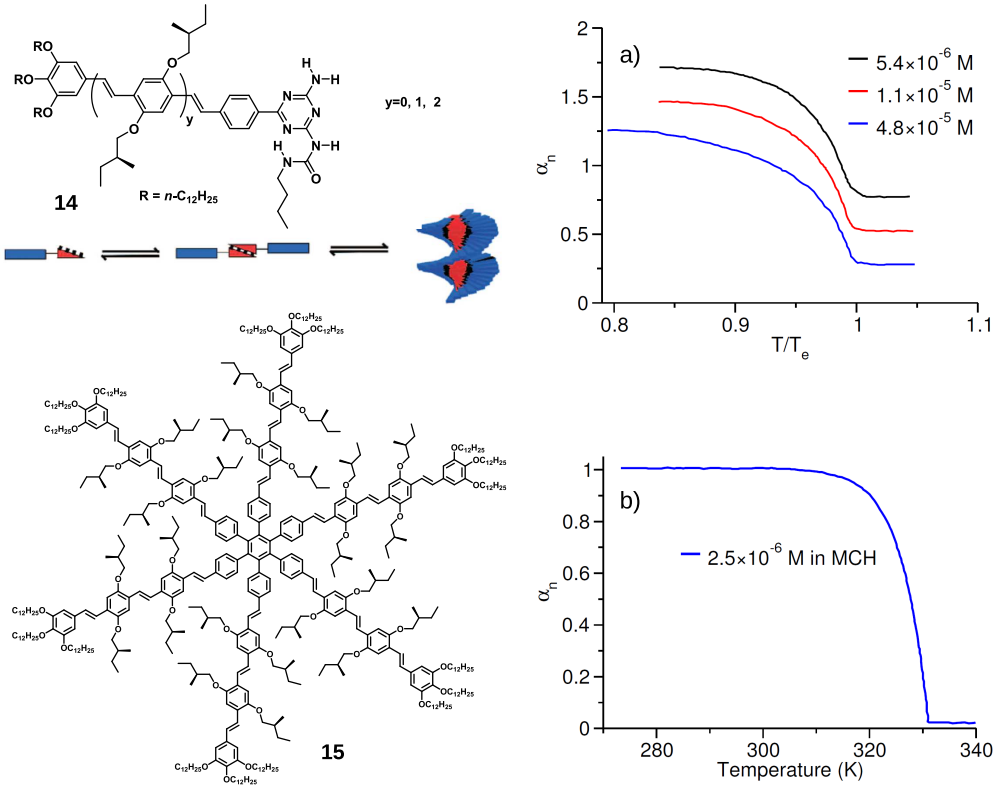

Figure 3.7: Structure of OPV UT (**14**) with a schematic of its self-assembly and hexa-OPV-substituted benzene (**15**). a) Normalized cooling curve for **14** with y=2 in dodecane at different concentrations (5.4×10^{-6} to 4.8×10^{-5} M). Reproduced with permission from ref. [6]. Copyright 2006 American Association for the Advancement of Science. b) Fraction of aggregates (α) versus temperature for **15** in MCH at 2.5×10^{-6} M fitted to the nucleation-elongation model. Reproduced with permission from ref. [36]. Copyright 2007 American Chemical Society.

The precise reason for cooperativity in these last two examples is unclear (from a molecular point of view) as they lack an apparent intermolecular hydrogen bond but still exhibit high cooperativity. Preliminary quantum chemical calculations from our group have shown that the gallic wedges on the periphery form weak C-H$\cdots$O hydrogen bonds between two molecules. These weak interactions are possible in this case because the two stacked dimers are rotated by not more than 8-10°. This might explain the cooperativity in **14**. Further efforts are under way to confirm this observation. A similar argument can hold for **15** and also in this case, cooperativity

might arise from the energy penalty one needs to pay to planarize the molecule and form a small stack, which can then act as the nucleus in the formation of larger aggregates.

Also, understanding of the mechanism in cases where a dimer or a small oligomer is formed through in-plane hydrogen bonding, which later grows in the out-of-plane direction through π-stacking, is still unclear. [37–39] In other words, in cases for which the two most dominant interactions, namely hydrogen bonding and π-stacking, are orthogonally oriented to each other, it becomes difficult to pinpoint the molecular-level origin of the mechanism of supramolecular polymerization. This is because of the challenge to ascertain whether the hydrogen-bonded motif precedes the π-stacking or vice versa.

3.3 Perspective on the Mechanism of Supramolecular Polymerization

Based on the examples discussed above, we conjecture that the presence of long-range interactions (any interaction which varies as R^{-n} where R is the distance between the two interacting systems and $n \leq 3$), such as the permanent dipole-permanent dipole interaction and electrostatic interactions in the direction of growth, is likely to lead to cooperative self-assembly; as a corollary, the lack of such specific interactions leads to isodesmic self-assembly. Intermolecular hydrogen bonding along the growth direction of the stack leads to a permanent dipole in the hydrogen-bonded complex. Such hydrogen-bonded complexes can further interact through long-range dipole-dipole interaction resulting in large aggregates. Thus, the presence of intermolecular hydrogen bonds in the growth direction invariably leads to a cooperative mechanism of polymerization. The cooperative mechanism of supramolecular polymerization was reported [2] to have three origins, namely electronic, structural and hydrophobic interactions. Examples of cooperative supramolecular polymerization (of synthetic origin) driven predominantly by structural or hydrophobic interactions are scarce. This again points to the profound importance of electronic effects in determining the cooperativity. If the self-assembly is mainly governed by π-stacking, hydrophobic and van der Waals interactions or a combination of these, then the process is likely to occur through an isodesmic mechanism.

If a self-assembled aggregate or molecule possesses a permanent dipole moment, it can interact through the long-range dipole-dipole interaction. Thus, when another molecule is added to such an existing stack or aggregate, it (the added molecule)

can interact with not only its nearest neighbours but also with the molecules distant from it, thus leading to a greater stabilization of the aggregate. This effect of greater stabilization of the stack (due to the interactions between many molecules) than the sum of its parts is termed cooperativity. [40] On the other hand, if a molecular stack lacks this kind of long-range interaction, then the stabilization gained by the stack is purely local, arising from interaction with the nearest neighbours, and this contribution remains more or less constant throughout the course of polymerization. Such a scenario is reflected in the monotonic decrease in ΔG^0 for the isodesmic mechanism of supramolecular polymerization. [2]

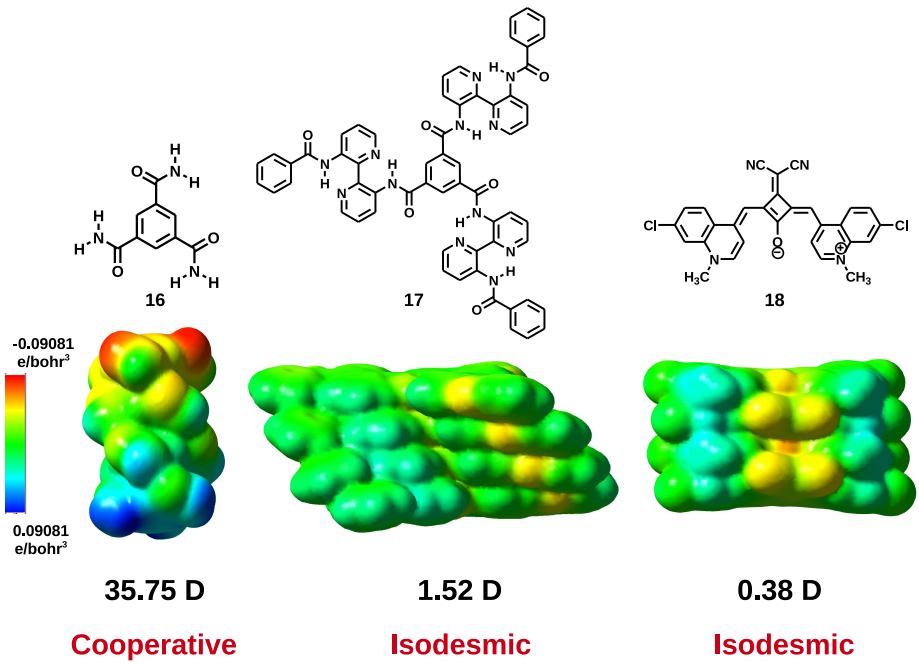

Figure 3.8: Structure of molecules (**16**-**18**) studied computationally. Electrostatic potential isosurfaces plotted on electronic density isosurfaces of 4×10^{-4} e/bohr^3 for the tetramer of all three classes of molecules. The dipole moments in the stacking direction for the tetramers of different molecules as obtained from the BLYP/DZVP//B97D/cc-PVDZ level of theory are mentioned below respective oligomers.

To test the validity of the above hypothesis, we chose three different systems (one cooperative and two isodesmic) to perform computational studies. The computational studies were performed at the BLYP/DZVP//B97D/cc-PVDZ level of theory. The optimization of the oligomers (up to tetramer) and the subsequent calculation of total self-consistent field electron density mapped on to isosurfaces of molecular potential was used to identify these long-range interactions, as shown in Figure 3.8.

The BTA (**16**) tetramer possesses a large dipole moment (35.75 D), as seen from the charge polarization along the stack direction. However, the chlorine-substituted squaraine (**18**) tetramer or the 3,3′-bis(acylamino)-2,2′-bipyridine substituted BTA (**17**) tetramer does not show any significant polarization along the stack direction. While **16** organizes cooperatively, **17** and **18** do so in an isodesmic manner. Moreover, two consecutive molecules are rotated by an angle of 18.5° in the tetramer of **17** and also possess a stacking distance of 3.44 Å. These values are in agreement with the previously reported calculation values of 28° for a dimer and the experimentally reported π-stacking distance of 3.4 Å. [5] Thus, about 19-20 molecules constitute a helical pitch and the observed helical twist is not complete for a tetramer, as can be seen in Figure 3.8. The molecule **18** stacks in an antiparallel manner as observed from our optimized geometries. This is in accord with the previous 2D-NMR studies and calculations. [23] Thus, such calculations can provide valuable insights into the mechanism of self-assembly.

The above reasoning considers only the enthalpic contribution to the change in standard Gibbs free energy (ΔG^0), but entropic contributions too need to be taken into account. If one takes a closer look at most of the above-mentioned examples, the H_e or ΔH^0 (enthalpy of polymerization) are between -50 and -180 kJ/mol, whereas the entropy of these polymerizations (ΔS^0) is typically between -60 and -200 J/(mol·K) and almost all of them are enthalpically driven polymerizations. [4, 6, 15, 25, 27, 33] Thus, enthalpic contributions outweigh the entropic contributions for most of the synthetic supramolecular polymerizations studied in the literature. This observation that most of the synthetic supramolecular polymerizations are enthalpically driven is also noted by de Greef et al. [2]

3.4 Conclusions and outlook

In summary, we have reviewed the mechanism of supramolecular polymerization from a molecular features point of view. Based on the examples considered, we conjecture that the presence of motifs that lead to long-range interactions, such as hydrogen bonding (along the growth direction), permanent dipole or electrostatic interactions, along the long axis of polymerization lead to a cooperative mechanism and a lack of such interactions could lead to an isodesmic mechanism of polymerization. Self-assembly driven mainly by π-stacking interactions and hydrophobic interactions will be isodesmic as shown in the case of HBC. [35]

As of now, the role of hydrogen bonding in determining the mechanism of

supramolecular polymerization seems to be clear, that is, the presence of hydrogen bonds along the growth axis leads to cooperativity. Even a small core such as benzene with attached groups that can form intermolecular hydrogen bonds leads to cooperative supramolecular polymerization, as shown in examples **10** and **11**. However, in a report on the self-assembly of ureido-pyrimidinones, which exhibit intermolecular lateral hydrogen bonds between the urea group, the mechanism of supramolecular polymerization has been reported to follow an isodesmic process. [41] But the cooling curves obtained seem to be non-sigmoidal and almost linear. Thus, we expect that monitoring of other properties that change upon polymerization (such as viscosity) as a function of temperature might give a better representation of the mechanism involved. But as far as the other long-range interactions such as permanent dipole-permanent dipole and electrostatics are concerned, there are very few examples in which the self-assembly is mainly driven by these interactions. Thus, the design and synthesis of supramolecular assemblies driven by these interactions is important to test this conjecture and these form the subject of further chapters in this thesis.

The present assumption that the nucleus is of size two in a cooperative-nucleation polymerization may not be valid across a wide range of molecules. Thus, further computational (molecular dynamics (MD) or Monte Carlo) studies are required to judge the size of the nucleus appropriately. Atomistic MD simulations seem to be an ideal tool for understanding the mechanisms at a microscopic level, [42] as one can vary the temperature or concentration and use explicit solvent molecules. But a drawback of this approach is the amount of time required to obtain trajectories comparable to timescales of experiments (micro- to milliseconds). This limitation can be overcome to some extent by using coarse-grained models in such simulations. [43] Also, MD studies can provide insights into many unanswered questions, such as: (1) the number of nuclei formed; (2) timescales of aggregation; (3) the occurrence of the odd-even effect of solvent on supramolecular polymerization, as observed in some cases; [6] and (4) the role of solvent in influencing the mechanism of polymerization. A long-term goal of such theoretical tools should be to build predictive capabilities- can one predict the mechanism of supramolecular polymerization given the molecular structure and the solvent?

3.5 Computational details

The geometry optimizations were carried out using periodic density functional theory (DFT) as implemented in CP2K package [44] using the QUICKSTEP module. [45] Combined plane wave and atom centered Gaussian basis sets were used to perform geometry optimization. In this method, the Kohn-Sham orbitals are expanded using atom centered Gaussian basis sets and the electronic density is treated using the plane wave basis set. BLYP exchange-correlation functional [46, 47] with double-zeta single polarized basis set [48] was used to describe the valence electrons. Since the van der Waals or dispersion interactions are important in describing the stacking of aromatic moieties, we have used dispersion correction (D2) prescribed by Grimme. [49] An energy cut-off of 280 Ry was used to describe the electron density and the Goedecker-Teter-Hutter pseudopotential [50] was used to represent the effect of core electrons and nuclei. LBFGS optimizer [51] was used for all optimizations. For molecules **16**, **17** and **18** cubical boxes with linear dimensions of 22 Å, 35 Å and 30 Å were used respectively and geometry optimization was performed for oligomers up to a tetramer. The atomic charges for generating the electrostatic surface potentials were obtained for all the oligomers of each molecule by performing a Self-Consistent-Field (SCF) calculation on the optimized coordinates (obtained from BLYP-DZVP) at B97D/cc-PVDZ level of theory [49, 52] using Merz and Kollman (MK) charge method [53, 54] as implemented in Gaussian-09 suite of programs. [55]

Note: *All the graphs were digitized from the original references by using g3data software and re-plotted using Xmgrace for the sake of clarity.*

Bibliography

[1] Rest, C.; Kandanelli, R.; Fernández, G. *Chem. Soc. Rev.* **2015**, *44*, 2543–2572.

[2] De Greef, T. F. A.; Smulders, M. M. J.; Wolffs, M.; Schenning, A. P. H. J.; Sijbesma, R. P.; Meijer, E. W. *Chem. Rev.* **2009**, *109*, 5687–5754.

[3] Cantekin, S.; de Greef, T. F. A.; Palmans, A. R. A. *Chem. Soc. Rev.* **2012**, *41*, 6125–6137.

[4] Smulders, M. M. J.; Schenning, A. P. H. J.; Meijer, E. W. *J. Am. Chem. Soc.* **2008**, *130*, 606–611.

[5] Metzroth, T.; Hoffmann, A.; Martin-Rapun, R.; Smulders, M. M. J.;

Pieterse, K.; Palmans, A. R. A.; Vekemans, J. A. J. M.; Meijer, E. W.; Spiess, H. W.; Gauss, J. *Chem. Sci.* **2011**, *2*, 69–76.

[6] Jonkheijm, P.; van der Schoot, P.; Schenning, A. P. H. J.; Meijer, E. W. *Science* **2006**, *313*, 80–83.

[7] Oosawa, F.; Kasai, M. *J. Mol. Biol.* **1962**, *4*, 10 – 21.

[8] Kulkarni, C.; Reddy, S. K.; George, S. J.; Balasubramanian, S. *Chem. Phys. Lett.* **2011**, *515*, 226–230.

[9] Filot, I. A. W.; Palmans, A. R. A.; Hilbers, P. A. J.; van Santen, R. A.; Pidko, E. A.; de Greef, T. F. A. *J. Phys. Chem. B* **2010**, *114*, 13667–13674.

[10] Fitié, C. F. C.; Roelofs, W. S. C.; Kemerink, M.; Sijbesma, R. P. *J. Am. Chem. Soc.* **2010**, *132*, 6892–6893.

[11] Palmans, A. R. A.; Vekemans, J. A. J. M.; Fischer, H.; Hikmet, R. A.; Meijer, E. W. *Chem. Eur. J.* **1997**, *3*, 300–307.

[12] Würthner, F. *Chem. Commun.* **2004**, 1564–1579.

[13] Huang, C.; Barlow, S.; Marder, S. R. *J. Org. Chem.* **2011**, *76*, 2386–2407.

[14] Kaiser, T. E.; Stepanenko, V.; Würthner, F. *J. Am. Chem. Soc.* **2009**, *131*, 6719–6732.

[15] Chen, Z.; Stepanenko, V.; Dehm, V.; Prins, P.; Siebbeles, L.; Seibt, J.; Marquetand, P.; Engel, V.; Würthner, F. *Chem. Eur. J.* **2007**, *13*, 436–449.

[16] Würthner, F.; Bauer, C.; Stepanenko, V.; Yagai, S. *Adv. Mater.* **2008**, *20*, 1695–1698.

[17] Sreejith, S.; Carol, P.; Chithra, P.; Ajayaghosh, A. *J. Mater. Chem.* **2008**, *18*, 264–274.

[18] Ajayaghosh, A. *Acc. Chem. Res.* **2005**, *38*, 449–459.

[19] Stoll, R.; Severin, N.; Rabe, J.; Hecht, S. *Adv. Mater.* **2006**, *18*, 1271–1275.

[20] Das, S.; Thomas, K. G.; Thomas, K. J.; Madhavan, V.; Liu, D.; Kamat, P. V.; George, M. V. *J. Phys. Chem.* **1996**, *100*, 17310–17315.

[21] Chen, H.; Farahat, M. S.; Law, K.-Y.; Whitten, D. G. *J. Am. Chem. Soc.* **1996**, *118*, 2584–2594.

[22] Mayerhöffer, U.; Würthner, F. *Chem. Sci.* **2012**, *3*, 1215–1220.

[23] Mayerhöffer, U.; Würthner, F. *Angew. Chem. Int. Ed.* **2012**, *51*, 5615–5619.

[24] Bunz, U. H. F. *Macromol. Rapid Commun.* **2009**, *30*, 772–805.

[25] Garc´ia, F.; Viruela, P. M.; Matesanz, E.; Ort´i, E.; Sánchez, L. *Chem. Eur. J.* **2011**, *17*, 7755–7759.

[26] Garc´ia, F.; Fernández, G.; Sánchez, L. *Chem. Eur. J.* **2009**, *15*, 6740–6747.

[27] Wang, F.; Gillissen, M. A. J.; Stals, P. J. M.; Palmans, A. R. A.; Meijer, E. W. *Chem. Eur. J.* **2012**, *18*, 11761–11770.

[28] Garc´ia, F.; Aparicio, F.; Fernández, G.; Sánchez, L. *Org. Lett.* **2009**, *11*, 2748–2751.

[29] Fernandez, G.; Garcia, F.; Aparicio, F.; Matesanz, E.; Sanchez, L. *Chem. Commun.* **2009**, 7155–7157.

[30] Fernández, G.; Garc´ia, F.; Sánchez, L. *Chem. Commun.* **2008**, 6567–6569.

[31] Helmich, F.; Lee, C.; Nieuwenhuizen, M.; Gielen, J.; Christianen, P.; Larsen, A.; Fytas, G.; Leclre, P.; Schenning, A.; Meijer, E. *Angew. Chem. Int. Ed.* **2010**, *49*, 3939–3942.

[32] Simic, V.; Bouteiller, L.; Jalabert, M. *J. Am. Chem. Soc.* **2003**, *125*, 13148–13154.

[33] Aparicio, F.; Matesanz, E.; Sánchez, L. *Chem. Commun.* **2012**, *48*, 5757–5759.

[34] Gopal, A.; Hifsudheen, M.; Furumi, S.; Takeuchi, M.; Ajayaghosh, A. *Angew. Chem. Int. Ed.* **2012**, *51*, 10505–10509.

[35] Kastler, M.; Pisula, W.; Wasserfallen, D.; Pakula, T.; Müllen, K. *J. Am. Chem. Soc.* **2005**, *127*, 4286–4296.

[36] Tomović, Ž.; van Dongen, J.; George, S. J.; Xu, H.; Pisula, W.; Lecl`ere, P.; Smulders, M. M. J.; De Feyter, S.; Meijer, E. W.; Schenning, A. P. H. J. *J. Am. Chem. Soc.* **2007**, *129*, 16190–16196.

[37] Yagai, S.; Usui, M.; Seki, T.; Murayama, H.; Kikkawa, Y.; Uemura, S.; Karatsu, T.; Kitamura, A.; Asano, A.; Seki, S. *J. Am. Chem. Soc.* **2012**, *134*, 7983–7994.

[38] Seki, T.; Asano, A.; Seki, S.; Kikkawa, Y.; Murayama, H.; Karatsu, T.; Kitamura, A.; Yagai, S. *Chem. Eur. J.* **2011**, *17*, 3598–3608.

[39] Würthner, F.; Chen, Z.; Hoeben, F. J. M.; Osswald, P.; You, C.-C.; Jonkheijm, P.; Herrikhuyzen, J. v.; Schenning, A. P. H. J.; van der Schoot, P. P. A. M.; Meijer, E. W.; Beckers, E. H. A.; Meskers, S. C. J.; Janssen, R. A. J. *J. Am. Chem. Soc.* **2004**, *126*, 10611–10618.

[40] Prins, L. J.; Reinhoudt, D. N.; Timmerman, P. *Angew. Chem. Int. Ed.* **2001**, *40*, 2382–2426.

[41] Nieuwenhuizen, M.; deGreef, T.; vanderBruggen, R.; Paulusse, J.; Appel, W.; Smulders, M.; Sijbesma, R.; Meijer, E. *Chem. Eur. J.* **2010**, *16*, 1601–1612.

[42] Bejagam, K. K.; Fiorin, G.; Klein, M. L.; Balasubramanian, S. *J. Phys. Chem. B* **2014**, *118*, 5218–5228.

[43] Bejagam, K. K.; Balasubramanian, S. *J. Phys. Chem. B* **2015**, *119*, 5738–5746.

[44] Hutter, J.; Iannuzzi, M.; Schiffmann, F.; VandeVondele, J. *Wiley Interdiscip. Rev. Comput. Mol. Sci.* **2014**, *4*, 15–25.

[45] VandeVondele, J.; Krack, M.; Mohamed, F.; Parrinello, M.; Chassaing, T.; Hutter, J. *Comp. Phys. Commun.* **2005**, *167*, 103 – 128.

[46] Becke, A. D. *Phys. Rev. A* **1988**, *38*, 3098–3100.

[47] Lee, C.; Yang, W.; Parr, R. G. *Phys. Rev. B* **1988**, *37*, 785–789.

[48] VandeVondele, J.; Hutter, J. *J. Chem. Phys.* **2007**, *127*, 114105–114114.

[49] Grimme, S. *J Comput. Chem.* **2006**, *27*, 1787–1799.

[50] Hartwigsen, C.; Goedecker, S.; Hutter, J. *Phys. Rev. B* **1998**, *58*, 3641–3662.

[51] Byrd, R.; Lu, P.; Nocedal, J.; Zhu, C. *J. Sci. Comput.* **1995**, *16*, 1190–1208.

[52] Dunning, T. H. *J. Chem. Phys.* **1989**, *90*, 1007–1023.

[53] Singh, U. C.; Kollman, P. A. *J. Comput. Chem.* **1984**, *5*, 129–145.

[54] Besler, B. H.; Merz, K. M.; Kollman, P. A. *J. Comput. Chem.* **1990**, *11*, 431–439.

[55] Frisch, M. J. et al. Gaussian 09 Revision D.01. Gaussian Inc. Wallingford CT 2009.

Chapter 4

Dipole-Moment-Driven Cooperativity in Perylene Bisimides

4.1 Introduction

Synthetic macromolecules assembled from monomers capable of exhibiting intermolecular interactions such as hydrogen bonding, π-stacking, amphiphilic, and electrostatic interactions have been studied to mimic their biological counterparts and for materials applications. [1–6] The investigation into the mechanism of supramolecular polymerization has gained importance in the past decade to allow for a better control over its structure and functions. [7–13] Thermodynamic aspects of self-assembly and their relationship with mechanism have been studied extensively. [14–16] In their seminal review, Meijer and co-workers suggested electronic, structural, and hydrophobic interactions as the cause of cooperativity in supramolecular polymers. [14]

Benzene-1,3,5-tricarboxamide [17–19] derivatives are seminal examples of cooperative supramolecular polymerization involving intermolecular hydrogen-bonding along the stacking direction. In addition, as we saw from Chapter 3 that many

Reprinted with permission from "Dipole-Moment-Driven Cooperative Supramolecular Polymerization" *J. Am. Chem. Soc.* **2015**, *137*, 3924-3932. Copyright 2015, American Chemical Society. http://pubs.acs.org/doi/abs/10.1021/jacs.5b00504

π-conjugated systems studied in the literature that are likewise capable of intermolecular hydrogen bonding have also been shown to follow the cooperative mechanism of self-assembly. [20–26] However, there are a few exceptions where the system apparently lacks hydrogen bonding along the stacking direction and yet shows a cooperative mechanism of self-assembly. [27, 28] Recently, cooperativity has also been observed in π-conjugated systems with metallophilic interactions, [29] fluorocarbon tails, [30] unconventional hydrogen bonding, [31] dative bonds, [32] and guest encapsulation [33]. In order to rationalize the observed mechanisms in a broader sense, in the previous Chapter we had proposed the necessity of anisotropic long-range interactions between monomers (or small stacks) for a cooperative self-assembly. [34] Dipolar interaction is one such, and it has also been used to construct supramolecular polymers. [35] The effect of dipolar groups present in a molecule on the mechanism of supramolecular polymerization has seldom been studied. Recently, Würthner and co-workers have shown the cooperative supramolecular polymerization of dipolar merocyanine dyes. [36]

Perylene-3,4,9,10-tetracarboxylic acid bisimides (PBIs) are well-known electron-deficient organic semiconductors and have been widely employed as active materials in organic electronics. [37, 38] PBI derivatives are known to follow an isodesmic mechanism of self-assembly. [39–42] However, there are only a few reports (by the groups of Würthner, Meijer, and Yagai) on the cooperative self-assembly of PBIs; these are mainly driven by either intermolecular hydrogen bonding or intramolecular hydrogen bonding together with π-stacking. [43–46]

In the present Chapter, we investigate the effect of dipolar groups and different self-assembling moieties appended to PBI on the mechanism of self-assembly. Here we observe cooperative self-assembly of PBI derivatives containing no apparent hydrogen-bonding groups. Extensive spectroscopy, molecular dynamics (MD) simulations, and bulk dielectric measurements were performed on these systems to shed light on the origin of cooperativity. In this Chapter, we show that dipole-dipole interaction between monomers along the stacking direction is the primary cause of cooperativity. The interaction is shown to arise from the dipolar nature of carbonate linkers and the rigidity of cholesterol self-assembling moieties. Thus, we present a unique example of non-hydrogen-bonded and dipole-moment-driven cooperativity in a supramolecular system.

4.2 Results

4.2.1 Molecular design

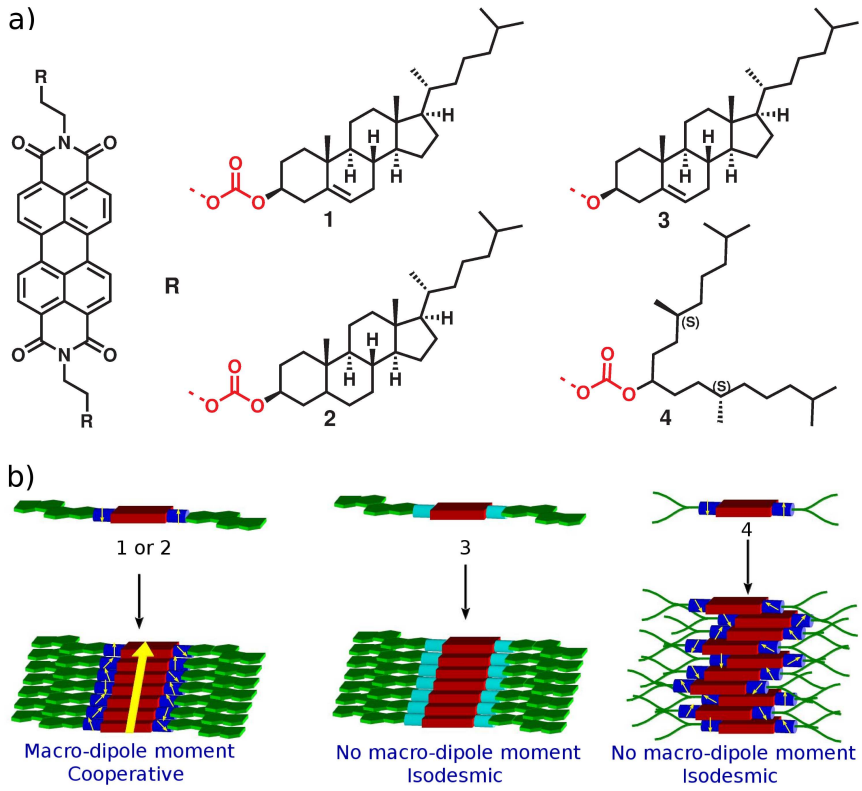

Figure 4.1: Molecules under study. (a) PBI is functionalized on both imide nitrogens with either carbonate or ether linker (marked in red). Cholesterol (**1** and **3**), dihydrocholesterol (**2**), and chiral swallowtail (**4**) are used as the self-assembling motifs. (b) Schematic representation of the assembly of different PBI derivatives. PBIs are depicted by red blocks. Blue and cyan cylinders represent carbonate and ether linkers, respectively. Self-assembling moieties are shown in green. Small yellow arrows indicate molecular dipoles along the carbonate C=O axis. Macro-dipole moment is shown as a large yellow arrow along the stacking direction.

The molecular design involves utilizing the optical properties of the PBI core to probe the mechanism of self-assembly by varying the linker group (either carbonate or ether) and self-assembling moiety (cholesterol or alkyl groups, Figure 6.1). Dialkyl carbonates are known to possess dipole moment in different conformations [47] and are thus utilized as the source of molecular dipole moment. An ethylene spacer is chosen to be placed between the imide nitrogen and the carbonate to provide appropriate solubility and rigidity to the molecule. **1** and **2** contain dipolar linkers

(carbonate) and a rigid steroid based self-assembling moiety. In contrast, **3**, possessing ether linkers, differs only in the absence of dipolar groups, thus allowing us to study the effect of linkers on the mechanism of self-assembly. In **4**, the steroid moiety of **1** is exchanged for a chiral swallowtail, so as to be able to examine the effect of this moiety on the mechanism of self-assembly. Synthesis of molecules **1**-**4** was carried out by coupling of the corresponding chloroformates [48] with N-Boc-ethanolamine, followed by deprotection to yield the respective amines. Condensation of the respective amines with perylene-3,4,9,10-tetracarboxylic acid dianhydride yielded the target molecules. All molecules were characterized by ^{1}H and ^{13}C NMR, IR, and mass spectroscopy (See experimental section for details).

4.2.2 Self-assembly studies

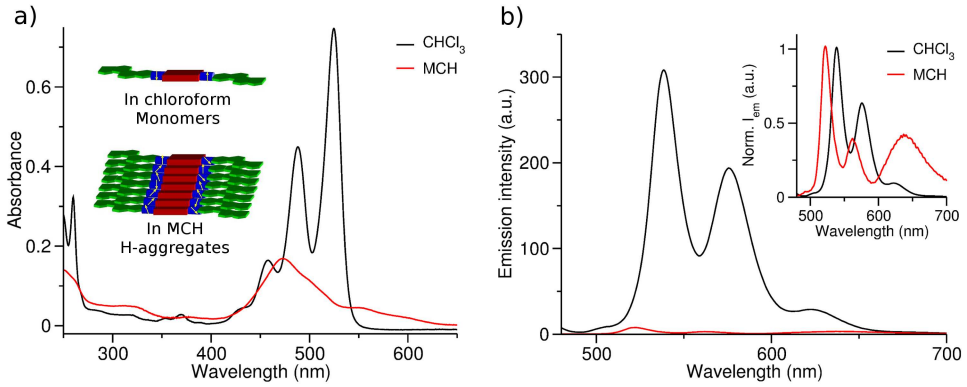

Figure 4.2: a) and b) UV/Vis absorption and fluorescence spectra respectively of **1** in chloroform and MCH (λ_{exc} = 450 nm). Inset of a) shows the schematic arrangement of **1** in chloroform and MCH. Inset of b) displays the normalized fluorescence spectra in different solvents. These spectra are recorded at room temperature.

UV/vis absorption spectrum of **1** in chloroform (c = 1×10^{-5} M) shows prominent peaks at 525 (ϵ = 74200 $M^{-1}cm^{-1}$), 488, 458, and 260 nm. The absorption features between 450 and 530 nm have been attributed to the vibronic bands of $S_0 \rightarrow S_1$ transition of PBIs along the long axis of the molecule. [49] The corresponding fluorescence spectrum shows a mirror image of the absorption spectrum with a maximum at 538 nm (Figure 7.2b). These absorption and fluorescence spectral features are characteristic of π-π^* transitions of PBIs devoid of intermolecular interactions. [38] The UV/vis absorption spectrum of **1** in methylcyclohexane (MCH) shows the loss of vibronic features, with an absorption maximum at 473 nm and a broad band centered around 555 nm. The fluorescence spectrum of **1** in MCH shows

the quenching of monomer emission (at 538 nm by 39 times) and the emergence of a new band at 640 nm (inset of Figure 7.2b).

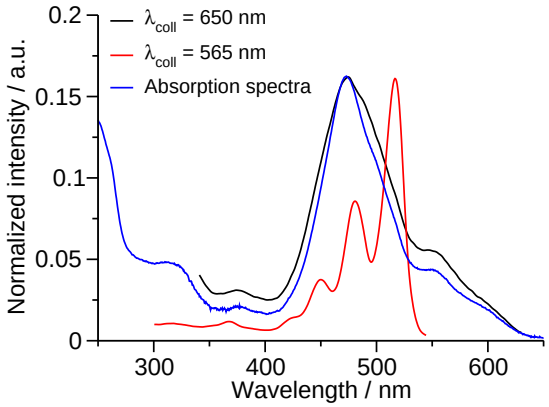

Figure 4.3: Normalized fluorescence excitation (by monitoring fluorescence intensity at 650 nm and 565 nm) and absorption spectrum of **1** in MCH (c = 1×10^{-5} M).

The fluorescence excitation spectrum of **1** in MCH obtained by monitoring the emission intensity at 565 and 650 nm shows well-resolved vibronic bands (400-550 nm) and a broad band centered around 470 nm, respectively (Figure 4.3). These spectral features indicate that the fluorescence of **1** at 565 nm is due to the residual monomers and that at 650 nm arises from the aggregates. The hypsochromic shift of the absorption maximum and quenching of monomer emission points to the face to face H-type of aggregate formation of **1** in MCH. [41]

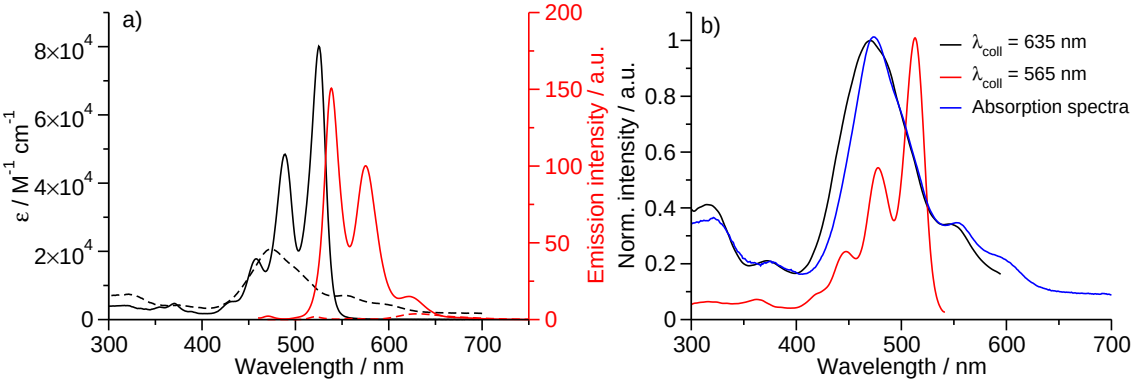

Figure 4.4: a) UV/Vis absorption (black curve) and fluorescence spectra (red curve) of **2** in chloroform (solid curve) and MCH (dashed curve) (c = 1×10^{-5}M, λ_{exc} = 450 nm). Studies were performed in a 10 mm cuvette. b) Excitation spectra of **2** in MCH (c = 1×10^{-5}M) overlaid with the corresponding absorption spectra. These studies were performed in 1 mm cuvette to minimize self-absorption.

Similar H-type aggregate formation has been observed for **2** (Figure 4.4), **3** (Figures 4.5) and **4** (Figure 4.6) in apolar solvents like MCH. The presence of chiral swallowtail in **4** increases the solubility in apolar solvents like MCH and *n*-dodecane. UV/vis absorption spectra of **4** in chloroform, MCH and *n*-dodecane show vibronic features between 400-550 nm, characteristic of molecularly dissolved PBIs. Also, the fluorescence spectra shows monomeric emission (Figure 4.6). Thus, **4** aggregates weakly in even apolar solvents.

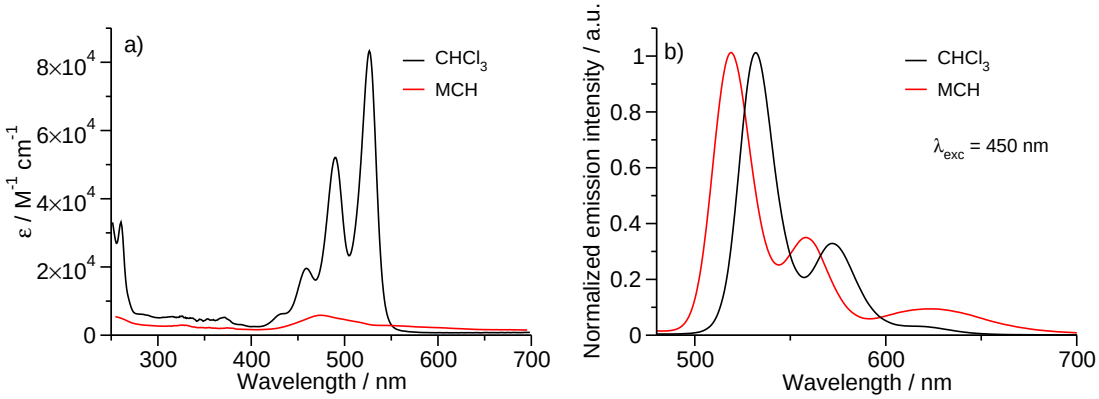

Figure 4.5: a) and b) UV/Vis absorption and fluorescence spectra respectively of **3** in chloroform (black curve) and MCH (red curve) (c = 5.21×10^{-6}M). Studies were performed in a 10 mm cuvette. Emission spectra of **3** in $CHCl_3$ was recorded in a 1 mm cuvette to reduce the self-absorption.

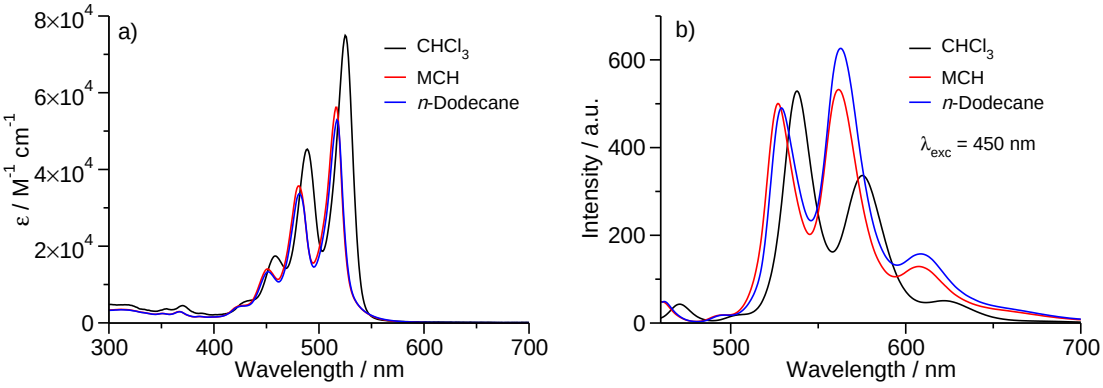

Figure 4.6: a) and b) UV/Vis absorption and fluorescence spectra respectively of **4** in different solvents. Concentration in different solvents are as follows, $CHCl_3$; c= 9.52×10^{-6} M, MCH; c = 2.45×10^{-5} M, *n*-dodecane; c = 3.6×10^{-5} M. Spectra were recorded in a 10 mm cuvette.

Aggregates of **1**-**4** have been characterized through dynamic light scattering (DLS) studies and atomic force microscopy (AFM). Size of aggregates obtaind from DLS studies for molecules **1** is of the order of few 100 nm (Figure 4.7a). This indicates that indeed assemblies are formed in solution state itself. Similar size distribution was observed for **2** and **4**. Also, 1-D aggregate structures were observed from AFM studies of **1** (Figure 4.7b). Molecule **3** also exhibits size distribution of aggregates in the range of 20-800 nm in the solution state (Figure 4.8a). On the other hand, **3** forms spherical particles (Figure 4.8b). It has been observed earlier that some of the bischolesterol derivatives self-assemble into 1-D structures, and further higher order aggregation leads to formation of spherical particles. [50]

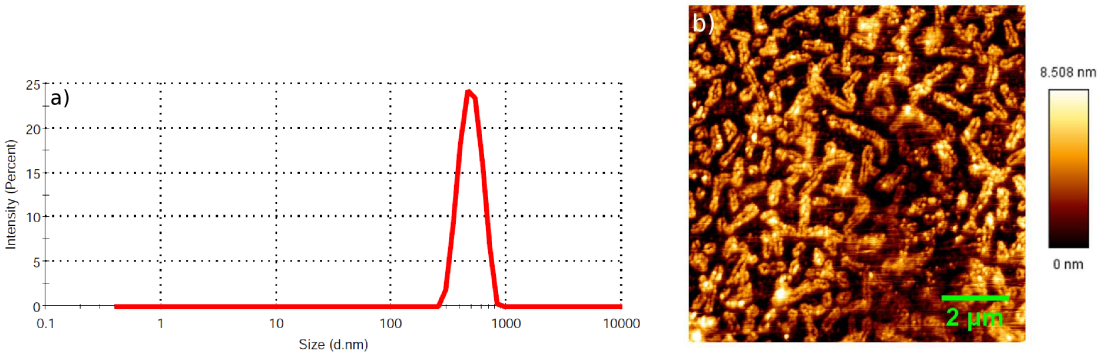

Figure 4.7: a) DLS size distribution of **1** in solution state (c = 1×10^{-5} M in 95:5 MCH:TCE (v/v)). b) AFM height profile of a film of **1** on a glass slide.

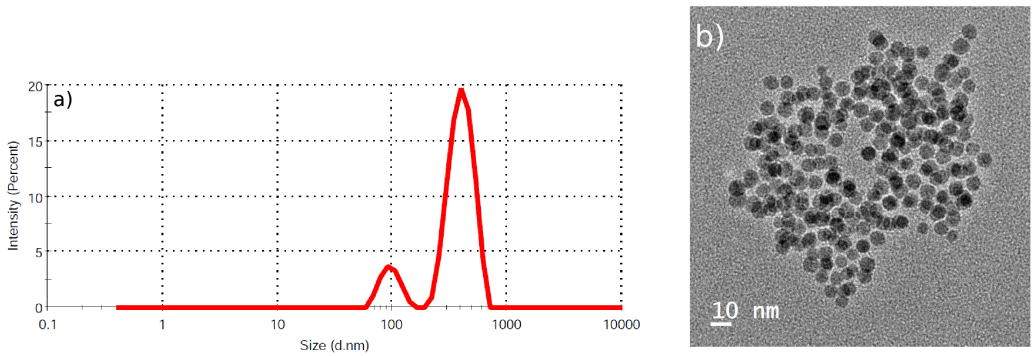

Figure 4.8: a) DLS size distribution of **3** in solution state. b) AFM height profile of a film of **3** on a glass slide. b) TEM micrograph of **3** obtained by drop-casting a solution on a copper grid. All these studies were performed in 80:20 MCH:TCE (v/v) at a concentration of 2×10^{-5} M.

The cholesterol moiety possessing chiral centers has been utilized for the organization of various chromophores. [51–53] It has an additional role in acting as a source of chiral bias to organize the π-conjugated molecules into helical assemblies by imparting van der Waals interaction to stabilize the assemblies. [54] Circular dichroism (CD) spectra of **1** in MCH and 1,1,2,2-tetrachloroethane (TCE) (95:5, v/v) (c = 1×10^5 M) showed a bisignated positive Cotton effect with positive and negative maximum at 485 and 450 nm, respectively (Figure 4.9a), suggesting the right handed chiral organization of the PBI core due to the presence of cholesterol moiety. [55] Further, by heating the solution, CD effect (mdeg) decreased in magnitude, and beyond 70 °C it vanishes (Figure 4.9a), suggesting the loss of chiral organization of the assembly. The corresponding temperature-dependent UV/vis absorption spectra show the evolution of vibronic features (characteristic of monomers) with an increase in temperature (Figure 4.9b). This observation indicates that the CD spectral changes (with temperature) are indeed due to the disassembly of the aggregates.

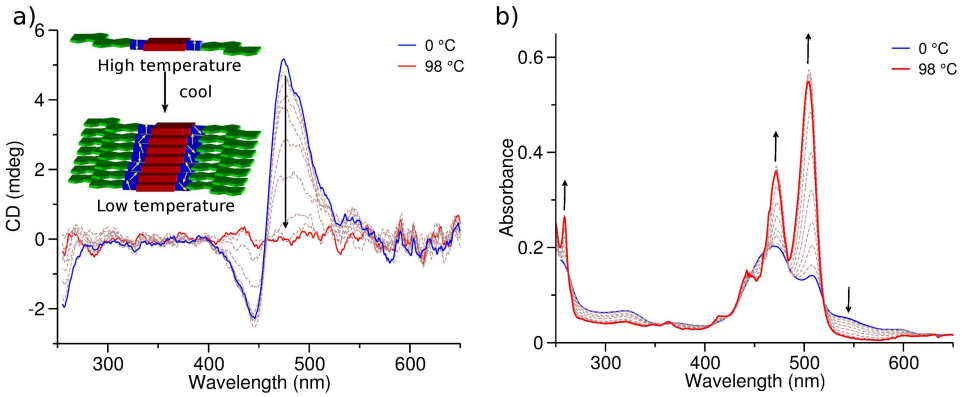

Figure 4.9: Temperature-dependent CD (a) and UV/vis absorption spectra (b) of **1** in MCH/TCE (95:5, v/v) at every 10 °C. All studies were done at a concentration of 1×10^{-5} M in a 10 mm cuvette. Inset of (a) shows a schematic representation of the assembly at high and low temperatures. Arrows indicate spectral changes with an increase in temperature.

CD spectra of dihydrocholesterol appended derivative with carbonate linker (**2**) (Figure 4.10a) and cholesterol tethered derivative (**3**) (Figure 4.10b) in the self-assembled state show positive and negative Cotton effect, respectively, indicating a chiral supramolecular organization. The sign and magnitude of the CD spectra vary with aging and cooling rate, [56] as observed in other cholesterol- and dihydrocholesterol-based gelators, [53, 57] probably due to the presence of multiple stereocenters (which compete among themselves) in the self-assembling moiety. On

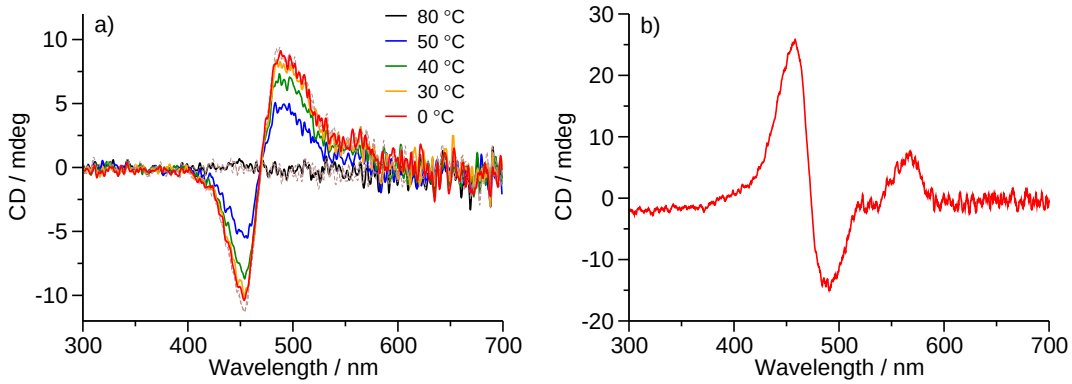

Figure 4.10: a)Temperature-dependent CD of **2** (c = 8×10^{-6} M) in MCH/TCE (95:5, v/v). b) CD spectra of **3** in MCH/TCE (80:20, v/v, c = 2×10^{-5} M). The spectra were recorded in a 10 mm cuvette.

the other hand, carbonate linker possessing **4** was CD silent, probably due to the high flexibility of the chiral swallowtails, which hinders any chiral organization in the assemblies (vide infra, MD simulations).

4.2.3 Mechanism of self-assembly

The temperature dependence of the degree of aggregation (α) has been employed in the literature to ascertain the mechanism of self-assembly. [24, 27, 58] Utilizing the same methodology, we study the self-assembly mechanism of **1**-**4** by monitoring changes in either CD or UV/vis absorption spectra at a particular wavelength (characteristic of the assemblies) as a function of temperature. The normalized change in CD monitored at 480 nm for a solution of **1** (carbonate linker and cholesterol motif) as a function of temperature (cooling curve) is clearly non-sigmoidal (Figure 5.5a).

The experimental data are in agreement with the fit obtained by the Eikelder-Markvoort-Meijer (EMM) model for a nucleation-elongation mechanism for a one-component system, [59, 60] indicating a cooperative (or nucleation-elongation) mechanism of self-assembly of **1**. The temperature in the cooling curve at which the self-assembly begins is termed as elongation temperature (T_e). The relevant thermodynamic parameters for the self-assembly of **1** at various concentrations have been obtained from the fitting of the cooling curves (Table 4.1). In addition, temperature-dependent UV/vis studies also exhibited a critical point in the cooling curve (Figure 4.12), reaffirming the cooperative nature of the self-assembly of **1**. It is observed that as the total concentration of the solution increases, T_e increases, while other thermodynamic parameters like ΔG^0 and cooperativity factor are nearly identical

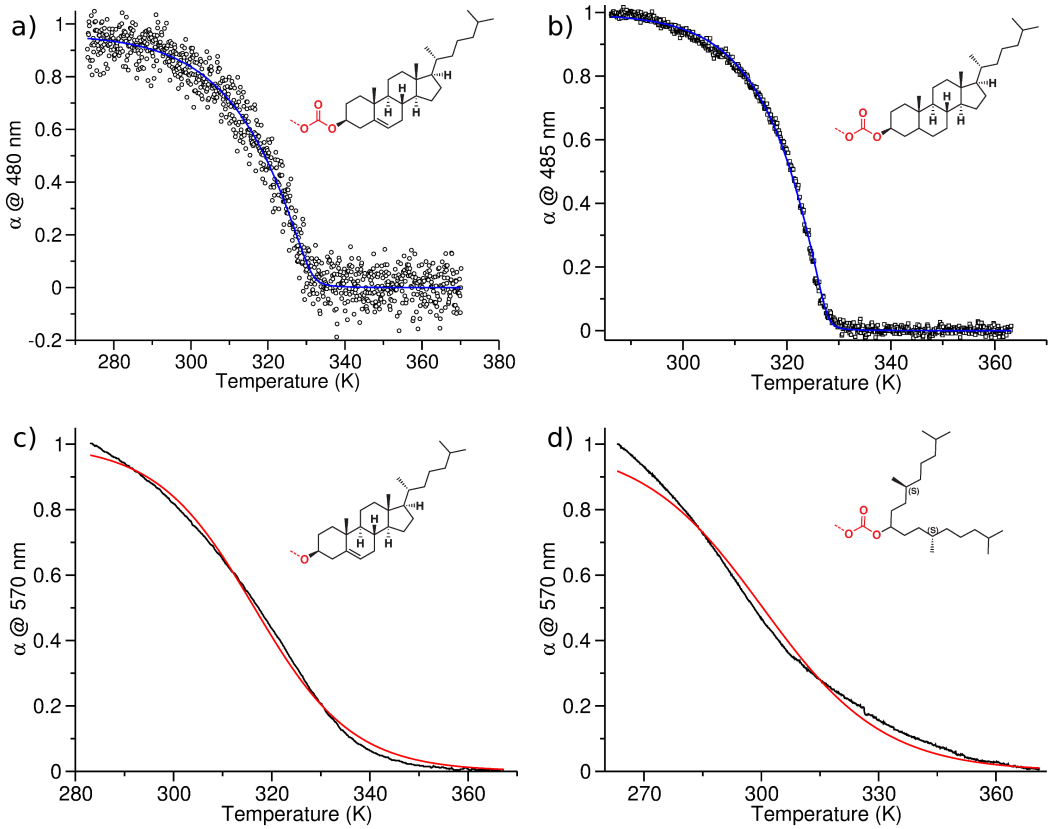

Figure 4.11: Mechanism of self-assembly of **1**-**4**. a) and b) Degree of aggregation (α) as a function of temperature (cooling curve) for a solution (95%MCH and 5% TCE) of **1** and **2**, respectively, by monitoring the CD effect at 480 nm (for **1**) and 485 nm (for **2**) at a cooling rate of 2 K/min (c = 8.0×10^{-6} M). c) Cooling curve obtained by monitoring changes in UV/vis absorbance of **3** at 570 nm at a cooling rate of 1 K/min (c = 2×10^{-5} M in 80% MCH and 20% TCE). d) Normalized change in UV/vis absorbance of **4** as a function of temperature, monitoring the absorbance at 570 nm (cooling rate 2 K/min, c = 4.69×10^{-4} M, in MCH). The solid blue and red lines are the fits obtained from nucleation-elongation and isodesmic models, respectively. The structures of linker and self-assembling group corresponding to each of the molecules are shown as insets.

(Table 4.1). Similar effects of concentration on T_e have been reported in literature for other systems. [17]

Concentration (M)	$\Delta H^0{}_e$ (kJ/mol)	ΔS^0 (kJ/mol·K)	$\Delta H^0{}_{nucl}$ (kJ/mol)	T_e (K)	σ	ΔG^0 (kJ/mol)
1.0×10^{-5}	-34.25 ±0.90	-0.0045 ±0.0027	-19.25 ±0.85	341.60 ± 0.44	4.2×10^{-4}	-32.90 ±0.1
8.0×10^{-6}	-56.06 ±2.06	-0.072 ±0.006	-19.51 ±1.80	330.30 ±0.46	3.8×10^{-4}	-34.59 ±0.27
6.0×10^{-6}	-42.62 ±2.19	-0.030 ±0.007	-14.17 ±0.95	327.74 ±0.72	3.3×10^{-3}	-33.67 ±0.1

Table 4.1: Thermodynamic parameters of **1** at different concentrations in MCH/TCE (95:5, v/v) obtained from temperature-dependent CD measurements. ΔG^0 was calculated at 298.15 K.

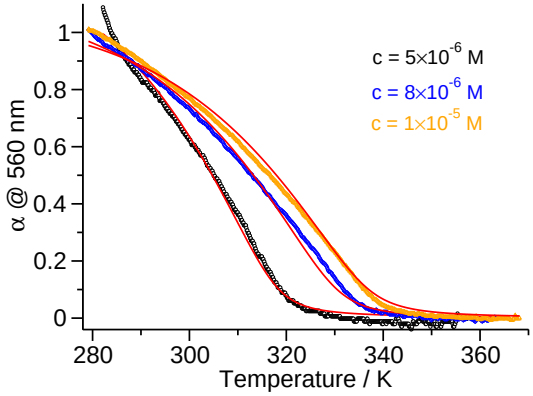

Figure 4.12: UV/Vis absorption cooling curves of **1** in 95% MCH and 5% TCE at different concentrations. Cooling rate of 1 K/minute was used. The red solid lines represent the fits obtained by the nucleation-elongation model.

Dihydrocholesterol- and cholestero-based ALS (where A = aromatic, L = linker, and S = steroidal groups) systems have been shown to differ significantly in their gelation properties. [61] Since dihydrocholesterol is a rarely used self-assembling motif, it is interesting to note its effect on the mechanism of self-assembly. Thus, the cooling curves obtained for **2** (carbonate linker and dihydrocholesterol motif) obtained from CD (Figure 5.5b) and UV/vis absorption studies(Figure 4.13a) showed a non-sigmoidal behavior and the experimental data are well described by the nucleation-elongation model. Cooling curves monitored at two different wavelengths (475 and 560 nm) show similar T_e, indicating that both absorption bands correspond to the same aggregate (Figure 4.13b).

Apart from temperature, concentration can also be used to vary the extent of aggregation, and such concentration-dependent studies have been extensively used by Würthner and co-workers to ascertain the mechanism of self-assembly. [36, 41]

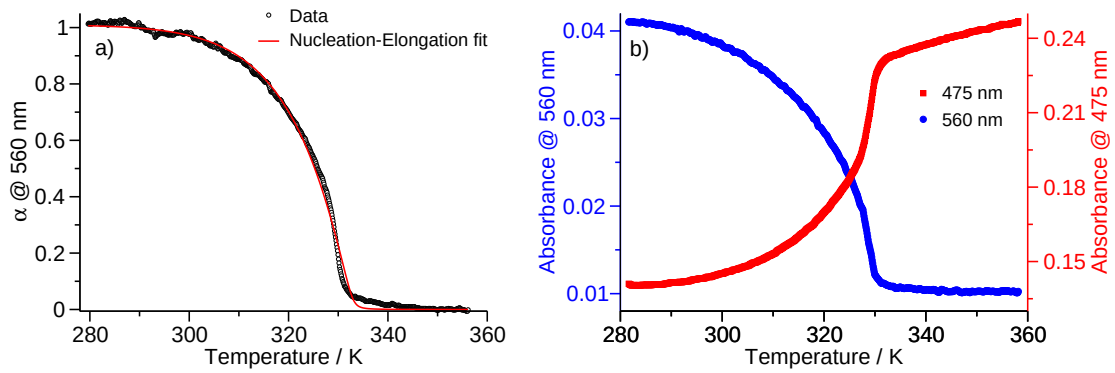

Figure 4.13: a) UV/Vis absorption cooling curves of **2** (c = 1×10^{-5}). b) Temperature-dependent UV/Vis cooling curves of **2** (c = 8×10^{-6} M) obtained by monitoring absorption at two different wavelengths with a cooling rate of 1 dpm. These studies were carried out in 95% MCH and 5% TCE solvent composition.

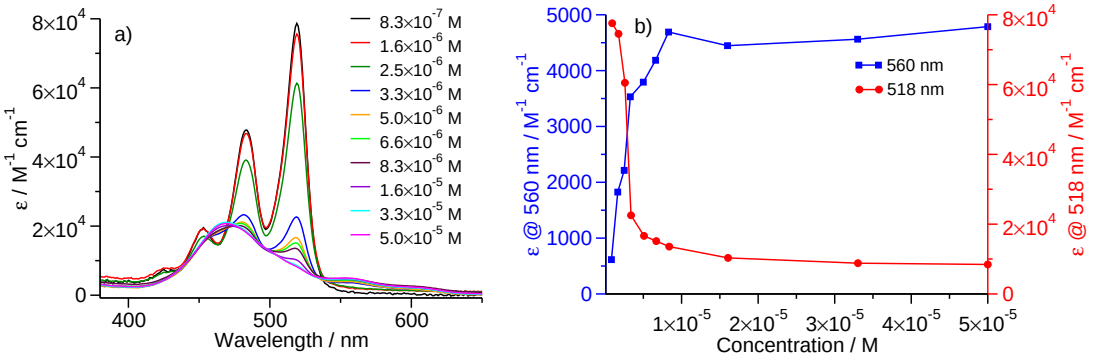

Figure 4.14: a) UV/Vis absorption spectra of **2** in 95:5 (MCH:TCE, v/v) at different concentrations. b) Molar extinction coefficient (ϵ) versus the concentration monitored at two different wavelengths (The value of ϵ are obtained from figure a).

Thus, concentration-dependent UV/vis absorption studies of **2** in MCH/TCE (95:5, v/v) were performed. The transition from monomers to aggregates occurs within a narrow concentration range of 2.5×10^{-6}-3.3×10^{-6} M (Figure 4.14), thus indicating the cooperative mechanism of self-assembly.

Interestingly, the cooperativity parameter (σ, obtained from fitting the experimental cooling curve to the EMM model [59, 60]) for **2** was found to be consistently (by both CD and UV/vis measurements) lower than that for **1** (Table 4.2), suggesting a higher degree of cooperativity in the former system compared to that in the latter. σ is of the order of 10^{-3} for **1**, whereas for systems containing intermolecular hydrogen bonds, it is found in the range of 10^{-3}-10^{-6}. [17, 20–26] Despite the lack of

Molecule	ΔH_e (kJ/mol)	ΔS_e (kJ/mol·K)	ΔG^0 (kJ/mol)	Cooperativity factor, σ
1	-41.61	-0.027	-33.45	2.4×10^{-3}
2	-89.98	-0.17	-37.25	2.0×10^{-4}

Table 4.2: Comparison of Thermodynamic Parameters for the Assembly of **1** and **2** (in 95% MCH and 5% TCE). Values presented are average of those obtained by fitting to the EMM model [59, 60] for **1** and **2** (from CD and UV/vis studies at different concentrations). The values for **1** are averages of those presented in Table 4.1 and the ones obtained from UV/vis studies. ΔG^0 was calculated at 298.15 K.

any apparent hydrogen-bonding motif, the present systems (**1** and **2**) show cooperativity comparable to conventional hydrogen-bonded systems. In addition, **2** shows: a lower cooperativity factor σ, more negative ΔG^0, and lower solubility compared to **1** (Table 4.2). These differences can be mainly attributed to the structural planarity of dihydrocholesterol compared to cholesterol, which enhances van der Waals interaction between the moieties in an assembly. [61]

The self-assembly mechanisms of **3** (ether linker and cholesterol motif) and **4** (carbonate linker and chiral swallowtail) were also studied using temperature-dependent UV/vis spectroscopy. [62] A solution (c = 2×10^{-5} M in MCH/ TCE (8:2, v/v)) of **3** showed the gradual evolution of the extent of aggregation with decrease in temperature (Figure 5.5c). The cooling curve could well be described by the isodesmic model, [58] yielding an enthalpy of polymerization (ΔH) of -92.0 kJ/mol and melting temperature (T_m, temperature at which $\alpha = 0.50$) of 316.5 K. Similarly, the cooling curve for **4** (in MCH, c = 4.69×10^{-4} M) showed a sigmoidal behavior and could be fit to an isodesmic model (Figure 5.5d), [63] yielding the thermodynamic parameters ΔH = -53.5 kJ/mol and T_m = 300.4 K. Thus, the linker group of the monomer significantly affects the mechanism of self-assembly.

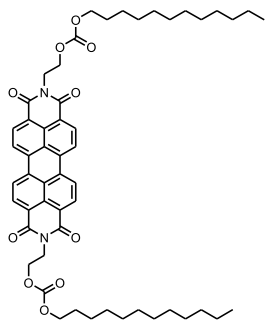

Figure 4.15: Molecular structure of **PBI_carb_dd**.

Since **4** is isodesmic and weakly aggregating, another derivative of PBI (**PBI_carb_dd**, Figure 4.15) possessing linear dodecyl chains in place of branched chains (**4**) was synthesized to investigate its effect on the mechanism of self-assembly.

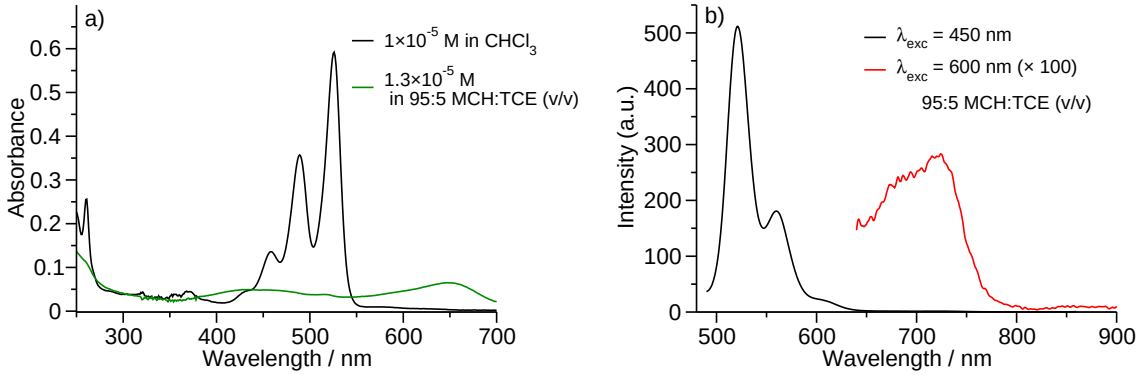

Figure 4.16: a) UV/Vis absorption cooling curve of **PBI_carb_dd**. b) Fluorescence spectra of **PBI_carb_dd** in 95:5 MCH:TCE (v/v) (c = 1.3×10^{-5} M). These studies are performed in a 1 mm cuvette at 20 °C.

PBI_carb_dd shows red-shifted absorption maximum (≈ 650 nm) in apolar solvents indicating the formation of J-type of aggregates. Also the emission from aggregates is red-shifted (725 nm, Figure 4.16). Similar red-shifted absorption peaks were observed for ester functionalized perylene bisimides. [64] Further, **PBI_carb_dd** exhibits a cooperative mechanism of self-assembly (Figure 4.17). The role of linear alkyl chains in affecting the intermolecular interaction between ester groups was observed in structurally similar perylene bisimide derivatives. [64, 65]

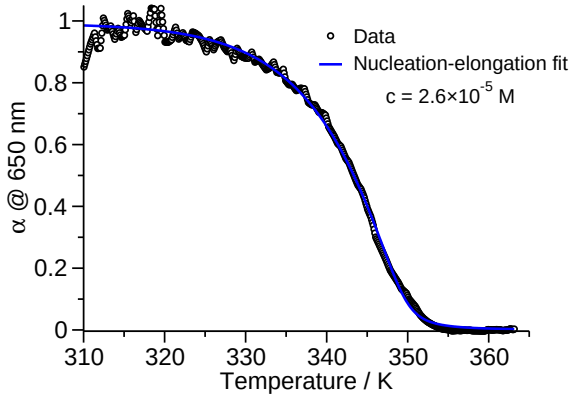

Figure 4.17: UV/Vis cooling curve of **PBI_carb_dd** (c = 2.6×10^{-5} M in 95:5 MCH:TCE (v/v)) with a cooling rate of 1 dpm. The spectra was recorded in a 10 mm cuvette.

4.2.4 Molecular Dynamics (MD) Simulations

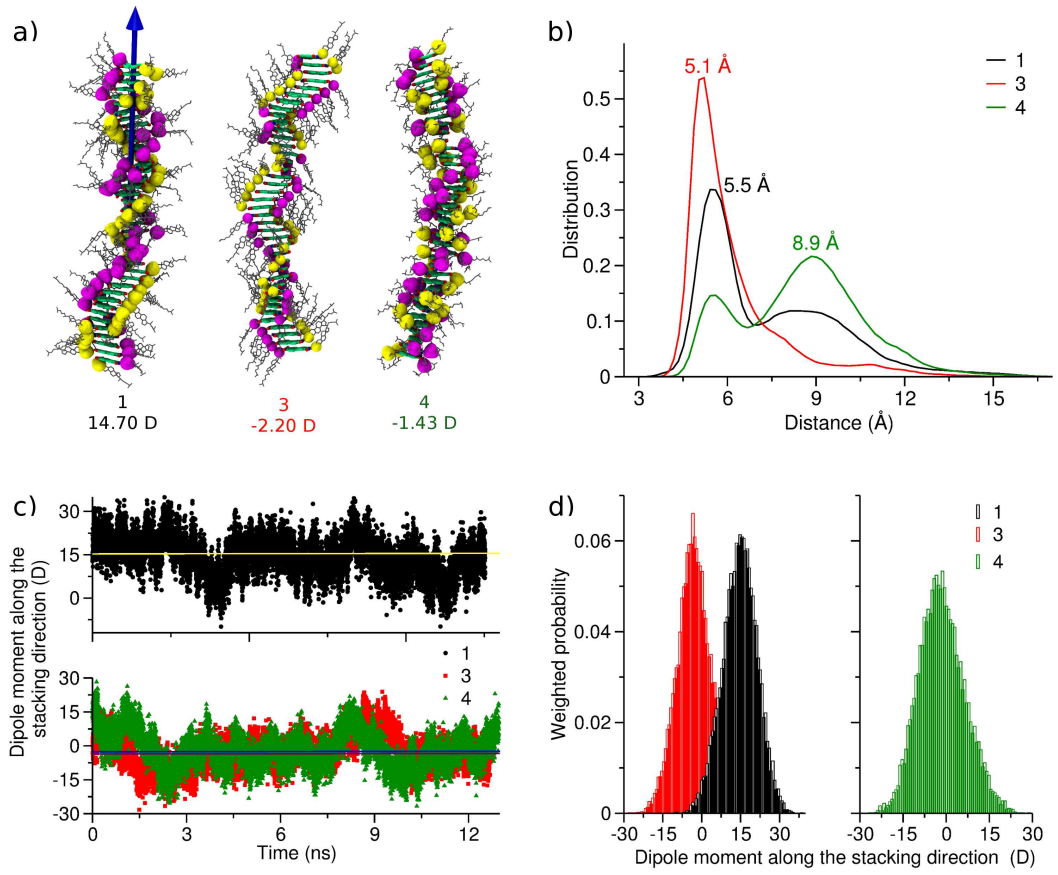

Figure 4.18: MD simulations of the assemblies of **1**, **3** and **4**. a) Snapshot illustrating the arrangement of molecules in the assembled state. Linkers are highlighted in yellow and magenta to aid in the visualization of the helical packing. Self-assembling groups are represented with thin sticks, and hydrogens are omitted for clarity. b) Distance distribution between the linkers of neighboring molecules. c) Macro-dipole along the stacking direction as a function of time. Solid horizontal lines (yellow for **1**, blue for **3**, and maroon for **4**) are drawn to represent the mean dipole moment value for each system. d) Weighted probability distribution of macro-dipole obtained from (c). All the analysis was performed on the last 12 ns of the MD trajectory.

Computational studies were undertaken to gain further insight into the molecular organization of the assemblies and to elucidate the role of different moieties on the self-assembly mechanism. Quantum chemical calculations are computationally expensive in determining the equilibrium structure of assemblies due to the large

MD simulations were carried out by Karteek Kumar Bejagam from JNCASR

number of atoms. On the other hand, MD simulations can describe the molecular packing in these supramolecular assemblies. [66–71] In particular, MD simulations are well suited to treat the effect of solvents and temperature, so as to realize experimental conditions. Thus, MD simulations were carried out to investigate the molecular packing in the aggregated state for **1**, **3** and **4** and to understand the mechanism of their selfassembly in terms of intermolecular interactions. MD simulations were not performed for **2** because of its structural similarity to molecule **1**. Simulations of pre-formed oligomeric stacks, each containing 40 molecules of **1**, **3** and **4** were performed in explicit cyclohexane at 298.15 K for 20 ns.

Snapshots at the end of the MD simulations for cholesterol appended molecules **1** and **3** exhibit helical packing of linker groups (carbonate or ether) around the PBI core (Figure 4.18a). This, in turn, is reflected in the ordered helical organization of the peripheral cholesterol groups and PBI core, in agreement with the experimental observation of bisignated CD signal (Figure 4.9a). On the other hand, the organization of linker groups (carbonate) in the assembly of **4** is ill-defined (Figure 4.18a) which can be attributed to the flexibility of the chiral swallowtail. Coincidentally, chiral organization in **4** is experimentally determined to be absent as well. The arrangement of linkers in the assembly can be further quantified by the distance between them across neighboring molecules in an assembly (Figure 4.18b). Assemblies of **1** and **4** exhibit a bimodal distribution of interlinker (carbonate) distances, centered at 5.5 Å and 9 Å. For **1**, the intensity at 5.5 Å is larger than at 9 Å, suggesting that the majority of carbonate groups are more closely arranged in an assembly of **1** compared to that of **4**. A unimodal probability distribution centered at 5.1 Å is observed for the assembly of **3** (ether linker), suggesting close and uniform packing of linkers. Thus, the differences in the structural organization can be attributed to the rigidity or flexibility of the self-assembling moiety.

The consequence of structural organization of linkers on the macro-dipole moment (along the stacking direction) is studied during the MD trajectory (Figure 4.18c and d). Macro-dipole is calculated as

$$\sum_{i=1}^{n} q_i \vec{r_i}$$

where q_i is the charge on the atoms and $\vec{r_i}$ the displacement vector from negative to positive charge, respectively, and the sum extends over all atoms. The mean macro-dipole moment for **1** (14.7 D) is an order of magnitude higher than that for **4** (1.43 D), although in both molecules (**1** and **4**), the carbonate linker is the

dipolar entity. In molecule **1**, the carbonate-linkers are ordered and interact with those from neighbouring molecules. This carbonate-carbonate inteaction along the stack gives rise to a significant macrodipole for **1**. However, in case of molecule **4**, because of the lack of inter-linker interactions between monomers in an assembly, the net macrodipole is much less. For molecule **3**, again the macrodipole moment is vanishly close to zero. This is due to the absence of any significant molecular dipole moment in **3**. Thus, a combination of the nature of linker-group and the peripheral self-assembling moiety dictates the mechanism of self-assembly.

4.2.5 Dielectric Measurements

A significant macro-dipole moment in **1** and none in **4** would be reflected in the dielectric constants of these molecules. Capacitance measurement is a direct experimental means of quantifying the extent of polarization in the system. Thus, we have measured the bulk (thin-film state) capacitance for assemblies of **1**-**4** to evaluate the magnitude of polarization and to correlate with the mechanism of self-assembly at the molecular level.

The dielectric constant, $\epsilon_r = \mathrm{Cd}/\epsilon_0\mathrm{A}$ (where C is capacitance, d film thickness, ϵ_0 vacuum permittivity, and A area of the film obtained from the capacitive response), is essentially a measure of the macroscopic dipole moment. [72] Molecules **1** and **2**, which exhibit a cooperative self-assembly, display higher polarization indicated by the higher magnitude of ϵ_r (Figure 4.19a). It should be noted that this magnitude of ϵ_r (≈ 16 for molecule **2**) is around 5 times higher than the ϵ_r observed for molecules **3** and **4**, which do not follow a cooperative mechanism of self-assembly.

Classical theory of linear dielectrics based on Clausius-Mossotti relation is used to estimate the polarizability at zero frequency of the molecules. [73] The effective dipole moment per molecule ($|\mu|$) estimated from the dielectric constant measurement of the assembly are 3.4, 0.7 and 0.5 D for molecules **1**, **3** and **4** respectively. In comparison, the the macrodipole moment obtained from MD simulation was divided by 40 (oligomer size) to obtain the dipole moment per molecule ($|\mu|$); dipole moments from simulations for **1**, **3** and **4** are 0.36, 0.005 and 0.03 D respectively. Thus, the value of $|\mu|$ for molecules **1**, **3** and **4** estimated from MD simulation is 10 times lower than the experimentally obtained value. This can be attributed to the difference in the measurement conditions (such as condensed phase) versus that in

These experiments were performed by Dr. Satyaprasad P. Senanayak from JNCASR.

the simulations which were carried out in the solution phase. However, the trends in dipole-moment values are same across different molecules obtained from both MD simulations and dielectric measurements.

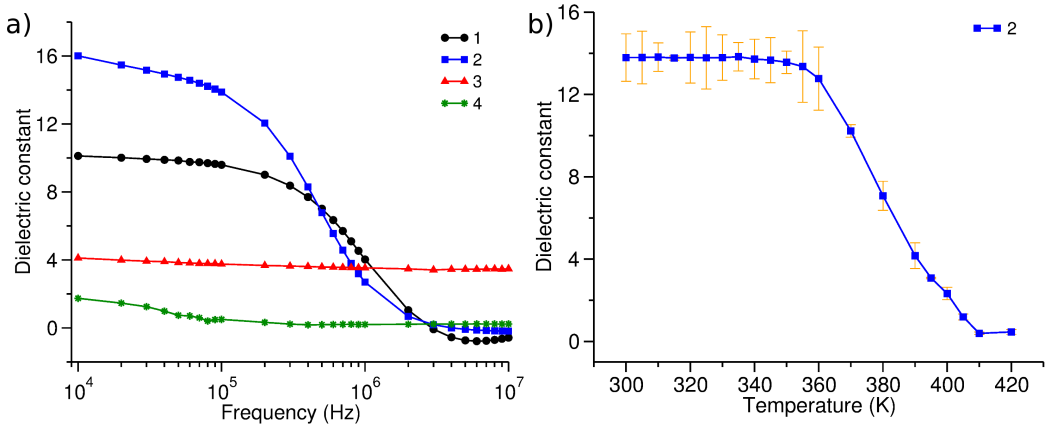

Figure 4.19: Bulk dielectric measurements. a) ϵ_r measurement as a function of frequency. b) ϵ_r variation with temperature for molecule **2** at 10 kHz. Inset in b) shows a schematic of the device and the dipole alignment at different temperatures. The oval-shaped dipoles represent the polarization of an aggregate and not that of individual molecules.

The relaxation dynamics involved in the dipole or an assembly of dipoles is probed by looking into the variation of ϵ_r as a function of frequency. A decrease in ϵ_r magnitude at high frequency is observed for molecules **1** and **2**, whereas molecules **3** and **4** demonstrated a flat frequency response (Figure 4.19a). This response can be directly correlated to the long-range interaction which drives the cooperative assembly. Due to the existence of long-range interaction, the dipoles behave as clusters or domains which have a relatively slower response compared to individual dipoles. [74] Thus, frequency-dependent dielectric studies confirm the presence of significant clustering of dipoles in condensed phase of **1** and **2** and a lack of such interactions for **3** and **4**.

The temperature dependence of dielectric constant reveals the significance of dipole-dipole interaction necessary to drive the cooperative behavior. The ϵ_r versus temperature curve for molecules **2** (Figure 4.19b) indicate a critical temperature where the ϵ_r starts to decrease, and for higher temperatures (390-420 K) ϵ_r = 1-2 is obtained. This behavior can be correlated to the cooperative nature of the individual molecular dipoles which result in a macroscopic polarization. As the temperature increases, the thermal-disorder decreases the dipole-dipole interaction between monomers in an assembly. It is to be noted here that the assembly is not

completely disassembled at higher temperatures; rather, the dipole-dipole interactions have vanished. Thus, cooperativity in an assembly mechanism can also be observed using dielectric measurements.

4.3 Discussion

The different mechanisms of self-assembly observed in the present systems can be rationalized at a molecular level, based on MD simulation and bulk dielectric measurements as summarized below. For molecules **1** and **2**, the carbonate linkers are closely packed in an ordered manner leading to an enhanced interaction between them, which is reflected in the magnitude of its macro-dipole moment and dielectric constant. Between **1** and **2**, the latter shows higher cooperativity, more negative free energy of polymerization, and higher dielectric constant. This could be mainly due to the planar and rigid conformation of dihydrocholesterol leading to stronger carbonate-carbonate interaction in the assembly compared to molecule **1**. In the case of **3**, although the assembly is ordered, it does not lead to a high macro-dipole moment since the dipole moment of ether linkers is small; no appreciable long-range interaction is possible, and the molecule assembles in an isodesmic manner. Similarly, although **4** possesses dipolar carbonate groups, because of the lack of ordered organization wrought by the flexibility of chiral swallowtails, no macro-dipole moment is observed, resulting in its isodesmic polymerization. Cooperative self-assembly is observed for **PBI_carb_dd** containing dodecycl chains as the self-assembling moiety and carbonate groups as linkers; this again suggests that the linear dodecyl chain can pack better through van der Waals interactions, leading to strengthening of the carbonate-carbonate interaction. Thus, the rigidity/flexibility of the selfassembling moiety reinforces the dipolar interactions between the monomers in the assembly.

4.4 Conclusions

We have studied the mechanism of self-assembly of five PBI derivatives appended with different linkers and self-assembling moieties, in an attempt to elucidate the molecular features governing the mechanism of supramolecular polymerization. For molecules following a cooperative mechanism of self-assembly (**1** and **2**), significant macro-dipole or polarization was observed through both MD simulation and bulk dielectric measurements. However, the absence of either the dipolar carbonate group, as in molecule **3**, or a suitable self-assembling moiety, as in molecule **4**, results in

an isodesmic self-assembly without any significant polarization for the assembly. Thus, with the aid of careful molecular design, MD simulation, and bulk dielectric measurements, we are able to provide a proof-of-concept example for the long-range interaction-driven cooperative self-assembly, as hypothesized earlier. [34] It is also to be noted that polarization or macro-dipole only in the stacking direction is critical in governing the mechanism of self-assembly.

4.5 Experimental section

4.5.1 General Methods

Chemicals and synthesis related: Cholesterol chloroformate (97%), Perylene-3,4,9,10-tetracarboxylic acid dianhydride (97%) and Ethanolamine (≥98%) were purchased from Sigma-Aldrich. Cholesterol (95%) was purchased from Acros-Organics. Triphosgene (98%) and dodecyl chloroformate (≥90%) were purchased from TCI-India and Di-tert-butyl-dicarbonate (99.5%) from SD-fine chemicals ltd. India. Pyridine stored over KOH was freshly distilled before use. Thin layer chromatography (TLC) was performed using Merck silica gel 60 F_{254} plates coated on aluminium. Column chromatography was performed using Merck silica gel 60 (230-400 mesh, 40-63 μm) under positive pressure of nitrogen gas.
Compounds **5**, [75] **12**, [76] **13** [77] and **20** [78] were synthesized according to the literature reports. Alcohols (**8** and **16**) were converted to the corresponding chloroformates using triphosgene. [79]

Optical studies: UV/Vis absorption and fluorescence spectra were recorded on a Perkin-Elmer Lambda 750 and Perkin-Elmer LS 55 spectrometer respectively. Temperature-dependent UV/Vis absorption spectra were recorded on Perkin-Elmer lambda 750 using PTP-1+1 Peltier and Templab 2.14 software. Circular dichroism (CD) spectra were recorded on a JASCO J-815 spectrometer using the following parameters; sensitivity = 100 mdeg, scan rate = 100 nm/minute, bandwidth = 1 nm, response time = 1 second and number of accumulations = 1. Temperature-dependent measurements were performed using a CDF-426S/15 Peltier type temperature controller with a temperature range of 263-370 K.

Mass spectroscopy details: Gas chromatography mass spectrometry (GC-MS) was performed on a Shimadzu GCMS-QP2010 Plus with a RTx-5M5 column (length = 30.0 m, thickness = 0.25 μm, diameter = 0.25 mm). The method details

are as follows; column oven temperature = 60 °C, injection temperature = 250.0 °C, ion source temperature = 200.0 °C, 60 °C hold for 2 mins then 10 °C/minute upto 300 °C and hold again at this temperature for 5 minutes. Initial 3 minutes of solvent cut-off was used. For electron-ionization (EI) method voltage of 70 eV was applied. High Resolution Mass Spectra (HRMS) were recorded on a Agilent 6538 Ultra High Definition (UHD) Accurate-Mass Q-TOF-LC/MS system using either atmospheric pressure chemical ionization (APCI) or electrospray ionization (ESI) mode. Matrix-Assisted Laser Desorption Ionization was performed on a Bruker daltonics autoflex (ST-A2130) spectrometer using trans-2-[3-(4-tert-Butylphenyl)-2-methyl-2-propenylidene]malononitrile (DCTB) as the matrix.

NMR spectroscopy: ^{1}H and ^{13}C-NMR spectra were recorded on a Bruker Avance 400 spectrometer operating at 400 MHz and 100 MHz respectively. Chemical shifts are reported with respect to the residual solvent peaks of chloroform-D (δ = 7.26 ppm for ^{1}H and 77.16 ppm for ^{13}C NMR). Notations; s, d, t, q, m and br stand for singlet, doublet, triplet, quartet, multiplet and broad respectively. All NMR spectra were recorded at 300 K unless otherwise mentioned.

Fitting of cooling curves: Nucleation elongation model was fitted using Matlab R2008b and the temperature-dependent isodesmic model using Xmgrace software.

Dynamic Light Scattering (DLS) studies: DLS studies were performed on Malvern UK NanoZS system using a 633 nm laser at a back scattering angle of 173°. For all the samples the count rates were more than 50 kcps.

Transmission Electron Microscopy (TEM): TEM micrographs were recorded on a JEOL, JEM 3010 with an operating voltage of 300 kV. The samples were prepared by drop-casting the solution of interest on a cooper grid and allowed to air dry followed by drying in vacuum. No staining agent was used.

Atomic Force Microscopy (AFM): AFM imaging was performed using JPK Nanowizard 3 instrudment in the contact mode with a conducting cantilever tips made of Cr/Pt coated on Silicon. Typical resonant frequency of the cantilever was in the range of 13 - 15 kHz and the spring constant was 0.2 N/m. The samples were prepared by drop-casting the solution containing aggregates of different molecules

on a glass slide and allowed to evaporate at room temperature, further the samples were dried under high vacuum at room temperature.

Sample preparation for studies: For spectroscopic studies of **1**, stock solution was prepared in methylcyclohexane (MCH) and diluted approripately with MCH and 1,1,2,2-tetrachloroethane (TCE) to obtain the desired concentration. For molecule **2** stock solution was prepared in TCE.

4.5.2 Synthetic details

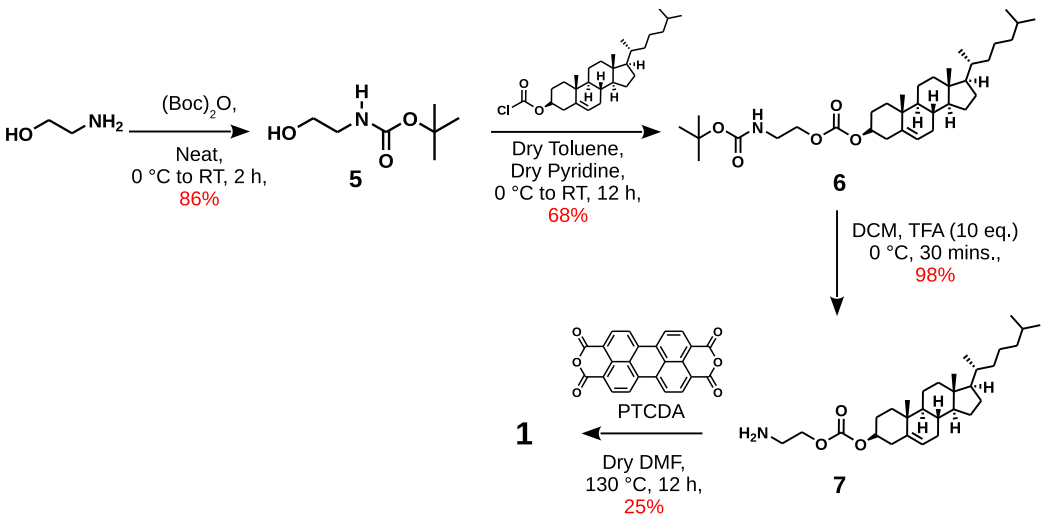

Figure 4.20: Synthetic route for **1**.

Synthesis of 5: Ethanolamine (1 g, 16.3 mmol, 1.0 eq.) was taken in a single necked RBF (50 mL). Di-tert-butyl dicarbonate (3.57 g, 16.3 mmol, 1.0 eq.) was added to the RBF at 0 °C. Evolution of effervescence (mostly CO_2) was observed. The reaction mixture was stirred at room temperature (RT) for another 2 hours. After 2 hours TLC of the reaction mixture indicated that ethanolamine was consumed. Thus the reaction was stopped. The reaction mixture was diluted with chloroform and extracted with water (3 × 50 mL). The combined organic layer was dried (anhydrous Na_2SO_4) and evaporated under reduced pressure to obtain a colorless oil (2.27 g, 86%).

R_f = 0.33 (10% MeOH in $CHCl_3$)

^{1}H-NMR (400 MHz, $CDCl_3$): δ = 0.49 (s, br, 1H), 3.70 (t, J = 5 Hz, 2H), 3.28 (q, J = 5.2 Hz, 2H), 1.44 ppm (s, 9H).

Synthesis of 6: **5** (1 g, 6.2 mmol, 1.0 eq.) was taken in 2-necked RBF (100 mL) fitted with a dropping funnel and a reflux condenser. Dry toluene (15 mL) and dry pyridine (1.5 mL, 18.6 mmol, 3.0 eq.) was added to the RBF and stirred at RT for 5 minutes. Cholesterol chloroformate (3.0 g, 6.8 mmol, 1.1 eq.) dissolved in dry toluene (10 mL) was added dropwise to the RBF through the dropping funnel at 0 °C. The solution was stirred at RT for 12 hours. TLC after 12 hours showed the absence of **5** in the reaction mixture, thus the reaction was stopped and the solvent was removed under reduced pressure to obtain a white solid.
Purification: A column chromatography (SiO_2, 100-200 mesh, packed with chloroform) was performed on the crude product with a gradient elution of 0-3% MeOH in $CHCl_3$ to obtain a white solid (2.42 g, 68%).
R_f = 0.71 (5% MeOH in $CHCl_3$)
^{1}H-NMR (400 MHz, $CDCl_3$): δ = 5.39 (d, J = 5.2 Hz, 1H), 0.48 (s, br, 1H), 4.51-4.43 (m, 1H), 4.17 (t, J = 5.2 Hz, 2H), 3.40 (q, br, J = 4.8 Hz, 2H), 2.43-2.32 (m, 2H), 2.02-1.77 (m, 6H), 1.68-1.47 (m, 8H), 1.43 (s, 9H), 1.39-1.05 (m, 12H), 1.00 (s, 3H), 0.91 (d, J = 6.4 Hz, 3H), 0.86 (d, J = 2 Hz, 3H), 0.85 (d, J = 1.6 Hz, 3H), 0.68 ppm (s, 3H).
^{13}C-NMR (100 MHz, $CDCl_3$): δ = 155.87, 154.51, 139.38, 123.21, 79.75, 78.28, 66.99, 56.84, 56.29, 50.15, 42.46, 39.87, 39.66, 38.16, 36.99, 36.68, 36.33, 35.93, 32.04, 31.99, 28.50, 28.36, 28.15, 27.83, 24.42, 23.97, 22.95, 22.70, 21.19, 19.40, 18.86, 12.00 ppm.
GC-MS (EI): m/z calculated for $C_{35}H_{59}NO_5$ 573.43 $[M]^+$; found 501 $[M\text{-}(t\text{-}BuO^-)]^{\cdot}$ $[C_{31}H_{50}NO_4]^{\cdot}$.

Synthesis of 7: **6** (1.0 g, 1.76 mmol, 1.0 eq.) was taken in a single necked RBF (100 mL) and DCM (10 mL) was added to it. The mixture was stirred for 5 minutes at RT. Trifluoroacetic acid (2 mL, 26.0 mmol, 15 eq.) dissolved in DCM (10 mL) was added to the RBF dropwise through the dopping funnel over a period of 15 minutes at 0 °C. The reaction was monitored by TLC (ninhydrin test). After 30 minutes all the starting material was consumed, thus the reaction was stopped and the contents of RBF (DCM and TFA) were evaporated under reduced pressure. The residue was dissolved in $CHCl_3$ (20 mL) and extracted with water, dried (anhydrous Na_2SO_4) and evaporated under reduced pressure to obtain a pale yellow oil (0.82 g, 98%).
R_f = 0.17 (in 5% MeOH in $CHCl_3$)
^{1}H-NMR (400 MHz, $CDCl_3$): δ = 5.38 (d, 1H), 4.48-4.45 (m, 2H), 3.35 (m, 2H) 2.42-2.31 (m, 2H), 2.02-1.04 (m, 24H), 1.00 (s, 3H), 0.91 (d, J = 6.4 Hz, 3H), 0.87

(d, J = 1.6 Hz, 3H), 0.85 (d, J = 1.6 Hz, 3H), 0.67 ppm (s, 3H).

Synthesis of 1: Perylene-3,4,9,10-tetracarboxylic acid dianhydride (PTCDA, 295 mg, 0.75 mmol, 1.0 eq.) and **7** (820 mg, 1.73 mmol, 2.3 eq.) were taken in a 3-necked RBF (50 mL) fitted with a reflux condenser. Dry DMF (25 mL) was added to the RBF and the reaction mixture was stirred at 130 °C for 12 hours. After 12 hours the reaction mixture was extracted with chloroform (3 × 150 mL). The combined organic layer was washed with water (3 × 150 mL), brine, dried (anhydrous Na_2SO_4) and evaporated under reduced pressure to obtain a red solid.
Purification: The crude product was purified by repeated column chromatography (SiO_2, 100-200 mesh) using 0-3% MeOH in $CHCl_3$ as the eluent. Also size exclusion chromatography (S-X1, THF) was used to purify the compound. Finally the compound was dissolved in minimum amount of n-hexane and excess of methanol was added to preciptate the product. The precipitation was repeated twice and the solid residue was dried to obtain a red colored powder (245 mg, 25%).
^{1}H-NMR (400 MHz, $CDCl_3$): δ = 8.50 (d, J = 7.6 Hz, 4H), 8.32 (d, J = 8 Hz, 4H), 5.33 (s, br, 2H), 4.56-4.42 (m, 10H), 2.40-2.30 (m, 4H), 2.00-1.78 (m, 12H), 1.52-1.01 (m, 40H), 0.99 (s, 6H), 0.90 (d, J = 6.8 Hz, 6H), 0.86 (d, J = 2 Hz, 6H), 0.85 (d, J = 1.6 Hz, 6H), 0.66 (s, 6H) ppm.
^{13}C-NMR (100 MHz, $CDCl_3$): δ = 163.33, 154.57, 139.52, 134.43, 131.44 (br), 129.28, 126.15, 123.08 (br), 78.22, 64.71, 56.81, 56.29, 50.11, 42.44, 39.85, 39.66, 39.36, 38.10, 37.0, 36.68, 36.32, 35.93, 32.02, 31.97, 28.35, 28.16, 27.78, 24.40, 23.99, 22.96, 22.70, 21.17, 19.42, 18.85, 12.00 ppm.
MALDI-TOF (DCTB, negative mode): m/z calculated for $C_{84}H_{106}N_2O_{10}$: 1302.78 $[M]^{-\cdot}$; found:1302.90.
FTIR (ATR, neat solid): ν = 2948, 2933, 2902, 2866, 2849, 1740 (carbonate C=O), 1697 and 1657 (imide C=O), 1592, 1440, 1401, 1362, 1346, 1253, 1180, 1096, 1065, 1020, 856, 806, 794, 744 (cm^{-1}).

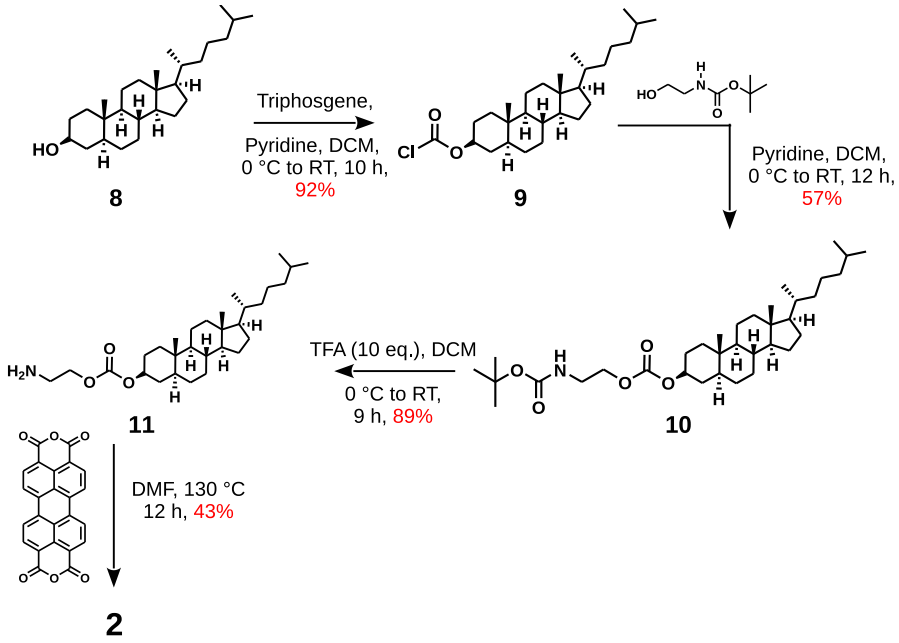

Figure 4.21: Synthetic route for **2**.

Synthesis of 9: Dihydrocholesterol (**8**, 2.0 g, 5.14 mmol, 1.0 eq.) was taken in a 3-necked RBF fitted with a dropping funnel and an argon balloon. Dry DCM (20 mL) was added to it and stirred at 0 °C for 15 minutes. Freshly distilled pyridine (100 μL) was added to the RBF. Triphosgene (0.53 g, 1.8 mmol, 0.35 eq.) dissolved in dry DCM (10 mL) was added to the RBF through the dropping funnel at 0 °C. The solution was allowed to warm to RT and stirring was continued for 10 hours. The solvent was removed under reduced pressure to obtain a white solid (2.61 g). Purification: The solid was dissolved in excess of *n*-hexane and filtered to remove the insoluble white mass (mostly unreacted triphosgene). The filtrate was concentrated under reduced pressure to obtain a white solid (2.4 g). A flash column chromatography (SiO_2) was performed on the obtained solid eluting with 30% DCM and 70% *n*-hexane to obtain the top spot as the product (2.13 g, 92%).
R_f = 0.68 (1:1 DCM and *n*-hexane)
^{1}H-NMR (400 MHz, $CDCl_3$): δ = 4.81-4.72 (m, 1H), 1.98-1.92 (m, 2H), 1.85-0.93 (m, 29H), 0.89 (d, J = 6.8 Hz, 3H), 0.86 (d, J = 1.6 Hz, 3H), 0.85 (d, J = 2.0 Hz, 3H), 0.82 (s, 3H), 0.64 ppm (s, 3H).
^{13}C-NMR (100 MHz, $CDCl_3$): δ = 149.99 (C=O), 83.34, 56.52, 56.42, 44.79, 42.74, 40.08, 39.67, 36.75, 36.32, 35.94, 35.57, 35.54, 33.63, 32.06, 28.66, 28.37, 28.16, 27.22, 24.34, 23.99, 22.96, 22.71, 21.38, 18.82, 12.33, 12.22 ppm.
GC-MS (EI): m/z calculated for $C_{28}H_{47}ClO_2$ 450.30 $[M]^+$; found 450.0

Synthesis of 10: **5** (0.39 g, 2.44 mmol, 1.1 eq.) was taken in a 3-necked RBF fitted with a nitrogen balloon and a dropping funnel. **9** (1.0 g, 2.22 mmol, 1.0 eq.) was taken in the dropping funnel. Dry DCM (20 mL) and pyridine (0.18 mL, 2.22 mmol, 1.0 eq.) was added to the RBF. The solution was stirred at 0 °C for 10 minutes. Dry DCM (10 mL) was added to the dropping funnel to dissolve **9** and this was added to the RBF dropwise at 0 °C and stirred at RT for 12 hours. After 12 hours TLC showed the absence of **9**. Thus the contents of the RBF was concentrated under reduced pressure to obtain a pasty solid (1.51 g).
Purification: A flash column chromatography (SiO_2, 220 g) was packed with 15% EtOAc in *n*-hexane. The solid was dissolved in minimum quantity of the solvent used for packing the column and applied to the column. Gradient elution of 15-22% EtOAc in *n*-hexane was used as elutent to obtain the second spot as a white solid (720 mg, 57%)
R_f = 0.35 (20% EtOAc in *n*-hexane). Also the compound is ninhydrin active.
^{1}H-NMR (400 MHz, $CDCl_3$): δ = 4.85 (s, br, N*H*, 1H), 4.62-4.48 (m, 1H), 4.16 (t, J = 5 Hz, 2H), 3.40 (q, br, J = 4.8 Hz, 2H), 1.98-1.93 (m, 1H), 1.92-1.85 (m, 1H), 1.84-1.72 (m, 2H), 1.70-1.63 (m, 2H), 1.52-1.46 (m, 2H), 1.43 (s, t-butyl, 9H), 1.38-0.93 (m, 23H), 0.89 (d, J = 6.4 Hz, 3H), 0.86 (d, J = 1.6 Hz, 3H), 0.85 (d, J = 2 Hz, 3H), 0.81 (s, 3H), 0.64 ppm (s, 3H).
^{13}C-NMR (100 MHz, $CDCl_3$): δ = 155.87, 154.64, 78.22, 66.95, 56.56, 56.42, 54.34, 44.75, 42.74, 40.12, 39.83, 39.66, 36.81, 36.31, 35.94, 35.61, 35.56, 34.03, 32.11, 28.73, 28.51, 28.38, 28.16, 27.54, 24.35, 23.98, 22.70, 21.37, 18.81, 12.32, 12.22 ppm.
GC-MS(EI): m/z calculated for $C_{30}H_{53}NO_3$ 475.40 $[M]^+$; found: 460 $[M\text{-}(NH_2)^{\cdot}]$ $[C_{30}H_{51}O_3]^{\cdot}$, 431 $[M\text{-}(C_2H_6N)^{\cdot}]$ $[C_{28}H_{47}O_3]^{\cdot}$, 388 $[M\text{-}(C_3H_6NO_2)^{\cdot}]$ $[C_{27}H_{47}O]^{\cdot}$.

Synthesis of 11: **10** (700 mg, 1.21 mmol, 1.0 eq.) was taken in single necked RBF and DCM (10 mL) was added to it. Trifluoroacetic acid (0.93 mL, 12.1 mmol, 10 eq.) dissolved in DCM (12 mL) was added to the RBF through a dropping funnel dropwise at 0 °C. The reaction mixture was stirred at RT and monitored by TLC (ninhydrin stain) till the complete consumption of **10**. After 9 hours the solvent was evaporated under reduced pressure and redissolved in minimum amount of DCM and washed with saturated $NaHCO_3$, water and brine. The combined organic layer was dried (Na_2SO_4) and evaporated under reduced pressure to obtain a white solid (520 mg).
The compound was not purified at this stage and used as such for the next reaction.

^{1}H-NMR (400 MHz, $CDCl_3$): δ = 4.66-4.52 (m, 1H), 4.21 (t, J = 4.6 Hz, 2H), 3.05 (t, br, J = 4.6 Hz, 2H), 1.94-0.93 (m, 31H), 0.89 (d, J = 6.8 Hz, 3H), 0.86 (d, J = 1.6 Hz, 3H), 0.85 (d, J = 2 Hz, 3H), 0.81 (s, 3H), 0.64 ppm (s, 3H).
^{13}C-NMR (100 MHz, $CDCl_3$) δ = 154.76, 78.24, 68.55, 56.57, 56.45, 54.35, 44.76, 42.74, 40.69, 40.13, 39.66, 36.82, 36.32, 35.95, 35.56, 34.03, 32.12, 28.74, 28.39, 28.16, 27.55, 24.35, 24.01, 22.96, 22.70, 21.38, 18.82, 12.34, 12.22 ppm.
FTIR (ATR, neat solid): ν = 3395 (NH_2), 2952, 2932, 2915, 2866, 2851, 1737 (carbonate C=O), 1469, 1446, 1394, 1287, 997, 966, 952, 930, 860, 789 (cm^{-1}).

Synthesis of 2: PCTDA (100 mg, 0.25 mmol, 1.0 eq.) and **11** (280 mg, 0.58 mmol, 2.3 eq.) were taken in a 3-necked RBF connected to a reflux condenser. Dry DMF (30 mL) was added to the RBF and stirred at 130 °C for 12 hours. After 12 hours, the solution had turned reddish and also TLC indicated a fluorescent spot. Thus the reaction was stopped and solvent was evaporated under reduced pressure to obtain a red solid (380 mg).
Purification: The product was purified by a combination of repeated flash column chromatography (SiO_2, packed with chloroform) by eluting with gradients of 0-2% MeOH in chloroform and size-exclusion chromatography (S-X3, chloroform) to obtain a red solid (38 mg, 43%). Only a part (70 mg) of the crude mixture was purified and yield reported is based on this.
R_f = 0.62 (2% MeOH in chloroform).
^{1}H-NMR (400 MHz, $CDCl_3$): δ = 8.40 (d, J = 8 Hz, 4H), 8.16 (d, J = 8 Hz, 4H), 4.53 (m, 10H), 2.09-0.85 (m, 80H), 0.79 (s, 6H), 0.63 (s, 6H) ppm.
^{13}C-NMR (100 MHz, $CDCl_3$): δ = 163.18, 154.68, 134.18, 131.24, 129.08, 125.92, 123.0, 122.91, 78.16, 64.67, 56.55, 56.44, 54.34, 44.75, 42.72, 40.12, 39.65, 39.38, 36.83, 36.31, 35.94, 35.58, 35.56, 34.03, 32.12, 28.77, 28.37, 28.15, 27.55, 24.34, 24.01, 22.95, 22.70, 21.36, 18.81, 12.35, 12.21 ppm.
MALDI-TOF (DCTB, negative mode): m/z calculated for $C_{84}H_{110}N_2O_{10}$: 1306.81 $[M]^{-\cdot}$; found:1306.89.
FTIR (ATR, neat solid): ν = 2949, 2930, 2866, 2849, 1741 (carbonate C=O), 1697 and 1658 (imide C=O), 1593, 1577, 1441, 1401, 1361, 1345, 1248, 1065, 1000, 856, 810, 791, 745 (cm^{-1}).

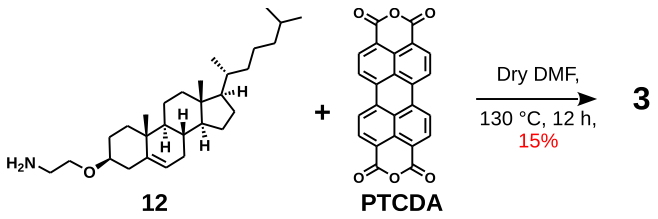

Figure 4.22: Synthetic route for **3**.

Synthesis of 3: PTCDA (98 mg, 0.25 mmol, 1.0 eq.) and **12** [76] (230 mg, 0.53 mmol, 2.1 eq.) were taken in 2-necked RBF (100 mL) fitted with a reflux condenser. Dry DMF (40 mL) was added to the RBF and the mixture was stirred at 130 °C for 12 hours. The solution was allowed to cool to room temperature and poured into MeOH (100 mL). The precipitate was filtered and dried at 70 °C to obtain flaky red solid.

Purification: The red solid was purified by flash column chromatography (SiO_2) eluting with 0-2% MeOH in $CHCl_3$. Further repeated column chromatography was performed using 0-5% acetone in $CHCl_3$ to yield a red colored solid (45 mg, 15%).

^{1}H-NMR (400 MHz, $CDCl_3$): δ = 8.71 (d, J = 8 Hz, 4H), 8.65 (d, J = 8 Hz, 4H), 5.31 (s, br, 2H), 4.50-4.41 (m, 4H), 3.83-3.79 (m, 4H), 3.29-3.23 (m, 2H), 2.37-0.81 (m, 80H), 0.66 (s, 6H) ppm.

^{13}C-NMR spectra of the molecule could not be recorded due to its poor solubility in $CDCl_3$ and TCE-D_2 at high concentrations.

MALDI-TOF (DCTB, negative mode): m/z calculated for $C_{82}H_{106}N_2O_6$: 1214.80 $[M]^{-\cdot}$; found:1214.86.

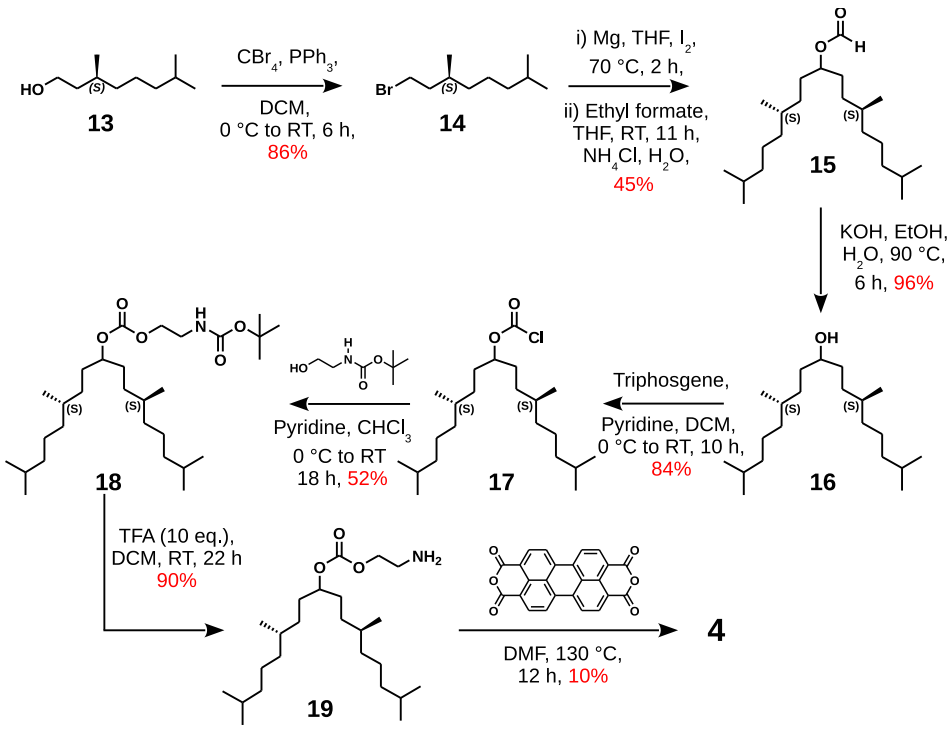

Figure 4.23: Synthetic route for **4**.

Synthesis of (*s*)-3,7-dimethyloctyl bromide (14): (*s*)-3,7-dimethyloctanol (**13**, 5 g, 31 mmol, 1.0 eq.) and CBr_4 (11.54 g, 34.8 mmol, 1.1 eq.) were taken in a 250 mL 3-necked RBF fitted with a dropping funnel and an argon balloon. Dry DCM (40 mL) was added to the RBF and stirred at 0 °C for 15 minutes. PPh_3 (9.12 g, 34.8 mmol, 1.1 eq.) dissolved in dry DCM (40 mL) was added to the RBF through the dropping funnel dropwise over a period of 30 minutes at 0 °C. Stirring was continued at RT and the reaction was monitored by GC-MS. After 6 hours the reactant had vanished and thus the reaction was stopped and the contents of the RBF were concentrated under reduced pressure to obtain a biphasic mixture.
Purification: A filteration flash column chromatography (SiO_2) was carried out by packing with *n*-hexane. The crude product was dissolved in minimum amount of *n*-hexane and applied to the column. *n*-hexane (300 mL) was used as the eluent to obtain the top spot as a colorless oil (6.9 g, quantitative). Average yield over two runs = 85%
^{1}H-NMR (400 MHz, $CDCl_3$): δ = 3.49-3.37 (m, 2H), 1.94-1.80 (m, 1H), 1.71-1.47 (m, 3H), 1.47-1.11 (m, 5H), 0.89-0.86 ppm (m, 9H).
^{13}C-NMR (100 MHz, $CDCl_3$): δ = 40.24, 39.33, 36.87, 32.34, 31.83, 28.09, 24.69, 22.82, 22.73, 19.11 ppm.

GC-MS: Retention time = 9.67 minutes. m/z calculated for $C_{10}H_{21}Br$ 220.08; found 220.0 $[M]^+$.

Synthesis of 15: Pre-heated cut Magnesium strips (0.69 g, 28.5 mmol, 1.1 eq.) were taken in a 2-necked RBF fitted with a dropping funnel and reflux condenser. A pinch of iodine and dry THF (20 mL) were added to the RBF and stirred at 40 °C for 10 mins. **14** (5.7 g, 25.9 mmol, 1.0 eq.) dissolved in dry THF (25 mL) (about 1-2 mL of this solution) was added to the RBF through the dropping funnel dropwise and the RBF was heated to 70 °C for 15 minutes. The solution became colorless (iodine coloration) and effervescence were observed, indicating that the formation of Grignard regeant has been initiated. The rest of **14** in THF was added dropwise over a period of 90 minutes with constant stirring at 70 °C. The solution was maintained at the same temperature for another 30 minutes to ensure the complete formation of Grignard regeant and then it was cooled down to RT. The solution had turned curdy with a few pieces of unreacted Magnesium in the RBF. Ethy formate (0.95 mL, 11.6 mmol, 0.45 eq.) in dry THF (15 mL) was added dropwise to the RBF through the dropping funnel with constant stirring over a period of 60 minutes at RT. The solution was further stirred at RT for another 11 hours. The reaction was quenched by adding 1M NH_4Cl (50 mL) dropwise at 0 °C to the RBF. The solution was extracted with excess of *n*-hexane, dried (anhydrous Na_2SO_4) and evaporated under reduced pressure to obtain a light yellow colored oil (3.5 g).
Purification: Flash column chromatography (SiO_2, 140 g) was performed by packing with 5% $CHCl_3$ in *n*-hexane. Gradient elution from 5 to 60% $CHCl_3$ in *n*-hexane was used to elute the compound. Second fraction contained the desired product (1.98 g, 45%).
^{1}H-NMR (400 MHz, $CDCl_3$): δ = 8.09 (s, 1H), 4.97-4.90 (m, 1H), 1.65-1.07 (m, 24H), 0.87-0.84 ppm (m, 18H).
^{13}C-NMR (100 MHz, $CDCl_3$): δ = 161.24, 75.35, 39.43, 37.31, 37.19, 32.85, 32.80, 32.52, 32.41, 31.68, 31.55, 28.10, 24.87, 22.84, 22.75, 19.77, 19.68 ppm.
GC-MS: Retention time = 19.37 minutes. m/z calculated for $C_{22}H_{44}O_2$ 340.33; found 340.0 $[M]^+$

Synthesis of 16: **15** (2.75 g, 8.0 mmol, 1.0 eq.) was taken in 250 mL 1-necked RBF and EtOH (30 mL) was added to it. KOH (0.9 g, 16 mmol, 2 eq.) dissolved in EtOH (30 mL) and H_2O (15 mL) was added to the RBF dropwise and refluxed at 90 °C for 6 hours. Then it was allowed to cool down to RT and acidified with

conc. HCl till the pH reaches 1-2. The solution was further diluted with water (100 mL) and extracted with chloroform (3 × 50 mL). The combined organic layer was washed with water (50 mL), brine (50 mL), dried (anhydrous Na_2SO_4) and evaporated under reduced pressure to obtain a light yellow oil.
Purification: Flash column chromatography (SiO_2) was performed with 60% $CHCl_3$ in *n*-hexane to obtain the second spot as the desired product (2.41 g, 96%).
R_f = 0.16 (1:1 $CHCl_3$ and *n*-hexane, also the product is $KMnO_4$ stain active)
^{1}H-NMR (400 MHz, $CDCl_3$): δ = 3.56-3.50 (m, 1H), 1.62-1.02 (m, 25H), 0.87-0.85 ppm (m, 18H).
^{13}C-NMR (100 MHz, $CDCl_3$): δ = 72.92, 39.49, 37.48, 37.29, 35.13, 34.98, 33.08, 33.07, 33.03, 32.95, 28.12, 24.93, 24.90, 22.85, 22.76, 19.90, 19.77 ppm.
GC-MS: Retention time = 19.12 minutes. m/z calculated for $C_{21}H_{44}O$ 312.33; found 312.0 $[M]^+$

Synthesis of 17: **16** (0.96 g, 3.0 mmol, 1.0 eq.) was taken in a 2-necked RBF fitted with an argon balloon and a dropping funnel. Dry DCM (10 mL) was added to the RBF and stirred at 0 °C for 10 minutes. Triphosgene (0.36 g, 1.2 mmol, 0.4 eq.) dissolved in dry DCM (5 mL) was added to the RBF through the dropping funnel at 0 °C. The reaction mixture was allowed to warm to RT and further stirred at RT for 10 hours. The reaction mixture was diluted with DCM and the contents were evaporated under reduced pressure to obtain a biphasic mixture (1.24 g).
Purification: The residue was dissolved in excess of *n*-hexane and filtered. The filtrate was concentrated under reduced pressure to obtain a light yellow oil (0.95 g, 84%).
R_f = 0.7 (1:1 $CHCl_3$ and *n*-hexane)
^{1}H-NMR (400 MHz, $CDCl_3$): δ = 4.91-4.82 (m, 1H), 1.78-1.08 (m, 24H), 0.87-0.86 ppm (m, 18H).
^{13}C-NMR (100 MHz, $CDCl_3$): δ = 150.43 (C=O), 85.72, 39.40, 37.21, 37.11, 32.76, 32.70, 32.23, 32.20, 31.40, 31.28, 28.11, 24.84, 22.84, 22.74, 19.70, 19.64 ppm.

Synthesis of 18: **5** (0.54 g, 3.33 mmol, 1.3 eq.) was taken in a 3-necked RBF fitted with an argon balloon and a dropping funnel. Dry $CHCl_3$ (20 mL) and dry pyridine (0.6 mL, 3.04 mmol, 1.2 eq.) were added to the RBF and stirred at 0 °C for 15 minutes. **17** (0.95 g, 2.53 mmol, 1.0 eq.) dissolved in dry $CHCl_3$ (9 mL) was added to the RBF through the dropping funnel dropwise at 0 °C. Stirring was continued at 0 °C for 2 hours followed by stirring at RT for 18 hours. TLC after

18 hours showed the absence of **17** in the reaction mixture, thus the reaction was stopped. The reaction mixture was diluted with $CHCl_3$ and evaporated under reduced pressure to obtain a light yellow oil (1.84 g).
Purification: A flash column chromatography (SiO_2, packed with 10% EtOAc in *n*-hexane) was performed on the crude product. The crude product was applied by dissolving in minimum amount of $CHCl_3$ and EtOAC and applied to the column. The column was eluted with 10% EtOAc in *n*-hexane. Only the base spot impurities were removed. The obtained top spot was again impure. Thus a second flash column chromatogrphy (SiO_2, packed with 5% EtOAc in *n*-hexane) was performed with a gradient elution of 5-10% EtOAc in *n*-hexane to obtain the third spot as the pure product (0.66 g, 52%).
$R_f = 0.23$ (10% EtOAc in *n*-hexane, The product is ninhydrin active)
^{1}H-NMR (400 MHz, $CDCl_3$): δ = 0.48 (s, br, 1H), 4.68-4.62 (m, 1H), 4.178 (t, J = 5.0 Hz, 2H), 3.41 (q, br, J = 4.8 Hz, 2H), 1.59-1.48 (m, 6H), 1.44 (s, 9H), 1.39-1.06 (m, 27H), 0.87-0.84 ppm (m, 18H).
^{13}C-NMR (100 MHz, $CDCl_3$): δ = 155.88, 155.15, 80.21, 79.74, 66.97, 39.88, 39.43, 37.27,37.20, 32.88, 32.42, 32.35, 31.57, 31.49, 28.51, 28.10, 24.88, 24.87, 22.84, 22.74, 19.72, 19.68 ppm.
GC-MS(EI): m/z calculated for $C_{29}H_{57}NO_5$ 499.7 m/z found 501 $[M+H]^+$

Synthesis of 19: **18** (0.65 g, 1.3 mmol, 1.0 eq.) was taken in single necked RBF fitted with a dropping funnel. DCM (20 mL) was added to the RBF. Trifluoroacetic acid (1.0 mL, 13 mmol, 10.0 eq.) dissolved in DCM (15 mL) was added dropwise to the RBF through the dropping funnel at 0 °C. Stirring was continued at RT and the reaction was monitored by TLC (ninhydrin stain). Most of the starting material was consumed after 22 hours. Thus the reaction was stopped and the contents of the RBF evaporated under reduced pressure to obtain a paste. This was dissolved in $CHCl_3$ (30 mL) and extracted with saturated $NaHCO_3$ (50 mL). The combined organic layer was washed with brine (30 mL) and dried (anhydrous Na_2SO_4) and evaporated under reduced pressure to obtain a light yellow oil (0.60 g).
Purification: A flash column chromatography (SiO_2, packed with 1% MeOH in $CHCl_3$) was performed on the crude product eluting with a gradient of 1 to 10 % MeOH in $CHCl_3$. Second fraction was the desired product (0.45 g, 86%)
$R_f = 0.31$ (5% MeOH in $CHCl_3$, also ninhydrin active)
^{1}H-NMR (400 MHz, $CDCl_3$): δ = 4.73-4.62 (m, 1H), 4.14 (t, J = 5.4 Hz, 2H), 2.96 (t, J = 5.4 Hz, 2H), 1.59-1.06 (m, 24H), 0.86-0.84 ppm (m, 18H).

^{13}C-NMR (100 MHz, $CDCl_3$): δ = 155.39, 79.96, 70.11, 41.15, 39.42, 37.28, 37.21, 32.88, 32.86, 32.43, 32.35, 31.63, 31.53, 28.10, 24.88, 24.86, 22.84, 22.75, 19.73, 19.68 ppm.

Synthesis of 4: PCTDA (35 mg, 0.089 mmol, 1.0 eq.) and **19** (90 mg, 0.22 mmol, 2.5 eq.) were taken in a 2-necked RBF (50 mL) fitted with a reflux condenser. Dry DMF (15 mL) was added to the RBF and stirred at 130 °C for 12 hours. The solution was homogenous and reddish. After 12 hours DMF was removed by distillation under reduced pressure to obtain a red residue.
Purification: The compound was purified by repeated flash column chromatography (SiO_2) eluting with 0-1 % MeOH in DCM. Also the product was purified by size exclusion chromatography (S-X3, $CHCl_3$) to obtain a red pasty solid (10 mg, 10%). R_f = 0.46 (1% MeOH in DCM).
^{1}H-NMR (400 MHz, $CDCl_3$): δ = 8.70 (d, J = 7.6 Hz, 4H), 8.63 (d, J = 8 Hz, 4H), 4.65-4.49 (m, 10H), 1.52-1.02 (m, 48H), 0.86-0.83 ppm (m, 36H).
^{13}C-NMR (100 MHz, $CDCl_3$): δ = 163.41, 155.17, 134.67, 131.55, 129.48, 126.42, 123.22, 123.13, 80.16, 64.68, 39.47, 37.33, 37.23, 32.96, 32.93, 32.38, 32.07, 31.54, 29.84, 29.50, 28.11, 24.92, 22.75, 19.72, 19.66 ppm.
MALDI-TOF (DCTB, negative mode): m/z calculated for $C_{72}H_{102}N_2O_{10}$: 1154.75 $[M]^{-\cdot}$; found:1154.82.
FTIR (ATR, neat solid): ν = 2953, 2924, 2861, 1730 (carbonate C=O), 1696 and 1658 (imide C=O), 1594, 1461, 1438, 1403, 1345, 1251, 1180, 1066, 991, 808, 790, 746 (cm^{-1}).

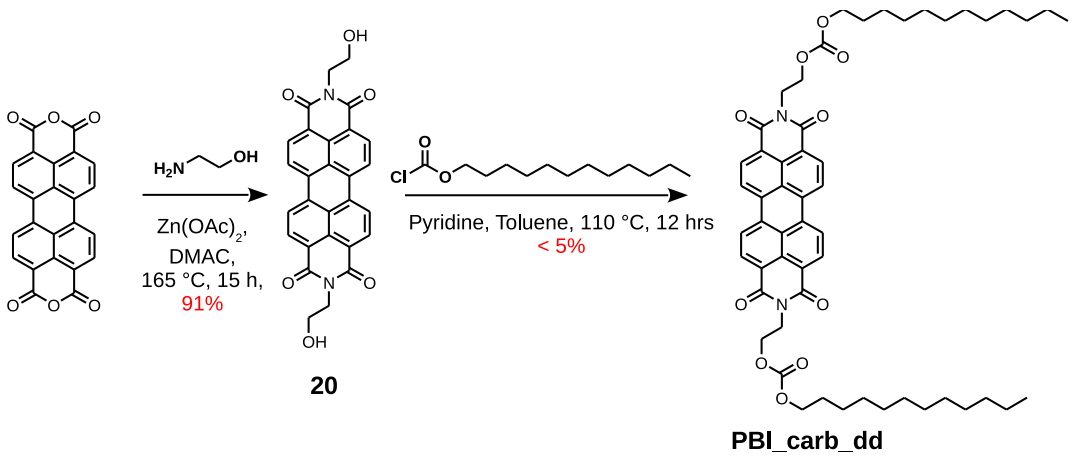

Figure 4.24: Synthetic route for **PBI_carb_dd**.

Synthesis of 20: Perylene-3,4,9,10-tetracarboxylic acid dianhydride (2 g, 5.1

mmol, 1 eq.), ethanol amine (0.93 g, 15.3 mmol, 3 eq.) and zinc acetate (0.28 g, 1.53 mmol, 0.3 eq.) were taken in a 3-necked round bottom flask fitted with a reflux condenser. Dimethyl acetamide (50 mL) was added to the RBF and stirred at 125 °C for 3 hours. Initially the reaction mixture was red and after 1 hour it turned to brown. After 3 hours the temperature was raised to 165 °C and the heating was continued for another 15 hours. Then the solution was allowed to cool down to room temperature and poured into a beaker containing water (250 mL) and methanol (150 mL) was added to precipitate the product. The obtained gelatinous precipitate was dried at 80 °C for 5 hours to obtain a bordeaux colored solid (2.45 g).
Purification: The crude product was refluxed with aq. 1% NaOH (50 mL) at 95-100 °C for 1 hour followed by filtration and washing with 1 M HCl and MeOH. The precipitate was dried at 75 °C under vacuum to obtain a bordeaux colored solid (2.2 g, 91% yield).
^{1}H-NMR (400 MHz, $CDCl_3$+TFA): $\delta = 8.80$ (s, 8 H), 4.62 (t, $J = 5.0$ Hz, 4 H), 4.24 ppm (t, $J = 4.9$ Hz, 4 H).

Synthesis of PBI_carb_dd: **20** (200 mg, 0.42 mmol, 1.0 eq.) was taken in a 3-necked (100 mL) RBF fitted with a dropping funnel and reflux condenser. Dry toluene (20 mL) and dry pyridine (0.34 mL, 1.25 mmol, 3.0 eq.) was added to the RBF and heated to 80 °C for 15 mins to form a dispersion. Dodecyl chloroformate (312 mg, 1.25 mmol, 3.0 eq.) dissolved in dry toluene (12 mL) was added to the RBF at 80 °C dropwise and further stirred at 110 °C for 12 hours. Then the solvent was removed under reduced pressure to obtain a dark brown solid.
Purification: A column chromatography (SiO_2, 230-400 mesh) was performed on the crude product eluting with 2-4 % MeOH in chloroform to obtain a mixture of spots containing perylene derivatives (second spot). This was further subjected to another chromatography (SiO_2, 230-400 mesh) eluting with 7-13% EtOAc in chloroform to obtain the second spot as the desired product (12 mg, 3% yield). The extremely low yield is due to the poor solubility of **20** in toluene.
$R_f = 0.33$ (10% EtOAc in chloroform).
^{1}H-NMR (400 MHz, $CDCl_3$): $\delta = 8.64$ (d, $J = 8$ Hz, 4 H), 8.53 (d, $J = 8.1$ Hz, 4 H), 4.58 (t, $J = 5.0$ Hz, 4 H), 4.52 (t, $J = 4.8$ Hz, 4 H), 4.13 (t, $J = 6.7$ Hz, 4 H), 1.68-1.61 (m, 4 H), 1.23 (m, 36 H), 0.86 ppm (t, $J = 6.9$ Hz, 6 H).
^{13}C-NMR (100 MHz, $CDCl_3$): δ = 163.57, 155.35,134.89, 131.73, 129.66, 126.65, 123.29 (one overlapping carbon), 68.56, 64.92, 39.37, 32.06, 29.82, 29.78, 29.74, 29.69, 29.45, 29.40, 28.82, 25.83, 22.83, 14.24 ppm.

MS (HRMS, APCI positive mode); m/z calculated for $C_{54}H_{66}N_2O_{10}$ 903.4790 $[M+H]^+$; found 903.4726.
FTIR (ATR, neat solid): ν = 2917 (CH_2 asymmetric stretching), 2853 (CH_2 symmetric stretching), 1740 (carbonate C=O), 1696 and 1662 (imide C=O), 1590, 1357, 1267, 1063, 951, 850, 809, 747, 650 (cm^{-1}).

It should be noted that the synthetic scheme followed for ***PBI_carb_dd*** *is different from those of* ***1****,* ***2*** *and* ***4****. Synthetic schemes similar to that employed for* ***1*** *was attempted with other derivatives like dodecyl, 3,4,5-tris((S)3,7-dimethyloctyl) benzyl and hydrogenated citronellol (****13****). The amine containing carbonates of these derivatives were found to be unstable and could not be isolated. Thus the general scheme for obtaining amine containing carbonates can only be applied to seconday or tertiary carbon attached to* α*-carbon of the carbonate but not primary. For derivatives containing primary alkyl substituents at the* α*-carbon position of carbonates, a scheme similar to that applied for* ***PBI_carb_dd*** *can be used.*

4.5.3 Capacitance fabrication and measurement

Metal-insulator-metal (M-I-M) sandwich device structures were fabricated on a patterned pre-cleaned ITO coated glass substrates. This was followed by introducing the self-assembled structures from methyl cyclohexane (10^{-4} M) by multiple drop-casting to obtain films of typical thickness in the range of 200 - 500 nm. The films were then dried under a vacuum of 10^{-3} mbar pressure to remove residual solvents. The devices were then completed by the deposition of Al electrode at 10^{-6} mbar, 1 Å/s by physical vapor deposition to obtain films of thickness 40 nm. Capacitances of these devices were measured using a Keithley 4200 semiconductor characterization system. Frequency sweep (10 kHz to 10 MHz) was performed on these devices to map the dynamic response of the devices. Furthermore, the leakage current density and breakdown field of the capacitors were obtained to estimate the strength of the assembly and the energy density of the devices. Temperature dependent capacitance measurement was performed using a He-gas based cryo set up from Cryogenics Inc. while the device was kept under a vacuum of 10^{-4} mbar.

Bibliography

[1] Hoeben, F. J. M.; Jonkheijm, P.; Meijer, E. W.; Schenning, A. P. H. J. *Chem. Rev.* **2005**, *105*, 1491–1546.

[2] Brunsveld, L.; Folmer, B. J. B.; Meijer, E. W.; Sijbesma, R. P. *Chem. Rev.* **2001**, *101*, 4071–4098.

[3] Babu, S. S.; Praveen, V. K.; Ajayaghosh, A. *Chem. Rev.* **2014**, *114*, 1973–2129.

[4] Aida, T.; Meijer, E. W.; Stupp, S. I. *Science* **2012**, *335*, 813–817.

[5] Stupp, S. I.; Palmer, L. C. *Chem. Mater.* **2014**, *26*, 507–518.

[6] Zelzer, M.; Ulijn, R. V. *Chem. Soc. Rev.* **2010**, *39*, 3351–3357.

[7] Faramarzi, V.; Niess, F.; Moulin, E.; Maaloum, M.; Dayen, J.-F.; Beaufrand, J.-B.; Zanettini, S.; Doudin, B.; Giuseppone, N. *Nat. Chem.* **2012**, *4*, 485–490.

[8] Ogi, S.; Sugiyasu, K.; Manna, S.; Samitsu, S.; Takeuchi, M. *Nat. Chem.* **2014**, *6*, 188–195.

[9] Gilroy, J. B.; Gädt, T.; Whittell, G. R.; Chabanne, L.; Mitchels, J. M.; Richardson, R. M.; Winnik, M. A.; Manners, I. *Nat. Chem.* **2010**, *2*, 566–570.

[10] Hudson, Z. M.; Lunn, D. J.; Winnik, M. A.; Manners, I. *Nat. Commun.* **2014**, *5*, Article.

[11] Kang, J.; Miyajima, D.; Mori, T.; Inoue, Y.; Itoh, Y.; Aida, T. *Science* **2015**, *347*, 646–651.

[12] Ogi, S.; Fukui, T.; Jue, M. L.; Takeuchi, M.; Sugiyasu, K. *Angew. Chem. Int. Ed.* **2014**, *53*, 14363–14367.

[13] Jain, A.; George, S. J. *Materials Today* **2015**, *18*, 206–214.

[14] De Greef, T. F. A.; Smulders, M. M. J.; Wolffs, M.; Schenning, A. P. H. J.; Sijbesma, R. P.; Meijer, E. W. *Chem. Rev.* **2009**, *109*, 5687–5754.

[15] Chen, Z.; Lohr, A.; Saha-Möller, C. R.; Würthner, F. *Chem. Soc. Rev.* **2009**, *38*, 564–584.

[16] Zhao, D.; Moore, J. S. *Org. Biomol. Chem.* **2003**, *1*, 3471–3491.

[17] Smulders, M. M. J.; Schenning, A. P. H. J.; Meijer, E. W. *J. Am. Chem. Soc.* **2008**, *130*, 606–611.

[18] Cantekin, S.; Balkenende, D. W. R.; Smulders, M. M. J.; Palmans, A. R. A.; W., M. *Nat. Chem.* **2011**, *3*, 42–46.

[19] Smulders, M. M. J.; Nieuwenhuizen, M. M. L.; Grossman, M.; Filot, I. A. W.; Lee, C. C.; de Greef, T. F. A.; Schenning, A. P. H. J.; Palmans, A. R. A.; Meijer, E. W. *Macromolecules* **2011**, *44*, 6581–6587.

[20] Wang, F.; Gillissen, M. A. J.; Stals, P. J. M.; Palmans, A. R. A.; Meijer, E. W. *Chem. Eur. J.* **2012**, *18*, 11761–11770.

[21] Garc´ia, F.; Viruela, P. M.; Matesanz, E.; Ort´i, E.; Sánchez, L. *Chem. Eur. J.* **2011**, *17*, 7755–7759.

[22] Helmich, F.; Lee, C.; Nieuwenhuizen, M.; Gielen, J.; Christianen, P.; Larsen, A.; Fytas, G.; Leclére, P.; Schenning, A.; Meijer, E. *Angew. Chem. Int. Ed.* **2010**, *49*, 3939–3942.

[23] Garc´ia, F.; Sánchez, L. *J. Am. Chem. Soc.* **2012**, *134*, 734–742.

[24] Mayerhöffer, U.; Würthner, F. *Chem. Sci.* **2012**, *3*, 1215–1220.

[25] Aparicio, F.; Matesanz, E.; Sánchez, L. *Chem. Commun.* **2012**, *48*, 5757–5759.

[26] Fenske, M. T.; Meyer-Zaika, W.; Korth, H.-G.; Vieker, H.; Turchanin, A.; Schmuck, C. *J. Am. Chem. Soc.* **2013**, *135*, 8342–8349.

[27] Jonkheijm, P.; van der Schoot, P.; Schenning, A. P. H. J.; Meijer, E. W. *Science* **2006**, *313*, 80–83.

[28] Tomović, V.; van Dongen, J.; George, S. J.; Xu, H.; Pisula, W.; Leclére, P.; Smulders, M. M. J.; De Feyter, S.; Meijer, E. W.; Schenning, A. P. H. J. *J. Am. Chem. Soc.* **2007**, *129*, 16190–16196.

[29] Mayoral, M. J.; Rest, C.; Stepanenko, V.; Schellheimer, J.; Albuquerque, R. Q.; Fernández, G. *J. Am. Chem. Soc.* **2013**, *135*, 2148–2151.

[30] Krieg, E.; Weissman, H.; Shimoni, E.; Bar On (Ustinov), A.; Rybtchinski, B. *J. Am. Chem. Soc.* **2014**, *136*, 9443–9452.

[31] Rest, C.; Mayoral, M. J.; Fucke, K.; Schellheimer, J.; Stepanenko, V.; Fernández, G. *Angew. Chem. Int. Ed.* **2014**, *53*, 700–705.

[32] Li, L.; Yuan, C.; Dai, L.; Thayumanavan, S. *Macromolecules* **2014**, *47*, 5869–5876.

[33] Allampally, N. K.; Florian, A.; Mayoral, M. J.; Rest, C.; Stepanenko, V.; Fernández, G. *Chem. Eur. J.* **2014**, *20*.

[34] Kulkarni, C.; Balasubramanian, S.; George, S. J. *ChemPhysChem* **2013**, *14*, 661–673.

[35] Würthner, F.; Yao, S.; Beginn, U. *Angew. Chem. Int. Ed.* **2003**, *42*, 3247–3250.

[36] Fernández, G.; Stolte, M.; Stepanenko, V.; Würthner, F. *Chem. Eur. J.* **2013**, *19*, 206–217.

[37] Würthner, F.; Stolte, M. *Chem. Commun.* **2011**, *47*, 5109–5115.

[38] Würthner, F. *Chem. Commun.* **2004**, 1564–1579.

[39] Ikeda, T.; Masuda, T.; Hirao, T.; Yuasa, J.; Tsumatori, H.; Kawai, T.; Haino, T. *Chem. Commun.* **2012**, *48*, 6025–6027.

[40] Würthner, F.; Thalacker, C.; Diele, S.; Tschierske, C. *Chem. Eur. J.* **2001**, *7*, 2245–2253.

[41] Chen, Z.; Stepanenko, V.; Dehm, V.; Prins, P.; Siebbeles, L.; Seibt, J.; Marquetand, P.; Engel, V.; Würthner, F. *Chem. Eur. J.* **2007**, *13*, 436–449.

[42] van Herrikhuyzen, J.; Syamakumari, A.; Schenning, A. P. H. J.; Meijer, E. W. *J. Am. Chem. Soc.* **2004**, *126*, 10021–10027.

[43] Kaiser, T. E.; Stepanenko, V.; Würthner, F. *J. Am. Chem. Soc.* **2009**, *131*, 6719–6732.

[44] van der Weegen, R.; Korevaar, P. A.; Voudouris, P.; Voets, I. K.; de Greef, T. F. A.; Vekemans, J. A. J. M.; Meijer, E. W. *Chem. Commun.* **2013**, *49*, 5532–5534.

[45] Yagai, S.; Usui, M.; Seki, T.; Murayama, H.; Kikkawa, Y.; Uemura, S.; Karatsu, T.; Kitamura, A.; Asano, A.; Seki, S. *J. Am. Chem. Soc.* **2012**, *134*, 7983–7994.

[46] Seki, T.; Asano, A.; Seki, S.; Kikkawa, Y.; Murayama, H.; Karatsu, T.; Kitamura, A.; Yagai, S. *Chem. Eur. J.* **2011**, *17*, 3598–3608.

[47] Reddy, S. K.; Balasubramanian, S. *J. Phys. Chem. B* **2012**, *116*, 14892–14902.

[48] Chloroformates were either obtained from commercial source or synthesized by the chloroformylation of the corresponding alcohols using triphosgene following the reported procedure.

[49] Adachi, M.; Murata, Y.; Nakamura, S. *J. Phys. Chem.* **1995**, *99*, 14240–14246.

[50] Abraham, S.; Vijayaraghavan, R. K.; Das, S. *Langmuir* **2009**, *25*, 8507–8513.

[51] Svobodova, H.; Noponen, V.; Kolehmainen, E.; Sievänen, E. *RSC Adv.* **2012**, *2*, 4985–5007.

[52] Sugiyasu, K.; Fujita, N.; Shinkai, S. *Angew. Chem. Int. Ed.* **2004**, *43*, 1229–1233.

[53] Murata, K.; Aoki, M.; Suzuki, T.; Harada, T.; Kawabata, H.; Komori, T.; Ohseto, F.; Ueda, K.; Shinkai, S. *J. Am. Chem. Soc.* **1994**, *116*, 6664–6676.

[54] Ajayaghosh, A.; Vijayakumar, C.; Varghese, R.; George, S. J. *Angew. Chem. Int. Ed.* **2006**, *45*, 456–460.

[55] Although **1** is completely soluble in MCH, the aggregates could not be disassembled with increase in temperature. Thus, to control the extent of self-assembly such that diassembly could be achieved, a fraction of good solvent (TCE) was used.

[56] The data are not shown. Also, a systematic study of the variation of CD spectra as a function of cooling rate and aging is beyond the scope of this work and will be investigated in detail as a separate work.

[57] Lu, L.; Cocker, T. M.; Bachman, R. E.; Weiss, R. G. *Langmuir* **2000**, *16*, 20–34.

[58] Smulders, M.; Nieuwenhuizen, M.; de Greef, T.; vanderSchoot, P.; Schenning, A.; Meijer, E. *Chem. Eur. J.* **2010**, *16*, 362–367.

[59] ten Eikelder, H. M. M.; Markvoort, A. J.; de Greef, T. F. A.; Hilbers, P. A. J. *J. Phys. Chem. B* **2012**, *116*, 5291–5301.

[60] Markvoort, A. J.; ten Eikelder, H. M. M.; Hilbers, P. A. J.; de Greef, T. F. A.; Meijer, E. W. *Nat. Commun.* **2011**, *2*, 509.

[61] Huang, X.; Raghavan, S. R.; Terech, P.; Weiss, R. G. *J. Am. Chem. Soc.* **2006**, *128*, 15341–15352.

[62] Because of the low solubility and the presence of multiple stereocenters in **3**, reliable CD spectra (under thermodynamic control) could not be achieved; thus, temperature-dependent UV/vis studies were performed.

[63] The isodesmic fits to the cooling curves for **3** and **4** show slight deviations from the experimental data. Since these cooling curves are obtained from UV/vis studies, the deviation could be due to the small change in absorbance at the monitored wavelength. The fit is subisodesmic in the case of **3**; thus, this molecule can be weakly cooperative, which adds further to the deviation from the fit.

[64] Xue, C.; Jin, S. *Chem. Mater.* **2011**, *23*, 2689–2692.

[65] Gunbas, D. D.; Xue, C.; Patwardhan, S.; Fravventura, M. C.; Zhang, H.; Jager, W. F.; Sudholter, E. J. R.; Siebbeles, L. D. A.; Savenije, T. J.; Jin, S.; Grozema, F. C. *Chem. Commun.* **2014**, *50*, 4955–4958.

[66] Brocorens, P.; Linares, M.; Guyard-Duhayon, C.; Guillot, R.; Andrioletti, B.; Suhr, D.; Isare, B.; Lazzaroni, R.; Bouteiller, L. *J. Phys. Chem. B* **2013**, *117*, 5379–5386.

[67] Bejagam, K. K.; Fiorin, G.; Klein, M. L.; Balasubramanian, S. *J. Phys. Chem. B* **2014**, *118*, 5218–5228.

[68] Danila, I.; Riobé, F.; Piron, F.; Puigmart´i-Luis, J.; Wallis, J. D.; Linares, M.; Ågren, H.; Beljonne, D.; Amabilino, D. B.; Avarvari, N. *J. Am. Chem. Soc.* **2011**, *133*, 8344–8353.

[69] Marty, R.; Nigon, R.; Leite, D.; Frauenrath, H. *J. Am. Chem. Soc.* **2014**, *136*, 3919–3927.

[70] Roche, C.; Sun, H.-J.; Prendergast, M. E.; Leowanawat, P.; Partridge, B. E.; Heiney, P. A.; Araoka, F.; Graf, R.; Spiess, H. W.; Zeng, X.; Ungar, G.; Percec, V. *J. Am. Chem. Soc.* **2014**, *136*, 7169–7185.

[71] Klein, M. L.; Shinoda, W. *Science* **2008**, *321*, 798–800.

[72] Senanayak, S. P.; Guha, S.; Narayan, K. S. *Phys. Rev. B* **2012**, *85*, 115311.

[73] Ashcroft, N.; Mermin, N. *Solid State Physics*; Saunders College: Philadelphia, 1976.

[74] Senanayak, S. P.; Narayan, K. S. *Adv. Funct. Mater.* **2014**, *24*, 3324–3331.

[75] Boros, E.; Häfeli, U. O.; Patrick, B. O.; Adam, M. J.; Orvig, C. *Bioconjugate Chem.* **2009**, *20*, 1002–1009.

[76] Nikolaeva, I. A.; Misharin, A. Y.; Ponomarev, G. V.; Timofeev, V. P.; Tkachev, Y. V. *Bioorg. Med. Chem. Lett.* **2010**, *20*, 2872 – 2875.

[77] Abbel, R.; Wolffs, M.; Bovee, R. A. A.; van Dongen, J. L. J.; Lou, X.; Henze, O.; Feast, W. J.; Meijer, E. W.; Schenning, A. P. H. J. *Adv. Mater.* **2009**, *21*, 597–602.

[78] Jancy, B.; Asha, S. K. *J. Phys. Chem. B* **2006**, *110*, 20937–20947.

[79] Eckert, H.; Forster, B. *Angew. Chem. Int. Ed.* **1987**, *26*, 894–895.

Chapter 5

Generality of Dipole-Moment-Driven Cooperativity and the Role of Linker

5.1 Introduction

Our hypothesis that long-range interaction between oligomers along the stacking direction leads to cooperativity, was tested in the last chapter using perylene bisimides as the model chromophores and carbonate group as the source of molecular dipole-moment. In order to rationalize the mechanisms based on the above hypothesis, it must be validated across different class of molecules. In the present chapter, we employ similar molecular design principles with carbonate groups to study the mechanism of self-assembly of other well studied chromophores such as perylene-3,4-dicarboximides and oligo(*p*-phenylenevinylene)s. Further, the ubiquitously found ester groups are also utilized as the source of molecular dipole-moment to achieve cooperative mechanism with perylene bisimides.

Manuscript based on this work is under preparation

5.2 Results and discussion

5.2.1 Perylene-3,4-dicarboximide

Perylene-3,4-dicarboimides (as known as perylene monoimide or PMI) are known to exhibit excellent photostability and strong solution and solid state fluorescence. [1, 2] PMI derivatives are employed as a part of multichromophoric units to study the energy- and electron-transfer processes in synthetic systems. [3] But there are very few reports on the self-assembly study of PMI either in solution or solid state. [4–6]

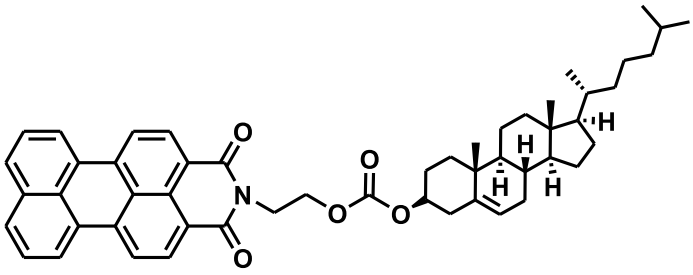

Figure 5.1: Structure of **PMI_carb_chol**.

Thus, here we have studied the mechanism of self-assembly and morphological characterization of a new derivative of PMI. The molecule under study (**PMI_carb_chol**) consists of a PMI core, an ethylene spacer followed by the carbonate linker and a cholesterol moiety at the periphery (Figure 5.1). **PMI_carb_chol** was synthesized by the imidation of perylene-3,4-dianhydride with the corresponding cholesterol amine and was characterized through ^{1}H- and ^{13}C-NMR spectroscopy and MALDI-TOF mass spectroscopy (see experimental section for details).

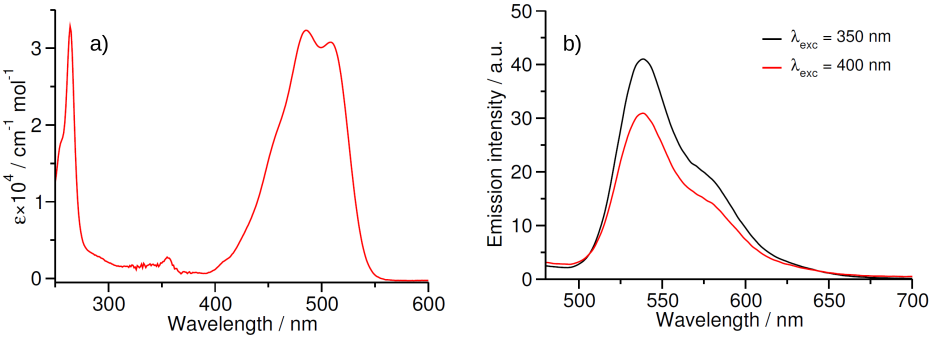

Figure 5.2: a) and b) UV/vis absorption and emission spectra respectively of **PMI_carb_chol** in chloroform (c = 1.15×10^{-5} M). Emission spectra were recorded in a 1 mm pathlength cuvette to minimize self-absorption.

UV/vis absorption spectrum of **PMI_carb_chol** in chloroform shows prominent peaks at 510, 486 and 264 nm, with a maximum at 486 nm (ϵ = 3.2×10^4 M^{-1} cm^{-1}, Figure 5.2a). These transitions at 486 and 510 nm are attributed in (0,1) and (0,0) low energy vibronic transitions respectively of the PMI core. [6] The corresponding emission spectra shows peaks at 538 and 580 nm (Figure 5.2b). Similar spectral characteristics are observed for other PMI derivatives and is attributed to the molecularly dissolved state (devoid of intermolecular interactions). [1]

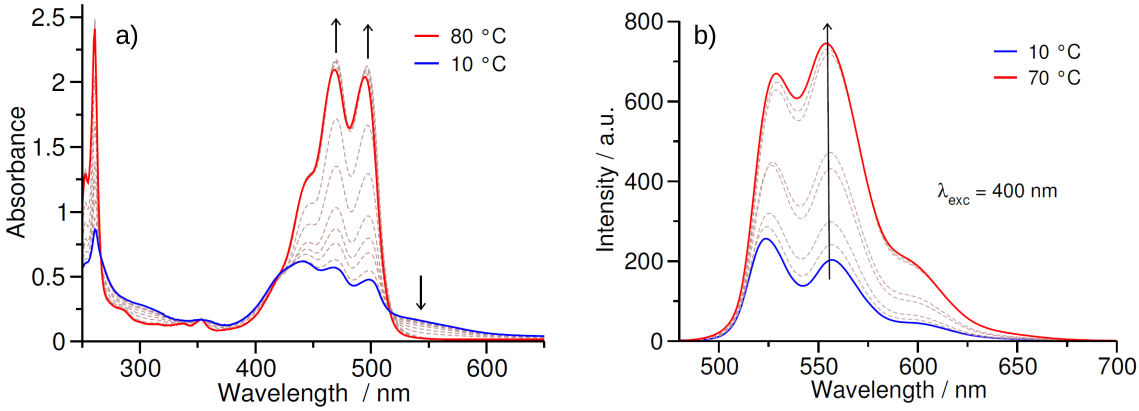

Figure 5.3: a) and b) Temperature-dependent UV/vis absorption and emission spectra respectively of **PMI_carb_chol** in MCH (c = 7.5×10^{-5} M). These studies were carried out in a 10 mm path length cuvette. Arrows indicate spectral changes with increase in temperature. The intensity of the emission peak at 524 nm is lower than the one at 557 nm at high temperature. At elevated temperature, the monomer concentration and the emission from them increases, since the studies are performed in a 10 mm cuvette a significant amount of self-absorption takes place leading to the lowering in the intensity of the first emission band.

PMI_carb_chol is also soluble in apolar solvents like MCH. UV/vis absorption spectra in MCH at low temperatures shows the broadening of the peaks (468 and 496 nm), also a new broad band is observed at 550 nm (Figure 5.3a). The absorption maximum in MCH at low temperature is at 440 nm. As the temperature is increased, the peaks become sharper, absorption maximum shifts to 468 nm and the broad band at 550 nm vanishes. These spectral changes suggest that **PMI_carb_chol** is aggregated at low temperature and reaches the molecularly dissolved state at high temperature. The fluorescence spectra at low temperature shows a decrease in the emission intensity of peaks at 524 and 557 nm (Figure 5.3b). With increase in temperature, the intensity of these peaks enhance without much shift in the position. Thus, the blue shift in UV/vis absorption maximum and the quenching of emission suggests that **PMI_carb_chol** forms H-type face-to-face aggregates in MCH.

The self-assembled nanostructures of **PMI_carb_chol** were studied through TEM to understand their morphology. TEM micrographs of **PMI_carb_chol**, shows long, twisted (chiral) and networked fibers (Figure 5.4). Most of the fibers are seen to be bundled. Interestingly, many of the fibers/bundles are chiral.

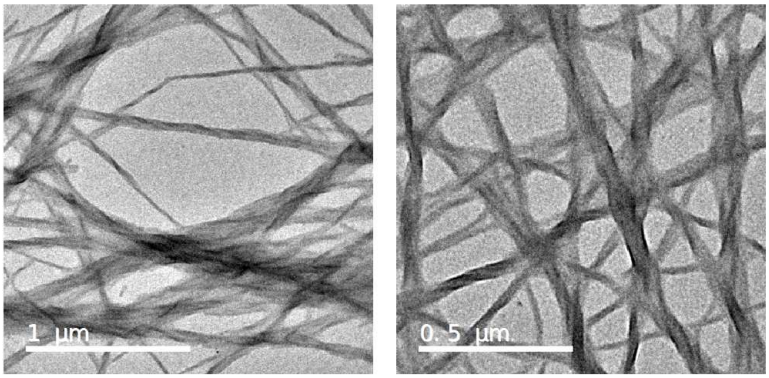

Figure 5.4: a) TEM micrographs of **PMI_carb_chol** obtained by drop-casting a solution (in MCH, c = 5×10^{-5} M) on a copper-grid without any staining.

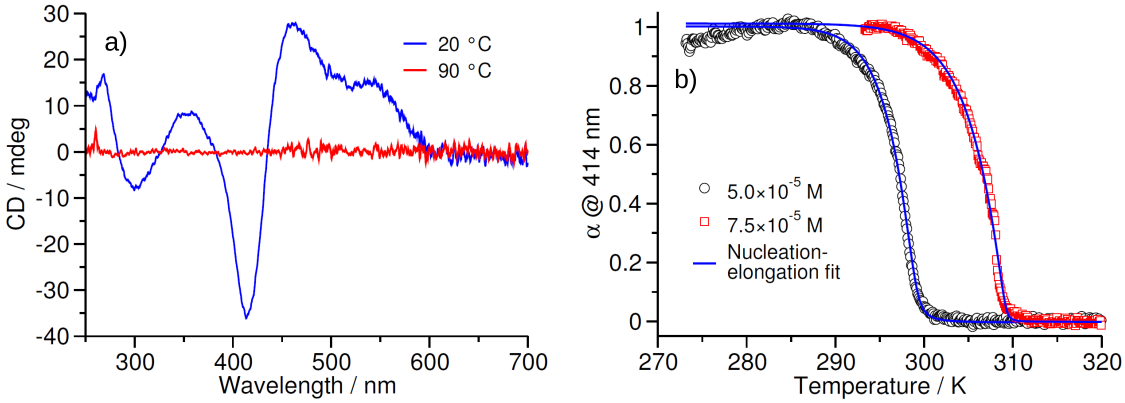

Figure 5.5: a) CD spectra of **PMI_carb_chol** in MCH (c = 5×10^{-5} M) at different temperatures. b) Cooling curves obtained from CD studies at two different concentrations.

Having studied the self-assembly of **PMI_carb_chol** in apolar solvent, we now embark on to study the mechanism of self-assembly. The CD spectrum of **PMI_carb_chol** in MCH shows a bisignated signal, with positive Cotton effect at higher wavelength, indicating that the aggregates are indeed chiral (Figure 5.5a). The chiral cholesterol moiety aids in rendering the aggregates chiral, as observed for PBI derivatives in the last chapter. At high temperature, the Cotton effect vanishes, indicating the

absence of chiral organization. Juxtaposition of temperature-dependent CD and UV/vis absorption studies reveals that at high temperature, **PMI_carb_chol** exists as individual molecules. Using these temperature-dependent studies, we further study the mechanism of self-assembly. The cooling curves obtained from CD studies shows a critical point and the experimental data fits the nucleation-elongation model (Figure 5.5b). [7, 8] Thus **PMI_carb_chol** follows a cooperative or nucleation-elongation mechanism of self-assembly. The various thermodynamic parameters of self-assembly are given in Table 5.1.

Concentration (M)	$\Delta H^0{}_e$ (kJ/mol)	ΔS^0 (kJ/mol·K)	$\Delta H^0{}_{nucl}$ (kJ/mol)	T_e (K)	σ	ΔG^0 (kJ/mol)
5.0×10^{-5}	-280.34 ±1.86	-0.856 ±0.0062	-12.02 ±0.12	298.75 ± 0.01	7.8×10^{-3}	-25.12 ±0.1
7.5×10^{-5}	-219.39 ±2.77	-0.63 ±0.009	-19.78 ±0.80	309.04 ±0.03	3.4×10^{-4}	-31.55 ±0.27

Table 5.1: Thermodynamic parameters of **PMI_carb_chol** at different concentrations in MCH obtained from temperature-dependent CD measurements. ΔG^0 was calculated at 298.15 K.

Since **PMI_carb_chol** assembles in an H-type manner, any two molecules in an aggregate will be oriented face-to-face. PMI itself has an inherent dipole-moment along the long-axis of the molecule. Thus, molecules can arrange either with parallel or anti-parallel dipolar alignment. In the parallel arrangement, peripheral cholesterol groups interact via van der Waals interaction and also the carbonate groups engage in dipolar interaction with the neighbouring molecules, stabilizing the assembly. As a consequence of the carbonate-carbonate interaction in an assembly, the aggregate develops a macrodipole. Thus, again dipole-moment seems to be the origin of cooperative mechanism of self-assembly for **PMI_carb_chol**.

5.2.2 Oligo-(*p*-phenylenevinylene) (OPV)

OPVs are one of the well studied class of p-type materials and the self-assembly of various OPV derivatives is extensively studied. [9, 10] OPV appended with carbonate linkers and cholesterol moiety (**OPV_carb_chol**) have been previously studied by ajayaghosh and coworkers to explore the effect of cholesterol motif on the photophysical and morphological features of assembly. [11] Here we study the mechanism of self-assembly of **OPV_carb_chol** in apolar solvent such as *n*-dodecane.

Since the self-assembly and morphological studies of this molecule are already

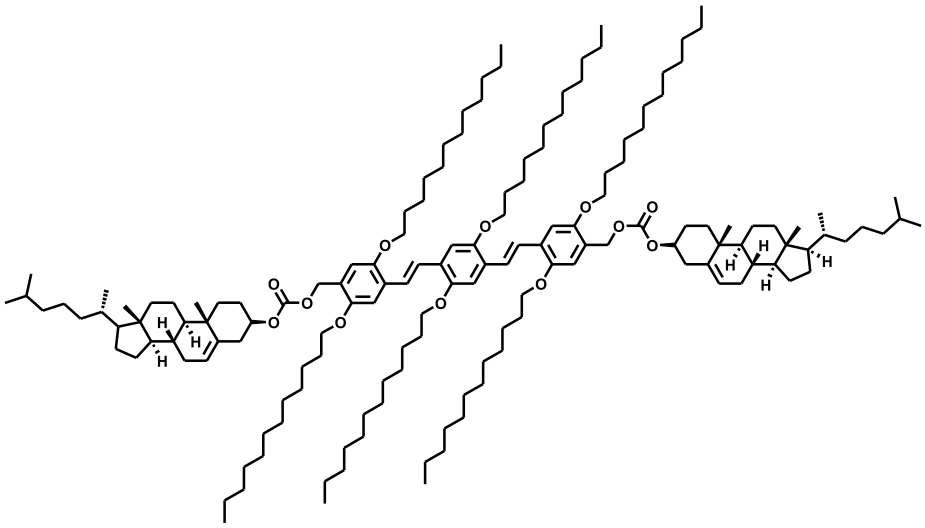

Figure 5.6: Structure of **OPV_carb_chol**.

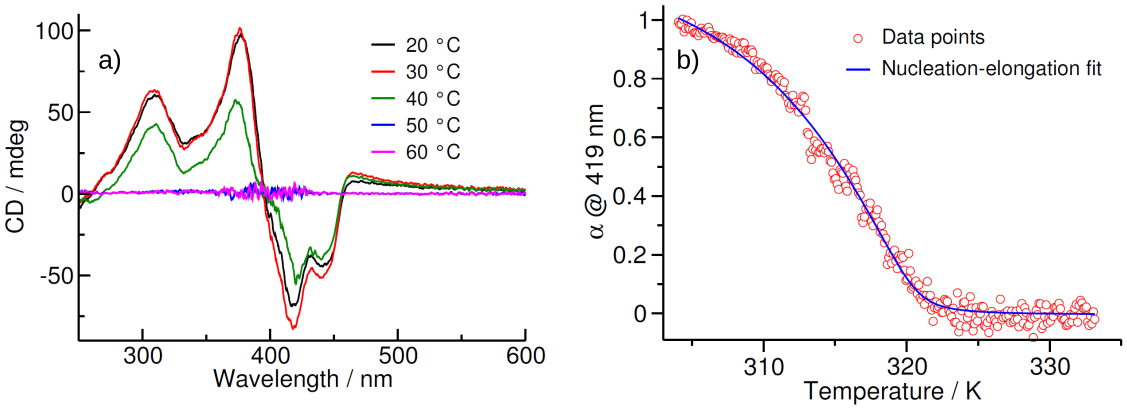

Figure 5.7: a) Temperature-dependent CD spectra of **OPV_carb_chol** in *n*-dodecane every 10 °C (c = 1×10^{-3} M). Spectra were recorded in a 10 mm cuvette. b) Heating curve obtained from CD studies with a ramp rate of 3 °C/minute.

reported, here we would not investigate them. The CD spectra of **OPV_carb_chol** shows a bisignated signal with a positive Cotton effect at higher wavelength. With an increase in temperature, the CD signal vanishes, indicating a molecularly dissolved state. Further, temperature-dependent heating experiments were performed to study the mechanism of self-assembly. During the cooling curve experiments of **OPV_carb_chol**, significant amount of precipitation was observed. In order to avoid the precipitation, heating curve experiments were performed, although these are not ideal method of studying the mechanisms. The obtained heating curve again shows a non-sigmoidal behaviour and is well described by the nucleation-elongation

model. [7, 8] Thus **OPV_carb_chol** also self-assembles cooperatively. The carbonate group could possibly engage in dipolar interactions across molecules in an assembly, leading to macrodipole-moment for the assembly. This, too highlights the role of dipolar groups in governing the mechanism of self-assembly irrespective of the chromophore under study.

5.2.3 Esters as source of dipole-moment

In the previous two examples, carbonate linker was utilized as the source of molecular dipole-moment to achieve cooperative mechanism in two different chromophores. Ester functional groups are also known to possess a significant dipole-moment. [12, 13] Herein, we examine the role of ester groups as linkers in affecting the mechanism of self-assembly of perylene bisimides.

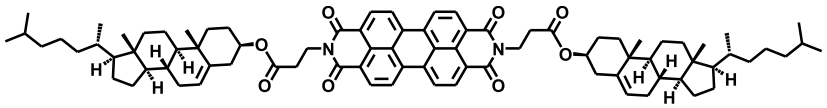

Figure 5.8: Structure of **PBI_est_chol**.

The molecule under study (**PBI_est_chol**) consists of a central PBI core followed by an ethylene spacer and an ester group. Cholesterol self-assembling moiety is attached to the other end of the ester (Figure 5.8). **PBI_est_chol** was synthesized by condensation reaction between perylene dianhydride and the amino ester derivative of cholesterol and was characterized through ^{1}H-NMR and MALDI mass spectroscopy.

UV/vis absorption spectrum of **PBI_est_chol** in chloroform shows sharp transitions at 526, 489 and 458 nm (Figure 5.9a). These have been atributed to the π-π^* transitions of PBI along the long axis of the molecule. The emission spectrum shows a mirror image of absorption, indicating that **PBI_est_chol** exists as individual molecules in chloroform (Figure 5.9b). UV/vis absorption spectrum of **PBI_est_chol** in apolar MCH shows the loss of vibronic features and hypsochromic shift of absorption maximum to 480 nm. The corresponding emission spectra shows highly quenched emission (Figure 5.9). Thus, we can conclude that **PBI_est_chol** forms H-type aggregates in apolar solvents.

The chiral cholesterol moiety on the periphery of **PBI_est_chol** renders the assembly chiral, as can be seen from the bisignated Cotton effect (Figure 5.10a). These assemblies could reach the molecularly dissolved state, i.e, lack of any chiral

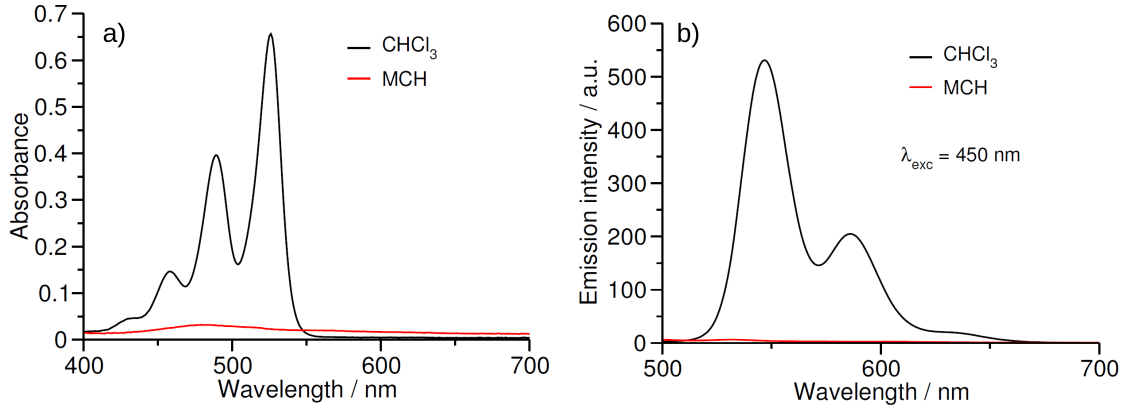

Figure 5.9: a) and b) UV/vis absorption and emission spectra of **PBI_est_chol** respectively in different solvents (c = 1×10^{-5} M). The emission spectra are recorded in 1 mm cuvette to minimize self-absorption.

organization at high temperatures. Cooling curves obtained from CD studies showed a non-sigmoidal behaviour (Figure 5.10b) and the experimental data could be fitted well by the nucleation-elongation model [7, 8] and the thermodynamic parameters of self-assembly are presented in Table 5.2.

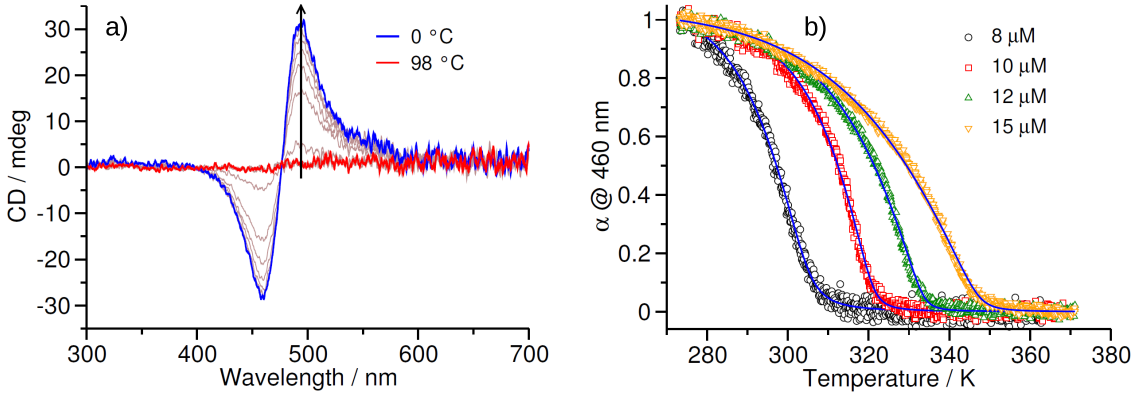

Figure 5.10: a) Temperature-dependent CD spectra of **PBI_est_chol** in MCH:TCE (8:2, v/v) every 10 °C (c = 1.2×10^{-5} M). Spectra were recorded in a 10 mm cuvette. Arrow indicates spectral changes with decrease in temperature. b) Cooling curve obtained from CD studies at different concentrations with a cooling rate of 2 °C/minute. Solid blue lines indicate the nucleation-elongation fits to the data.

Concentration (M)	$\Delta H^0{}_e$ (kJ/mol)	ΔS^0 (kJ/mol·K)	$\Delta H^0{}_{nucl}$ (kJ/mol)	T_e (K)	σ	ΔG^0 (kJ/mol)
8.0×10^{-6}	-66.73 ±1.77	-0.122 ±0.0059	-11.14 ±0.12	303.10 ± 0.20	1.1×10^{-2}	-30.35 ±0.01
1.0×10^{-5}	-72.60 ±0.82	-0.131 ±0.002	-15.17 ±0.33	319.75 ±0.11	2.2×10^{-3}	-33.54 ±0.22
1.2×10^{-5}	-53.88 ±0.48	-0.067 ±0.0014	-19.57 ±0.43	332.38 ± 0.11	3.7×10^{-4}	-33.90 ±0.06
1.5×10^{-5}	-37.36 ±0.27	-0.015 ±0.0008	-21.10 ±0.33	345.70 ±0.12	2.0×10^{-4}	-32.88 ±0.04

Table 5.2: Thermodynamic parameters of **PBI_est_chol** at different concentrations in MCH:TCE (8:2, v/v) obtained from temperature-dependent CD measurements. ΔG^0 was calculated at 298.15 K.

5.3 Conclusions

In the present study, we observe that irrespective of the central chromophore, the combination of carbonate group, which is the source of molecular dipole-moment and the rigid self-assembly moiety (cholesterol) leads to a cooperative mechanism of self-assembly. In addition, we have seen that the ubiquitously found ester groups can also lead to cooperative mechanism due to their significant dipole-moment. Thus, we can generalize that any combination of dipolar groups interacting in the growth direction combined with rigid self-assembling moieties which reinforce such interactions will lead to a cooperative mechanism of self-assembly.

5.4 Experimental details

5.4.1 General Methods

Chemicals and synthesis related: All chemicals were purchased from commercial sources and used without further purification unless and untill specified. Thin layer chromatography (TLC) was performed using Merck silica gel 60 F_{254} plates coated on aluminium. Column chromatography was performed using Merck silica gel 60 (230-400 mesh, 40-63 μm) under positive pressure of nitrogen gas.
Compounds **OPV_carb_chol**, [11] **2** [1] and **3** [14] were synthesized according to the literature reports.

Optical studies: UV/vis absorption and fluorescence spectra were recorded on a Perkin-Elmer Lambda 750 and Perkin-Elmer LS 55 spectrometer respectively.

Temperature-dependent UV/Vis absorption spectra were recorded on Perkin-Elmer lambda 750 using PTP-1+1 Peltier and Templab 2.14 software. Circular dichroism (CD) spectra were recorded on a JASCO J-815 spectrometer using the following parameters; sensitivity = 100 mdeg, scan rate = 100 nm/minute, bandwidth = 1 nm, response time = 1 second and number of accumulations = 1. Temperature-dependent measurements were performed using a CDF-426S/15 Peltier type temperature controller with a temperature range of 263-370 K.

Mass spectroscopy details: Matrix-Assisted Laser Desorption Ionization was performed on a Bruker daltonics autoflex (ST-A2130) spectrometer using trans-2-[3-(4-tert-Butylphenyl)-2-methyl-2-propenylidene]malononitrile (DCTB) as the matrix.

NMR spectroscopy: ^{1}H and ^{13}C-NMR spectra were recorded on a Bruker Avance 400 spectrometer operating at 400 MHz and 100 MHz respectively. Chemical shifts are reported with respect to the residual solvent peaks of chloroform-D (δ = 7.26 ppm for ^{1}H and 77.16 ppm for ^{13}C NMR). Notations; s, d, t, q, m and br stand for singlet, doublet, triplet, quartet, multiplet and broad respectively. All NMR spectra were recorded at 300 K unless otherwise mentioned.

Fitting of cooling curves: Nucleation-elongation model was fitted using Matlab R2008b.

Transmission Electron Microscopy (TEM): TEM micrographs were recorded on a JEOL, JEM 3010 with an operating voltage of 300 kV. The samples were prepared by drop-casting the solution of interest on a cooper grid and allowed to air dry followed by drying in vacuum. No staining agent was used.

5.4.2 Synthetic details

Synthesis of PMI_carb_chol: **1** (110 mg, 0.23 mmol, 1.5 eq.) and **2** (50 mg, 0.15 mmol, 1.0 eq.) were taken in a 50 mL 2-necked RBF equiped with a refluc condenser and a nitrogen balloon. Dry DMF (15 mL) was added to the RBF and stirred at 120 °C for 8 hours. After 1 hour of heating, the reaction mixture turned to orange and finally after 8 hours it was dark brownish. At the end of the reaction, the solvent was evaporated under reduced pressure and dried at 60 °C under vacuum for 10 hours to remove trace amounts of DMF. The contents of the 2-necked were transfered to

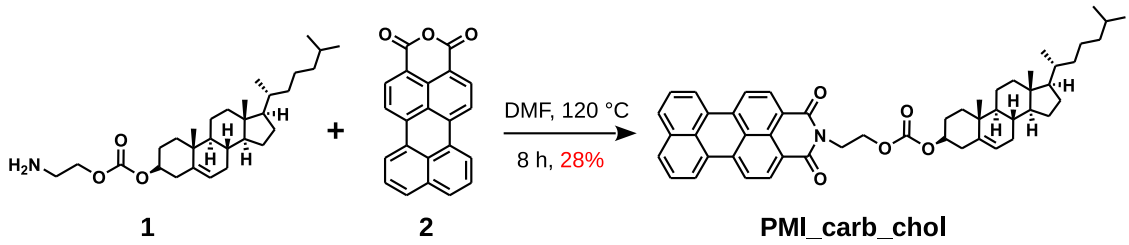

Figure 5.11: Synthetic route to **PMI_carb_chol**.

a single necked RBF and dried to obtain a bordeaux colored semisolid (280 mg).
Purification: The crude product was initially purified by a column chromatography (SiO_2, 230-400 mesh) eluting with 0-1$ MeOH in chloroform. The second fraction was further subjected to alumina chromatography (neutral), by eluting with 0-0.3% MeOH in chloroform. Finally the product was purified using size exclusion chromatography (S-X3, chloroform) twice to obtain a dark red solid (34 mg, 28%) and it was stored at 0-5 °C.
^{1}H-NMR (400 MHz, $CDCl_3$): δ = 8.09 (d, J = 7.6 Hz, 2H), 7.93 (d, J = 7.2 Hz, 2H), 7.80 (d, J = 7.6 Hz, 2H), 7.70 (d, J = 8 Hz, 2H), 7.39 (t, J = 7.6 Hz, 2H), 5.34 (d, J = 5.2 Hz, 1H), 4.53-4.43 (m, 5H), 2.44-2.32 (m, 2H), 2.0-1.03 (m, 19H), 1.00 (s, 3H), 0.90 (d, J = 6.4 Hz, 3H), 0.875 (d, J = 1.6 Hz, 3H), 0.858 (d, J = 1.6 Hz, 3H), 0.66 ppm (s, 3H).
^{13}C-NMR (100 MHz, $CDCl_3$): δ = 163.73, 154.59, 139.57, 136.74, 134.07, 131.12, 130.86, 129.37, 128.72, 127.40, 126.86, 126.17, 123.45, 123.00, 120.28, 119.75, 78.16, 64.77, 56.83, 56.31, 50.15, 42.46, 39.88, 39.68, 38.92, 38.17, 37.04, 36.69, 36.35, 35.93, 32.02, 31.99, 29.84, 28.36, 28.16, 27.86, 24.40, 24.01, 22.95, 22.70, 21.19, 19.42, 18.87, 11.99 ppm.
MALDI-TOF (DCTB, negative mode): m/z calculated for $C_{52}H_{59}NO_5$: 777.43 $[M]^{-\cdot}$; found: 777.42

Synthesis of PBI_est_chol: **PTCDA** (85 mg, 0.22 mmol, 1.0 eq.) and **3** (220 mg, 0.48 mmol, 2.2 eq.) were taken in 50 mL 2-necked RBF. Dry DMF (15 mL) wad added to the RBF and stirred at 120 °C for 10 hours. After this, the solvent was removed under reduced pressure to obtain a dark red solid.
Purification: The crude product was purified by column chromatography (SiO_2, 230-400 mesh) eluting with 5-10% acetone in chloroform. The fraction of chromatography which contained the product was further purified by dissolving it in excess of n-hexane and cooling to 0 °C. This was filtered and washed with excess of n-hexane.

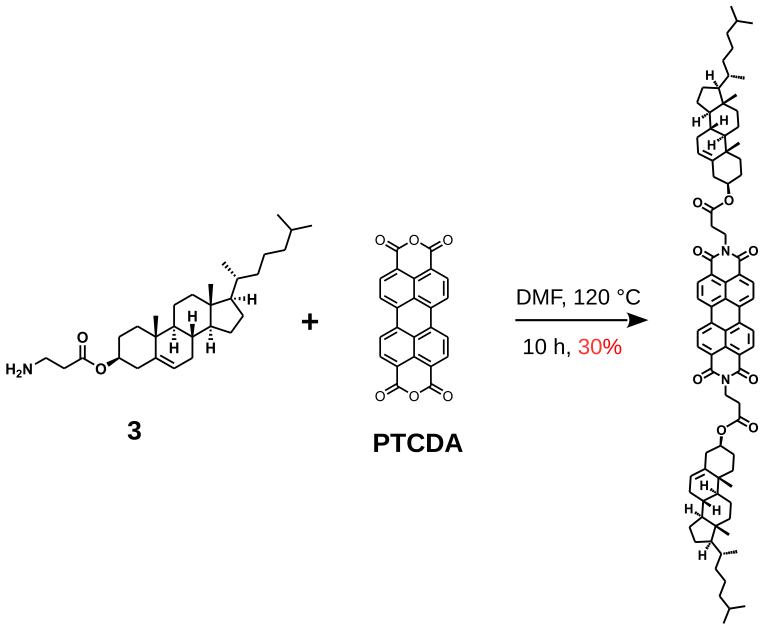

Figure 5.12: Synthetic route to **PBI_est_chol**.

This process was repeated twice to a pure red solid (80 mg, 30%).
^{1}H-NMR (400 MHz, $CDCl_3$): δ = 8.64 (d, J = 7.96 Hz, 4H), 8.58 (d, J = 8.16 Hz, 4H), 5.29 (brs, 2H), 4.60-4.58 (m, 2H), 4.46 (t, J = 7.32 Hz, 4H), 2.72 (t, J = 7.52 Hz, 4H), 2.24 (m, 4H), 1.95-0.92 (m, 52H), 0.91 (s, 6H), 0.84 (d, J = 6.44 Hz, 6H), 0.80 (d, J = 1.72 Hz, 6H), 0.78 (d, J = 1.72 Hz, 6H), 0.60 ppm (s, 6H).
^{13}C-NMR could not be recorded due to the low solubility of the compound at the required concentration for NMR studies.
MALDI-TOF (DCTB, negative mode): m/z calculated for $C_{84}H_{106}N_2O_8$: 1270.79 $[M]^{-\cdot}$; found: 1270.81

Bibliography

[1] Feiler, L.; Langhals, H.; Polborn, K. *Liebigs Ann.* **1995**, *1995*, 1229–1244.

[2] Li, C.; Schöneboom, J.; Liu, Z.; Pschirer, N.; Erk, P.; Herrmann, A.; Müllen, K. *Chem. Eur. J.* **2009**, *15*, 878–884.

[3] Cotlet, M.; Vosch, T.; Habuchi, S.; Weil, T.; Müllen, K.; Hofkens, J.; De Schryver, F. *J. Am. Chem. Soc.* **2005**, *127*, 9760–9768.

[4] Weingarten, A. S.; Kazantsev, R. V.; Palmer, L. C.; McClendon, M.; Koltonow, A. R.; S., S. P.; Kiebala, D. J.; Wasielewski, M. R.; Stupp, S. I. *Nat. Chem.* **2014**, *6*, 964–970.

[5] Lewandowska, U.; Zajaczkowski, W.; Chen, L.; Bouillière, F.; Wang, D.; Koynov, K.; Pisula, W.; Müllen, K.; Wennemers, H. *Angew. Chem. Int. Ed.* **2014**, *53*, 12537–12541.

[6] Lindquist, R. J.; Lefler, K. M.; Brown, K. E.; Dyar, S. M.; Margulies, E. A.; Young, R. M.; Wasielewski, M. R. *J. Am. Chem. Soc.* **2014**, *136*, 14912–14923.

[7] ten Eikelder, H. M. M.; Markvoort, A. J.; de Greef, T. F. A.; Hilbers, P. A. J. *J. Phys. Chem. B* **2012**, *116*, 5291–5301.

[8] Markvoort, A. J.; ten Eikelder, H. M. M.; Hilbers, P. A. J.; de Greef, T. F. A.; Meijer, E. W. *Nat. Commun.* **2011**, *2*, 509.

[9] Praveen, V. K.; Ranjith, C.; Bandini, E.; Ajayaghosh, A.; Armaroli, N. *Chem. Soc. Rev.* **2014**, *43*, 4222–4242.

[10] Ajayaghosh, A.; Praveen, V. K. *Acc. Chem. Res.* **2007**, *40*, 644–656.

[11] Ajayaghosh, A.; Vijayakumar, C.; Varghese, R.; George, S. J. *Angew. Chem. Int. Ed.* **2006**, *45*, 456–460.

[12] Xue, C.; Jin, S. *Chem. Mater.* **2011**, *23*, 2689–2692.

[13] Gunbas, D. D.; Xue, C.; Patwardhan, S.; Fravventura, M. C.; Zhang, H.; Jager, W. F.; Sudholter, E. J. R.; Siebbeles, L. D. A.; Savenije, T. J.; Jin, S.; Grozema, F. C. *Chem. Commun.* **2014**, *50*, 4955–4958.

[14] Stone, D. A.; Hsu, L.; Wheeler, N. R.; Wilusz, E.; Zukas, W.; Wnek, G. E.; Korley, L. T. J. *Soft Matter* **2011**, *7*, 2449–2455.

Chapter 6

Carbonate Linkage Bearing Naphthalenediimides: Self-Assembly and Photophysical Properties

6.1 Introduction

Naphthalene diimides (NDIs) are one of the most studied class of n-type organic semiconductors for their application in organic field-effect transistors and solar cells. [1–4] The morphology of the active material plays a crucial role in determining their device characteristics. [5–10] Thus, the self-assembly properties of NDIs has been extensively investigated to control their supramolecular organization. [11–18] On the other hand, the optical properties of core unsubstituted NDIs are seldom explored for functional applications, as they show weak fluorescence with low quantum yields. [11] One of the strategies utilized to overcome this limitation is the use of core-substitution of NDIs with electron-donating groups, like alkoxy and amines, to bathchromically shift the absorption spectra and increase the fluorescence quantum yield. [19, 20]

Tang and co-workers have introduced aggregation-induced enhanced emission

Reprinted with permission from "Carbonate Linkage Bearing Naphthalenediimides: Self-Assembly and Photophysical Properties" *Chem. Eur. J.* **2014**, *20*, 4537-4541. Copyright 2014, Wiley-VCH. http://onlinelibrary.wiley.com/doi/10.1002/chem.201304857/abstract

(AIEE) strategy to increase the fluorescence quantum yield of chromophoric assemblies. [21–23] However, the AIEE phenomenon operates on the prerequisite that typically the molecule is nonplanar and has the freedom to undergo free-rotation about the bond connecting the chromophore and backbone moieties, like ethylene or silole; upon aggregation the rotation is restricted, minimizing the non-radiative processes, thus resulting in enhanced fluorescence quantum yield. [21] Although this is an efficient strategy to enhance the fluorescence quantum yield, the structural constraint on the molecule prohibits its application to conventional π-conjugated molecules, like NDIs. In this respect, our group has reported pre-associated (static) excimer emission [24] as an alternative way to enhance the fluorescence quantum yield of core-unsubstituted NDI assemblies. [25, 26] This strategy relies on the formation of ground-state assemblies, which upon excitation lead to excimers. Excimer emission from NDIs obtained by the self-assembly approach is generally green (500 nm). [26] Few recent studies have reported the red-shifted excimer emission from core unsubstituted NDI. [27–29] However, a clear understanding of such optical properties at a molecular level is lacking.

Here, we report the self-assembly and unusually red-shifted excimer emission resulting from the NDI chromophores bearing a carbonate linkage. We utilize the self-assembly-based static excimer (pre-associated) approach along with the role of linker group (carbonate) to tune the optical properties of NDI, thus emphasizing the role of linkers in influencing the optical properties of NDI. Photophysical comparison of carbonate and ether linkage bearing NDIs reiterated the importance of linker groups in tuning the excimer emission. X-ray diffraction and computational studies have provided insight into the molecular organization of NDIs in the assemblies. Further, temperature-dependent chiroptical studies have been undertaken to elucidate the mechanisms of self-assembly.

6.2 Results

6.2.1 Molecular design

The molecules under study (**1-3**) possess cholesteryl or dodecyl moieties on both imide positions of NDI chromophore through a carbonate or ether linkage (Figure 6.1). Cholesteryl is a well-known self-assembling motif, since it has the dual role of acting as a hydrophobic segment to induce aggregation and also renders a chiral bias to the molecular organization because of the presence of stereocenters. [30, 31]

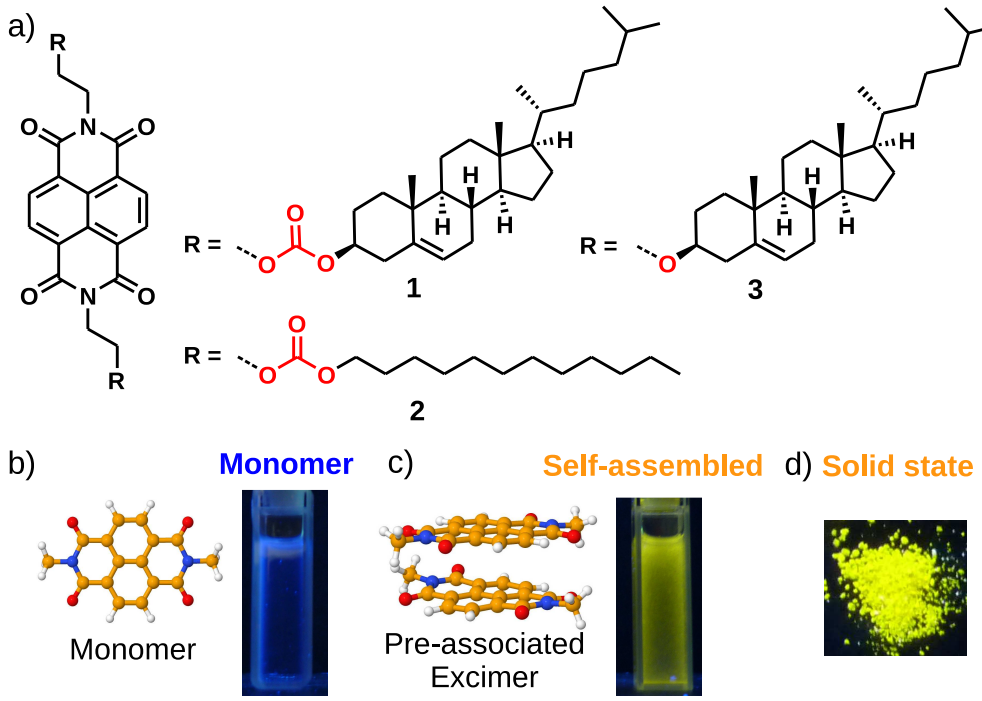

Figure 6.1: a) Structure of molecules under study. b)-d) Different emissive states of **1**. Photographs show the emission in different states along with the schematic of corresponding photophysical states.

Although self-assembly of cholesteryl appended chromophores has been extensively studied, [32–34] this is the first report of their use for the organization of NDIs. Remarkably, **1** showed different optical behavior in various solvents leading to excimer (yellow) in self-assembled and solid state (Figure 6.1). To understand the origin of optical properties, emission spectra and life-time studies of **1** were compared with that of **2** and **3**. Morphological investigation of **1** shows the presence of fluorescent nanoparticles in both solution and on substrates.

6.2.2 Self-assembly studies

1 is molecularly dissolved in 1,2-dichloroethane (DCE, c = 5×10^{-5} M), as can be seen from the characteristic π-π^* absorption features of NDI between 300-400 nm with a λ_{max} at 379 nm (ϵ = 2.65×10^{4} $Lmol^{-1}cm^{-1}$; Figure 6.2a). [35] The corresponding emission spectra show a maximum at 407 nm, and are a mirror image of its absorption spectra (Figure 6.2b). With an increase in the percentage of acetonitrile (ACN) in DCE/ACN solvent mixture, the absorbance decreases, the ratio of the vibronic features $I_{(00)}/I_{(01)}$ decreases from 1.27 in pure DCE to 0.94 in 40:60

DCE/ACN mixture and the absorption maximum is blue-shifted (to 359 nm) at higher percentages of ACN (60 %). Furthermore, a broad absorption band centered at 400 nm is observed along with scattering at higher percentage of ACN in DCE (Figure 6.2a). All these features indicate the formation of H-type excitonically coupled aggregates. [36]

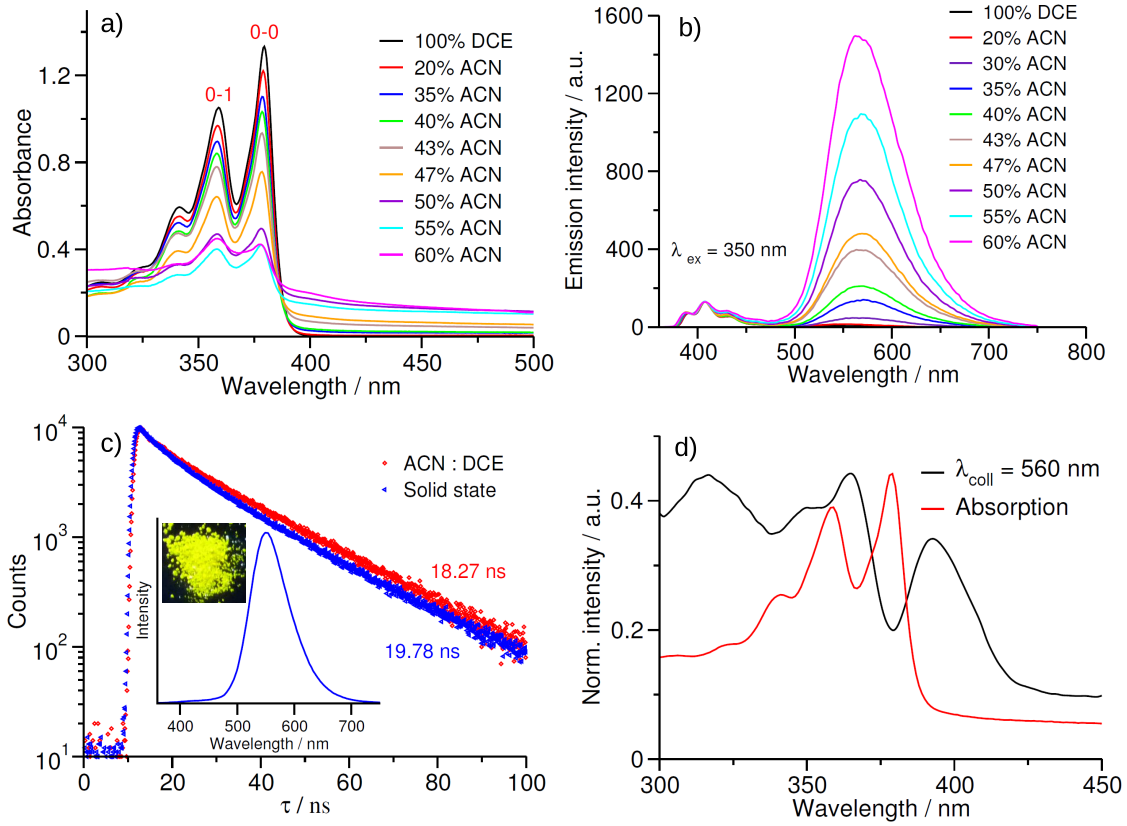

Figure 6.2: Self-assembly of **1**. a) UV/vis absorption and b) emission (λ_{exc} = 350 nm) spectra of **1** in ACN/DCE solvent mixture (path length, l = 10 mm). Notations 0-0 and 0-1 indicate the vibrionic transitions of NDI. Emission spectra were normalized at 407 nm. c) Life-time decay profiles of **1** in DCE/ACN solvent mixture and film state (λ_{exc} = 380 nm; $\lambda_{monitored}$ = 550 nm). Inset: the solid-state emission spectrum of **1** along with a photograph of the sample under 365 nm UV lamp. d) Excitation and UV/vis absorption spectra of **1** in 1:1 DCE/ACN. All solution-state studies were carried out at a concentration of 5×10^{-5} M. Arrows indicate the spectral changes with increasing percentage of ACN in DCE.

Emission spectra of **1** in DCE/ACN mixtures show an initial decrease in monomer emission intensity at 408 nm (up to 35% of ACN; Figure 6.2b) followed by the emergence of a new structure-less band centered at 560 nm; this new band grows in intensity with increase in the amount of ACN (Figure 6.2b). This yellow emissive

species could be attributed to the excimer of **1** in 50:50 (v/v) of DCE/ACN. The observed emission maximum is unusually red-shifted when compared to the typical green emissive NDI excimers reported in the literature. [26] Emission of **1** in the solid state is also centered at 560 nm as seen in DCE/ACN mixture, suggesting a similar molecular organization in both self-assembled and solid states (inset, Figure 6.2c). To understand the nature of emission arising at 560 nm, time-correlated single photon counting (TCSPC) experiments were conducted with a nanosecond excitation on a 1:1 DCE/ACN mixture containing **1** and in the film state (obtained by drop casting a solution of **1** in chloroform on a glass slide). The resultant decay profiles showed a biexponential decay with the major contribution having a life-time of 20.11 ns (92%, DCE/ACN) and 19.02 ns (84%, film state; Figure 6.2c). [37] Significantly a long life-time suggests that the excimer formation from pure collision in the excited state is not the sole reason for the observed yellow emission. In addition, the emission from the excimer is not observed until a certain degree of aggregation is reached in the ground state, which indicates that preorganization in the ground state is indeed necessary for the formation of excimer (Figure 6.2b). The excitation spectra of aggregates in the solution state collected selectively at the excimer emission (550 nm) showed blue-shifted absorption maximum compared to the corresponding monomer absorption and also showed a red-shifted band at 403 nm (Figure 6.2d). This reiterates the pre-associated or static origin of the excimer emission. [14, 24] It has also been shown that excitation of chromophores with H-dimer arrangement (in the ground-state) leads to a red-shifted emission arising from the lower energy level exciton and is attributed to excimer emission. [38] Since **1** forms H-type aggregates in the ground-state, a similar mechanism would be operative in the present instance as well. The yellow excimer formation is also observed in a variety of solvents ranging from cyclohexane to ethanol.

To understand whether the cholesteryl group is responsible for the observed red-shifted excimer of the NDI assemblies, molecule **2** bearing a dodecyl group in place of cholesteryl was synthesized and its optical properties were studied in its aggregated state. The absorption and emission features of **2** in chloroform (c = 1×10^{-4} M) resemble the characteristic features of NDI monomers (Figure 6.3a). Molecule **2** aggregates in a solvent mixture of polar DMSO and chloroform (c = 1×10^{-4} M) with the absorption band extending up to 425 nm. [39] Emission spectra show two prominent bands centered at 460 and 550 nm (Figure 6.3b). TCSPC studies of **2** (c = 1×10^{-4} M, 90% DMSO, 10% $CHCl_3$) with a nanosecond excitation monitoring of the emission at 460 and 560 nm showed triexponential decay profile

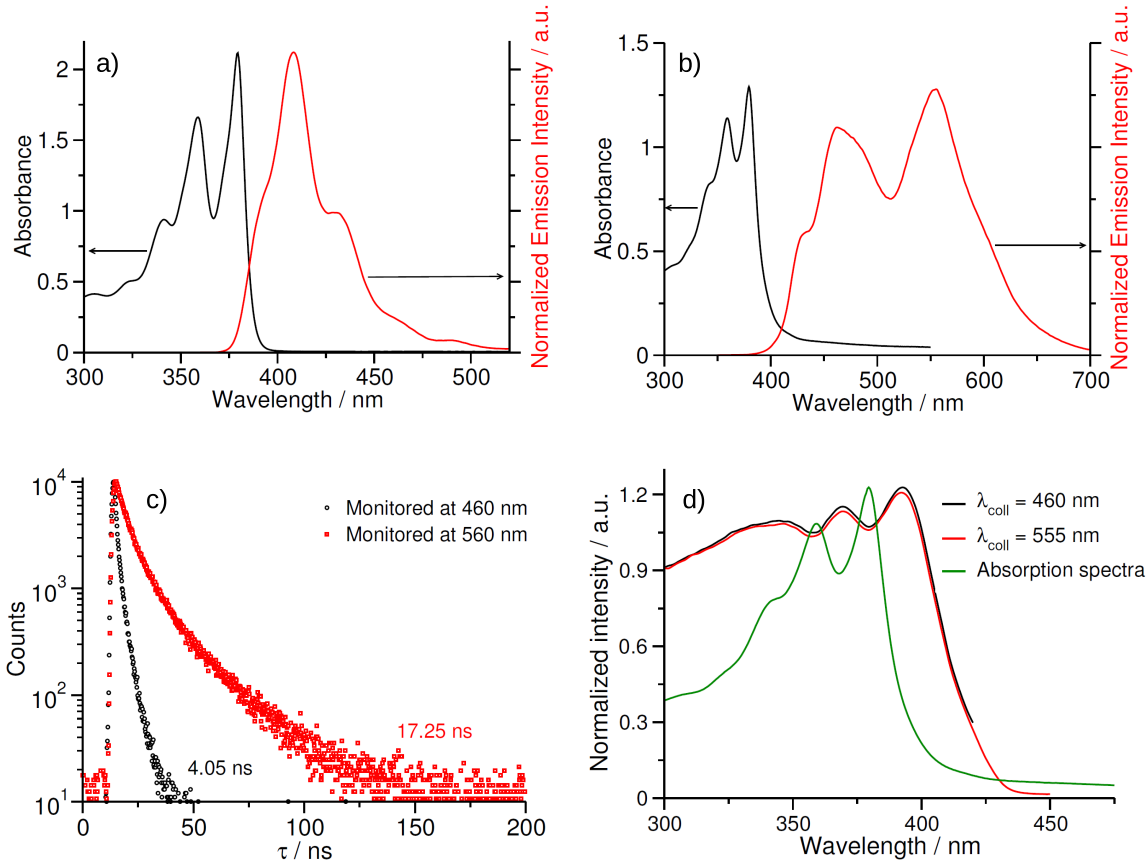

Figure 6.3: a) UV/vis absorption and emission spectra of **2** in chloroform (c = 1×10^{-4} M, λ_{exc} = 350 nm) b) UV/vis absorption and emission (λ_{exc} = 350 nm) spectra of **2** in 90% DMSO and 10% chloroform. c) TCSPC decay profiles of **2** monitored at two different wavelengths with a 380 nm excitation. The average life-time values are given in the graph. d) Absorption and excitation spectra of **2**. Spectra b) to d) were recorded with a concentration of 1×10^{-4} M in 90% DMSO and 10% Chloroform. All studies were performed in a 10 mm cuvette.

at both wavelengths (Figure 6.3c). Life-time values monitored at 460 nm are: 1.08 ns (55.23%), 3.27 ns (40.65%) and 10.54 ns (4.12%). The first two components of the decay at 460 nm is typical of NDI aggregates [25] and amounts to about 95% of the decay, the larger life-time of the third component (≈5%) could be arising from the overlap of the 560 nm band. At 560 nm, the life-time values are 3.88 ns (26%), 9.04 ns (45.2%) and 24.04 ns (28.8%), which are significantly larger than the ones at 460 nm. Also, the 3.88 ns component at 560 nm can have a contribution from the emission at 460 nm. Based on the red-shifted excitation spectra compared to monomer absorption (Figure 6.3d) and the life-time studies, the emissions at 460 and 560 nm are ascribed to the J-aggregate and pre-associated excimer emission of

2, respectively. The emission from the excimeric state of **2** is even maintained in the solid state and different solvents. Remarkably, both **1** and **2** show similar emission maxima (≈ 550 nm) and the average life-time (≈ 18 ns) values for the excimer state. Thus, the peripheral self-assembly group does not affect the photophysical properties drastically. [40]

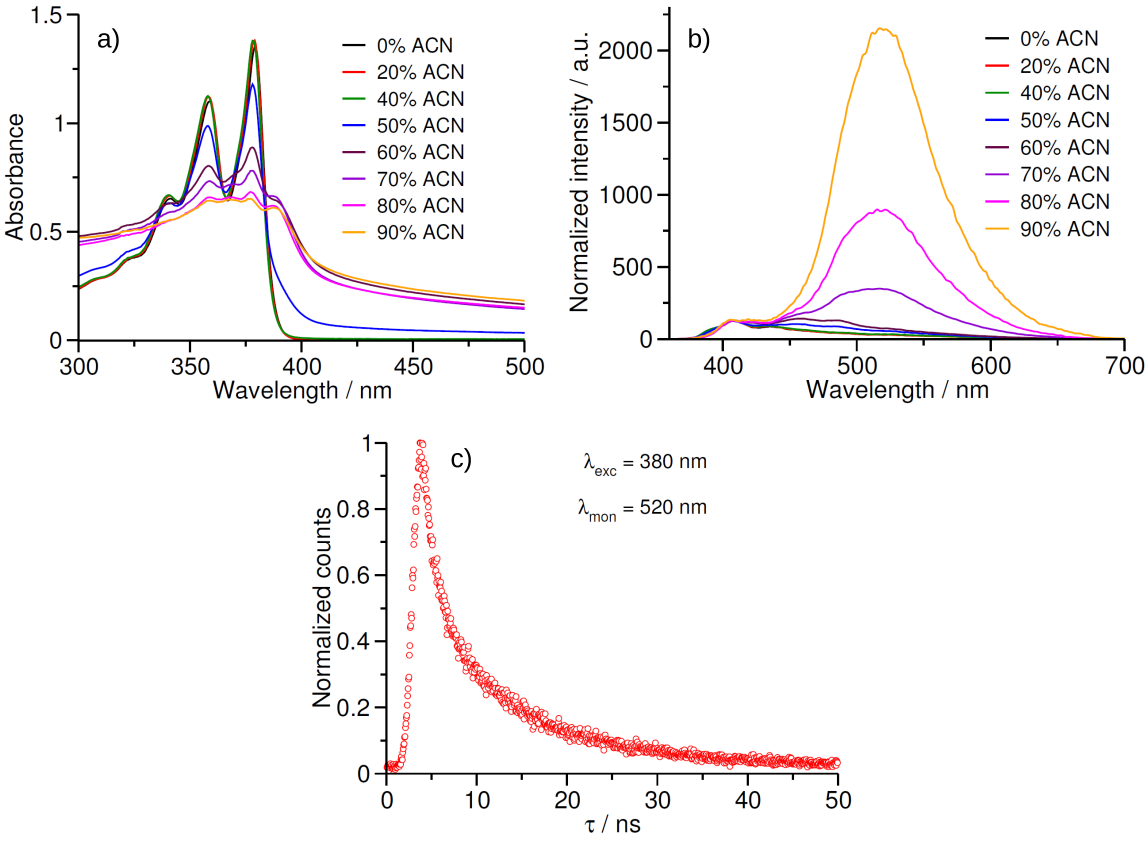

Figure 6.4: a) UV/vis absorption b) emission spectra of **3** in DCE/ACN solvent mixtures (λ_{exc} = 350 nm). Emission spectra are normalized at 408 nm. c) TCSPC decay profile of **3** in 90% ACN and 10% DCE with an λ_{exc} of 380 nm and $\lambda_{monitoring}$ of 520 nm. All studied were performed in a 10 mm cuvette with a concentration of 5×10^{-5} M.

Further, the optical properties of **3** (containing an ether linker) were studied to investigate the role of linkers to influence the photophysical properties. Molecule **3** is molecularly dissolved in DCE (Figure 6.4a) and with increasing amounts of ACN in DCE a new red-shifted band at 390 nm appears with concomitant decrease in the absorbance of the 0-0 (380 nm) and 0-1 (360 nm) vibronic bands, characteristic of NDI intermolecular interactions. The emission spectra show a broad, structureless band centered at 520 nm beyond 50% of ACN in DCE (Figure 6.4b). TCSPC experiments with a nanosecond excitation showed a biexponential (τ_1 = 1.72 ns,

15.15% and $\tau_2 = 10.85$ ns, 84.85%, $\chi^2 = 1.01$) decay at 520 nm with long-lived species (Figure 6.4c). The position, shape and the life-time of the species emitting at 520 nm is typical of NDI pre-associated excimers reported in the literature (**NDI_Bola**, Figure 6.5). [26] This clearly indicates that the carbonate linkage plays an important role in controlling the organization leading to the formation of red-shifted excimer.

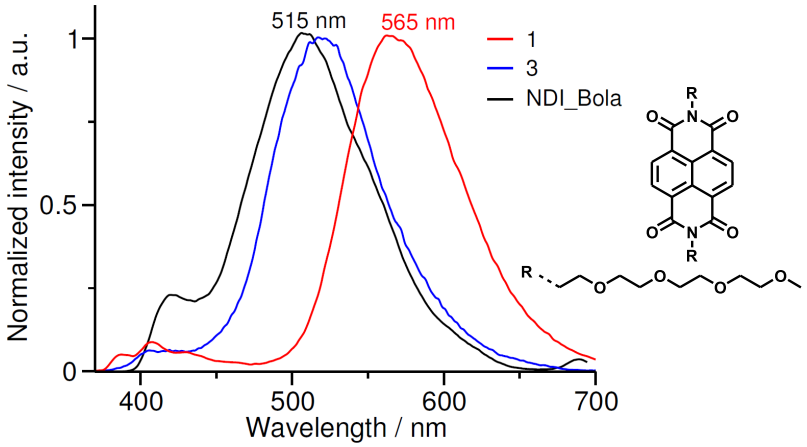

Figure 6.5: Normalized emission spectra of **1** (c = 5×10^{-5} M in 60:40 ACN to DCE), **3** (c = 5×10^{-5} M in 90:10 ACN:DCE) and **NDI_Bola** (c = 1×10^{-3} M in 85:15 Water:Methanol). λ_{exc} = 350 nm. Structure of **NDI_Bola** is shown on the right side of the graph.

6.2.3 Morphological and structural studies

Morphological studies were performed to further understand the molecular packing in the self-assembled aggregates of **1**. AFM of a film obtained by drop casting a 60:40 (v/v) DCE/ACN solution of **1** on glass substrate shows the formation of spherical nanoparticles with a mean diameter of 300 nm (Figure 6.6a). Dynamic light-scattering experiment of the same solution shows an apparent hydrodynamic radius of 200-400 nm (Figure 6.6b), suggesting that nanoparticles are indeed self-assembled in solution. Bischolesteryl appended chromophores are known to form nanoparticles. [41] Confocal fluorescence microscopy images of the self-assembled solution of **1**, sealed between glass-slides, showed yellow fluorescent nanoparticles and the emission maximum (560 nm) also matches well with that obtained from the solution-state spectroscopic studies (Figure 6.6c). Molecule **2** also formed nanoparticles as revealed by transmission electron microscopy (Figure 6.6d). Thus, pre-associated excimer emission is an alternative to AIEE mechanism for obtaining fluorescent organic nanoparticles formed by the self-assembly of π-conjugated molecules. [42, 43]

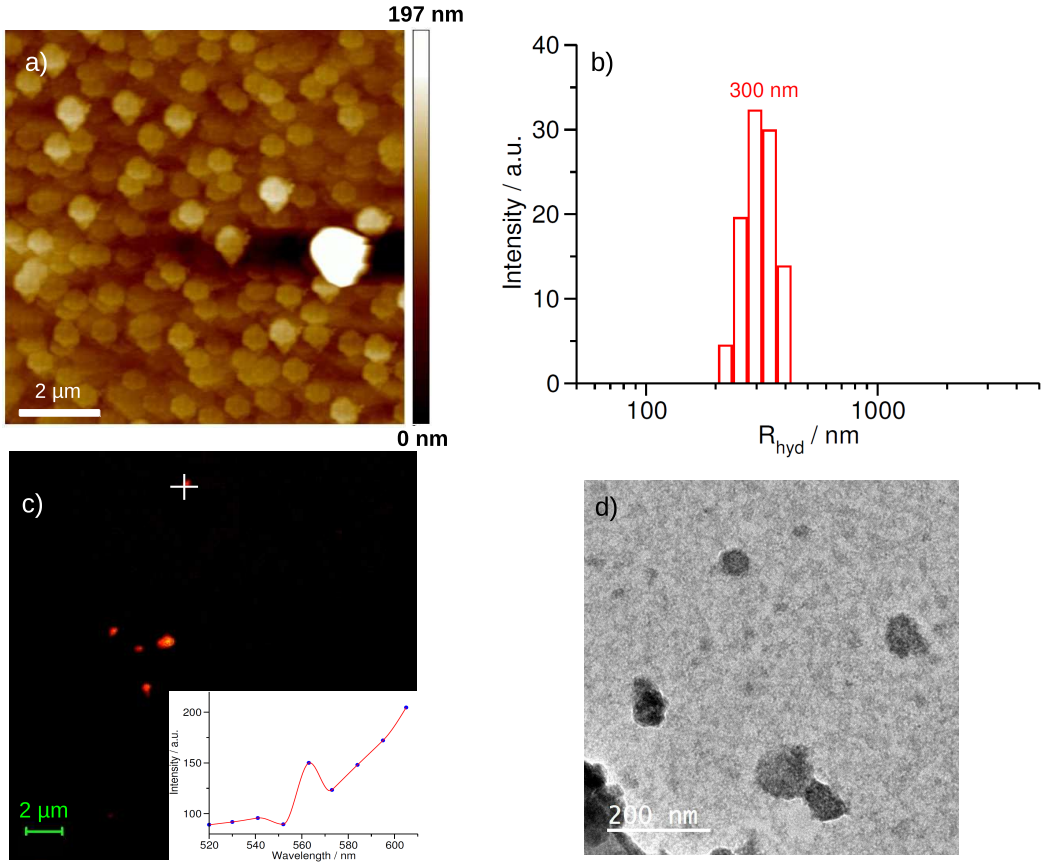

Figure 6.6: a) AFM height image of **1** obtained in the film state. b) DLS particle size distribution of **1**. c) Confocal microscopy image of the nanoparticles of **1**. The inset shows the fluorescence spectrum recorded at the plus sign shown on the Figure. A 6:4 (ACN:DCE) solution of **1** with a concentration of 5×10^{-5} M was for a) to c) studies. d) TEM micrograph of **2** (c = 1×10^{-4} M in 90% DMSO and 10% $CHCl_3$) obtained by dropcasting on a copper grid. Uranyl acetate (1% aqueous) was used for staining.

Powder XRD of **1** showed a sharp reflection at low-angle region and other higher angle reflections as well. The d-spacing corresponding to the low-angle reflection (47 Å) matches with the molecular dimension (49 Å) including the cholesteryl moiety and the reflection at around 27° (2θ) shows a d-spacing of 3.28 Å(Figure 6.7), which could be identified as the π-stacking distance. Such a small π-stacking distance indicates the presence of strong interchromophoric interaction. Powder XRD of **2** also showed similar small angle reflection and a stacking distance of 3.6 Å. Sharp reflections were observed for **2** when compared **1**, indicating the higher crystallinity of the former because of the ordered packing of linear alkyl chains.

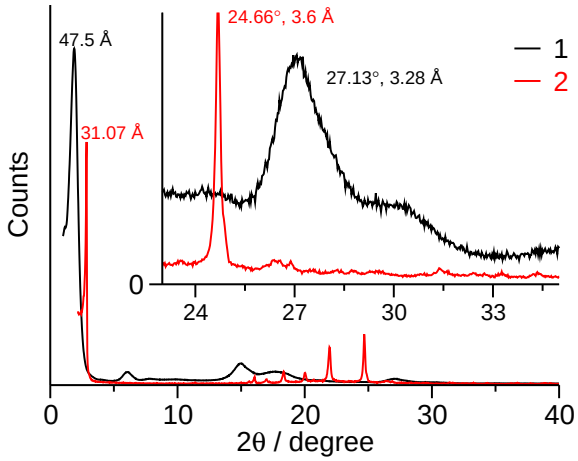

Figure 6.7: Powder XRD pattern of **1** and **2**. Inset: the zoom-in of the wide-angle region corresponding to the stacking distances.

6.2.4 Computational studies

Computational studies on the dimer of the model compounds (obtained by replacing the cholesteryl or dodecyl moiety with a methyl group and keeping the carbonate group to reduce the computational cost, Figure 6.8 left panel) shows a stacking distance of 3.35 Å, in agreement with experiments. Further, the optimized geometry of dimer and trimer show the presence of weak C-H$\cdots$O hydrogen bonds involving the oxygen of carbonate or imide group and C-H of ethylene spacer (Figure 6.8 right panel). These multiple interactions result in strong interchromophoric interactions and this could possibly be the reason for the observed red-shifted excimer emission.

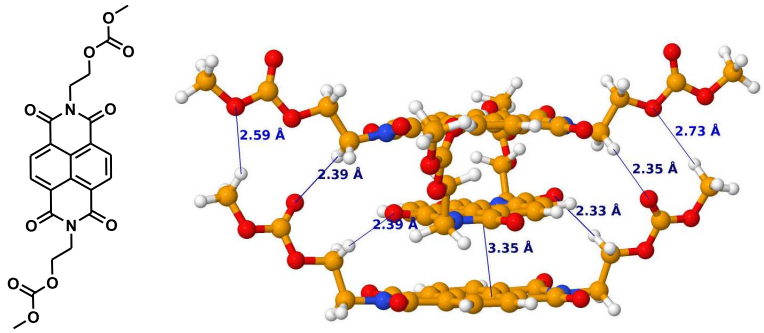

Figure 6.8: Structure of the model compound used for computational studies is shown on the left. Right hand side figure shows the geometry-optimized structure of the trimer of model compound. The solid lines indicate the C-H$\cdots$O and π-stacking interactions along with the corresponding distances.

6.2.5 Chiroptical studies

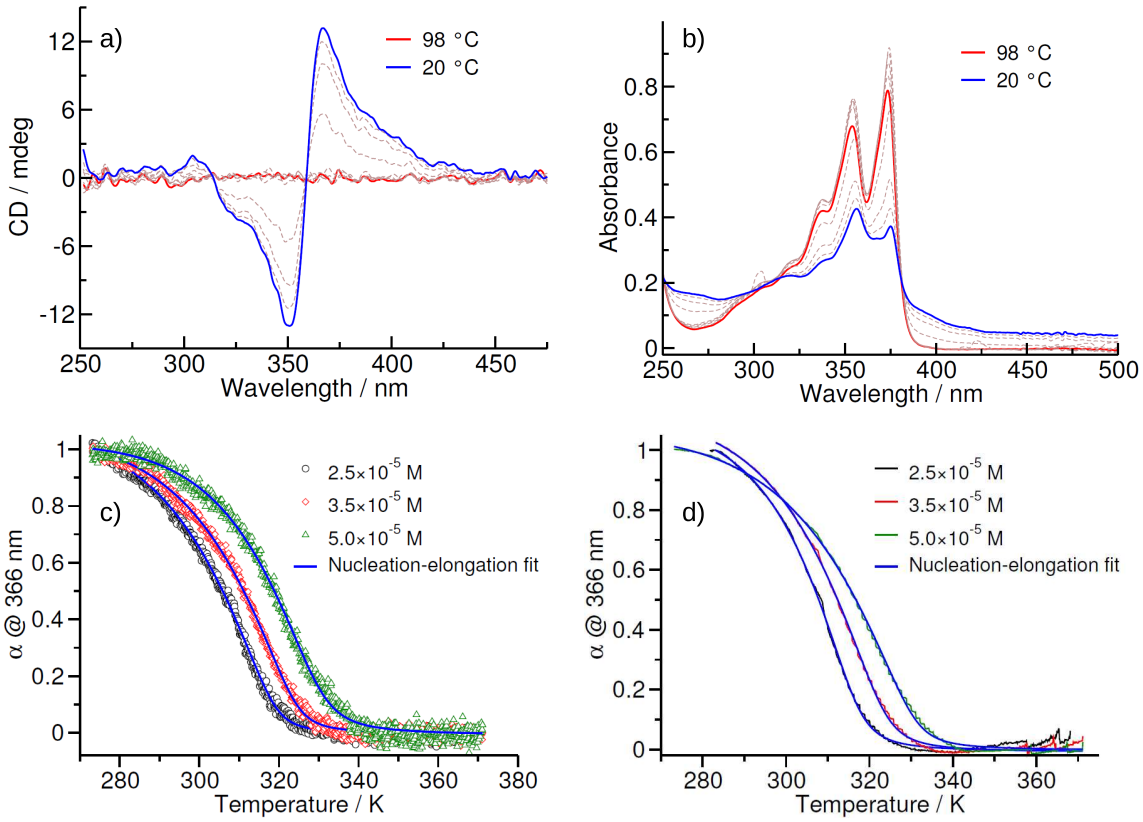

Figure 6.9: a) and b) Temperature-dependent CD and UV/vis spectra respectively of **1** in 95% MCH and 5% TCE (c = 5×10^{-5} M). Spectra are recorded every 10 °C while cooling down from high temperature in a 10 mm cuvette. c) and d) Cooling curves obtained from CD and UV/vis studies respectively by monitoring spectral changes at 366 nm with a cooling rate of 2 K/minute at different concentrations.

The effect of chiral cholesteryl moiety on the organization of the assemblies was studied using circular dichroism (CD) spectroscopy. CD spectra of the self-assembly was studied in a mixture of MCH and TCE solvent composition. CD spectra showed a positive bisignated Cotton effect in the π-π^* region, suggesting the chiral bias in the supramolecular organization of NDI molecules, which is induced by the peripheral cholesteryl groups (Figure 6.9a). The bisignated nature of the CD curve, characteristic of excitonic interactions, further suggests strong π-π interactions between the NDI chromophores in the self-assembled state. [44] Temperature dependent CD spectra of **1** shows that the Cotton effect vanishes at high temperatures, indicating that the NDIs exists as individual molecules. The vibronic features of the UV/vis absorption spectra show a complete reversal in the ratio of 0-0 and 0-1

band intensities, indicating the formation of H-type aggregates in MCH/TCE solvent composition. With the increase in temperature, the UV/vis absorption spectra resembles that of molecularly dissolved state indicating the diassembly of aggregates at high temperature. Utilizing the temperature-dependent CD and UV/vis studies, we have investigated the mechanism of self-assembly. The obtained cooling curves (Figure 6.9c and d) showed a reasonable fit to nucleation-elongation model [45, 46] of supramolecular polymerization and the relevant thermodyanmic parameters are obtained from fits to the cooling curves (Table 6.1). We strongly believe that the origin of cooperativity in the present system is due to the same reasons as found in the PBI derivatives appended with similar linkers and self-assemblying moieties.

Concentration (M)	ΔH^0_e (kJ/mol)	ΔS^0 (kJ/mol·K)	ΔH^0_{nucl} (kJ/mol)	T_e (K)	σ	ΔG^0 (kJ/mol)
2.5×10^{-5}	-41.85 ±0.60	-0.044 ±0.0019	-14.74 ±0.25	316.72 ± 0.15	2.6×10^{-3}	-28.73 ±0.03
3.5×10^{-5}	-44.24 ±0.59	-0.052 ±0.0019	-14.60 ±0.25	322.16 ±0.16	2.8×10^{-3}	-28.73 ±0.02
5.0×10^{-5}	-53.89 ±0.89	-0.082 ±0.002	-11.70 ±0.28	327.90 ±0.24	8.9×10^{-3}	-29.44 ±0.29

Table 6.1: Thermodynamic parameters of **1** at different concentrations in MCH/TCE (95:5, v/v) obtained from temperature-dependent CD measurements. ΔG^0 was calculated at 298.15 K.

6.3 Conclusion

In conclusion, we have shown the self-assembly of two novel NDI derivatives bearing a carbonate linkage resulting in unusually red-shifted excimer emission in both solid and self-assembled states. The ether linkage containing NDI derivative shows typical NDI excimer emission. Detailed spectroscopic analysis has revealed the pre-associated (static) nature of excimer emission. These findings highlight the role of linker functional groups to fine-tune the properties of self-assembled systems. Although many reports in the literature have reported uncharacteristic optical properties of chromophores, seldom has the linker or spacer been considered to play an important role. Thus, the present work might stimulate researchers to examine the role of spacers from an altogether different point of view. Also molecule **1** shows a cooperative mechanism of self-assembly. From Chapter 3, we saw that a PBI analogue of **1** also showed cooperative pathway of supramolecular polymerization. This

again reaffirms the hypothesis that long-range intermolecular interaction is necessary to achieve cooperativity in an assembly [47] and is mostly independent of the chromophore under study.

6.4 Experimental section

6.4.1 General methods

Materials: Ethanol amine (≥98%), naphthalene dianhydride and cholesteryl chloroformate (97%) were purchased from Sigma-Aldrich and dodecyl chloroformate (>90%) from TCI chemicals and used without further purification. Pyridine was freshly distilled before use. All spectroscopic studies were carried out using spectroscopic grade solvents.

NMR spectroscopy: ^{1}H and ^{13}C NMR spectra were recorded on a BRUKER AVANCE-400 fourier transformation spectrometer with 400 and 100 MHz respectively. The spectra are calibrated with respect to the residual solvent peaks. The chemical shifts are reported in parts per millon (ppm) with respect to TMS. Short notations used are, s for singlet, d for doublet, t for triplet, q for quartet and m for multiplet.

Optical spectroscopy: Electronic absorption spectra were recorded on a Perkin Elmer Lambda 900 UV-Vis-NIR spectrometer. Emission spectra were recorded on a Perkin Elmer Ls 55 luminescence spectrometer. Jasco J-815 spectrometer was used to measure the Circular Dichroism (CD) spectra with a standard sensitivity (100 mdeg), scan rate of 100 nm/second, bandwidth of 1 nm and single accumulation for each spectra.

Mass spectrometry: Matrix Assisted Laser Desorption Ionization Time of flight (MALDI-TOF): MALDI-TOF spectra were obtained on a Bruker daltonics autoflex (ST-A2130) MALDI-TOF spectrometer using trans-2-[3-(4-tert-Butylphenyl)-2-methyl-2-propenylidene]malononitrile (DCTB) as the matrix.

Atomic Force Microscopy (AFM) imaging: AFM measurements were performed on a Veeco diInnova SPM operating in tapping mode regime. Micro-fabricated silicon cantilever tips doped with phosphorus and with a frequency between 235 and 278 kHz and a force constant of 20-40 Nm^{-1} were used. AFM images were recorded at a rate of 512×512 pixels per minute. The appropriate solution was drop-casted on a clean glass surface and allowed to dry at room temperature first followed by drying under vacuum.

Dynamic Light Scattering (DLS): DLS measurements were performed on a NanoZS (Malvern UK) using a 532 nm LASER at a back scattering angle of 173°.

Time-correlated Single Photon Counting (TCSPC): Fluorescence decay profiles were recorded using FLSP 920 spectrometer, Edinburgh Instrument. EPLED source of 380 nm was used for excitation.

X-ray diffraction (XRD): XRD measurements were performed with DY 1042-Empyrean XRD with Programmable Divergence Slit (PDS) and PIXcel 3D detector and CuK_{α} source of 1.54060 Å wavelength.

Confocal Microscopy Imaging: Confocal microscopy imaging was carried out at room temperature using a Zeiss LSM META laser scanning confocal microscope.

GC-MS: Mass spectrum of A was recorded using SHIMADZU GCMS-Qp2010 Plus in the direction injection mode by dissolving a small amount of **A** in dimethyl sulfoxide.

HR-MS: HR-MS was carried out using Agilent Technologies 6538 UHD Accurate-Mass Q-TOF LC/MS.

Transmission Electron Miscroscopy (TEM): TEM measurements were carried out on JOEL, JEM 3010 operated at 310 kV. The sample was drop cast on a copper grid along with a drop of 1% aqueous uranyl acetate and dried under vacuum overnight.

Elemental analysis was performed using Carlo-Erba 1106 analyzer.

FT-IR spectra were recorded on a Bruker IFS 66v/S spectrometer.

6.4.2 Computational details

To understand the origin of unusually red-shifted excimer, geometry optimization of the oligomers of a model compound (cholesteryl and dodecyl groups were replaced by methyl group to reduce the computational cost) was undertaken. B97-D exchange correlation functional [48] which includes dispersion correction and 6-31G(d,p) basis set was employed for geometry optimization using Gaussian-09 [49] of dimer and trimer of the model compound. Jmol software [50] was used for visualizing the molecular structures.

6.4.3 Synthetic details

Synthesis of **A**: Naphthalene dianhydride (500 mg, 1.86 mmol, 1 eq.) and ethanolamine (341 mg, 5.6 mmol, 3 eq.) were taken in a two necked round bottom flask (RBF) connected to a condenser and purged with nitrogen atmosphere for 15 mins. 15 mL of

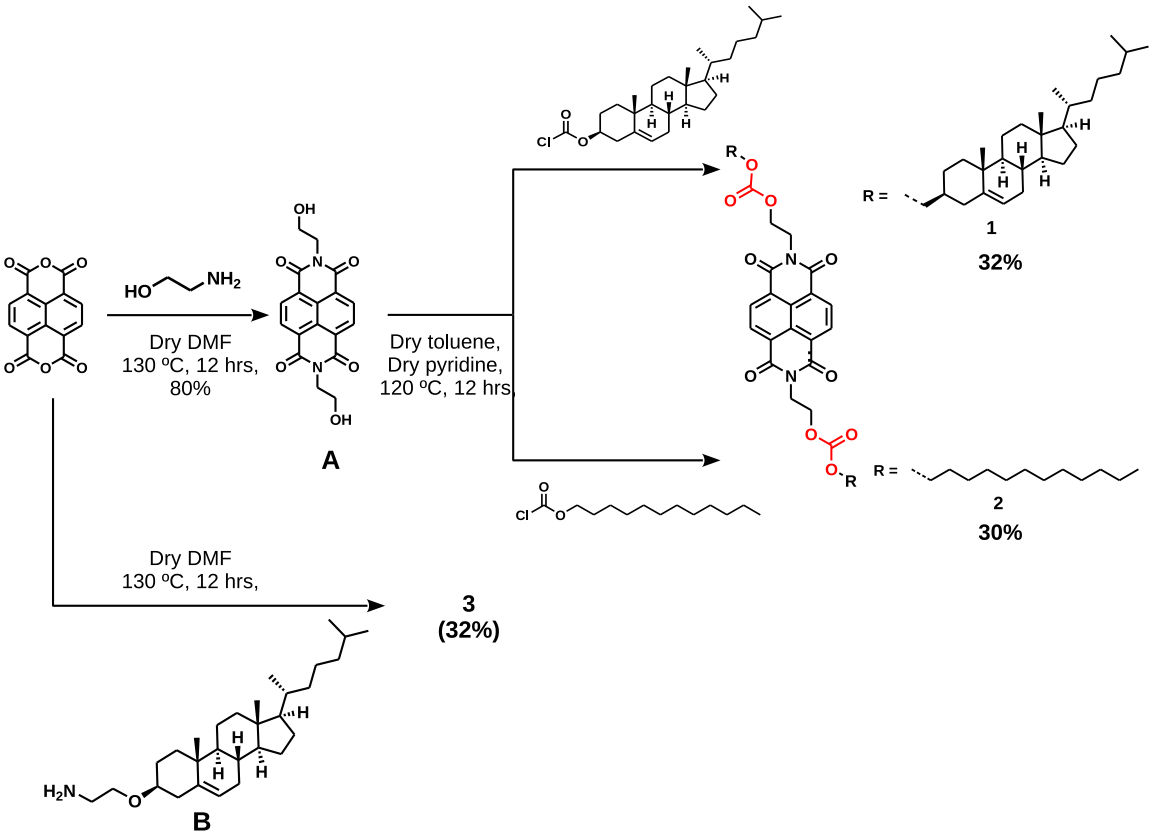

Figure 6.10: Synthetic route to molecules **1**-**3**

dry DMF was added to the RBF and the mixture was heated to 130 °C with stirring for 12 hours. It was allowed to cool down to room temperature and chloroform (10 mL) was added to obtain a precipitate. This was filtered under suction and washed with excess chloroform to remove DMF. The precipitate was dried under vacuum to obtain a brown colored solid (530 mg, 80% yield).
^{1}HNMR (400 MHz, DMSO-D_6): δ = 8.63 (s, 4H), 4.83 (t, J = 6 Hz, 2H, $HOCH_2$), 4.16 (t, J = 6.4 Hz, 4H, NCH_2), 3.65 ppm (q, J = 6.4 Hz, 4H, CH_2OH).
^{13}C NMR (100 MHz, DMSO-D_6): δ = 162.69, 130.32, 126.28, 126.06, 57.6, 42.2 ppm.
GC-MS (EI): m/z calcd: $C_{18}H_{14}N_2O_6$: 354.085, found: 354.0 $[M]^+$

Synthesis of **1**: A (450 mg, 1.27 mmol, 1 eq.) and cholesterol chloroformate (1.42 g, 3.17 mmol, 2.5 eq.) were taken in a two necked RBF connected to a condenser and 20 mL of dry toluene was added to it under nitrogen atmosphere. Dry pyridine (1.5 mL, 19.05 mmol, 15 eq.) dissolved in 10 mL of dry toluene was added to the RBF and the mixture was refluxed at 120 °C with constant stirring for 12 hours.

The reaction mixture was allowed to cool to room temperature and solvent was evaporated under reduced pressure to obtain a yellow solid. The solid was washed with excess of hexane to remove the unreacted cholesterol chloroformate. This was further purified by column chromatography using silica gel (100-200 mesh) as stationary phase and toluene/methanol (98:2 v/v) mixture as eluent to obtain a yellow solid (475 mg, 32% yield)
^{1}H-NMR (400 MHz, $CDCl_3$) δ = 8.77 (s, 4H), 5.33 (d, J = 4.8 Hz, 2H, CH=C), 4.60-4.40 (m, 10 H, OCH_2CH_2 and OCH), 2.35-1.04 (m, 56H), 0.99 (s, 6H), 0.91 (d, J = 6.4 Hz, 6H), 0.87 (d, J = 1.6 Hz, 6H), 0.85 (d, J = 2.0 Hz, 6H), 0.67 ppm (s, 6H).
^{13}C-NMR (100 MHz, $CDCl_3$) δ = 163.06 (C=O imide), 154.58 (C=O carbonate), 139.47 (CH=C cholesteryl), 131.28, 127.01, 126.71, 123.10 (C=CH cholesteryl), 78.30 (C-O cholesteryl), 64.60, 56.84, 56.30, 50.13, 42.46, 39.86, 39.74, 39.67, 38.08, 36.97, 36.68, 36.33, 35.93, 32.04, 31.99, 28.37, 28.16, 27.75, 24.43, 23.98, 22.96, 22.70, 21.18, 19.42, 18.86, 12.00 ppm.
IR (KBr), ν : 3081, 2958-2850, 1752 (carbonate C=O), 1709 and 1671 (imide C=O stretch), 1581, 1467, 1453, 1375, 1337, 1270, 1252, 1194, 1144, 1070, 1028, 999, 974, 949, 890, 878, 825, 787, 769, 764, 585, 437 cm^{-1}.
MALDI-TOF (DCTB matirx): m/z calcd: $C_{74}H_{102}N_2O_{10}$: 1178.75, found: 1178.82 $[M]^+$
Elemental analysis calcd (%) for $C_{74}H_{102}N_2O_{10}$: C 75.35, H 8.72, N 2.37; found: C 74.88, H 8.98, N 2.19.

Synthesis of **2**: A (340 mg, 0.96 mmol, 1 eq.) was taken in a three necked RBF connected to a reflux condenser and a dropping funnel. Dry pyridine (1.13 mL, 14.4 mmol, 15 eq.) was added to the RBF followed by 20 mL of dry toluene. Dodecyl chloroformate (0.65 mL, 2.4 mmol, 2.5 eq.) dissolved in dry toluene (15 mL) was added drop-wise to the reaction mixture through a dropping funnel. The reaction mixture was heated at 120 °C with constant stirring for 12 hours. Then the reaction mixture was allowed to cool down to room temperature. The solvent was evaporated under reduced pressure and methanol was added to the residue to obtain a brown colored powder. This was dissolved in minimum amount of chloroform and filtered to remove the unreacted A. The filtrate was concentrated under reduced pressure and the obtained solid was further purified by column chromatography (SiO_2, 230-400 mesh) using an elution of chloroform to 0.5% methanol in chloroform. The obtained mixture was further subjected to a size exclusion chromatography (S-X3)

in chloroform to obtain an off-white colored powder (230 mg, 30%).
^{1}H-NMR (400 MHz, $CDCl_3$) δ = 8.76 (s, 4H), 4.56 (t, J = 5.2 Hz, 4H, CH_2OCO_2), 4.49 (t, J = 5.2 Hz, 4H, NCH_2CH_2O), 4.11 (t, J = 6.6 Hz, 4H, $OCO_2CH_2(CH_2)_{11}$), 1.67-1.60 (m, 4H), 1.39-1.25 (m, 36H, $OCO_2CH_2CH_2(CH_2)_9CH_3$), 0.87 ppm (t, J = 6.6 Hz, 6H, $(CH_2)_9CH_3$)
^{13}C-NMR (100 MHz, $CDCl_3$) δ = 163.05 (C=O imide), 155.30 (C=O carbonate), 131.27, 127.01, 126.71, 68.62, 64.75, 39.70, 32.02, 29.79, 29.77, 29.72, 29.67, 29.48, 29.37, 28.76, 22.83, 14.25 ppm.
IR (KBr), ν : 3079, 3067, 3041, 2955, 2922, 2871, 2853, 1746 (carbonate C=O), 1706 and 1671 (imide C=O stretch), 1579, 1483, 1472, 1466, 1455, 1427, 1407, 1393, 1372, 1357, 1334, 1300, 1251, 1205, 1152, 1096, 1070, 1059, 1011, 993, 979, 946, 931, 904, 807, 795, 773, 734, 718, 638, 574, 553, 438, 430, 404 cm^{-1}.
HR-MS (ESI): m/z calcd: $[C_{44}H_{62}N_2O_{10}+Na]^+$: 801.4297, found: 801.4293.

Synthesis of **3**: Napthalene dianhydride (72 mg, 0.26 mmol, 1 eq.) and **B** [51] (235 mg, 0.54 mmol, 2.1 eq.) were taken in a 3-necked RBF fitted to a reflux condenser. Dry DMF (15 mL) was added to the RBF and was heated to 130 °C with constant stirring for 12 hours. After 12 hours it was allowed to cool down to room temperature and excess of methanol (50 mL) was added to obtain brown colored precipitate. The precipitate was filtered and washed with methanol and dried at 60 °C. The solid was purified by column chromatography (SiO_2, 230-400 mesh) eluting initially with pure dichloromethane (DCM) followed by 1-2% methanol in DCM. A bio-beads (S-X3) size exclusion chromatography was performed on the mixture obtained from the SiO_2 column. The product was finally purified by repeated (thrice) precipitation by adding excess nhexane to a solution of product in minimum amount of chloroform to obtain pure product (95 mg, 33%).
^{1}H-NMR (400 MHz, $CDCl_3$) δ = 8.76 (s, 4H), 5.30 (d, J = 5.2 Hz, 2H, CH=C), 4.46-4.41 (m, 4H), 3.83-3.77 (m, 4H), 3.27-3.19 (m, 2H), 2.33-2.28 (m, 2H), 2.18-2.11 (m, 2H), 2.00-0.98 (m, 52H), 0.95 (s, 6H), 0.90 (d, J = 6.4 Hz, 6H), 0.865 (d, J = 2 Hz, 6H), 0.849 (d, J = 1.6 Hz, 6H), 0.65 (s, 6H) ppm.
^{13}C-NMR (100 MHz, $CDCl_3$) δ = 163.02 (C=O imide), 140.93 (CH=C cholesteryl), 131.18, 126.94, 126.78, 121.81 (CH=C cholesteryl)), 79.35 (C-O cholesteryl), 64.38, 56.92, 56.31, 50.31, 42.47, 40.49, 39.93, 39.67, 39.13, 37.32, 36.98, 36.34, 35.93, 32.08, 32.03, 28.47, 28.37, 28.16, 24.43, 23.97, 22.96, 22.71, 21.21, 19.51, 18.86, 12.00 ppm.
IR (NaCl), ν : 2936, 2903, 2873, 2850, 1705 and 1661 (imide C=O stretch), 1581, 1454, 1435, 1372, 1353, 1330, 1267, 1244, 1188, 1111, 1055, 769, 730, 715 cm^{-1}.
MALDI-TOF (DCTB matrix): m/z calculated for $C_{72}H_{102}N_2O_6$: 1090.77, found:

1090.79.

Bibliography

[1] Laquindanum, J. G.; Katz, H. E.; Dodabalapur, A.; Lovinger, A. J. *J. Am. Chem. Soc.* **1996**, *118*, 11331–11332.

[2] Facchetti, A. *Mater. Today* **2007**, *10*, 28 – 37.

[3] Meng, Q.; Hu, W. *Phys. Chem. Chem. Phys.* **2012**, *14*, 14152–14164.

[4] Earmme, T.; Hwang, Y.-J.; Murari, N. M.; Subramaniyan, S.; Jenekhe, S. A. *J. Am. Chem. Soc.* **2013**, *135*, 14960–14963.

[5] Beaujuge, P. M.; Fréchet, J. M. J. *J. Am. Chem. Soc.* **2011**, *133*, 20009–20029.

[6] Mei, J.; Diao, Y.; Appleton, A. L.; Fang, L.; Bao, Z. *J. Am. Chem. Soc.* **2013**, *135*, 6724–6746.

[7] Würthner, F.; Meerholz, K. *Chem. Eur. J.* **2010**, *16*, 9366–9373.

[8] Wang, M.; Wudl, F. *J. Mater. Chem.* **2012**, *22*, 24297–24314.

[9] Hoeben, F. J. M.; Jonkheijm, P.; Meijer, E. W.; Schenning, A. P. H. J. *Chem. Rev.* **2005**, *105*, 1491–1546.

[10] Babu, S. S.; Praveen, V. K.; Ajayaghosh, A. *Chem. Rev.* **2014**, *114*, 1973–2129.

[11] Bhosale, S. V.; Jani, C. H.; Langford, S. J. *Chem. Soc. Rev.* **2008**, *37*, 331–342.

[12] Molla, M. R.; Ghosh, S. *Chem. Mater.* **2011**, *23*, 95–105.

[13] Ponnuswamy, N.; Pantoş, G. D.; Smulders, M. M. J.; Sanders, J. K. M. *J. Am. Chem. Soc.* **2012**, *134*, 566–573.

[14] Shao, H.; Nguyen, T.; Romano, N. C.; Modarelli, D. A.; Parquette, J. R. *J. Am. Chem. Soc.* **2009**, *131*, 16374–16376.

[15] Aparicio, F.; Sánchez, L. *Chem. Eur. J.* **2013**, *19*, 10482–10486.

[16] Anderson, T. W.; Sanders, J. K. M.; Pantoş, G. D. *Org. Biomol. Chem.* **2010**, *8*, 4274–4280.

[17] Bell, T. D. M.; Bhosale, S. V.; Forsyth, C. M.; Hayne, D.; Ghiggino, K. P.; Hutchison, J. A.; Jani, C. H.; Langford, S. J.; Lee, M. A.-P.; Woodward, C. P. *Chem. Commun.* **2010**, *46*, 4881–4883.

[18] Pantoş, G.; Pengo, P.; Sanders, J. *Angew. Chem. Int. Ed.* **2007**, *46*, 194–197.

[19] Bhosale, S. V.; Bhosale, S. V.; Bhargava, S. K. *Org. Biomol. Chem.* **2012**, *10*, 6455–6468.

[20] Würthner, F.; Ahmed, S.; Thalacker, C.; Debaerdemaeker, T. *Chem. Eur. J.* **2002**, *8*, 4742–4750.

[21] Hong, Y.; Lam, J. W. Y.; Tang, B. Z. *Chem. Commun.* **2009**, 4332–4353.

[22] Hong, Y.; Lam, J. W. Y.; Tang, B. Z. *Chem. Soc. Rev.* **2011**, *40*, 5361–5388.

[23] Zhao, Z.; Lam, J. W. Y.; Tang, B. Z. *J. Mater. Chem.* **2012**, *22*, 23726–23740.

[24] Winnik, F. M. *Chem. Rev.* **1993**, *93*, 587–614.

[25] Kumar, M.; George, S. J. *Chem. Eur. J.* **2011**, *17*, 11102–11106.

[26] Kumar, M.; George, S. J. *Nanoscale* **2011**, *3*, 2130–2133.

[27] Molla, M. R.; Ghosh, S. *Chem. Eur. J.* **2012**, *18*, 1290–1294.

[28] Basak, S.; Nanda, J.; Banerjee, A. *Chem. Commun.* **2013**, *49*, 6891–6893.

[29] Bodapati, J. B.; Icil, H. *Photochem. Photobiol. Sci.* **2011**, *10*, 1283–1293.

[30] Murata, K.; Aoki, M.; Suzuki, T.; Harada, T.; Kawabata, H.; Komori, T.; Ohseto, F.; Ueda, K.; Shinkai, S. *J. Am. Chem. Soc.* **1994**, *116*, 6664–6676.

[31] Svobodova, H.; Noponen, V.; Kolehmainen, E.; Sievanen, E. *RSC Adv.* **2012**, *2*, 4985–5007.

[32] Wang, R.; Geiger, C.; Chen, L.; Swanson, B.; Whitten, D. G. *J. Am. Chem. Soc.* **2000**, *122*, 2399–2400.

[33] Sugiyasu, K.; Fujita, N.; Shinkai, S. *Angew. Chem. Int. Ed.* **2004**, *43*, 1229–1233.

[34] Kawano, S.-i.; Fujita, N.; Shinkai, S. *Chem. Eur. J.* **2005**, *11*, 4735–4742.

[35] Gawroński, J.; Brzostowska, M.; Kacprzak, K.; Kobon, H.; Skowronek, P. *Chirality* **2000**, *12*, 263–268.

[36] Shao, H.; Parquette, J. R. *Chem. Commun.* **2010**, *46*, 4285–4287.

[37] The life-time components are as follows; for 1:1 ACN/DCE (v/v) A_1 = 7.86%, τ_1 = 5.21 ns A_2 = 92.14%, τ_2 = 20.11 ns, and for film state A_1 = 16.06%, τ_1 = 6.09 ns A_2 = 83.94%, τ_2 = 19.02 ns. Here A denotes the prefactor for each decay and τ the corresponding life-time.

[38] Kumar, N. S. S.; Varghese, S.; Suresh, C. H.; Rath, N. P.; Das, S. *J. Phys. Chem. C* **2009**, *113*, 11927–11935.

[39] Molecule **2** aggregates in a range of polar and apolar solvents leading to same photophysical states. It has lower aggregation tendency in acetonitrile, and thus the more polar DMSO was used for the studies. We anticipate that any combination of good solvent and a bad solvent should lead to the same photophysical state.

[40] Although **1** and **2** show H- and J-type aggregation, respectively, in the ground state, on excitation there might be some structural rearrangement leading to a supramolecular organization, which is different from the ground state, thus resulting in similar red-shifted excimer emission.

[41] Abraham, S.; Vijayaraghavan, R. K.; Das, S. *Langmuir* **2009**, *25*, 8507–8513.

[42] Kaeser, A.; Schenning, A. P. H. J. *Adv. Mater.* **2010**, *22*, 2985–2997.

[43] González-Rodr´iguez, D.; Janssen, P. G. A.; Mart´in-Rapún, R.; Cat, I. D.; Feyter, S. D.; Schenning, A. P. H. J.; Meijer, E. W. *J. Am. Chem. Soc.* **2010**, *132*, 4710–4719.

[44] Kumar, M.; Jonnalagadda, N.; George, S. J. *Chem. Commun.* **2012**, *48*, 10948–10950.

[45] ten Eikelder, H. M. M.; Markvoort, A. J.; de Greef, T. F. A.; Hilbers, P. A. J. *J. Phys. Chem. B* **2012**, *116*, 5291–5301.

[46] Markvoort, A. J.; ten Eikelder, H. M. M.; Hilbers, P. A. J.; de Greef, T. F. A.; Meijer, E. W. *Nat. Commun.* **2011**, *2*, 509.

[47] Kulkarni, C.; Balasubramanian, S.; George, S. J. *ChemPhysChem* **2013**, *14*, 661–673.

[48] Grimme, S. *J Comput. Chem.* **2006**, *27*, 1787–1799.

[49] Frisch, M. J. et al. Gaussian 09 Revision D.01. Gaussian Inc. Wallingford CT 2009.

[50] a) Jmol: An open-source Java viewer for chemical structures in 3D, to be found under http://www.jmol.org; b) McMahon B.; Hanson, R. M. *J. Appl. Crystallogr.* **2008**, *41*, 811.

[51] Nikolaeva, I. A.; Misharin, A. Y.; Ponomarev, G. V.; Timofeev, V. P.; Tkachev, Y. V. *Bioorg. Med. Chem. Lett.* **2010**, *20*, 2872 – 2875.

Chapter 7

Charge-transfer Complexation between Naphthalene Diimides and Aromatic Solvents

7.1 Introduction

Naphthalene diimides (NDIs) are one of the well studied class of *n*-type semiconductors for application in organic electronics. [1–7] Since the imide nitrogens of NDIs are electronic nodes, they can be functionalized with a wide variety of functional groups giving rise to a plethora of supramolecular assemblies. [8–19] Self-assembly is influenced not only by the functional group at the imide position but also by the nature of solvent. [20–23] Since aromatic solvents such as chlorobenzene and *o*-dichlorobenzene are generally used for processing in organic electronics, [24] the nature of interaction between NDIs and aromatic solvents is important to understand. Aromatic solvents of varying electron donating capacity have been shown to influence the position of the emission maximum of NDI; however, corresponding changes in its absorption spectrum have not received much attention. The nature of interaction was attributed as excimer [25] or exciplex [26] formation. Recently, Kitagawa and co-workers have observed similar emission changes brought about by confining different aromatic molecules in a metal-organic framework with NDI

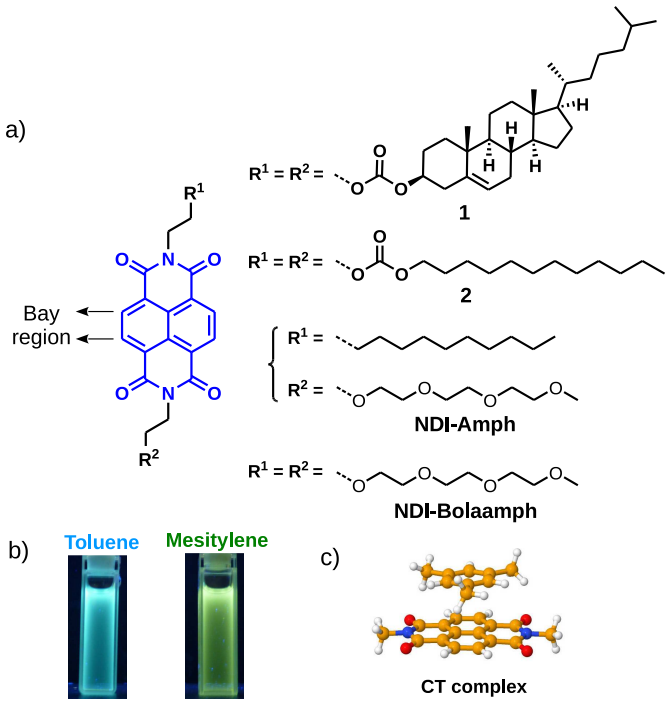

Figure 7.1: a) Structure of molecules studied. b) Photographs of tunable emission of **1** in different solvents excited at 365 nm. c) Schematic showing the interaction between NDIs and an aromatic solvent molecule.

as a ligand. The same has been attributed to exciplex emission based on charge-transfer (CT) formation between NDIs and aromatic guest molecules. [27] Banerjee and co-workers have recently described the gelation of a NDI appended with peptides in aromatic solvents assisted by charge-transfer interaction. [28] During our study of NDIs substituted with carbonate linkers and cholesterol/dodecyl self-assembling group (previous Chapter), [29] we observed interesting changes in absorption and emission spectra of NDIs in aromatic solvents. Spurred by this observation, herein we investigate NDIs in different aromatic solvents of varying electron donating capacity using both experiments and computation. Detailed studies indicate CT interaction between NDIs and aromatic solvents and its contribution to tunable emission. Further, the generality of the CT formation is confirmed by studies of other derivatives of NDI.

1 and **2** (Figure 7.1a) have been studied in detail in the previous chapter and are shown to form pre-associated excimers in their self-assembled state. [29] Both molecules are soluble in a variety of aromatic solvents and their emission maximum is located between 440 nm (toluene) to 530 nm (mesitylene) (Figure 7.1b). The present study considers those NDIs without any bay substitution.

7.2 Results and discussion

7.2.1 Interaction of 1 and 2 with aromatic solvents

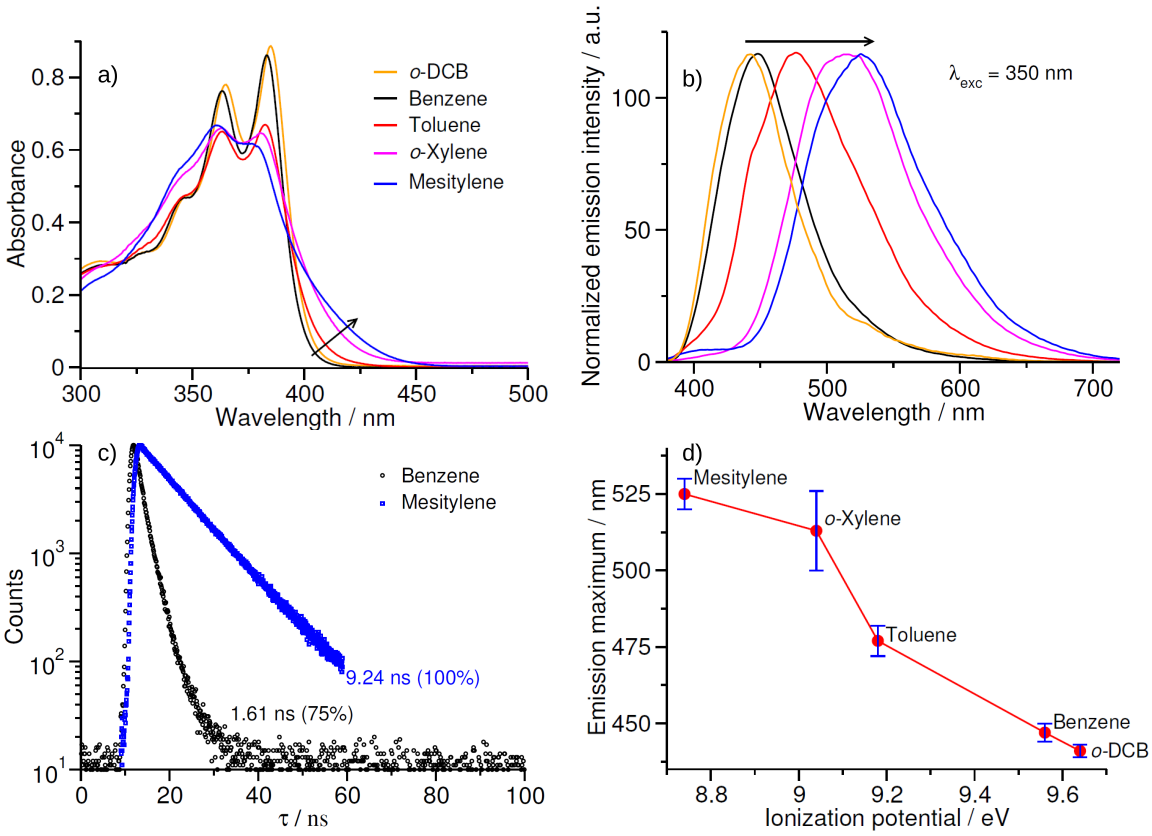

Figure 7.2: a) and b) UV/vis and fluorescence spectra of **1** (c = 5×10^{-5} M) in different aromatic solvents, respectively. Arrows indicate spectral changes from *o*-DCB to mesitylene. c) TCSPC decay profiles of **1** in benzene ($\lambda_{monitored}$ = 445 nm) and mesitylene ($\lambda_{monitored}$ = 528 nm) for an excitation at 380 nm (c = 5×10^{-5} M). d) A plot of emission maximum (obtained from b)) versus the ionization potential [30] of aromatic solvent molecules. Error bars correspond to the spread in the emission maxima.

The absorption spectrum of **1** shows a gradual evolution of a broad band between 400-450 nm, correlated with an increase in the electron donating capacity of aromatic solvent (from benzene to mesitylene) (Figure 7.2a). Interestingly, the emission spectra show structureless bands, which red-shifts on moving from benzene to mesitylene (440 nm to 530 nm), resulting in fluorescence from blue to greenish-yellow (Figure 7.2b and Figure 7.1b). Time-Correlated Single Photon Counting (TCSPC) experiments conducted on solutions of **1** in toluene and mesitylene showed life-times of 1.61 ns (75%) and 9.25 ns (100%) (Figure 7.2c). The excited state complex of

1 with mesitylene is thus significantly more stable than that with benzene. Similar UV/vis absorption and emission changes were observed for **2** in different aromatic solvents.

Earlier reports in literature attributed similar spectral features to the formation of exciplex [26] or excimer [25] between the solute and aromatic molecules. However, a recent report [31] in which aromatic guest molecules are confined in a metal-organic framework composed of NDI as ligands suggests that the complex can possess significant charge-transfer characteristics in addition to the exciplex contribution and it is hard to distinguish them. Since most studies of NDIs are in solution, it is important to understand the nature of interaction between NDIs and aromatic molecules in solution state. The absorption maximum of a CT complex varies linearly with the ionizaion potential of donor. [32, 33] Since the changes in emission spectrum are more pronounced than in the absorption, a plot of emission maximum versus ionization potential of the solvent was examined. The linear variation (Figure 7.2d) indicates that the emission has a major contribution from charge-transfer complexation. However, the observed changes in UV/vis absorption and emission spectra (Figure 7.2a and b) can also arise from aggregtion of **1** or exciplex (excited-state complex) formation. Thus, in the next section we have performed detailed photophysical studies to understand the same.

7.2.2 Role of aggregation

Concentration-dependent UV/vis absorption and emission spectra of **1** in toluene show minimal changes at even 3.3×10^{-6} M (Figure 7.3a and b). Also, the excitation spectrum of **1** in toluene (monitored at 540 nm) matches well with the absorption spectrum, indicating that the emission is arising from the ground-state complex (Figure 7.3c). CD spectra of **1** in all the aromatic solvents show no Cotton effect, indicating the absence of inter-chromophoric interactions in these solvents (Figure 7.3d).

Temperature-dependent UV/vis absorption and fluorescence spectra of **2** in mesitylene show minimal changes with increase in temperature (Figure 7.4). Although the emission intensity decrease with increase in temperature, monomeric emission (at 410 nm) does not increase. This observation suggests that the UV/vis absorption and fluorescence changes are not due to aggregation.

Further ^{1}H-NMR spectra of **2** in deuterated aromatic solvents shows a) sharp singlet for NDI protons even at 2.5 mM concentrations and b) an upfield shift of $\approx$0.5 δppm from chloroform-D to toluene-D_8 (FIgure 7.5). The observed magnitude

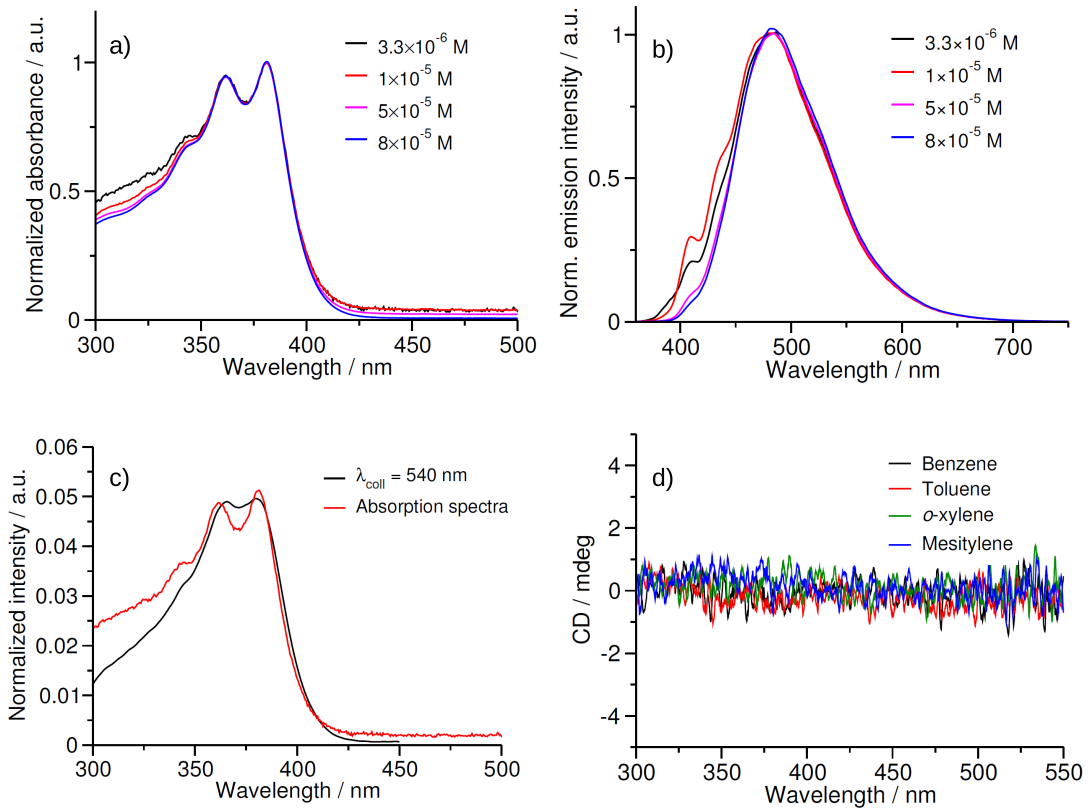

Figure 7.3: a) and b) Normalized UV/vis absorption and emission spectra (λ_{exc} = 350 nm) respectively of **1** in toluene at different concentrations. c) Excitation spectra of **1** in toluene overlapped with the corresponding UV/vis absorption spectra (c = 3.3×10^{-6} M). d) CD spectra of **1** in different aromatic solvents (c = 5×10^{-5} M).

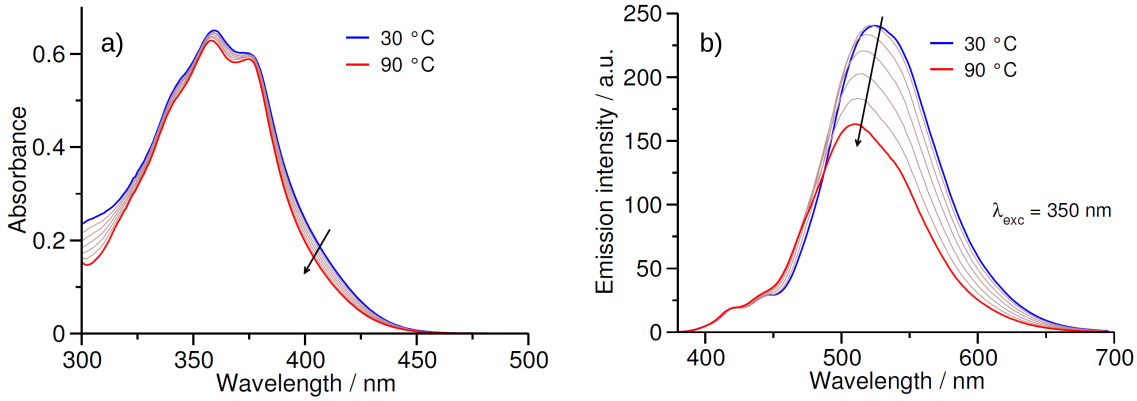

Figure 7.4: Temperature-dependent UV/Vis absorption (a) and emission spectra (b) of **2** in mesitylene at every 10 °C (c = 5×10^{-5} M). Arrows indicates spectral changes with increase in temperature.

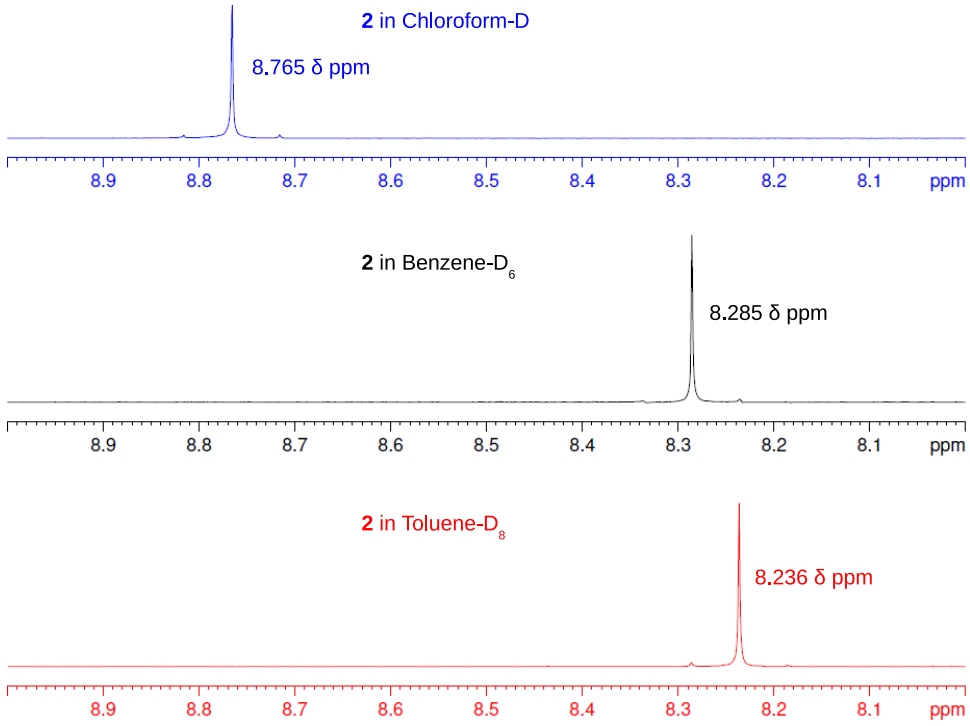

Figure 7.5: Partial ^{1}H-NMR spectra of **2** in different deuterated solvents (c = 2.5×10^{-3} M)

of chemical shift cannot be account for by the change in solvent polarity, suggesting the interaction between **2** and aromatic solvent is responsible for the observed chemical shift. Thus we can conclude that there is no inter-chromophoric interaction (aggregation) between **1** or **2** in aromatic solvents and **1**/**2** forms ground-state complexes with aromatic solvents. In addition, the ground-state UV/vis absorption changes rule out exciplex formation.

7.2.3 Effect of imide substitution

To examine the effect of functional groups on the CT formation of NDIs with aromatic solvent molecules, other derivatives of NDI, containing dodecyl or tetraethylene glycol groups on the imide nitrogen of NDI were studied. Spectral properties of these systems had earlier been reported. [34, 35] Both **NDI-Amph** [34] and **NDI-Bolaamph** [35] showed absorption and emission spectra similar to that of **1** and **2** with comparable emission maxima (in Mesitylene; **NDI-Amph** = 520 nm and **1** = 525 nm) (Figure 7.6 and 7.7). Further, selective excitation of the CT band (λ_{exc} > 400 nm) show emission spectra identical to that obtained from excitation at 350 nm (Figure 7.6 and 7.7).

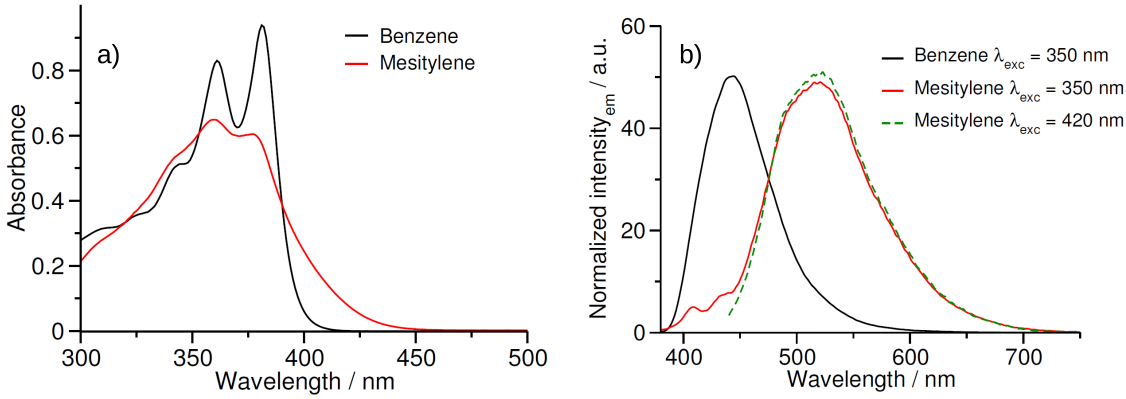

Figure 7.6: a) and b) UV/Vis absorption and emission spectra respectively of **NDI-Amph** (c = 5×10^{-5} M).

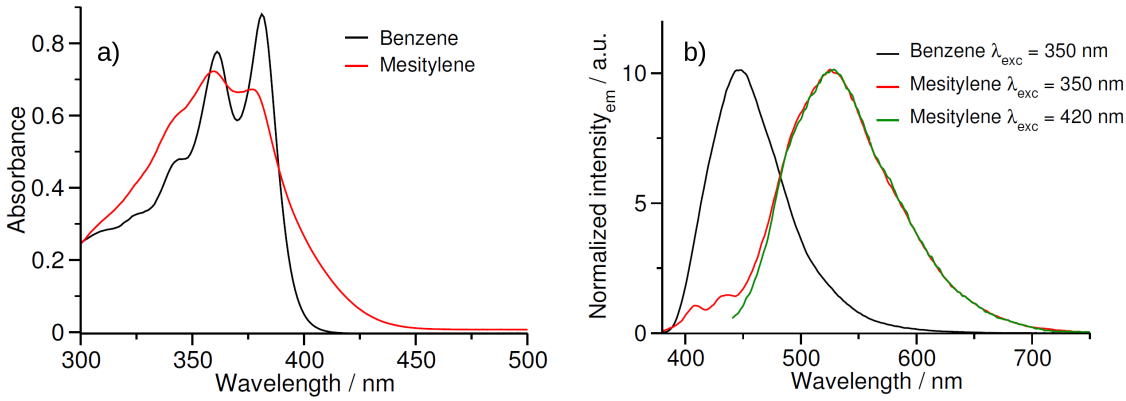

Figure 7.7: a) and b) UV/Vis absorption and emission spectra respectively of **NDI-Bolaamph** (c = 5×10^{-5} M).

Molecule	Fluorescence quantum yield (Φ_f) in				
	o-DCB	Benzene	Toluene	*o*-Xylene	Mesitylene
2	0.0067	0.0628	0.0222	0.0208	0.0100
NDI-Bolaamph	0.0040	0.0153	0.0137	0.0127	0.0072
NDI-Amph	0.0044	0.0135	0.0129	0.0138	0.0077

Table 7.1: Fluorescence quantum yield (Φ_f) of different molecules in various aromatic solvents (c = 5×10^{-5} M)

Generally the fluorescence intensity quenches with the formation of charges-transfer complexes [14] and the same is observed for various derivatives (Table 7.1). The observed decrease in Φ_f from benzene to mesitylene (Table 7.1) points to stronger CT of NDIs with mesitylene leading to lower Φ_f.

7.2.4 Computational studies

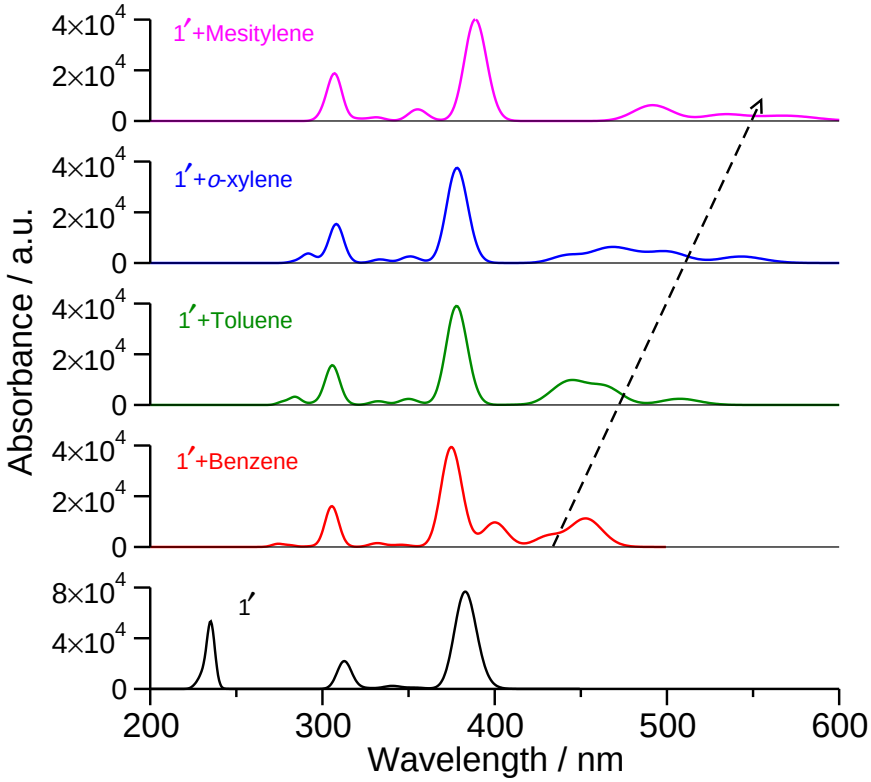

Figure 7.8: Calculated vertical transitions of **1′**-solvent complexes using BLYP-D3/DZVP//B3LYP/6-31+G(d,p) level of theory (fwhm = 1000 cm^{-1}). Four aromatic molecules were considered in each complex. The black dashed arrow indicates the changes in the CT transition with increasing electron donating capacity of the solvent molecule. [36]

Computational studies were undertaken to understand the origin of changes in ground-state absorption spectra observed in different aromatic solvents. Model compound (**1′**, derived from **1** by replacing the cholesterol group with methyl for computational tractability) and its complex with four aromatic molecules were geometry optimized in gas phase at BLYP-D3/DZVP level of theory. [37] Time-dependent Density Functional Theory (TD-DFT) calculations (at B3LYP/6-31+G(d,p) level of theory) were performed on the optimized geometries to obtain the characteristics of the vertical absorption transitions. The calculated position of absorption maximum of the **1′** at 383 nm is in agreement with experimental value of the monomeric form of **1** or **2** (379 nm). Complexes of NDI with different aromatic solvents showed transitions at higher wavelength (>400 nm) of low oscillator strength, without much change in the position of absorption maximum (383 nm) (Figure 7.8).

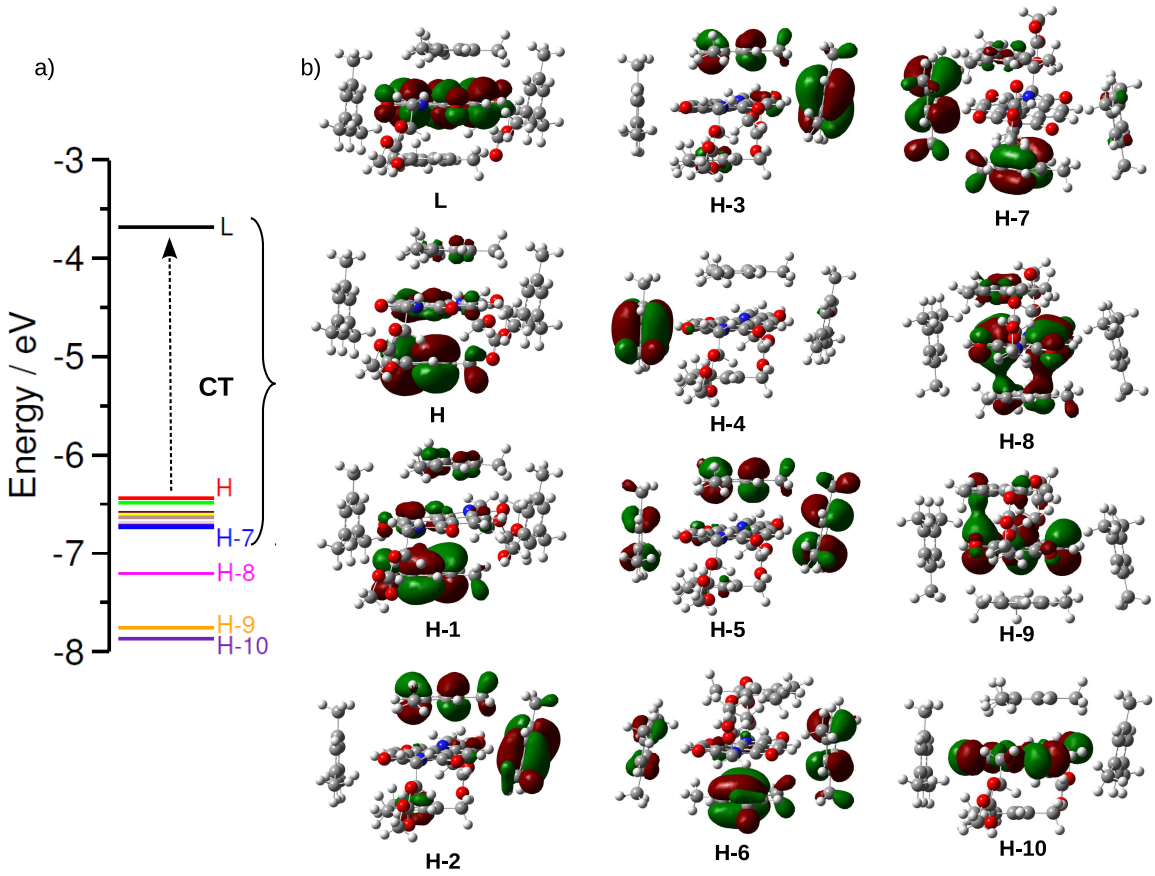

Figure 7.9: a) Computed energy level diagram of **1′**+four molecules of mesitylene. b) Frontier molecular orbtials of **1′**+four molecules of mesitylene. H and L stand for HOMO and LUMO respectively. Isovalue of 0.02 e(bhor)$^{-3}$ was used for molecular orbital plots.

Visualization of the frontier molecular orbtials of a complex of **1′** and four mesitylene molecules shows higher wavelength (> 400nm) transitions arising from HOMO to LUMO and HOMO-n (n=1-7) to LUMO (Figure 7.9). HOMO and HOMO-n (n=1-7) molecular orbitals are delocalized over the mesitylene molecules and the LUMO on NDI core of **1′**. This observation is a clear indication of a ground-state CT from the mesitylene molecules to the **1′**. Similar behaviour was observed for other aromatic solvents as well. Further, the lowest energy band corresponding to CT transition, shifts to lower energy as the electron donating capacity of the solvent increases (from benzene to mesitylene) (Figure 7.8). The calculated wavelength of CT band does not quantitatively match the experimentally observed tailing of bands (CT band) in different solvents, but it qualitatively captures the nature of interaction leading to such effects. Thus, the present optimized geometries should be considered as a model to explain the observed phenomena rather than as an

actual representation of the solution state. NDI derivatives in solution can interact with more than four solvent molecules. Despite the limited number of solvents molecules employed here, the present calculations clearly bring out the CT nature of interaction between NDI derivatives and aromatic molecules.

7.3 Conclusions

In conlusion, bay unsubtituted NDIs have been shown to form emissive ground-state charge-transfer complexes with various aromatic solvents using both experiments and computation. Results on various NDI derivatives presented here and those observed by other groups [28] suggest that the propensity of CT complexation is not affected by the substituents on the imide nitrogens in NDI. [38] Thus care must be taken while using aromatic solvents in studies of self-assembly of NDIs. Since many of the NDI derivatives studied in literature possess bay substitution, [39–41] similar studies on such derivatives in aromatic solvents will aid in the proper choice of solvent for their processing towards organic electronic devices.

7.4 Experimental details

Electronic absorption spectra were recorded on a Perkin Elmer Lambda 900 UV-Vis-NIR spectrometer. Emission spectra were recorded on a Perkin Elmer LS 55 luminescence spectrometer. Temperature-dependent UV/Vis absorption and emission studies were performed using a Perkin Elmer LS 55 with a PTP-1 and Lambda 750 attached to PTP-1+1 Peltier system respectively. Jasco J-815 spectrometer was used to measure Circular Dichroism (CD) spectra with a standard sensitivity (100 mdeg), scan rate of 100 nm/minute, bandwidth value of 1 and single accumulation for each spectra. Time-Correlated Single Photon Counting (TCSPC) experiments were performed using FLSP 920 spectrometer, Edinburgh Instrument. EPLED source of 380 nm was used for excitation. Unless otherwise mentioned all the optical studies were performed in 10 mm path length cuvettes. Fluorescence quantum yield was calculated using Quinine sulphate dihydrate as the standard with a quantum yield of 0.577 at an excitation of 350 nm using the standard formula. [42] The integrated area was calculated for all spectra from 370 nm to 650 nm. The solvent polarity parameter $E_T(30)$ [43] was used to analyze the influence of solvent polarity on the observed fluorescence spectral changes. ^{1}H-NMR spectra were recorded on a Bruker AVANCE-400 spectrometer operating at 400 MHz at 27 °C.

7.5 Computational details

Time-Dependent Density-Functional Theory (TD-DFT) studies were performed to understand the origin of changes observed in the experimental UV/vis absorption spectra of **1** and **2** in different aromatic solvents. Geometry optimization of model compound (**1′**; obtained by replacing cholesterol in **1** by methyl groups) and the complex of **1′** with four molecules of different aromatic molecules was carried out using periodic density functional theory and the QUICKSTEP module [44] as implemented in CP2K package. [45] Combined atom centered and plane wave basis sets were used to carry out geometry optimization. BLYP exchange-correlation functional, [46, 47] double-zeta single polarized basis set [48] and Grimme's empirical dispersion correction (D3) [49] were used for geometry optimization. Goedecker-Teter-Hutter pseudopotential [50, 51] to describe the effect of core electrons on the nuclei and an energy cut-off of 280 Ry was used. A cubical box length of 32 Å was used for all the systems. LBFGS optimizer [52] and Wavelet poission solver was used for all geometry optimizations. Vertical transitions were calculated on optimized geometries at B3LYP/6-31+G(d,p) level of theory for root = 1 and nstates = 24 using Gaussian-09. [53] The molecular orbitals were visualized suing GaussView 5.0. [54]

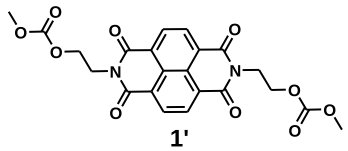

1'

Bibliography

[1] Stolte, M.; Gsanger, M.; Hofmockel, R.; Suraru, S.-L.; Würthner, F. *Phys. Chem. Chem. Phys.* **2012**, *14*, 14181–14185.

[2] Zhan, X.; Facchetti, A.; Barlow, S.; Marks, T. J.; Ratner, M. A.; Wasielewski, M. R.; Marder, S. R. *Adv. Mater.* **2011**, *23*, 268–284.

[3] Sommer, M. *J. Mater. Chem. C* **2014**, *2*, 3088–3098.

[4] Katz, H. E.; Lovinger, A. J.; Johnson, J.; Kloc, C.; Siegrist, T.; Li, W.; Lin, Y.-Y.; Dodabalapur, A. *Nature* **2000**, *404*, 478–481.

[5] Singh, T.; Erten, S.; Günes, S.; Zafer, C.; Turkmen, G.; Kuban, B.; Teoman, Y.; Sariciftci, N.; Icli, S. *Org. Electron.* **2006**, *7*, 480 – 489.

[6] Laquindanum, J. G.; Katz, H. E.; Dodabalapur, A.; Lovinger, A. J. *J. Am. Chem. Soc.* **1996**, *118*, 11331–11332.

[7] Lee, Y.-L.; Hsu, H.-L.; Chen, S.-Y.; Yew, T.-R. *J. Phys. Chem. C* **2008**, *112*, 1694–1699.

[8] Bhosale, S. V.; Jani, C. H.; Langford, S. J. *Chem. Soc. Rev.* **2008**, *37*, 331–342.

[9] Bulheller, B. M.; Pantoş, G. D.; Sanders, J. K. M.; Hirst, J. D. *Phys. Chem. Chem. Phys.* **2009**, *11*, 6060–6065.

[10] Kumar, M.; Jonnalagadda, N.; George, S. J. *Chem. Commun.* **2012**, *48*, 10948–10950.

[11] Molla, M. R.; Ghosh, S. *Chem. Eur. J.* **2012**, *18*, 9860–9869.

[12] Shao, H.; Nguyen, T.; Romano, N. C.; Modarelli, D. A.; Parquette, J. R. *J. Am. Chem. Soc.* **2009**, *131*, 16374–16376.

[13] Ikkanda, B. A.; Samuel, S. A.; Iverson, B. L. *J. Org. Chem.* **2014**, *79*, 2029–2037.

[14] Gujrati, M. D.; Kumar, N. S. S.; Brown, A. S.; Captain, B.; Wilson, J. N. *Langmuir* **2011**, *27*, 6554–6558.

[15] Basak, S.; Nanda, J.; Banerjee, A. *Chem. Commun.* **2013**, *49*, 6891–6893.

[16] Hoeben, F. J. M.; Jonkheijm, P.; Meijer, E. W.; Schenning, A. P. H. J. *Chem. Rev.* **2005**, *105*, 1491–1546.

[17] Babu, S. S.; Praveen, V. K.; Ajayaghosh, A. *Chem. Rev.* **2014**, *114*, 1973–2129.

[18] Kartha, K. K.; Mukhopadhyay, R. D.; Ajayaghosh, A. *CHIMIA* **2013**, *67*, 51–63.

[19] Ajayakumar, M. R.; Mukhopadhyay, P. *Chem. Commun.* **2009**, 3702–3704.

[20] Gillissen, M. A. J.; Koenigs, M. M. E.; Spiering, J. J. H.; Vekemans, J. A. J. M.; Palmans, A. R. A.; Voets, I. K.; Meijer, E. W. *J. Am. Chem. Soc.* **2014**, *136*, 336–343.

[21] Flamigni, L.; Wyrostek, D.; Voloshchuk, R.; Gryko, D. T. *Phys. Chem. Chem. Phys.* **2010**, *12*, 474–483.

[22] Ponnuswamy, N.; Pantoş, G. D.; Smulders, M. M. J.; Sanders, J. K. M. *J. Am. Chem. Soc.* **2012**, *134*, 566–573.

[23] Rajaganesh, R.; Gopal, A.; Mohan Das, T.; Ajayaghosh, A. *Org. Lett.* **2012**, *14*, 748–751.

[24] Kolhe, N. B.; Devi, R. N.; Senanayak, S. P.; Jancy, B.; Narayan, K. S.; Asha, S. K. *J. Mater. Chem.* **2012**, *22*, 15235–15246.

[25] Bell, T. D. M.; Bhosale, S. V.; Forsyth, C. M.; Hayne, D.; Ghiggino, K. P.; Hutchison, J. A.; Jani, C. H.; Langford, S. J.; Lee, M. A.-P.; Woodward, C. P. *Chem. Commun.* **2010**, *46*, 4881–4883.

[26] Barros, T. C.; Brochsztain, S.; Toscano, V. G.; Filho, P. B.; Politi, M. J. *J. Photochem. Photobio. A* **1997**, *111*, 97 – 104.

[27] Takashima, Y.; Mart´inez-Mart´inez, V.; Furukawa, S.; Kondo, M.; Shimomura, S.; Uehara, H.; Nakahama, M.; Sugimoto, K.; Kitagawa, S. *Nat. Commun.* **2011**, *2*, 168.

[28] S. Basak, S. Bhattacharya, A. Datta, and A. Banerjee, *Chem. Eur. J.*, 2014, doi:10.1002/chem.201303889.

[29] Kulkarni, C.; George, S. J. *Chem. Eur. J.* **2014**, *20*, 4537–4541.

[30] Crable, G. F.; Kearns, G. L. *J. Phys. Chem.* **1962**, *66*, 436–439.

[31] Mart´inez-Mart´inez, V.; Furukawa, S.; Takashima, Y.; López Arbeloa, I.; Kitagawa, S. *J. Phys. Chem. C* **2012**, *116*, 26084–26090.

[32] Foster, R. *Tetrahedron* **1960**, *10*, 96 – 101.

[33] Slifkin, M. A. *Nature* **1963**, *200*, 766–767.

[34] Kumar, M.; George, S. J. *Chem. Eur. J.* **2011**, *17*, 11102–11106.

[35] Kumar, M.; George, S. J. *Nanoscale* **2011**, *3*, 2130–2133.

[36] The absence of peak at 240 nm in **1′**+solvent complexes could be due to the same number of states (24) used for the absorption spectra calculation of both pristine **1′** and **1′**+complexes. Use of more number of states for the complex can capture the low energy transition.

[37] Since the dielectric constant of the choosen aromatic molecules is very similar (2.3 for benzene and 2.4 for mesitylene) solvation models will not be able to capture the effect of solvents.

[38] This is provided the substituent on the imide nitrogens do not change the electronic properties of the NDI core through electron transfer or any such processes.

[39] Thalacker, C.; Röger, C.; Würthner, F. *J. Org. Chem.* **2006**, *71*, 8098–8105.

[40] Bell, T.; Yap, S.; Jani, C.; Bhosale, S.; Hofkens, J.; DeSchryver, F.; Langford, S.; Ghiggino, K. *Chem. Asian J.* **2009**, *4*, 1542–1550.

[41] Bhosale, S. V.; Bhosale, S. V.; Bhargava, S. K. *Org. Biomol. Chem.* **2012**, *10*, 6455–6468.

[42] Lakowicz, J. R. *Principles of Fluorescence Spectroscopy*, 3rd ed.; Springer, 2006.

[43] Reichardt, C. *Solvents and Solvent Effects in Organic Chemistry*, 3rd ed.; WILEY-VCH Verlag, 2003.

[44] VandeVondele, J.; Krack, M.; Mohamed, F.; Parrinello, M.; Chassaing, T.; Hutter, J. *Comp. Phys. Commun.* **2005**, *167*, 103 – 128.

[45] Hutter, J.; Iannuzzi, M.; Schiffmann, F.; VandeVondele, J. *Wiley Interdiscip. Rev. Comput. Mol. Sci.* **2014**, *4*, 15–25.

[46] Becke, A. D. *J. Chem. Phys.* **1993**, *98*, 5648–5652.

[47] Lee, C.; Yang, W.; Parr, R. G. *Phys. Rev. B* **1988**, *37*, 785–789.

[48] VandeVondele, J.; Hutter, J. *J. Chem. Phys.* **2007**, *127*, 114105–114114.

[49] Grimme, S.; Antony, J.; Ehrlich, S.; Krieg, H. *J. Chem. Phys.* **2010**, *132*, 154104.

[50] Hartwigsen, C.; Goedecker, S.; Hutter, J. *Phys. Rev. B* **1998**, *58*, 3641–3662.

[51] Goedecker, S.; Teter, M.; Hutter, J. *Phys. Rev. B* **1996**, *54*, 1703–1710.

[52] Byrd, R.; Lu, P.; Nocedal, J.; Zhu, C. *J. Sci. Comput.* **1995**, *16*, 1190–1208.

[53] Frisch, M. J. et al. Gaussian 09 Revision D.01. Gaussian Inc. Wallingford CT 2009.

[54] Dennington, R.; Keith, T.; Millam, J. GaussView; Version 5.0. Semichem Inc.: Shawnee Mission, KS, 2009.

Chapter 8

Self-Assembly of Coronene Bisimides: Mechanistic Insight and Chiral Amplification

8.1 Introduction

The self-assembly of π-conjugated molecules, through various noncovalent interactions, such as hydrogen bonding, π-stacking, and van der Waals interactions to achieve functional 1D nanostructures has been an active area of research. [1–11] The immense interest in this field is due to the tunability of noncovalent interactions that enable better control over the resulting nanostructure, thereby improving their optoelectronic functionality. [12, 13] Varied classes of both n- and p-type chromophores, such as triphenylenes, [14–16] perylene bisimides, [17–22] naphthalene bisimides, [23–30] oligo(para-phenylenevinylenes), [31–36] porphyrins, [37–47] and so forth, have been extensively studied for self-assembly and potential applications. Coronene bisimides (CBIs) bearing six-membered imide rings are another class of n-type chromophore, and they can be obtained by the core expansion of perylene bisimides. [48–53] Another class of CBI that possesses five-membered imide rings instead of six-membered rings have been synthesized from a two-fold benzogenic Diels-Alder reaction that starts from perylene. [54–56] CBIs were mainly studied

Reprinted with permission from "Self-Assembly of Coronene Bisimides: Mechanistic Insight and Chiral Amplification" *Chem. Eur. J.* **2013**, *19*, 11270-11278. Copyright 2013, Wiley-VCH. http://onlinelibrary.wiley.com/doi/10.1002/chem.201301251/abstract

for liquid-crystalline properties. [57–59] A recent report has used dithienocoronene bisimide as acceptors with thiophenes as donors to form copolymers, thus showing promising thin-film-transistor properties. [60] However, the self-assembly of coronene imide derivatives in solution has seldom been reported. [55, 56]

Chiral amplification has been studied quite extensively in both macromolecular (polymer) and supramolecular assemblies by using the principles of sergeant and soldiers and majority rules. [61–63] In the sergeant-and-soldiers experiment, a small amount of a chiral derivative dictates the handedness of a pool of achiral derivatives; [64, 65] however, in majority rules, a slight excess of one enantiomer guides the chirality of the complete assembly toward itself. [64, 65] In synthetic supramolecular polymers, these two modes of chiral amplification are observed for systems mainly following a cooperative mechanism. [66–70] An exception to the above is benzene-1,3,5- tricarboxamide (BTA) substituted with 3,3′-diamino-2,2′-bipyridine groups, which self-assembles in an isodesmic manner and exhibits the principle of sergeant and soldiers. [71, 72] Also these BTA derivatives have been shown to display the phenomenon of majority rules. [67] The compounds studied herein belong to a rare class of molecule that follows an isodesmic mechanism while still exhibiting chiral amplification.

In the previous chapters, we have seen the effect of long-range interactions such as dipole-moment on the mechanism of self-assembly. Here, we make use of π-stacking and van der Waals interaction as the driving force for supramolecular polymerization and examine their effect on the mechanism of self-assembly. CBIs possessing large π-surface substituted with 3,4,5-trialkoxy gallic wedges are studied in detailed using various optical spectroscopy and microscopy techniques. Chiroptical probing and microscopic studies of these CBI derivatives revealed that they self-assemble into 1D nanostructures in an isodesmic manner. Furthermore, we observe chiral amplification through the sergeant and soldiers experiment in the co-assemblies of these two derivatives.

8.2 Results and Discussion

8.2.1 Molecules under study

The molecules under study contain 3,4,5-trialkoxyphenyl wedges attached at the imide positions of CBI, with the following alkyl chains: dodecyl and (S)-(-)-3,7-dimethyloctyl in **CBI-GACH** and **CBI-GCH**; respectively (Figure 8.1). **CBI-GCH** and **CBI-GACH** were synthesized by condensation reaction between coronene dianhydride and corresponding aminobenzenes. Both the molecules were completely characterized by ^{1}H and ^{13}C NMR spectroscopy, matrix-assisted laser desorption/ionization (MALDI) mass-spectrometry and high-resolution mass spectrometery (HRMS) (see experimental section for details).

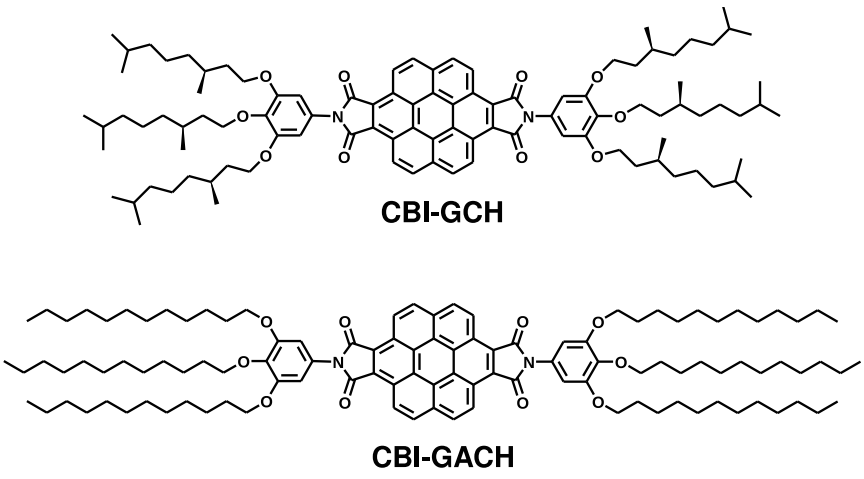

Figure 8.1: Coronene bisimide molecules **CBI-GCH** and **CBI-GACH** under study.

8.2.2 Self-assembly of CBI-GCH

UV/vis absorption spectra of **CBI-GCH** in chloroform (c = 1×10^{-5} M) show characteristic absorption features of the CBI chromophore (Figure 8.2a) with the maximum at λ_{max} = 346 nm ($\epsilon = 1.0\times10^{5}$ Lmol^{-1}cm^{-1}), accompanied by three vibronic features between λ = 425 and 500 nm. These spectral features indicate a molecularly dissolved state in chloroform. [55] On the other hand, **CBI-GCH** in methylcyclohexane (MCH) shows a broad hypsochromically shifted absorption maximum at λ_{max} = 325 nm, along with the loss of vibronic features and the emergence of a new broad band between λ = 500 and 520 nm. These features indicate the presence of π-stacking in MCH; leading to H-type excitonically coupled aggregates. Although

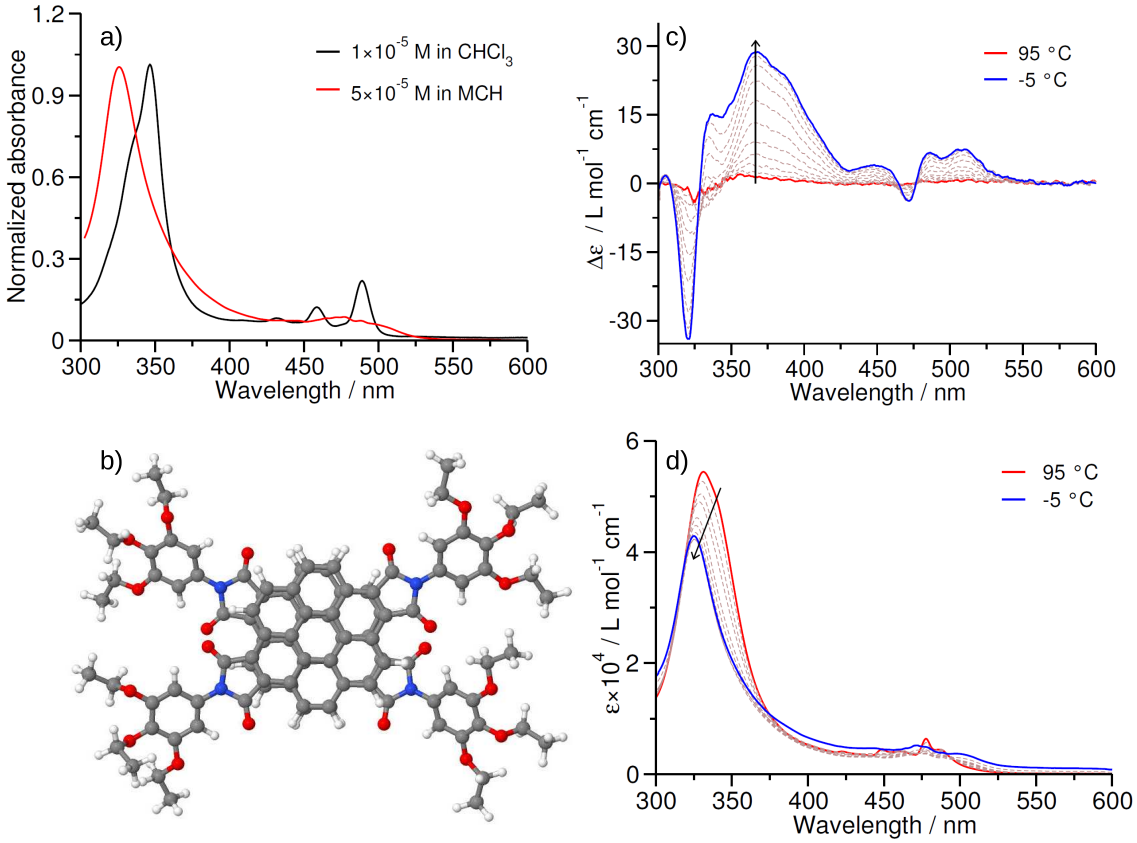

Figure 8.2: Self-assembly of **CBI-GCH**. a) Normalized UV/vis spectra in two different solvents at 20 °C. b) Top view of the optimized geometry of the CBI dimer (with 3,4,5-triethoxyphenyl groups) by using DFT-based calculations. Carbon: gray, hydrogen: white, oxygen: red and nitrogen: blue. Temperature-dependent c) CD and d) UV/vis spectra (c = 5×10^{-5} M in MCH, 1 cm cuvette). The arrows indicate the spectral changes with decrease in temperature.

fluorescence spectroscopy can offer valuable insight into the type of aggregate, the CBI derivatives under study are non-fluorescent, even in their molecularly dissolved state in chloroform, probably due to the presence of phenoxy groups in the imide region. Similar effects were observed for perylene bisimides containing phenoxy wedges and were attributed to the electron transfer from the phenoxy groups to the perylene bisimide core. [73, 74] Because **CBI-GCH** assembles in an H-type aggregate, the angle between the transition dipole moments of two consecutive monomers should be greater than 54.7°. [75–77] To understand the possible packing in the aggregates, computational studies were carried out on a dimer. This reveals a rotational angle of approximately 64° (without much sliding) in the dimer (Figure 8.2b), thus ascertaining the formation of H-type aggregates.

The presence of chiral centers on the phenoxy wedge aids the organization of the

1D assemblies into a preferred helical direction. This helical bias in molecular organization can be monitored by means of circular dichroism (CD) spectroscopy. The CD spectra (Figure 8.2c) of **CBI-GCH** in MCH (c = 5×10^{-5} M) shows four clear zero crossings at λ = 476, 465, 327, and 307 nm with bisignated exciton coupling in both the vibronic and π-π^* regions (λ = 425-500 and 300-375 nm, respectively). The CD spectra show a positive followed by negative Cotton effect in both the regions when viewed from the region of higher wavelength to the lower wavelength. Also, the wavelength that corresponds to two major zero crossings in the CD spectra match well with the absorption maxima (λ_{max} = 327 and 476 nm), thus indicating that the type of excitonic coupling observed by using both spectroscopic techniques (i.e., UV/vis and CD) is similar. Thus, we can conclude that the molecular chirality present in the peripheral side chains of **CBI-GCH** has been transferred to the supramolecular level when self-assembled in MCH. [78]

The molar ellipticity $\Delta\epsilon$ or magnitude of CD effect (mdeg) decreases with an increase in temperature and almost vanishes at temperatures above 95 °C, thus indicating the absence of excitonically coupled helical aggregates at high temperatures (Figure 8.2c). Correspondingly, the molar extinction coefficient (ϵ) increases, and the absorption maxima red-shifts with the appearance of vibronic features as the temperature is increased (Figure 8.2d). These absorption changes reiterate that the molecules exist in their monomeric form at high temperature. Although the molecularly dissolved state is observed in chloroform at room temperature and in MCH at high temperatures, the absorption spectra in these two states are not identical (λ_{max} = 346 and 331 nm in $CHCl_3$ at 20 °C and MCH at 95 °C). This distinction is due to the difference in the polarity of the two solvents (ϵ_r = 2.02 and 4.81 for MCH and $CHCl_3$, respectively), or in other words solvatochromism.

8.2.3 Mechanism of self-assembly of CBI-GCH

Having studied the aggregation behavior of **CBI-GCH**; we examined the mechanism of self-assembly. Solutions of **CBI-GCH** in MCH at various concentrations were heated to 371 K to obtain a molecularly dissolved state and then were slowly cooled (2 K/min) to form a supramolecular polymer, while monitoring the CD effect at λ = 322 nm. No hysteresis in the CD effect was observed between the heating and cooling cycles (c = 3×10^{-5} M) with a temperature gradient of 2 K/min. This suggests that the assembly process is under thermodynamic control when cooled at a rate of 2 K/min. The normalized cooling curves and the corresponding fits to the temperature- dependent isodesmic model [79] are shown in Figure 8.3. This

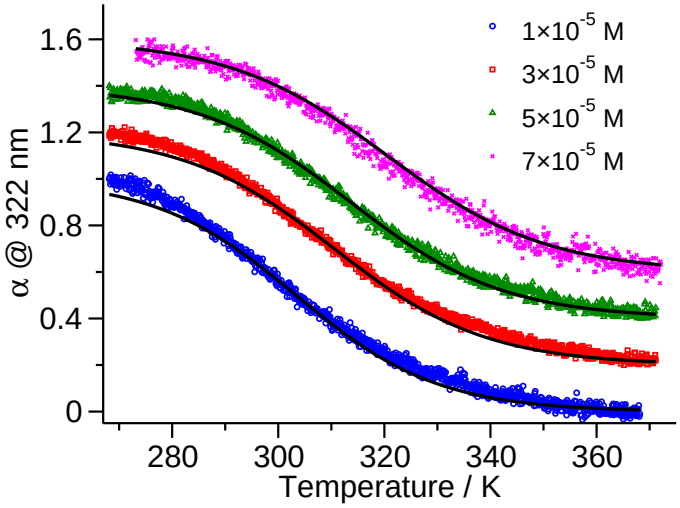

Figure 8.3: Mechanism of self-assembly of **CBI-GCH**. Fraction of aggregates (α) monitored at λ = 322 nm versus temperature at four different concentrations in MCH, with a cooling rate of 2 K/min. The solid line for each curve shows the fit to the temperature-dependent isodesmic model. Each curve is displaced vertically by 0.20 from each other for clarity.

model described the cooling curves fairly accurately. Thus,**CBI-GCH** follows an isodesmic pathway.

In chapter 3 we had hypothesized that the lack of long-range interactions leads to an isodesmic mechanism. [80] Since the molecule under consideration has mainly a central π-surface and van der Waals interactions of the peripheral side chains, there does not seem to be any moiety that can produce long-range interactions. One possibility is the interaction between the phenoxy wedges through weak hydrogen bonds, but since the molecules are rotated by more than 54.7° in the dimer due to H-type aggregation (as seen from Figure 8.2b), this interaction seems improbable. Thus **CBI-GCH** provides an example of a system which self-assembles mainly through π-stacking and van der Waals interactions, and thus self-assembles via an isodesmic mechanism.

By using the temperature-dependent isodesmic model, [79] various thermodynamic parameters that govern supramolecular polymerization are obtained (Table 8.1).

The equilibrium constant (K_e) of polymerization was calculated at 298.15 K from the relation, $K_e = [DP_N \times (DP_N\text{-}1)]/c$ where c is the total concentration of the solution. The van't Hoff plot ($\ln(K_e)$ vs. 1/T) at various concentrations were obtained, and the entropy of polymerization was calculated (Figure 8.4). The average values

Concentration (M)	Melting temperature, T_m (K)	Enthalpy of polymerization, ΔH (kJ/mol)	Number-average degree of polymerization, DP_N
1×10^{-5}	303.35	-63.20	1.54
3×10^{-5}	310.55	-61.84	1.90
5×10^{-5}	313.65	-62.50	2.00
7×10^{-5}	320.55	-62.85	2.16

Table 8.1: Thermodynamic parameters for the self-assembly of **CBI-GCH** in MCH. DP_N was calculated at 298.15 K.

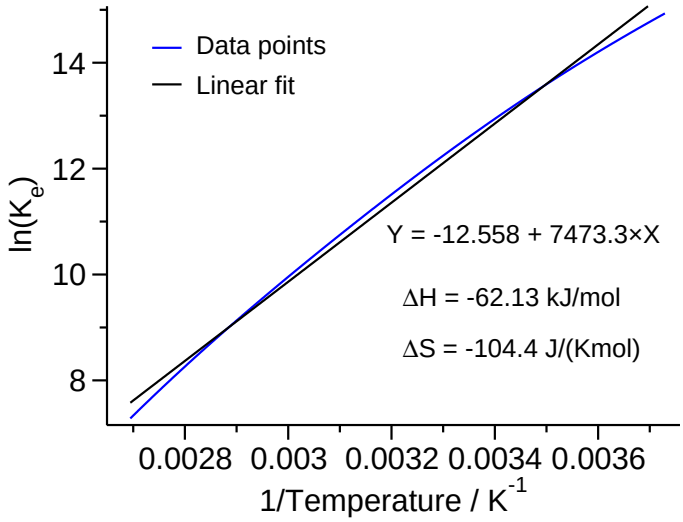

Figure 8.4: van't Hoff plot for **CBI-GCH** in MCH (c = 5×10^{-5} M).

of enthalpy, entropy, and the equilibrium constant of polymerization are ΔH = -62.6 kJ/mol, ΔS = -104.4 J/(mol·K) and $K_e = 5.4\times10^4$ M^{-1} respectively.

8.2.4 Morphological studies of CBI-GCH

To obtain insight into the morphology of the **CBI-GCH** assembly in MCH (c = 5×10^{-5} M), Field emission scanning electron microscopy (FE-SEM), atomic force microscopy (AFM), dynamic light scattering (DLS) and XRD studies were performed.

FE-SEM images recorded on a glass substrate (Figure 8.5a) show the presence of 1D fibers of several microns in length. AFM imaging was performed by drop casting a solution of **CBI-GCH** in MCH on a freshly cleaved mica surface showed uniform distribution of the 1D fibers (Figure 8.5b). A detailed height-profile analysis of the fibers showed an average height of 14 nm. The height of an isolated individual fiber was around 5 nm (inset of Figure 8.5c), which matches well with

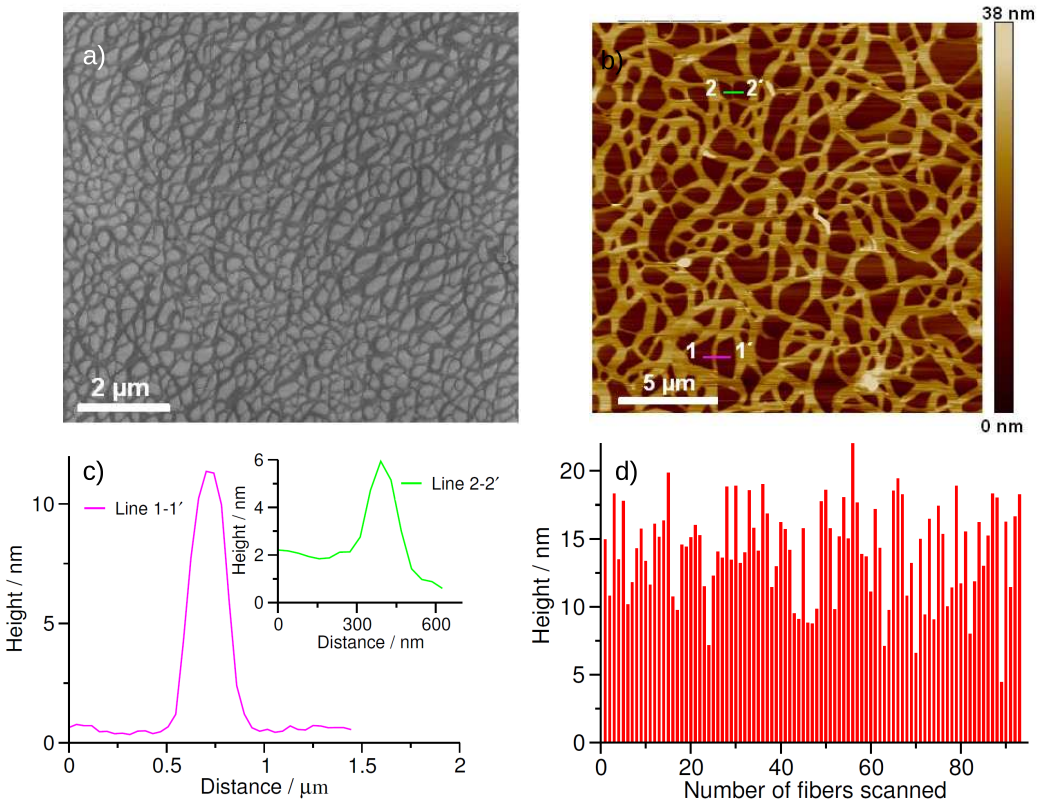

Figure 8.5: Morphological studies of **CBI-GCH** (c = 5×10^{-5} M in MCH). a) FESEM image of the film recorded on a glass substrate in the low-vacuum mode. b) AFM height image of a film obtained by drop-casting a solution of in MCH on a freshly cleaved mica surface. c) Cross-sectional analysis along the lines shown in (b). The inset shows the presence of individual fibers with a typical height of 4 nm. d) Histogram of fiber heights obtained from the analysis of four or five independent images with areas of 20×20 μm and 10×10 μm.

the dimension of **CBI-GCH** (i.e., 4.4 nm), thus indicating that these fibers consist of π-stacks of individual molecules. These individual fibers further come together to form larger aggregates, which is evident from the increase in the height of the larger bundles. The height analysis of the fibers in four or five independent images gives a histogram shown in Figure 8.5d. This histogram indicates that the fibers are present throughout the sample and provides a realistic representation of the fiber heights (Figure 8.5d).

Although **CBI-GCH** follows an isodesmic mechanism of supramolecular polymerization, long fibers were observed in morphological studies, which could be partly due to the drying effect on the substrate. DLS experiments were performed to study the formation of aggregates in solution. DLS (c = 5×10^{-5} M) shows an apparent

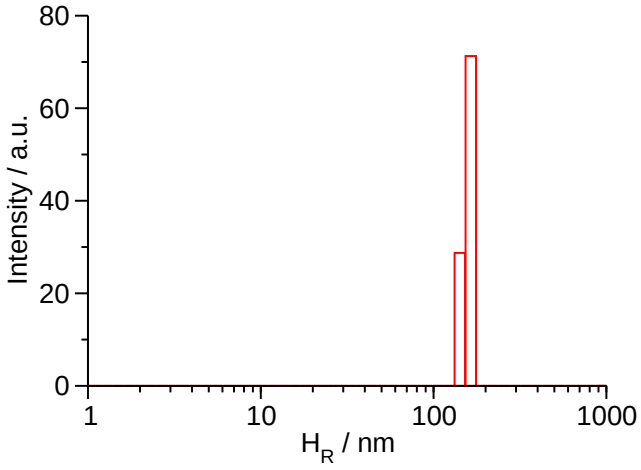

Figure 8.6: Dynamic Light Scattering (DLS) of **CBI-GCH** in MCH (c = 5×10^{-5} M).

hydrodynamic radii of 100-200 nm (Figure 8.6), which suggests that the aggregates are indeed present in the solution state as well. Thus, **CBI-GCH** forms individual π-stacked aggregates that lead to fibers, which further aggregate through van der Waals interactions of the side chains to form fiber bundles in solution.

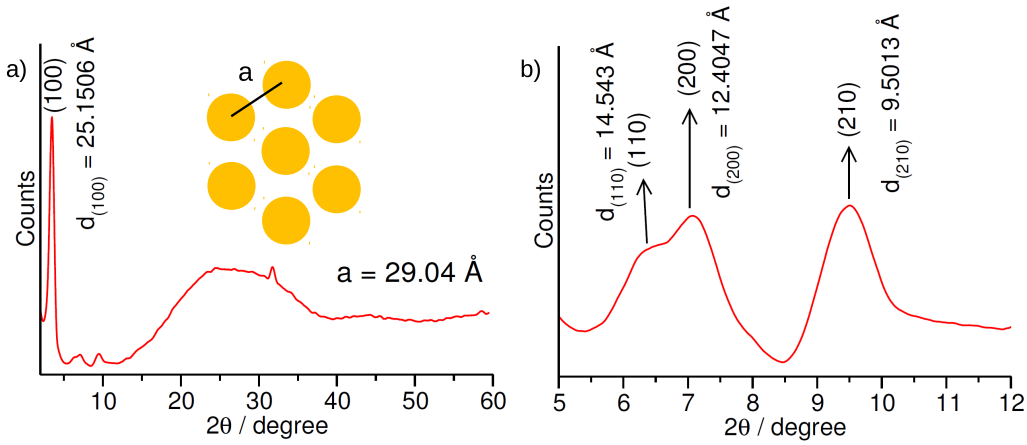

Figure 8.7: a) XRD pattern of **CBI-GCH** on a glass substrate. The inset shows the hexagonal columnar arrangement with lattice parameter (a). b) Low-angle reflections of the XRD pattern that show the peak indexing and d-spacing.

X-ray diffraction studies of the films obtained by drop casting solutions of **CBI-GCH** in MCH on a glass substrate showed the presence of low-angle reflections (Figure 8.7a and b). The ratio of the d-spacing was $1:1/\sqrt{3}:1/2:1/\sqrt{7}$ for the first four reflections (Table 8.2). Also a broad reflection was observed between 20° and 30° (2θ). This ratio of d spacing and the broad reflection at higher 2θ is characteristic

of a 2D hexagonal columnar lattice (inset of Figure 8.7a). [81, 82] The higher 2θ peaks correspond to the alkyl-chain interaction and core-core distance within the columns. The lattice parameter (a) for **CBI-GCH** was 29.04 Å.

2θ (°)	d-spacing (Å)	Miller indices (hkl)	Ratio of Miller indices $= d_{(hkl)}/d_{(100)}$
3.510	25.1506	(100)	1.00
6.07	14.543	(110)	0.578
7.12	12.4047	(200)	0.4932
9.30	9.5013	(210)	0.3777

Table 8.2: Assingment of Miller indices to XRD peaks of **CBI-GCH**.

8.2.5 Self-assembly of CBI-GACH

Having studied the chiral CBI derivative, we further explored the self-assembly of the achiral analogue, **CBI-GACH** bearing dodecyl group on the phenoxy wedges. This molecule was also molecularly dissolved in chloroform at dilute concentration (c = 1×10^{-5} M), which is evident from the characteristic CBI spectral features such as the absorption maximum at λ_{max} = 346 nm (ϵ = 1.3×10^{5} $Lmol^{-1}cm^{-1}$) with vibronic features between λ = 425 and 500 nm. **CBI-GACH** forms H-type aggregates in MCH (c = 5×10^{-5} M), indicated by the hypsochromic shift of the absorption maximum to λ = 325 nm, with the loss of vibronic features (Figure 8.8a). With an increase in temperature, a red-shifted absorption maximum at λ_{max} = 331 nm and vibronic features is observed, thus indicating a lesser degree of aggregation (Figure 8.8b). Because of the achiral nature of the molecule, CD spectroscopy could not be used to monitor the self-assembly.

Temperature-dependent UV/vis spectroscopy was used to understand the mechanism of self-assembly of **CBI-GACH**. The cooling curves obtained at two different concentrations by monitoring the absorbance at λ = 472 nm in UV/vis spectra shows a sigmoidal nature and fits to the temperature-dependent isodesmic model (Figure 8.8c). A higher temperature region (greater than 350 K) of the cooling curves, deviation from the fitted curve is observed probably due to the contribution from monomer absorption at the monitored temperature. Thus, we defer any thermodynamic analysis from the obtained cooling curves.

FE-SEM and AFM were used to understand the morphology of aggregates of

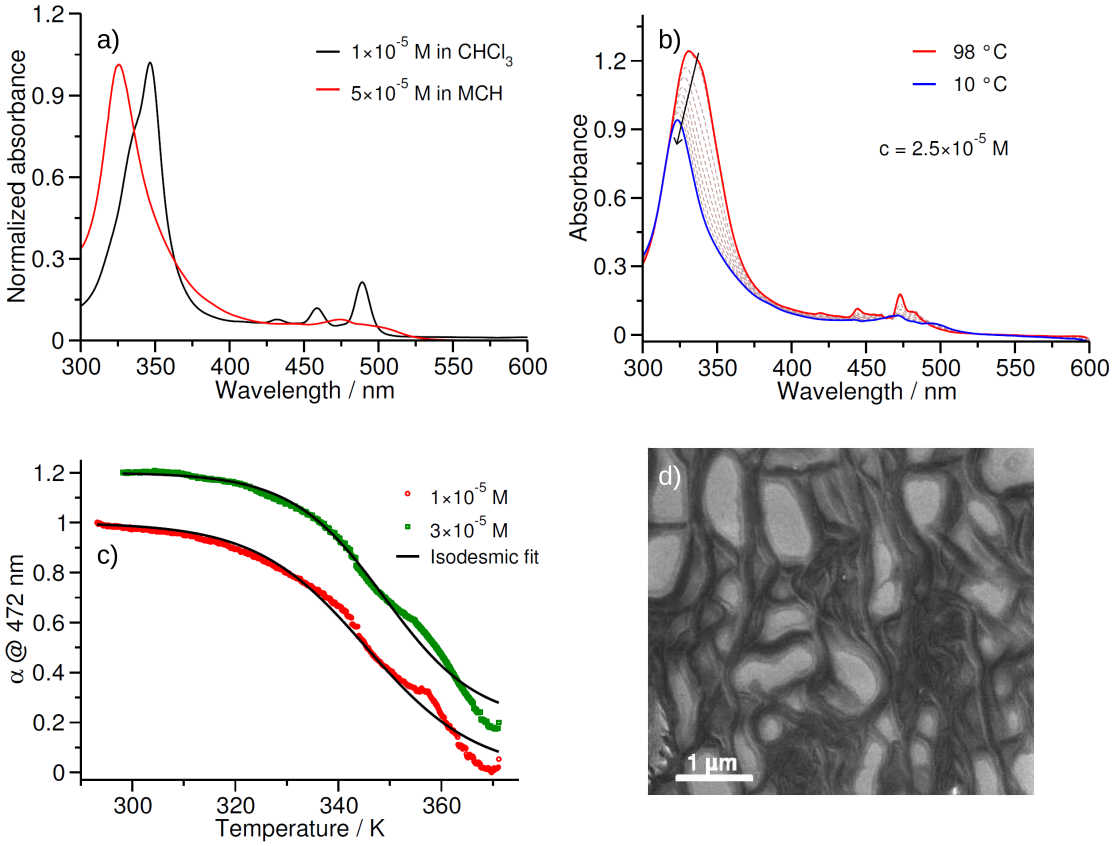

Figure 8.8: Self-assembly of **CBI-GACH**. a) Normalized UV/vis spectra in chloroform and MCH in a 1 cm cuvette. b) Temperature-dependent UV/vis spectra of in MCH (c = 2.5×10^{-5} M). Arrow indicates spectral changes with decrease in temperature. c) Cooling curves obtained by monitored the absorbance at 472 nm from temperature-dependent UV/vis absorption studies. The solid black line indicates the corresponding fit to the temperature-dependent isodesmic model. [79] d) FESEM image of a film obtained by drop-casting a solution (c = 5×10^{-5} M in MCH) on a glass substrate.

CBI-GACH (c = 5×10^{-5} M) on glass and mica substrates, respectively. The FE-SEM images showed the formation of long fibrillar networks (Figure 8.8d). AFM images show a fibrous network with an average height of 11 nm (Figure 8.9b). A significant amount of isolated fibers showed an average height of 5-7 nm, which is very close to the molecular dimension of 5.4 nm. Furthermore, these isolated fibers interdigitate through van der Waals interactions to form larger aggregates with heights of 15-25 nm. The XRD pattern of **CBI-GACH** also showed a similar 2D hexagonal columnar arrangement with a lattice parameter of 29.63 Å.

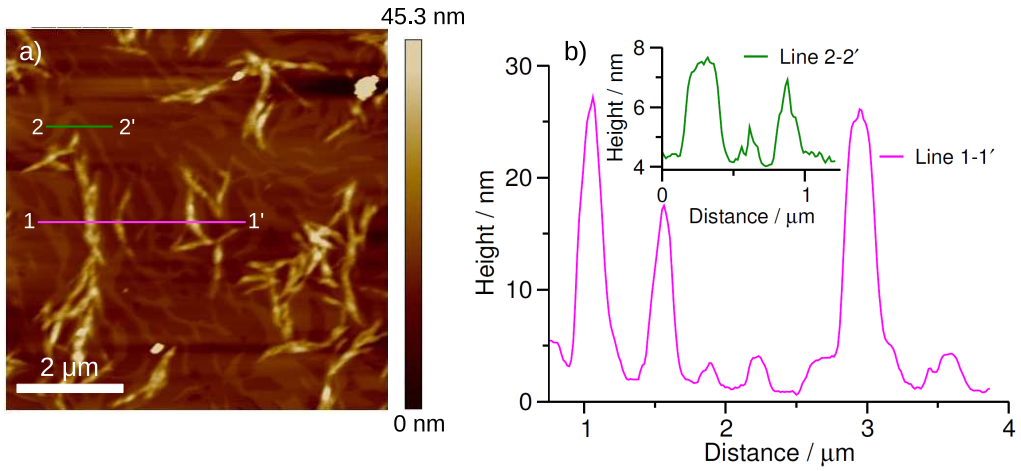

Figure 8.9: a) AFM height profile of **CBI-GACH** film on mica surface. b) Height analysis along the lines shown in Figure a).

8.2.6 CBI co-assembly: sergeant-and-soldiers experiment

We have performed the sergeant-and-soldiers experiment to understand chiral amplification in the co-assemblies of **CBI-GCH** and **CBI-GACH** in MCH. Different amounts of **CBI-GCH** were co-assembled with **CBI-GACH** (c = 2.5×10^{-5} M), and their chiroptical properties were probed. Even with a small amount (3%) of the chiral derivative (**CBI-GCH**) or sergeant, the CD spectra of the co-assembly shows a bisignated Cotton effect (Figure 8.10a) with very little change in the absorption spectra (Figure 8.10b). [83] Also the X-ray diffraction studies of a mixture of **CBI-GCH** and **CBI-GACH** shows a similar 2D hexagonal columnar arrangement with a slight change in the basal (100) reflection and lattice parameter (a = 30.11 Å), thus suggesting a co-assembly. The anisotropy factor or g value ($\Delta\epsilon/\epsilon$) monitored at λ = 320 nm shows nonlinear behavior (Figure 8.10c), which reaches the corresponding value of the pure chiral assembly at around 50% of the sergeant. This suggests a rather weak chiral amplification in this system. We further used chiral amplification to probe the dynamics of the molecules in the CBI stacks. An aliquot of 35% of the sergeant solution in its assembled state was added to the solution of pre-assembled **CBI-GACH** in MCH at the same concentration, and the evolution of the CD effect was monitored at λ = 320 nm as a function of time. The CD effect saturates to its equilibrium value within 3-4 minutes (Figure 8.10d). Thus, the rapid attainment of an equilibrium CD effect indicates that the co-assembly and aggregates are dynamic.

Since the chiral-amplification experiment was performed at a temperature (293 K) close to the T_m (ca. 308 K) of **CBI-GCH** (c = 2.5×10^{-5} M), the extent of

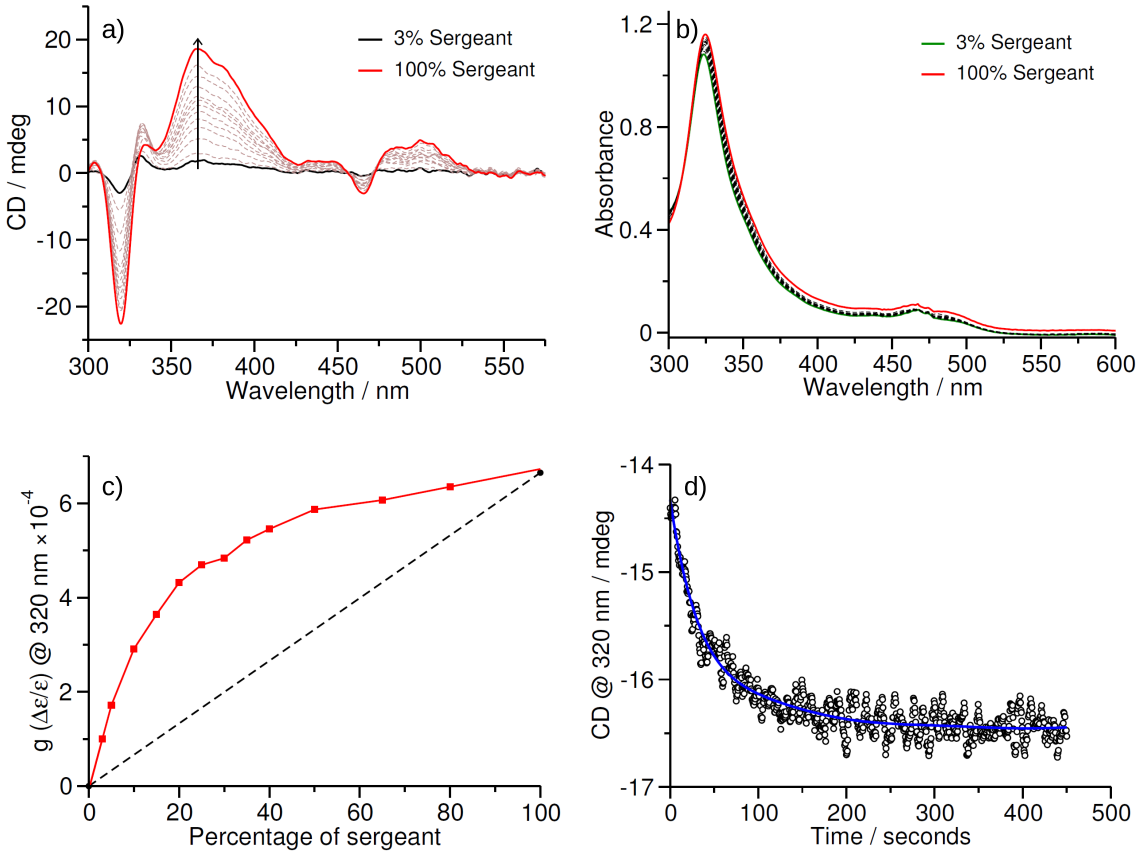

Figure 8.10: Coassembly of **CBI-GCH** and **CBI-GACH** and resultant chiral amplification. All the experiments were done in MCH (c = 2.5×10^{-5} M). a) and b) CD and UV/vis absorption spectra of the coassembly at different percentages of **CBI-GCH** in a 1 cm cuvette at 20 °C. The arrow indicates the spectral change with an increase in the percentage of the sergeant. c) Anisotropy (g) value monitored at λ = 320 nm as a function of the percentage of **CBI-GCH**. The dashed line that connects the fraction of **CBI-GCH** indicates the linear variation of the g value in the absence of any chiral amplification. d) The kinetics of the assembly seen by monitoring the time taken to reach the CD effect at λ = 320 nm when preassembled **CBI-GCH** (35%) was added to CBI-GACH at a constant concentration.

chiral amplification could be low. To investigate the effect of temperature on chiral amplification, either the temperature at which the experiments are performed can be varied or the total concentration of solution. We have used the latter to perform the sergeant-and-soldiers experiments at a higher concentration (1×10^{-4} M), and we indeed observed that the amount of sergeant required for complete chiral bias is around 30% (Figure 8.11). This finding indicates that the extent of amplification increases at higher concentration. These results concur with a recent theoretical treatment of the effect of temperature on the principle of sergeant-and-soldiers, [84]

which shows that at higher temperatures the extent of the chiral amplification or CD effect decreases.

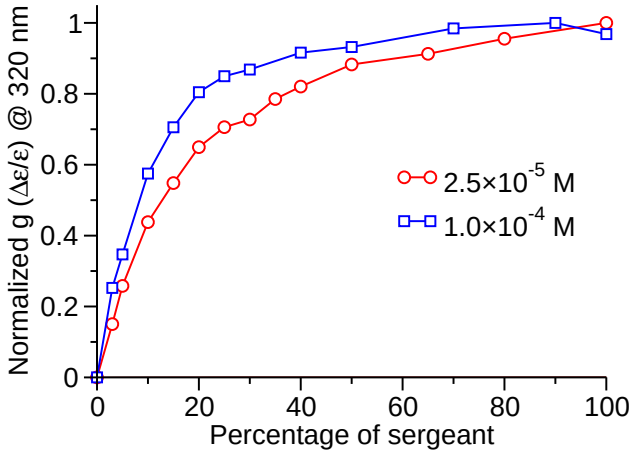

Figure 8.11: Normalized g ($\Delta\epsilon/\epsilon$) value at different concentrations (in MCH) for the co-assembly of **CBI-GCH** and **CBI-GACH**.

Morphological details of the mixed stacks or co-assembly were studied by FE-SEM and AFM. The FE-SEM images (40% sergeant) obtained on a glass substrate showed the presence of 1D fibers (Figure 8.12a). AFM images obtained by drop-casting a solution of 40% sergeant on a freshly cleaved mica surface shows the presence of fibers with an average height of the isolated fiber of 4 nm (Figure 8.12b and c). Thus, the co-assembly too forms fibers as observed for the individual components.

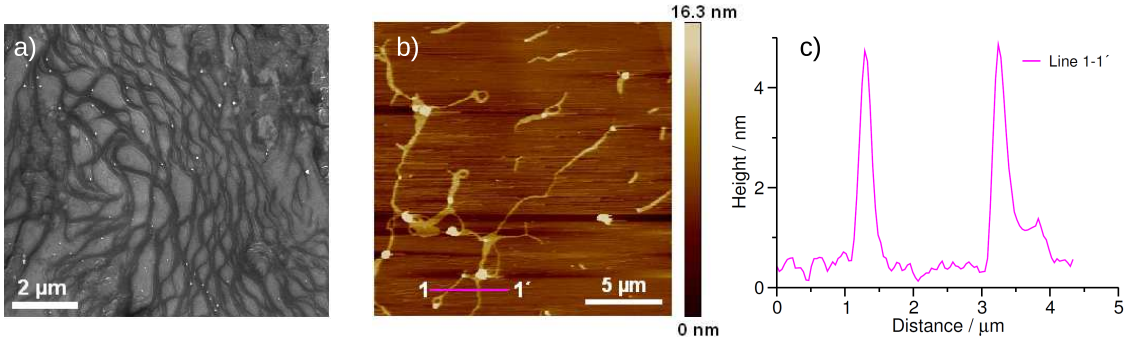

Figure 8.12: a) FESEM and b) AFM images of a film obtained by drop-casting a solution (c = 2.5×10^{-5} M in MCH) containing 40% **CBI-GCH** on glass and freshly cleaved mica surface, respectively. c) AFM cross-sectional analysis of fibers in (b) along the line 1-1′ showing the presence of individual fibers.

8.3 Conclusion

Two novel CBI derivatives (**CBI-GCH** and **CBI-GACH**) have been synthesized, and their self-assembly behavior in non-polar solvents has been investigated in detail by using various spectroscopic and microscopic tools. Temperature-dependent chrioptical probing revealed that **CBI-GCH** follows an isodesmic mechanism of self-assembly with an association constant of 5.4×10^4 M^{-1} in MCH. Assembly of **CBI-GCH** appearently lack any long-range interaction in the stacking direction and the observed isodesmic mechanism again reaffirms our earlier hypothesis (chapter 3). Both the CBI derivatives form 1D fibers with a H-type or face-to-face organization of chromophores. **CBI-GCH** and **CBI-GACH** form a 2D-hexagonal columnar arrangement in thin film state, as evidenced from XRD studies. Co-assemblies of chiral and achiral CBI derivatives (sergeant-and-soldiers experiment) exhibited chiral amplification, as seen by the saturation of the anisotropy factor (i.e., g value) at ≈30-50% of the sergeant. Thus, more work on different types of systems is necessary to establish a relation between the mechanisms of supramolecular polymerization and chiral amplification.

8.4 Experimental section

8.4.1 General methods

Materials: All the solvents and reagents were used as purchased without further purification unless mentioned. All the moisture sensitive reactions were carried out under an argon atmosphere. Quinoline was distilled under reduced pressure and stored in the dark to avoid degradation (this compound becomes dark brown on exposure to light). Analytical TLC was performed on silica gel (60 F_{254} Merck) pre-coated on aluminium plate and column chromatography was carried out using silica gel (100-200 mesh).

NMR Measurements: ^{1}H and ^{13}C NMR spectra were recorded on a BRUKER AVANCE 400 Fourier Transform spectrometer with 400 MHz and 100 MHz respectively. Short notations used are; s for singlet, d for doublet, t for triplet, m for multiplet and br for broad peak. All the spectra were recorded at 25 °C. ^{1}H and ^{13}C NMR spectra were calibrated with respect to 7.26 and 77.16 δppm respectively, the residual peak of $CDCl_3$.

Optical spectroscopy: Electronic absorption spectra were recorded on a Perkin

Elmer Lambda 900 UV-vis-NIR spectrometer with a scan rate of 375 nm/s in the absorbance mode. Jasco J-815 spectrometer was used to measure the Circular Dichroism (CD) spectra with a standard sensitivity (100 mdeg), scan rate of 100 nm/second, bandwidth of 1 nm and single accumulation for each spectra. CD effect is converted into the molar ellipticity ($\Delta\epsilon$) using the relation (8.1).

$$\Delta\epsilon = \frac{CD(mdeg)}{32980 \times c \times l} \tag{8.1}$$

where "c" is the concentration of the solution and "l" is the path length of the cuvette. Temperature-dependent CD measurements were performed using a CDF-426S/15 Peltier-type temperature controller with a temperature range of 268-381 K and a temperature slope of 2 K/min. The anisotropy factor or g-value was calculated using the below given relation.

$$g = \frac{\Delta\epsilon}{\epsilon} = \frac{CD(mdeg)}{32980 \times A}$$

Atomic Force Microscopy (AFM) imaging: AFM measurements were performed on a Veeco diInnova SPM operating in tapping mode regime. Micro-fabricated silicon cantilever tips doped with phosphorus and with a frequency of 235-278 kHz and a force constant of 20-40 N/m were used. AFM images were recorded at a rate of 512×512 pixels per minute. Respective solutions were drop casted on a freshly cleaved mica surface and allowed to dry at room temperature followed by drying under vacuum for 12 hours at room temperature. The AFM images were analyzed using Nanoscope 7.3. A first order flattening was performed to remove tilts, followed by the height analysis.

Field Emission Scanning Electron Microscopy (FE-SEM): FE-SEM measurements were performed on a NOVA NANO SEM 600 (FEI) operating with an accelerating voltage of 30 kV. The samples were prepared by drop casting the solution on a clean glass surface and drying in ambient conditions followed by vacuum drying at room temperature. Glass surface was cleaned by first sonicating with isopropyl alcohol followed by double distilled water and lastly by acetone. This process is repeated thrice and dried by passing a stream of nitrogen gas.

Matrix-Assisted Laser Desorption/Ionization Time of flight (MALDI-TOF): MALDI-TOF spectra were obtained on a Bruker daltonics autoflex (ST-A2130) MALDI-TOF spectrometer using DCTB as the matrix. The concentration

of all the samples was 0.1 g in 100 μL of chloroform.

X-ray diffraction (XRD): XRD was measured on films obtained from drop casting the respective solutions (concentration $> 10^{-3}$ M) on a glass substrate. XRD was recorded on Rigaku Machine with Cu K_α ($\lambda = 1.54$ Å) source from 1.2° to 60° (2θ) at a scanning rate of 0.8°/min.

Dynamic Light Scattering (DLS): DLS measurements were carried out on a NanoZS (Malvern UK) employing a 532 nm laser at a back scattering angle of 173°.

Analysis of the cooling curves: Equations and relations used in the analysis are from the temperature-dependent isodesmic model. [79] Equilibrium constant (K_e) was rendered dimensionless by dividing it by the molar volume (0.128 L/mol) of MCH. From the plot of natural logarithm of dimensionless K_e versus the reciprocal temperature (van't Hoff plot) the change in entropy of polymerization was obtained.

8.4.2 Computational details

Geometry optimization of monomers of **CBI-GCH** and **CBI-GACH** was carried out at the B3LYP/6-31G [85, 86] level of theory with the Gaussian 09 package [87] to obtain the molecular dimensions of the monomers. The molecules were visualized by using visual molecular dynamics. [88]

The geometry optimization of the dimer in the gas phase was carried out by using periodic DFT calculations, as implemented in CP2K package [89] by means of the QUICKSTEP module. [90] BLYP exchange-correlation functional [86, 91] was used along with double zet-valence polarized basis set and the Grimme D2 [92] dispersion correction. An energy cut-off of 280 Ry for electron density, Goedecker-Teter- Hutter (GTH) pseudopotential, [93] wavelet Poisson solver, and L-BFGS optimizer [94] were used. A cubic box of dimension 36 Å was used. Jmol software was employed to visualize the dimer geometry. [95]

The alkyl chains of the gallic wedge were replaced by ethyl groups to reduce the computational cost. First monomer optimization was carried out followed by single point SCF energy calculations at different angles (Figure 8.13). The minimum-energy configuration obtained in the scan run was used as the initial geometry for optimization of the dimer.

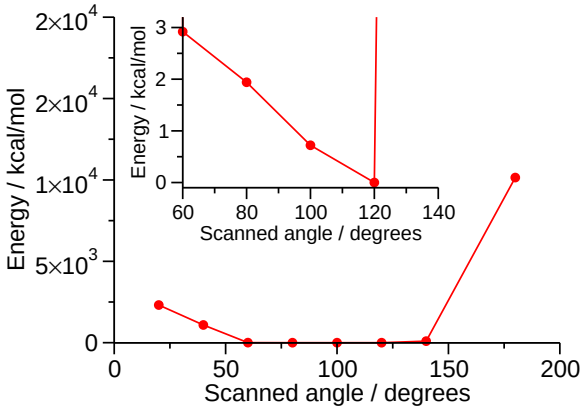

Figure 8.13: Energy as a function of angle between the molecules of a dimer of CBI with 3,4,5-triethoxy phenyl substitution on the imide position studied at BLYP/DZVP using CP2K package.

8.4.3 Synthetic details

Coronene dianhydride (**1**), [54] 3,4,5-tris[(S)-3,7-dimethyloctyloxy]- 1-aminobenzene (**2**), [96] and 3,4,5-tris(dodecyloxy)-1-aminobenzene (**3**) [96] were synthesized following reported procedures.

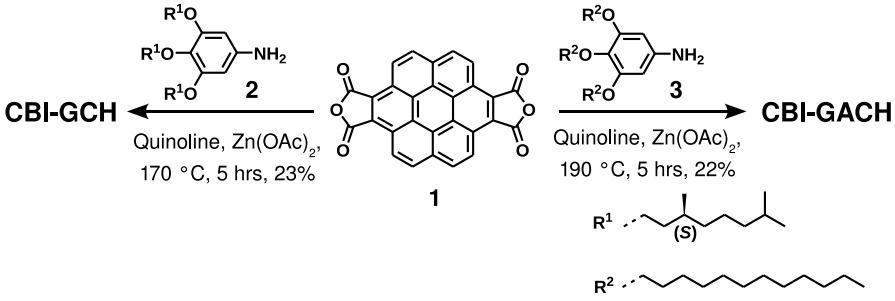

Figure 8.14: Synthetic routes to obtain **CBI-GCH** and **CBI-GACH**.

Synthesis of CBI-GCH: Freshly distilled quinoline (25 mL) was added to **1** (150 mg, 0.34 mmol), **2** (457 mg, 0.81 mmol), and zinc acetate (75 mg, 0.4 mmol) in a 100 mL three-necked round-bottom flask connected to a reflux condenser. The reaction mixture was heated at 170 °C with constant stirring for 5 h under argon and then allowed to cool to room temperature. An orange precipitate settled at the bottom of the flask. Methanol (50 mL) was added to ensure complete precipitation of the product followed by filtration under suction to obtain an orange crude product. This product was purified by repeated column chromatography ($CHCl_3$/hexane 95:5) and size-exclusion chromatography (Biobeads, S-X3; $CHCl_3$ as the solvent) to obtain

a pure dark-orange solid (120 mg, 23%). R_f = 0.48 ($CHCl_3$); ^{1}H NMR (400 MHz, $CDCl_3$): d = 9.50 (br, 4H; Ar_{coro}), 8.38 (br, 4H; Ar_{coro}), 7.20 (s, 4H; H_{Ph}), 4.13-4.21 (m, 12H; -OCH_2), 1.99, 1.85, 1.68, 1.54, 1.38, 1.20 (six multiplets, 60 H), 1.06 (d, J = 6.4 Hz, 6H; -$CHCH_3$), 0.97 (d, J = 6.4 Hz, 12H; -$CHCH_3$), 0.95 (d, J = 6.8 Hz, 12H; -$CH(CH_3)_2$), 0.87 ppm (d, J = 6.4 Hz, 24H; -$CH(CH_3)_2$); ^{13}CNMR (100 MHz, $CDCl_3$): δ = 168.4 ($C_{C=O}$), 153.8, 138.4, 128.1, 126.6, 123.6, 122.6, 120.7, 106.6, 71.9, 67.8, 39.7, 39.6, 37.9, 37.8, 36.6, 30.2, 30.0, 29.8, 29.5, 28.26, 28.20, 25.0, 24.9, 22.9, 22.88, 22.86, 19.8, 19.5 ppm; IR (KBr): ν = 3108 (aromatic C-H stretching), 2954, 2927, 2897, 2869, 2843 (aliphatic C-H stretching), 1764, 1708 (imide C=O stretching), 1597, 1506, 1468, 1438, 1416, 1382, 1339, 1300, 1240, 1119, 851, 795, 751, 702, 573 cm^{-1}; MALDI-TOF (DCTB): m/z calcd for $C_{100}H_{138}N_2O_{10}$: 1527.03515 $[M]^+$; found: 1527.04 and 1550.03 $[M+Na]^+$; HRMS (APCI): m/z calcd for 1528.0424 $[M+H]^+$; found: 1528.0467. APCI = atmospheric pressure chemical ionization, DCTB = trans-2-[3-(4-tert-Butylphenyl)-2-methyl-2-propenylidene]malononitrile.

Synthesis of CBI-GACH:Freshly distilled quinoline (20 mL) was added to **1** (150 mg, 0.34 mmol), **3** (660 mg, 1.02 mmol), and zinc acetate (63 mg, 0.34 mmol) in a 50 mL three-necked round-bottom flask connected to a reflux condenser. The reaction mixture was heated at 190 °C with constant stirring for 5 h under argon and then was allowed to cool to room temperature. The reaction mixture was transferred to a 250 mL beaker and 1 M HCl (150 mL) was added to obtain the precipitate. The precipitate was collected by filtration under suction and washed thoroughly with water followed by methanol. The obtained product was dissolved in a minimum amount of chloroform and reprecipitated with an excess of methanol. The formed precipitate was collected by filtration. The crude product was purified by a combination of column chromatography ($CHCl_3$/hexane 95:5) and size-exclusion chromatography (Biobeads, S-X3; $CHCl_3$) to obtain a pure dark-orange solid (130 mg, 22%). R_f = 0.40 ($CHCl_3$); ^{1}H NMR (400 MHz, $CDCl_3$): δ = 9.16 (br, 4H; Ar_{coro}), 7.97 (br, 4H; Ar_{coro}), 7.19 (s, 4H; H_{Ph}), 4.15 (t, J = 6.2 Hz, 6H; -OCH_2), 4.08 (m, 8H; -OCH_2), 1.86-1.94 (m, 12H; -OCH_2CH_2), 1.20-1.70 (m, 108H; n-CH_2 of alkyl chains), 0.93 (t, J = 6.2 Hz, 6H; n-CH_2CH_3), 0.83 ppm (t, J = 6.4 Hz, 12H; n-CH_2CH_3); ^{13}C NMR (100 MHz, $CDCl_3$): δ = 168.4 ($C_{C=O}$), 153.7, 138.3, 128.1, 126.5, 123.6, 122.6, 120.7, 106.7, 73.7, 69.4, 32.19, 32.13, 30.8, 30.1, 30.09, 30.00, 29.9, 29.8, 29.7, 29.67, 29.64, 26.5, 26.4, 22.9, 22.8, 14.3, 14.2 ppm; IR (KBr): ν = 3103 (aromatic C-H stretching), 2954, 2922, 2871, 2851 (aliphatic C-H stretching), 1762, 1707 (imide C=O stretching), 1596, 1507, 1467, 1437, 1414, 1392, 1338, 1300,

1261, 1240, 1120, 1011, 852, 796, 767, 750, 721, 702, 624, 572, 542 cm^{-1}; MALDI-TOF (DCTB): m/z calcd for $C_{112}H_{162}N_2O_{10}$: 1695.2229 $[M]^+$;found 1695.33; HRMS (APCI): m/z calcd for $C_{112}H_{162}N_2O_{10}$: 1696.2302 $[M+H]^+$; found: 1696.2310.

Bibliography

[1] Zang, L.; Che, Y.; Moore, J. S. *Acc. Chem. Res.* **2008**, *41*, 1596–1608.

[2] Wasielewski, M. R. *Acc. Chem. Res.* **2009**, *42*, 1910–1921.

[3] Kim, F. S.; Ren, G.; Jenekhe, S. A. *Chem. Mater.* **2011**, *23*, 682–732.

[4] Hoeben, F. J. M.; Jonkheijm, P.; Meijer, E. W.; Schenning, A. P. H. J. *Chem. Rev.* **2005**, *105*, 1491–1546.

[5] González-Rodr´iguez, D.; Schenning, A. P. H. J. *Chem. Mater.* **2011**, *23*, 310–325.

[6] Rybtchinski, B. *ACS Nano* **2011**, *5*, 6791–6818.

[7] Würthner, F.; Meerholz, K. *Chem. Eur. J.* **2010**, *16*, 9366–9373.

[8] Bosman, A. W.; Sijbesma, R. P.; Meijer, E. *Mater. Today* **2004**, *7*, 34 – 39.

[9] Aida, T.; Meijer, E. W.; Stupp, S. I. *Science* **2012**, *335*, 813–817.

[10] Babu, S. S.; Prasanthkumar, S.; Ajayaghosh, A. *Angew. Chem. Int. Ed.* **2012**, *51*, 1766–1776.

[11] An, B.-K.; Gierschner, J.; Park, S. Y. *Acc. Chem. Res.* **2012**, *45*, 544–554.

[12] Yan, X.; Wang, F.; Zheng, B.; Huang, F. *Chem. Soc. Rev.* **2012**, *41*, 6042–6065.

[13] Safont-Sempere, M. M.; Fernández, G.; Würthner, F. *Chem. Rev.* **2011**, *111*, 5784–5814.

[14] Kong, X.; He, Z.; Zhang, Y.; Mu, L.; Liang, C.; Chen, B.; Jing, X.; Cammidge, A. N. *Org. Lett.* **2011**, *13*, 764–767.

[15] Koshkakaryan, G.; Jiang, P.; Altoe, V.; Cao, D.; Klivansky, L. M.; Zhang, Y.; Chung, S.; Katan, A.; Martin, F.; Salmeron, M.; Ma, B.; Aloni, S.; Liu, Y. *Chem. Commun.* **2010**, *46*, 8579–8581.

[16] Miao, J.; Zhu, L. *Chem. Mater.* **2010**, *22*, 197–206.

[17] Kaiser, T.; Wang, H.; Stepanenko, V.; Würthner, F. *Angew. Chem. Int. Ed.* **2007**, *46*, 5541–5544.

[18] Yagai, S.; Usui, M.; Seki, T.; Murayama, H.; Kikkawa, Y.; Uemura, S.; Karatsu, T.; Kitamura, A.; Asano, A.; Seki, S. *J. Am. Chem. Soc.* **2012**, *134*, 7983–7994.

[19] Würthner, F. *Chem. Commun.* **2004**, 1564–1579.

[20] Dehm, V.; Chen, Z.; Baumeister, U.; Prins, P.; Siebbeles, L. D. A.; Würthner, F. *Org. Lett.* **2007**, *9*, 1085–1088.

[21] Weil, T.; Vosch, T.; Hofkens, J.; Peneva, K.; Müllen, K. *Angew. Chem. Int. Ed.* **2010**, *49*, 9068–9093.

[22] Huang, C.; Barlow, S.; Marder, S. R. *J. Org. Chem.* **2011**, *76*, 2386–2407.

[23] Pantoş, G.; Pengo, P.; Sanders, J. *Angew. Chem. Int. Ed.* **2007**, *46*, 194–197.

[24] Shao, H.; Nguyen, T.; Romano, N. C.; Modarelli, D. A.; Parquette, J. R. *J. Am. Chem. Soc.* **2009**, *131*, 16374–16376.

[25] Molla, M. R.; Ghosh, S. *Chem. Eur. J.* **2012**, *18*, 9860–9869.

[26] Kumar, M.; George, S. J. *Chem. Eur. J.* **2011**, *17*, 11102–11106.

[27] Sakai, N.; Lista, M.; Kel, O.; Sakurai, S.-i.; Emery, D.; Mareda, J.; Vauthey, E.; Matile, S. *J. Am. Chem. Soc.* **2011**, *133*, 15224–15227.

[28] Würthner, F.; Stolte, M. *Chem. Commun.* **2011**, *47*, 5109–5115.

[29] Bhosale, S. V.; Jani, C. H.; Langford, S. J. *Chem. Soc. Rev.* **2008**, *37*, 331–342.

[30] Bhosale, S. V.; Bhosale, S. V.; Bhargava, S. K. *Org. Biomol. Chem.* **2012**, *10*, 6455–6468.

[31] Jonkheijm, P.; Miura, A.; Zdanowska, M.; Hoeben, F. J. M.; De Feyter, S.; Schenning, A. P. H. J.; De Schryver, F. C.; Meijer, E. W. *Angew. Chem. Int. Ed.* **2004**, *43*, 74–78.

[32] Hoeben, F. J. M.; Wolffs, M.; Zhang, J.; De Feyter, S.; Leclre, P.; Schenning, A. P. H. J.; Meijer, E. W. *J. Am. Chem. Soc.* **2007**, *129*, 9819–9828.

[33] Praveen, V. K.; George, S. J.; Varghese, R.; Vijayakumar, C.; Ajayaghosh, A. *J. Am. Chem. Soc.* **2006**, *128*, 7542–7550.

[34] Yagai, S.; Kubota, S.; Saito, H.; Unoike, K.; Karatsu, T.; Kitamura, A.; Ajayaghosh, A.; Kanesato, M.; Kikkawa, Y. *J. Am. Chem. Soc.* **2009**, *131*, 5408–5410.

[35] Ajayaghosh, A.; Praveen, V. K. *Acc. Chem. Res.* **2007**, *40*, 644–656.

[36] Ajayaghosh, A.; George, S. J. *J. Am. Chem. Soc.* **2001**, *123*, 5148–5149.

[37] Helmich, F.; Smulders, M. M. J.; Lee, C. C.; Schenning, A. P. H. J.; Meijer, E. W. *J. Am. Chem. Soc.* **2011**, *133*, 12238–12246.

[38] Helmich, F.; Lee, C.; Nieuwenhuizen, M.; Gielen, J.; Christianen, P.; Larsen, A.; Fytas, G.; Leclère, P.; Schenning, A.; Meijer, E. *Angew. Chem. Int. Ed.* **2010**, *49*, 3939–3942.

[39] Ishizuka, T.; Sankar, M.; Yamada, Y.; Fukuzumi, S.; Kojima, T. *Chem. Commun.* **2012**, *48*, 6481–6483.

[40] Nieto-Ortega, B.; Ramirez, F. J.; Amabilino, D. B.; Linares, M.; Beljonne, D.; Navarrete, J. T. L.; Casado, J. *Chem. Commun.* **2012**, *48*, 9147–9149.

[41] Engelkamp, H.; Middelbeek, S.; J. M., R.; Nolte, *Science* **1999**, *284*, 785–788.

[42] van Hameren, R.; Schn, P.; van Buul, A. M.; Hoogboom, J.; Lazarenko, S. V.; Gerritsen, J. W.; Engelkamp, H.; Christianen, P. C. M.; Heus, H. A.; Maan, J. C.; Rasing, T.; Speller, S.; Rowan, A. E.; Elemans, J. A. A. W.; Nolte, R. J. M. *Science* **2006**, *314*, 1433–1436.

[43] Kataoka, Y.; Shibata, Y.; Tamiaki, H. *Bioorg. Med. Chem. Lett.* **2012**, *22*, 5218 – 5221.

[44] Jesorka, A.; Holzwarth, A. R.; Eichhofer, A.; Reddy, C. M.; Kinoshita, Y.; Tamiaki, H.; Katterle, M.; Naubron, J.-V.; Balaban, T. S. *Photochem. Photobiol. Sci.* **2012**, *11*, 1069–1080.

[45] Hizume, Y.; Tashiro, K.; Charvet, R.; Yamamoto, Y.; Saeki, A.; Seki, S.; Aida, T. *J. Am. Chem. Soc.* **2010**, *132*, 6628–6629.

[46] Charvet, R.; Jiang, D.-L.; Aida, T. *Chem. Commun.* **2004**, 2664–2665.

[47] Aimi, J.; Nagamine, Y.; Tsuda, A.; Muranaka, A.; Uchiyama, M.; Aida, T. *Angew. Chem. Int. Ed.* **2008**, *47*, 5153–5156.

[48] Lütke Eversloh, C.; Li, C.; Müllen, K. *Org. Lett.* **2011**, *13*, 4148–4150.

[49] Yan, Q.; Cai, K.; Zhang, C.; Zhao, D. *Org. Lett.* **2012**, *14*, 4654–4657.

[50] Müller, S.; Müllen, K. *Chem. Commun.* **2005**, 4045–4046.

[51] Nolde, F.; Pisula, W.; Müller, S.; Kohl, C.; Müllen, K. *Chem. Mater.* **2006**, *18*, 3715–3725.

[52] Hao, L.; Jiang, W.; Wang, Z. *Tetrahedron* **2012**, *68*, 9234 – 9239.

[53] Zhang, Y.; Zhao, Z.; Huang, X.; Xie, Y.; Liu, C.; Li, J.; Guan, X.; Zhang, K.; Cheng, C.; Xiao, Y. *RSC Adv.* **2012**, *2*, 12644–12647.

[54] Alibert-Fouet, S.; Seguy, I.; Bobo, J.-F.; Destruel, P.; Bock, H. *Chem. Eur. J.* **2007**, *13*, 1746–1753.

[55] Rao, K. V.; George, S. J. *Org. Lett.* **2010**, *12*, 2656–2659.

[56] Jain, A.; Rao, K. V.; Kulkarni, C.; George, A.; George, S. J. *Chem. Commun.* **2012**, *48*, 1467–1469.

[57] Rohr, U.; Kohl, C.; Müllen, K.; van de Craats, A.; Warman, J. *J. Mater. Chem.* **2001**, *11*, 1789–1799.

[58] An, Z.; Yu, J.; Domercq, B.; Jones, S. C.; Barlow, S.; Kippelen, B.; Marder, S. R. *J. Mater. Chem.* **2009**, *19*, 6688–6698.

[59] Rohr, U.; Schlichting, P.; Böhm, A.; Gross, M.; Meerholz, K.; Bräuchle, C.; Müllen, K. *Angew. Chem. Int. Ed.* **1998**, *37*, 1434–1437.

[60] Usta, H.; Newman, C.; Chen, Z.; Facchetti, A. *Adv. Mater.* **2012**, *24*, 3678–3684.

[61] Palmans, A.; Meijer, E. *Angew. Chem. Int. Ed.* **2007**, *46*, 8948–8968.

[62] Yashima, E.; Maeda, K.; Nishimura, T. *Chem. Eur. J.* **2004**, *10*, 42–51.

[63] Green, M. M.; Park, J.-W.; Sato, T.; Teramoto, A.; Lifson, S.; Selinger, R. L. B.; Selinger, J. V. *Angew. Chem. Int. Ed.* **1999**, *38*, 3138–3154.

[64] Langeveld-Voss, B. M. W.; Waterval, R. J. M.; Janssen, R. A. J.; Meijer, E. W. *Macromolecules* **1999**, *32*, 227–230.

[65] Smulders, M. M. J.; Schenning, A. P. H. J.; Meijer, E. W. *J. Am. Chem. Soc.* **2008**, *130*, 606–611.

[66] Green, M. M.; Garetz, B. A.; Munoz, B.; Chang, H.; Hoke, S.; Cooks, R. G. *J. Am. Chem. Soc.* **1995**, *117*, 4181–4182.

[67] van Gestel, J.; Palmans, A. R. A.; Titulaer, B.; Vekemans, J. A. J. M.; Meijer, E. W. *J. Am. Chem. Soc.* **2005**, *127*, 5490–5494.

[68] Smulders, M. M. J.; Filot, I. A. W.; Leenders, J. M. A.; van der Schoot, P.; Palmans, A. R. A.; Schenning, A. P. H. J.; Meijer, E. W. *J. Am. Chem. Soc.* **2010**, *132*, 611–619.

[69] Garc´ia, F.; Viruela, P. M.; Matesanz, E.; Ort´i, E.; Sánchez, L. *Chem. Eur. J.* **2011**, *17*, 7755–7759.

[70] Garc´ia, F.; Sánchez, L. *J. Am. Chem. Soc.* **2012**, *134*, 734–742.

[71] Brunsveld, L.; Lohmeijer, B. G. G.; Vekemans, J. A. J. M.; Meijer, E. W. *Chem. Commun.* **2000**, 2305–2306.

[72] Palmans, A. R. A.; Vekemans, J. A. J. M.; Havinga, E. E.; Meijer, E. W. *Angew. Chem. Int. Ed.* **1997**, *36*, 2648–2651.

[73] Würthner, F.; Thalacker, C.; Diele, S.; Tschierske, C. *Chem. Eur. J.* **2001**, *7*, 2245–2253.

[74] van Herrikhuyzen, J.; Syamakumari, A.; Schenning, A. P. H. J.; Meijer, E. W. *J. Am. Chem. Soc.* **2004**, *126*, 10021–10027.

[75] Chen, Z.; Stepanenko, V.; Dehm, V.; Prins, P.; Siebbeles, L.; Seibt, J.; Marquetand, P.; Engel, V.; Würthner, F. *Chem. Eur. J* **2007**, *13*, 436–449.

[76] Würthner, F.; Kaiser, T. E.; Saha-Möller, C. R. *Angew. Chem. Int. Ed.* **2011**, *50*, 3376–3410.

[77] Seibt, J.; Marquetand, P.; Engel, V.; Chen, Z.; Dehm, V.; Würthner, F. *Chem. Phys.* **2006**, *328*, 354–362.

[78] No artifacts arising from linear dichroism were observed.

[79] Smulders, M.; Nieuwenhuizen, M.; deGreef, T.; vanderSchoot, P.; Schenning, A.; Meijer, E. *Chem. Eur. J.* **2010**, *16*, 362–367.

[80] Kulkarni, C.; Balasubramanian, S.; George, S. J. *ChemPhysChem* **2013**, *14*, 661–673.

[81] Laschat, S.; Baro, A.; Steinke, N.; Giesselmann, F.; Hägele, C.; Scalia, G.; Judele, R.; Kapatsina, E.; Sauer, S.; Schreivogel, A.; Tosoni, M. *Angew. Chem. Int. Ed.* **2007**, *46*, 4832–4887.

[82] Yoshio, M.; Kagata, T.; Hoshino, K.; Mukai, T.; Ohno, H.; Kato, T. *J. Am. Chem. Soc.* **2006**, *128*, 5570–5577.

[83] Further evidence of coassembly comes from a subtle change in the CD spectra; that is, the CD effect at $\lambda = 332$ nm is higher with an increasing amount of sergeant than the pure sergeant; this change in the CD spectra indicates that the packing in the aggregates is altered, thus suggesting a coassembly between the sergeant and soldier.

[84] Markvoort, A. J.; ten Eikelder, H. M. M.; Hilbers, P. A. J.; de Greef, T. F. A.; Meijer, E. W. *Nat. Commun.* **2011**, *2*, 509.

[85] Becke, A. D. *J. Chem. Phys.* **1993**, *98*, 5648–5652.

[86] Lee, C.; Yang, W.; Parr, R. G. *Phys. Rev. B* **1988**, *37*, 785–789.

[87] Frisch, M. J. et al. Gaussian 09 Revision D.01. Gaussian Inc. Wallingford CT 2009.

[88] Humphrey, W.; Dalke, A.; Schulten, K. *J. Mol. Graphics* **1996**, *14*, 33–38.

[89] Hutter, J.; Iannuzzi, M.; Schiffmann, F.; VandeVondele, J. *Wiley Interdiscip. Rev. Comput. Mol. Sci.* **2014**, *4*, 15–25.

[90] VandeVondele, J.; Krack, M.; Mohamed, F.; Parrinello, M.; Chassaing, T.; Hutter, J. *Comp. Phys. Commun.* **2005**, *167*, 103 – 128.

[91] Becke, A. D. *Phys. Rev. A* **1988**, *38*, 3098–3100.

[92] Grimme, S. *J. Comput. Chem.* **2006**, *27*, 1787–1799.

[93] Hartwigsen, C.; Goedecker, S.; Hutter, J. *Phys. Rev. B* **1998**, *58*, 3641–3662.

[94] Byrd, R.; Lu, P.; Nocedal, J.; Zhu, C. *J. Sci. Comput.* **1995**, *16*, 1190–1208.

[95] a) Jmol: An open-source Java viewer for chemical structures in 3D, to be found under http://www.jmol.org; b) McMahon B.; Hanson, R. M. *J. Appl. Crystallogr.* **2008**, *41*, 811.

[96] Pieterse, K. Thesis:*Electron deficient materials based on azaheterocycles*, Ph.D. Dissertation, Eindhoven University of Technology, Eindhoven (The Netherlands), 2001. Chapter 4 in the above mentioned thesis describes the synthesis of **2** and **3**.

Chapter 9

Mechanism of Self-Assembly and Temperature-dependent Reversal of Supramolecular Chirality in a CBI derivative

9.1 Introduction

Coronene bisimides (CBIs) are an important class of electron-deficient compounds with potential applications in opto-electronic devices [1–3] and liquid crystalline materials [4–7]. CBIs are synthesized by the core expansion of perylene bisimides. [8–11] Recently, the solution state self-assembly of CBIs has also gained importance. [12, 13] The mechanism of self-assembly and morphological properties of two such coronene bisimides (with five membered imide rings) was extensively discussed in the previous Chapter.

Herein, we study the mechanism of self-assembly of a structurally similar analogue of CBI. During this study, we serendipitously observed the reversal of supramolecular chirality with change in temperature. There are reports in literature on the reversal of supramolecular chirality with external stimuli like light, [14] metal ions, [15] guests [16] and solvent. [17–19] Reversal of handedness in covalent polymers with temperature has been ascribed to conformational changes. [20–22] However, there are

Manuscript based on this work is under preparation

few reports of temperature-dependent reversal of supramolecular chirality. [23, 24] Extensive circular dichroism studies in both cyclic and linear solvents combined with molecular dynamics simulations suggest that the solvent-accessible pockets of the monomer plays a key role in the reversal of supramolecular chirality as a function of temperature. Since molecular pockets or voids are generally encountered in biological macromolecules, these motifs can greatly influence their behaviour with change in external stimuli.

9.2 Results and discussion

The molecule under study, **CBI-35CH** consists of a central five membered coronene bisimide with 3,5-di((*s*)-3,7-dimethyloctyl)phenoxy groups on the imide position. The 3,5-disubstitution creates a pocket in the molecule. **CBI-35CH** was synthesized by the imidaztion of coronene dianhydride with the corresponding phenyl amine in quinoline and it was thoroughly characterized using ^{1}H- and ^{13}-NMR spectroscopy and high resultion mass spectrometry (HRMS) (see experimental section for details).

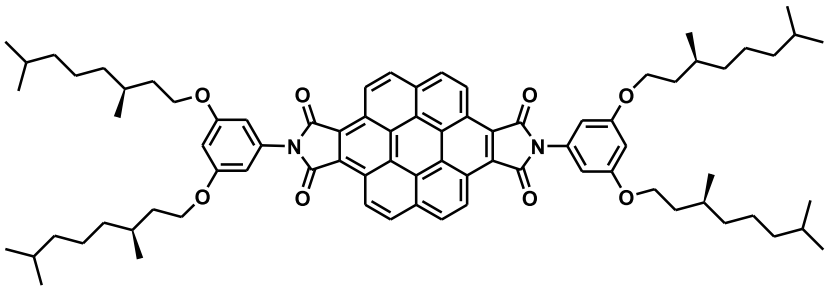

Figure 9.1: Structure of **CBI-35CH**.

9.2.1 Mechanisms of self-assembly and morphology

UV/vis absorption spectra of **CBI-35CH** in MCH shows a maximum at 325 nm with broad bands between 450 to 550 nm at room temperature. With increase in temperature, the maximum red-shifts to 332 nm and the the bands at 450, 477 and 488 nm become sharp (Figure 9.2a). The self-assembly of **CBI-35CH** is mainly driven by the π-π stacking of the coronene core and the van der Waals interactions of the peripheral phenoxy wedges. The hypsochromic shift in absorption maximum suggests that the aggregates are of H-type. **CBI-35CH** is non-fluorescent even in the molecularly dissolved state due to electron transfer from the phenoxy wedge

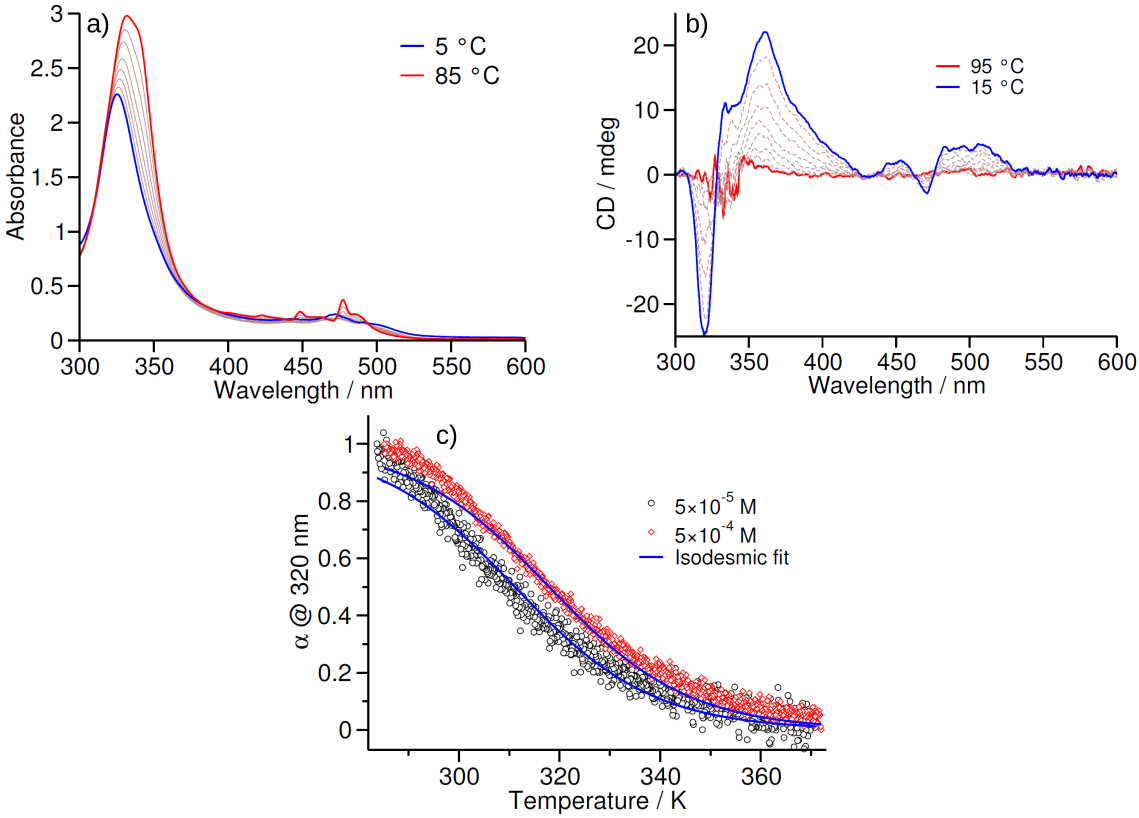

Figure 9.2: a) and b) Temperature-dependent UV/vis absorption and CD spectra respectively of **CBI-35CH** in MCH (c = 5×10^{-5} M). c) Cooling curves of **CBI-35CH** obtained from CD studies at different concentrations with a cooling rate of 2 K/minute.

to the CBI core, as seen in the case of **CBI-GCH** and **CBI-GACH** (Chapter 8). Further, the assembly of **CBI-35CH** is seen to exhibit a bisignated Cotton effect, indicating that the molecular level chirality is transcripted to the supramolecular level (Figure 9.2b). The zero-crossing points in CD spectra, 328 and 477 nm match well with UV/vis absorption maxima, suggesting that the monomers in an aggregate are excitonically coupled. The assembly of **CBI-35CH** was found to disassemble at high temperatures.

The cooling curves obtained from CD studies showed a gradual transition from monomers to aggregates (Figures 9.2c). The experimental data could be well described by the temperature-dependent isodesmic model. [25] From the isodesmic model and the van't Hoff plot, different thermodynamic parameters of self-assembly were calculated (Table 9.1). The variation in melting temperature (T_m) was only 10 K over an order of magnitude change in concentration. Such a weak dependence of T_m on concentration is rare and this could be due to the difficulty in assigning

the temperature at which the reversal begins. In other words, defining the exact temperature range for "state B" (vide infra) of cooling curve is difficult. The assembly of **CBI-35CH** seems to lack any apparent long-range interactions and they follow an isodesmic mechanism of self-assembly. Thus, this example again reaffirms our hypothesis that long-range interaction in the growth direction is necessary to observe a cooperative mechanism.

Concentration (M)	Melting temperature T_m (K)	Enthalpy of polymerization, ΔH (kJ/mol)	Entropy of polymerization, ΔS (kJ/mol/K)	Free energy of polymerization, ΔG (kJ/mol)
1×10^{-5}	304.60	-67.03 (-71.50)	0.143	-26.63
3×10^{-5}	309.50	-66.24 (-69.82)	0.144	-25.09
5×10^{-5}	310.30	-62.01 (-65.36)	0.133	-24.03
1×10^{-4}	314.70	-68.70 (-71.10)	0.154	-23.98
5×10^{-4}	319.70	-67.18 (-68.83)	0.158	-20.89

Table 9.1: Thermodynamic parameters for the self-assembly of **CBI-35CH** in MCH. ΔH values in paranthesis and the ΔS values are obtained from van't Hoff plot ($\ln(K_e)$ vs $1/T$) at different concentrations. ΔH values in the column three are obtained from isodesmic fit to the experimental data. Average ΔH values were used to calculate the ΔG at 298.15 K.

Morphological studies of **CBI-35CH** using AFM on a freshly cleaved mica surface showed networks of fibers (Figure 9.3a). Height analysis showed that, most of the fibers are not composed of individual molecular fibers, but they are an agglomeration of individual fibers (Figure 9.3b).

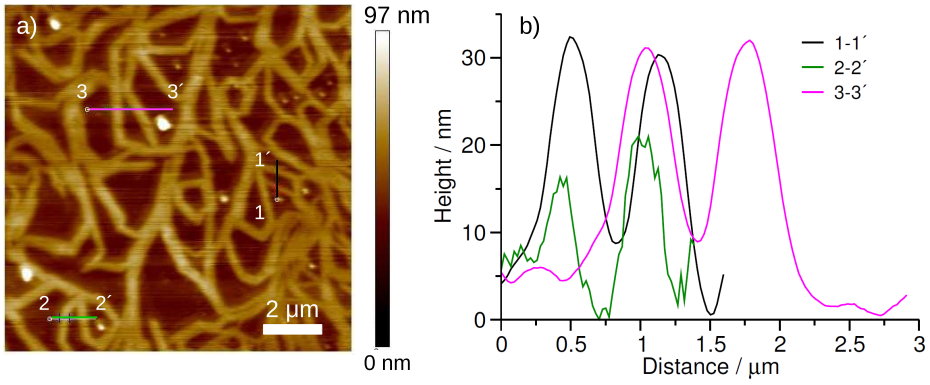

Figure 9.3: a) AFM height image of a film obtained by drop-casting a solution of **CBI-35CH** in MCH ($c = 1\times10^{-4}$ M) on a freshly cleaned glass surface. b) Height profile along the lines indicated in Figure a).

9.2.2 Reversal of supramolecular chirality in cyclic solvents

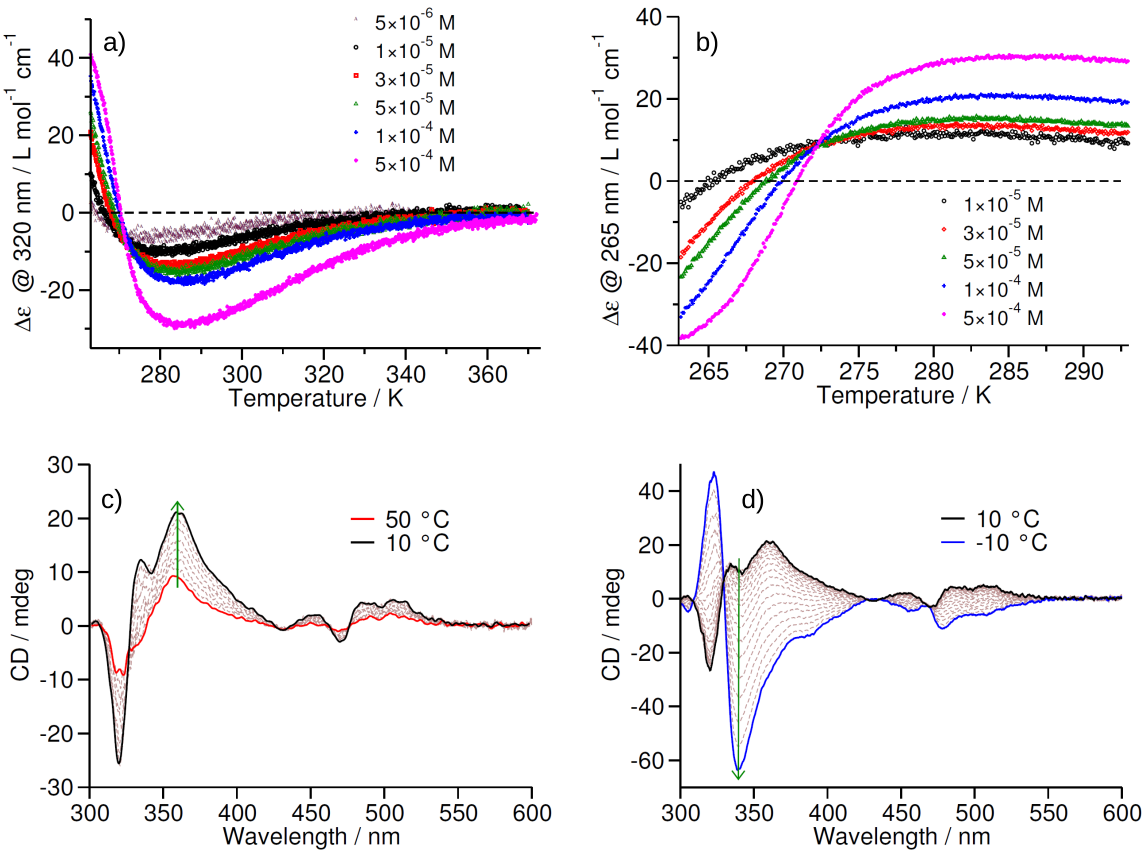

Figure 9.4: a) and b) Full cooling curves of **CBI-35CH** at different concentrations by monitoring CD spectral changes at 320 and 265 nm respectively. c) and d) Temperature-dependent CD spectra in "state A" and "state B" respectively. In c) and d) CD spectra are recorded every 5 °C and 1 °C respectively (c = 5×10^{-5} M). Green arrows indicate spectral changes with decrease in temperature. All studies were performed in MCH.

During the study of the mechanism of self-assembly, when the temperature was lowered below 10 °C the sign of CD spectra reversed and increased in magnitude in the opposite direction with further dip in temperature (Figure 9.4a and b). The range of temperatures from the highest value to that at which the sign of CD signal starts to invert is termed as "state A" and the temperature range below the reversal start temperature is termed "state B" (Figure 9.4c and d). The temperature at which the CD signal crosses zero is termed as T_{cross} and this quantity shifts to higher value as the concentration is increased. There are two ways in which the reversal can occur firstly, the reversal can be completely within the stack and at a particular temperature, the reversal kicks in at a certain part of the assembly and propagates from thereon, this is termed as intra-stack mechanism. Secondly, the

interconversion between the two types of helices can take place through monomer exchange (inter-stack process). The intra-assembly helix reversal is expected to be concentration independent, whereas the latter depends on concentration of the solution. The concentration dependence of T_{cross} suggests that the helix inversion in **CBI-35CH** could proceed through monomers. Also, the handedness reversal occurs over a small temperature range (Figure 9.4d).

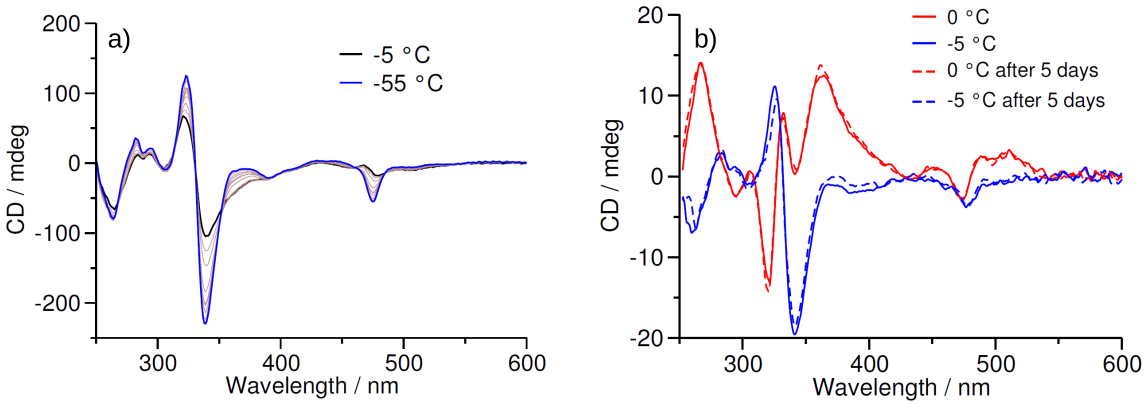

Figure 9.5: a) Temperature-dependent CD spectra of **CBI-35CH** in "state B" (MCH, c = 5.9×10^{-5} M). b) Comparison of the CD spectra after 5 days at 0 °C ("state A") and -5 °C ("state B") of **CBI-35CH** (MCH, c = 5×10^{-5} M).

The magnitude of CD effect continued to increase in "state B" with further lowering in temperature to -55 °C. Further, no discernible change in the shape of the CD spectra was observed between -5 to -55 °C (Figure 9.5a), suggesting that no new structural transitions occur leading to change in the shape of the CD spectra. To understand the kinetic stability of the inversion, CD spectra were recorded in both states (0 °C "state A" and -5 °C "state B") as a function of time. Even after 5 days of keeping in ambient, the CD spectra at both the states overlapped with the ones recorded soon after preparation (Figure 9.5b). This observation indicates that the reversal is thermodynamic and is not an artifact or kinetic trap.

Similar reversal in handedness of supramolecular chirality was observed in various cyclic solvents such as, cyclohexane, 1,2-dimethylcyclohexane (cis and mixture of cis-trans) and a mixture of cis-trans decalin (Figure 9.6a and b). Interestingly, the T_{cross} temperature shows a correlation with the crystallization temperature of the cyclic solvents (Table 9.2). Crystallization temperature indicates the point where the molecules lose their degrees of freedom and crystallize into a lattice. Since the T_{cross} and crystallization temperature show similar behaviour across solvents, we hypothesize that the various cyclic solvents tend to occupy the pocket in the

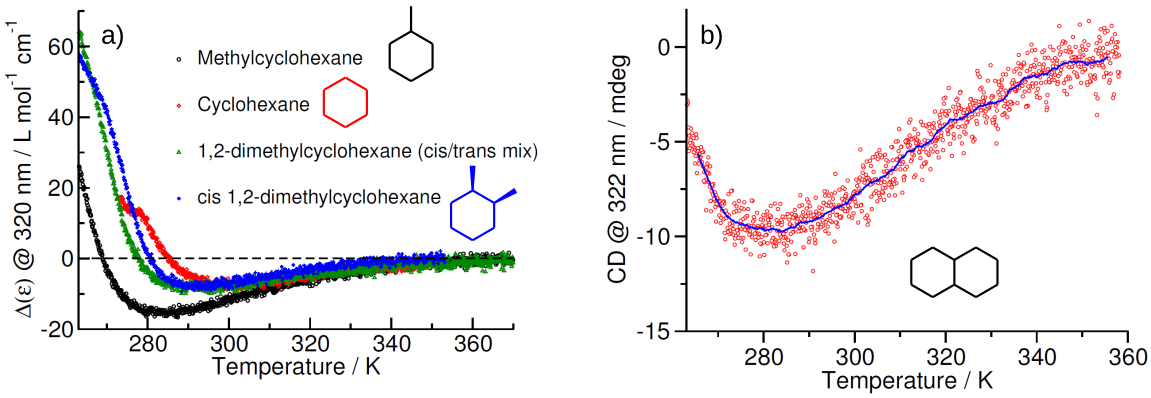

Figure 9.6: a) Full cooling curves of **CBI-35CH** in different cyclic solvents (c = 7×10^{-5} M for cis-1,2-dimethylcyclohexane and for the rest of the solvents, c = 5×10^{-5} M). The structure of the solvents is shown in the inset of the graph. b) Full cooling curve of **CBI-35CH** in a mixture of cis-trans decalin (c = 3×10^{-5} M). All cooling curves were recorded with a rate of 2 K/minute cooling.

molecule and rigidify at low temperature. This further triggers a conformational change in the molecule leading to the reversal of handedness.

Solvent	T_{cross} (K)	Crystallization temperature (K)
Methylcyclohexane	269.0	146.85
cis 1,2-dimethylcyclohexane	280.7	223.15
Cyclohexane	285.4	279.62

Table 9.2: Comparison of the transition temperature (CD effect = 0, T_{cross}) of **CBI-35CH** with crystallization temperature for different cyclic solvents (c = 5×10^{-5} M).

9.2.3 Reversal of supramolecular chirality in *n*-heptane

In order to understand the role of the solvent structure in affecting the reversal of supramolecular chirality, low temperature CD studies were performed in *n*-heptane. CD spectra shows a positive bisignated Cotton effect even till -10 °C. On further lowering the temperature, the reversal starts and the magnitude of CD effect increases at lower temperature (Figure 9.7).

Although the reversal in the sign of CD signal is observed in a linear alkane solvent such as *n*-heptane, the temperature where the reversal begins is about 10 °C lower compared to that in other cyclic solvents. Since *n*-heptane has a linear

geometry, the solvent molecules can enter and leave the pocket of **CBI-35CH** without any constraint. Only when a sufficient number of *n*-heptane solvent molecules (can be termed as solvent aggregate) occupy the pocket, they will be able to influence the conformation of **CBI-35CH** in the aggregate. The clustering of *n*-heptane molecules in the pocket requires low temperature due to the increased number of degrees of freedom for linear solvent. As a result, the reversal starts at a lower temperature in linear solvent compared to cyclic counterpart. Thus the nature of the solvent molecule does affect the transition temperature, but the phenomena of reversal is still observed.

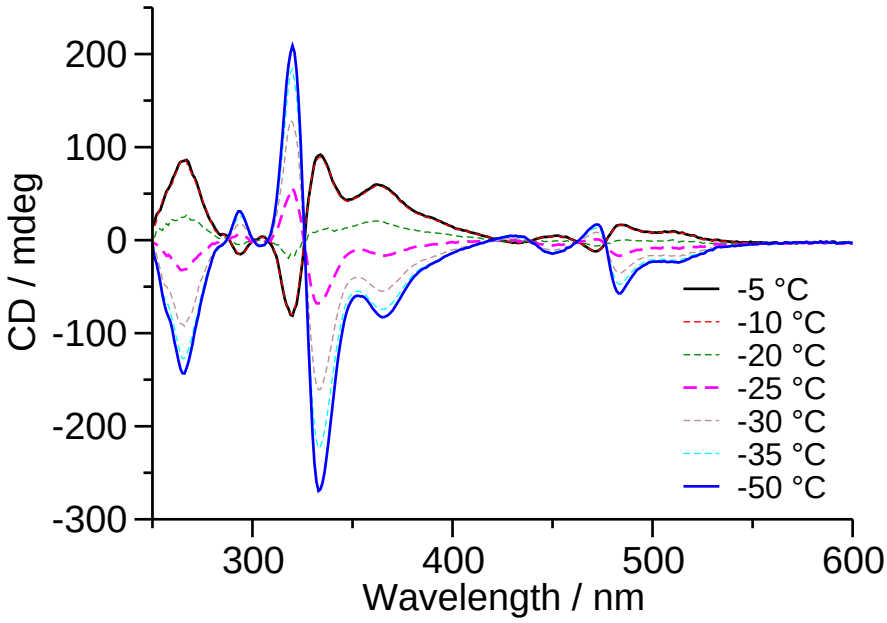

Figure 9.7: a) Temperature-dependent CD spectra of **CBI-35CH** in *n*-heptane (c = 6.5×10^{-5} M).

9.2.4 Role of molecular structure in chirality reversal

Temperature-dependent CD studies were performed on **CBI-GCH** and compared with that of **CBI-35CH** to understand the role of molecular structure in governing the reversal of supramolecular chirality. CD spectra of **CBI-GCH** shows a positive bisignated Cotton effect in both MCH (cyclic) and *n*-heptane (linear) solvents even till -38 °C (Figure 9.8a and b). In comparison, **CBI-35CH** displays a reversal in chirality below -20 °C for both MCH and *n*-heptane. These observations suggest that in **CBI-GCH**, the solvent molecules cannot penetrate the phenoxy wedge closely

due to the 3,4,5-trisubstitution which does not leave much room. Whereas in **CBI-35CH**, because of the 3,5-disubstitution of the phenoxy wedge, a pocket is created, which can be accessed by the solvent molecules. Thus, the lack of reversal of chirality in **CBI-GCH** again points to the important role of the pocket of **CBI-35CH** in leading to reversal of supramolecular chirality.

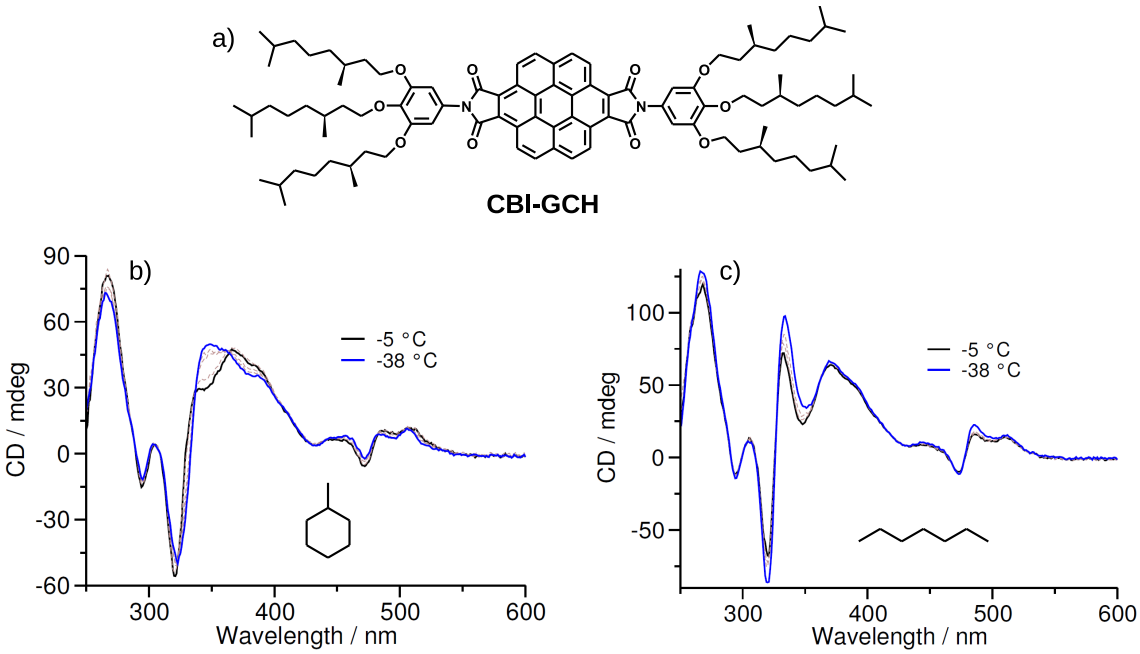

Figure 9.8: a) Structure of **CBI-GCH**. b) and c) Temperature-dependent CD spectra of **CBI-GCH** in MCH and *n*-heptane respectively (c = 5×10^{-5} M). The structure of solvent is shown in the inset of graphs.

9.2.5 Molecular dynamics simulations

MD simulations were carried out in explicit cyclohexane solvent for both **CBI-GCH** and **CBI-35CH** at different temperature to understand the molecular level changes leading to the reversal of supramolecular chirality. Stacked 15 mer in both right and left handed helical fashions were used as the initial configuration for MD simulations. Pair-correlation function (g(r)) between the solvent molecules and the center of mass of stereo centers on one arm of the molecule was determined. g(r) peaks at a much lower distance in a left handed (LH) stack at 250 K compared to it the right handed (RH) stack at 350 K,(Figure 9.10a) indicating that more

MD simulations were carried out by Karteek Kumar Bejagam from JNCASR

number of molecules can approach the pocket at lower temperature. The probability distribution as a function of dihedral angle also shows that at low temperature in a LH stack, the probability of solvent entering the pocket is high (Figure 9.10b).

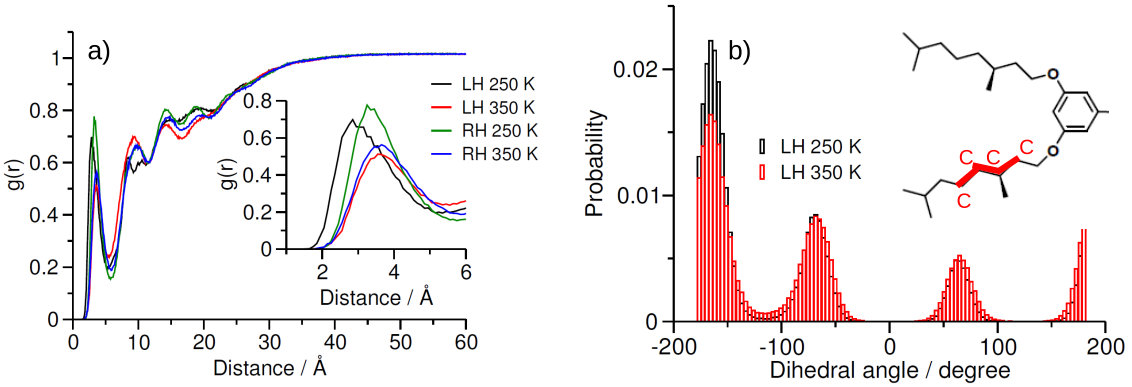

Figure 9.9: a) Pair correlation function (g(r)) as a function of distance between the center of alkyl tails on the phenoxy wedge to the solvent molecules at different temperatures. b) Probability distribution of **CBI-GCH** as a function of dihedral angle. The scanned dihedral angle is shown in the inset.

Moreover, the number of gauche defects at low temperature is larger compared to that at high temperature (Table 9.3). This again points to the increased probability of accommodating the solvent molecules at low temperature and further leading to the reversal of supramolecular handedness in **CBI-35CH**.

CBI-35CH	trans %	gauche %
250 K	61.12	35.88
350 K	52.54	42.44

Table 9.3: Percentage of defects in an assembly of **CBI-35CH** at different temperatures.

9.3 Conclusions

CBI-35CH self-assembles in apolar solvents such as MCH in an isodesmic manner. Further, reversal of supramolecular chirality was observed for **CBI-35CH** in various cyclic solvents. Although the reversal was observed in *n*-heptane, it occurred at a much lower temperature compared to cyclic solvents. **CBI-GCH** without a

molecular pocket did not exhibit reversal in chirality in both cyclic and linear solvents, thus emphasizing the role of structure. Further, MD simulations suggest that the solvent molecules occupy the pocket of **CBI-35CH** leading to a conformational change manifesting as the reversal of supramolecular chirality.

9.4 Experimental details

9.4.1 General methods

Chemicals and synthesis related: All chemicals were purchased from commercial sources and used without further purification unless and untill specified. Quinoline and thionyl chloride were freshly distilled before use. Thin layer chromatography (TLC) was performed using Merck silica gel 60 F_{254} plates coated on aluminium. Column chromatography was performed using Merck silica gel 60 (100-200 or 230-400 mesh) under positive pressure of nitrogen gas. Molecule **2** was synthesized by the tosylation of dihydro-citronellol using reported procedure. [26]

Optical studies: UV/vis absorption and fluorescence spectra were recorded on a Perkin-Elmer Lambda 750 and Perkin-Elmer LS 55 spectrometer respectively. Temperature-dependent UV/Vis absorption spectra were recorded on Perkin-Elmer lambda 750 using PTP-1+1 Peltier and Templab 2.14 software. Circular dichroism (CD) spectra were recorded on a JASCO J-815 spectrometer using the following parameters; sensitivity = 100 mdeg, scan rate = 100 nm/minute, bandwidth = 1 nm, response time = 1 second and number of accumulations = 1. Temperature-dependent measurements were performed using a CDF-426S/15 Peltier type temperature controller with a temperature range of 263-370 K. Low temperature (<) -10 °C CD studies were performed at TU/e Eindhoven by coupling an oxford cryo set-up with the JASCO J-815 instrument.

NMR spectroscopy: ^{1}H and ^{13}C-NMR spectra were recorded on a Bruker Avance 400 spectrometer operating at 400 MHz and 100 MHz respectively. Chemical shifts are reported with respect to the residual solvent peaks of chloroform-D (δ = 7.26 ppm for ^{1}H and 77.16 ppm for ^{13}C NMR). Notations; s, d, t, q, m and br stand for singlet, doublet, triplet, quartet, multiplet and broad respectively. All NMR spectra were recorded at 300 K unless otherwise mentioned.

Atomic Force Microscopy (AFM) imaging: AFM measurements were performed on a Veeco diInnova SPM operating in tapping mode regime. Micro-fabricated silicon cantilever tips doped with phosphorus and with a frequency between 235 and 278 kHz and a force constant of 20-40 Nm^{-1} were used. AFM images were recorded at a rate of 512×512 pixels per minute. The appropriate solution was drop-casted on a clean glass surface and allowed to dry at room temperature first followed by drying under vacuum.

Mass spectrometry: HR-MS was carried out using Agilent Technologies 6538 UHD Accurate-Mass Q-TOF LC/MS. Matrix-Assisted Laser Desorption Ionization Time of Flight (MALDI-TOF) was performed on a Bruker daltonics autoflex (ST-A2130) spectrometer using trans-2-[3-(4-tert-Butylphenyl)-2-methyl-2-propenylidene]malononitrile (DCTB) as the matrix.

9.4.2 Synthetic details

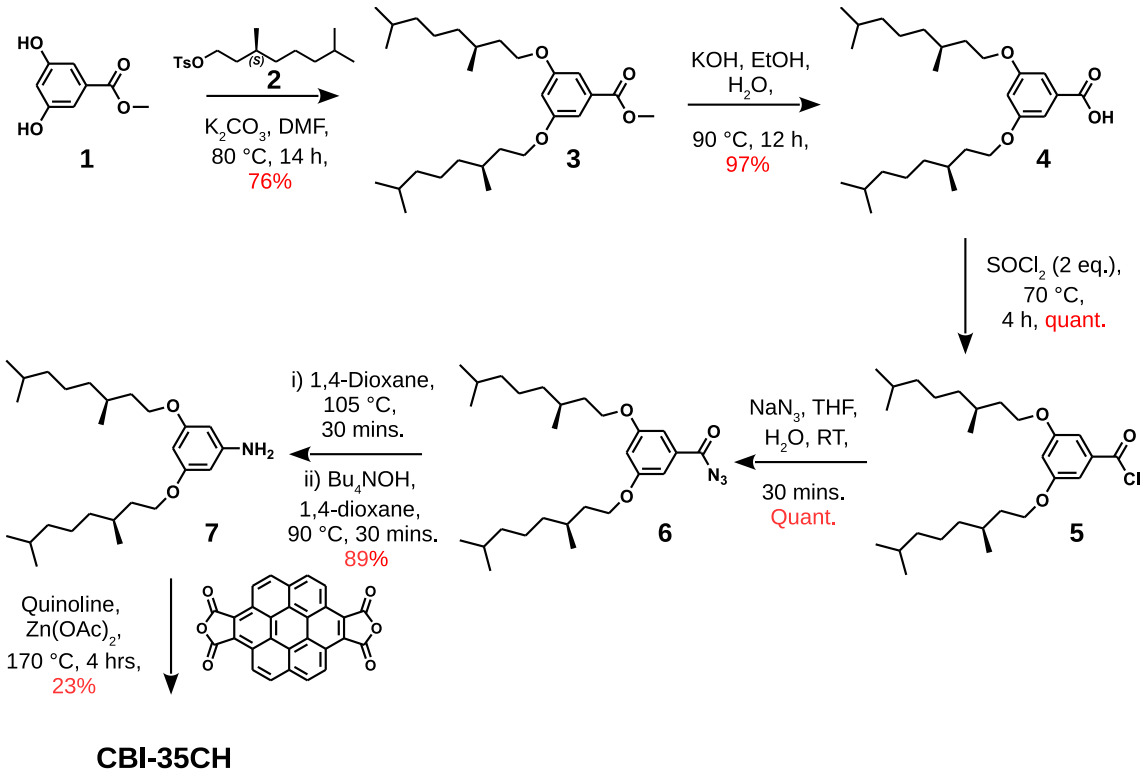

Figure 9.10: Synthetic route to **CBI-35CH**

Synthesis of 3: Methyl-3,5-dihydroxy benzoate (**1**, 4.7 g, 27.9 mmol, 1.0 eq.), **2** (19 g, 61.3 mmol, 2.2 eq.) and potassium carbonate (27 g, 195.3 mmol, 7 eq.)

were taken in a 250 mL 2-necked RBF fitted with a reflux condenser and magnetic stir bar. Dry DMF (100 mL) was added to the RBF and the reaction mixture was heated to 80 °C for 14 hours. The reaction was monitored by TLC. After complete consumption of **1**, the reaction mixture was allowed to cool down to room temperature and poured into 200 mL of DI water. The water layer was repeated extracted with *n*-hexane (150 mL×5). The collected organic layer was washed with water (150 mL×2), dried over anhydrous Na_2SO_4 and evaporated under reduced pressure to obtain a dark viscous liquid.
Purification: The crude product was purified by column chromatography (SiO_2, 100-200 mesh) eluting with 60% chloroform in hexane to obtain a pure colorless liquid (9.54 g, 76%).
^{1}H-NMR (400 MHz, $CDCl_3$) δ = 7.15 (d, J = 2.4. Hz, 2H), 6.63 (t, J = 2.4 Hz, 1H), 4.04-3.95 (m, 4H), 3.89 (s, 3H), 1.84-1.79 (m, 2H), 1.67-1.49 (m, 6H), 1.34-1.12 (m , 12H), 0.93 (d, J = 6.4 Hz, 6H), 0.868 ppm (d, J = 6.8 Hz, 12H).
HR-MS (ESI): m/z calcd: $[C_{28}H_{48}O_4+H]^+$: 449.3625, found: 449.3609.

Synthesis of 4: **3** (9.54 g, 21.2 mmol, 1.0 eq.) was taken in a 250 mL 1-necked RBF. KOH (2.53 g, 45.1 mmol, 2.13 eq.) dissolved in 10% water in EtoH (50 mL) solution was added dropwise to the RBF at room temperature. The reaction mixture was refulexed at 90 °C for 12 hours. After 12 hours, the reaction mixture was cooled to room temperature and conc. HCl was added dropwise to the RBF till the pH reaches 2. During the addition of conc. HCl, formation of a white precipitate was observed. The solution was diluted with water and extracted with chloroform (100 mL×3). The collected organic layer was washed with water (100 mL×2), dried over anhydrous Na_2SO_4 and evaporated under reduced pressure to obtain a colorless oil (9.06 g, 97%).
^{1}H-NMR (400 MHz, $CDCl_3$) δ = 7.22 (d, J = 2.32 Hz, 2H), 6.68 (t, J = 2.32 Hz, 1H), 4.06-3.97 (m, 4H), 1.86-1.78 (m, 2H), 1.69-1.48 (m, 6H), 1.37-1.12 (m, 12H), 0.94 (d, J = 6.52 Hz, 6H), 0.87 ppm (d, J = 6.6 Hz, 12H).
HR-MS (ESI): m/z calcd: $[C_{27}H_{46}O_4+H]^+$: 435.3469, found: 435.3467.

Synthesis of 5: **4** (1.50 g, 3.45 mmol, 1.0 eq.) was taken in a 2-necked RBF fitted with a dropping funnel. Freshly distilled thionyl chloride (1.64 g, 13.80 mmol, 4.0 eq.) was taken in the dropping funnel and added dropwise to the RBF at room temperature. Then the reaction mixture was heated at 70 °C for 4 hours. The excess thionyl chloride was distilled off at 70 °C and dried in vacuum oven for 2 hours to obtain a pale yellow oil (1.56 g, quant.).
The product was used as such in the next reaction, as it was found to be sufficiently

pure and also acid chlorides degrade on SiO_2 columns.
^{1}H-NMR (400 MHz, $CDCl_3$) δ = 7.22 (d, J = 2.28 Hz, 2H), 6.73 (t, J = 2.28 Hz, 1H), 4.05-3.96 (m, 4H), 1.87-1.79 (m, 2H), 1.73-1.50 (m, 6H), 1.39-1.11 (m, 12H), 0.94 (d, J = 6.52 Hz, 6H), 0.87 ppm (t, J = 6.6 Hz, 12H).
^{13}C-NMR (100 MHz, $CDCl_3$): δ = 168.51, 160.50, 134.99, 109.62, 108.92, 67.07, 39.38, 37.40, 36.17, 29.97, 28.13, 24.80, 22.84, 22.74, 19.78 ppm.

Syntehsis of 6: **5** (1.56 g, 3.45 mmol, 1.0 eq.) was dissolved in THF (15 mL) and added dropwise to a solution of NaN_3 (2.69 g, 41.4 mmol, 12 eq.) dissolved in water (15 mL) at 0 °C. The solution was stirred at room temperature for another half and hour and then extracted with chloroform, dried over Na_2SO_4 and evaporated under pressure to obtain a colorless oil (1.63 g, quant.).
The product was used as such in the next reaction without further purification.
^{1}H-NMR (400 MHz, $CDCl_3$) δ = 7.14 (d, J = 2.32 Hz, 2H), 6.68 (t, J = 2.4 Hz, 1H), 4.04-3.94 (m, 4H), 1.88-1.77 (m, 2H), 1.68-1.48 (m, 6H), 1.37-1.11 (m, 12H), 0.94 (d, J = 6.52 Hz, 6H), 0.87 ppm (d, J = 6.6 Hz, 12H).

Synthesis of 7: **6** (1.63 g, 3.54 mmol, 1.0 eq.) was taken in a 100 mL 1-necked RBF fitted with refulx condenser and a nitrogen inlet. Dry 1,4-dioxane (45 mL) was added to the RBF and heated at 105 °C till the evolution of nitrogen gas ceases (30-40 minutes). The the solution was cooled to 80 °C. In another 3-necked RBF fitted with a dropping funnel and a condenser, Bu_4NOH (2.4 mL) and dry 1,4-dioxane (45 mL) are taken and heated to 90 °C. The hot (80 °C) solution of isocyanate is added to the 3-necked RBF through the dropping funnel dropwise over a period of 15 minutes. With the addition of the hot solution the color of the solution changes from colorless to brownish-yellow. After the complete addition, the solution was heated at 90 °C for 15 minutes more. Then the reaction mixture is cooled to room temperature, diluted with water and the aqueous layer was extracted with chloroform. The combined organic layer was washed with water, brine, dried over anhydrous Na_2SO_4 and evaporated under reduced pressure to obtain a yellowish-brown oil (1.55 g).
Purification: The crude product was purified by column chromatography (SiO_2, 230-400 mesh) eluting with chloroform to obtain the pure product (yellowish oil, 1.39 g, 89%).
^{1}H-NMR (400 MHz, $CDCl_3$) δ = 5.91 (t, J = 2.08 Hz, 1H), 5.857 (d, J = 2.08 Hz, 2H), 3.96-3.87 (m, 4H), 3.61 (br, 2H), 1.82-1.74 (m, 2H), 1.68-1.47 (m, 6H), 1.37-1.11 (m, 12H), 0.921 (d, J = 6.52 Hz, 6H), 0.868 ppm (d, J = 6.68 Hz, 12H).

^{13}C-NMR (100 MHz, $CDCl_3$): δ = 161.38, 148.33, 94.47, 92.28, 63.40, 39.41, 37.44, 36.39, 30.02, 28.13, 24.80, 22.85, 22.75, 19.80 ppm.
HR-MS (ESI): m/z calcd: $[C_{26}H_{47}NO_2+H]^+$: 406.3680, found: 406.3676.

Synthesis of CBI-35CH: Coronene dianhydride (150 mg, 0.34 mmol, 1.0 eq.), **7** (345 mg, 0.85 mmol, 2.5 eq.), zinc acetate (100 mg, 0.54 mmol, 1.6 eq.) and freshly distilled quinoline (20 mL) were taken in a 2-necked 50 mL RBF fitted with reflux condenser and heated to 170 °C for 4 hours. Initially the reactants are insoluble in quinoline. After half an hour of heating, a yellowish-orange precipitate starts forming. At the end of 4 hours, the solution was homogeneous. The reaction was allowed to cool down to room temperature and poured into a 2:1 mixture of 1M HCl and methanol. The obtained precipitate was filtered under suction and washed with methanol to obtain an orange powder.
Purification: The crude product was purified by column chromatography (SiO_2, 230-400 mesh) eluting with 70% chloroform in *n*-hexane. Further, the fractions containing the product were subjected to repeated size exclusion chromatography (S-X3, chloroform) to obtain a dark orange product (90 mg, 23%).
^{1}H-NMR (400 MHz, $CDCl_3$) δ = 8.56 (brs, 4H), 7.40 (brs, 4H), 7.05 (br, 4H), 6.66 (br, 2H), 4.12-4.07 (m, 8H), 1.91-1.89 (m, 4H), 1.66-1.56(m, 12H), 1.43-1.32 (m, 12H), 1.27-1.19 (m, 12H), 0.98 (d, J = 6.08 Hz, 12H), 0.94 ppm (d, J = 6.6 Hz, 24H).
^{13}C-NMR (100 MHz, $CDCl_3$): δ = 167.95, 160.84, 130.03, 127.80 (br), 123.35, 122.33, 120.50 (br), 116.98, 106.29, 103.10, 67.10, 39.56, 37.70, 36.53, 30.21, 28.22, 24.91, 22.98, 22.89,2 19.79 ppm.
MALDI-TOF (DCTB, negative mode): m/z calculated for $C_{80}H_{98}N_2O_8$: 1214.73 $[M]^{-\cdot}$; found: 1214.75

Bibliography

[1] Zhang, Y.; Zhao, Z.; Huang, X.; Xie, Y.; Liu, C.; Li, J.; Guan, X.; Zhang, K.; Cheng, C.; Xiao, Y. *RSC Adv.* **2012**, *2*, 12644–12647.

[2] An, Z.; Yu, J.; Domercq, B.; Jones, S. C.; Barlow, S.; Kippelen, B.; Marder, S. R. *J. Mater. Chem.* **2009**, *19*, 6688–6698.

[3] Usta, H.; Newman, C.; Chen, Z.; Facchetti, A. *Adv. Mater.* **2012**, *24*, 3678–3684.

[4] Nolde, F.; Pisula, W.; Müller, S.; Kohl, C.; Müllen, K. *Chem. Mater.* **2006**, *18*, 3715–3725.

[5] Alibert-Fouet, S.; Seguy, I.; Bobo, J.-F.; Destruel, P.; Bock, H. *Chem. Eur. J.* **2007**, *13*, 1746–1753.

[6] Rohr, U.; Kohl, C.; Müllen, K.; van de Craats, A.; Warman, J. *J. Mater. Chem.* **2001**, *11*, 1789–1799.

[7] Rohr, U.; Schlichting, P.; Böhm, A.; Gross, M.; Meerholz, K.; Bräuchle, C.; Müllen, K. *Angew. Chem. Int. Ed.* **1998**, *37*, 1434–1437.

[8] Lütke Eversloh, C.; Li, C.; Müllen, K. *Org. Lett.* **2011**, *13*, 4148–4150.

[9] Yan, Q.; Cai, K.; Zhang, C.; Zhao, D. *Org. Lett.* **2012**, *14*, 4654–4657.

[10] Müller, S.; Müllen, K. *Chem. Commun.* **2005**, 4045–4046.

[11] Hao, L.; Jiang, W.; Wang, Z. *Tetrahedron* **2012**, *68*, 9234 – 9239.

[12] Rao, K. V.; George, S. J. *Org. Lett.* **2010**, *12*, 2656–2659.

[13] Jain, A.; Rao, K. V.; Kulkarni, C.; George, A.; George, S. J. *Chem. Commun.* **2012**, *48*, 1467–1469.

[14] Kim, J.; Lee, J.; Kim, W. Y.; Kim, H.; Lee, S.; Lee, H. C.; Lee, Y. S.; Seo, M.; Kim, S. Y. *Nat. Commun.* **2015**, *6*.

[15] Park, S. H.; Jung, S. H.; Ahn, J.; Lee, J. H.; Kwon, K.-Y.; Jeon, J.; Kim, H.; Jaworski, J.; Jung, J. H. *Chem. Commun.* **2014**, *50*, 13495–13498.

[16] Kumar, M.; Jonnalagadda, N.; George, S. J. *Chem. Commun.* **2012**, *48*, 10948–10950.

[17] Duan, P.; Li, Y.; Li, L.; Deng, J.; Liu, M. *J. Phys. Chem. B* **2011**, *115*, 3322–3329.

[18] Nagata, Y.; Yamada, T.; Adachi, T.; Akai, Y.; Yamamoto, T.; Suginome, M. *J. Am. Chem. Soc.* **2013**, *135*, 10104–10113.

[19] Nakako, H.; Nomura, R.; Masuda, T. *Macromolecules* **2001**, *34*, 1496–1502.

[20] Fujiki, M.; Koe, J. R.; Motonaga, M.; Nakashima, H.; Terao, K.; Teramoto, A. *J. Am. Chem. Soc.* **2001**, *123*, 6253–6261.

[21] Yashima, E.; Maeda, K.; Sato, O. *J. Am. Chem. Soc.* **2001**, *123*, 8159–8160.

[22] Fujiki, M. *J. Am. Chem. Soc.* **2000**, *122*, 3336–3343.

[23] Kumar, J.; Nakashima, T.; Kawai, T. *Langmuir* **2014**, *30*, 6030–6037.

[24] Jyothish, K.; Hariharan, M.; Ramaiah, D. *Chem. Eur. J.* **2007**, *13*, 5944–5951.

[25] Smulders, M.; Nieuwenhuizen, M.; deGreef, T.; vanderSchoot, P.; Schenning, A.; Meijer, E. *Chem. Eur. J.* **2010**, *16*, 362–367.

[26] Kabalka, G. W.; Varma, M.; Varma, R. S.; Srivastava, P. C.; Knapp, F. F. *J. Org. Chem.* **1986**, *51*, 2386–2388.

Chapter 10

Conclusions and Future Outlook

The mechanisms of supramolecular polymerization gained importance post 2006, and many π-conjugated systems were investigated. But a molecular level rationale for the mechanisms was lacking. To this end, in the present thesis we hypothesized that "long-range interactions between oligomers along the growth direction of stack leads to cooperative or nucleation-elongation mechanism of self-assembly" (Chapter 3). The same was successfully tested on various chromophores such as perylene bisimides, perylene monoimide, naphthalene diimide and oligo(*p*-phenylenevinylene) using either carbonate or ester as the source of long-range dipolar interaction and cholesterol as a rigid self-assembling moiety (Chapters 4, 5 and 6). In addition, we have also observed that systems such as coronene bisimides which lack such long-range interaction, self-assemble isodesmically (Chapters 8 and 9). Thus, a molecular level understanding of the mechanisms operating in supramolecular systems was achieved.

In spite of this progress, it is difficult to pin-point the nucleation process in systems which have two competing orthogonal interactions. The understanding gained from this thesis can be used to address some of the important challenges such as achieving low polydispersity in supramolecular polymers by control of the size and number of nuclei formed. Since many biological systems also self-assemble through nucleation-elongation mechanism, it will be worth testing our hypothesis on such systems as well.

List of Publications

From the thesis

- Dipole-Moment-Driven Cooperative Supramolecular Polymerization
  Kulkarni, C.; Bejagam, K. K; Senanayak, S. P.; Narayan, K. S.; Balasubramanian, S.; George, S. J.
  J. Am. Chem. Soc. **2015**, *137* , 3924-3932.

- Carbonate Linkage Bearing Naphthalenediimides: Self-Assembly and Photophysical Properties
  Kulkarni, C.; George, S. J.
  Chem. Eur. J. **2014**, *20* , 4537-4541.

- Charge-transfer Complexation between Naphthalene Diimides and Aromatic Solvents
  Kulkarni, C.; Periyasamy, G.; Balasubramanian, S.; George, S. J.
  Phys. Chem. Chem. Phys. **2014**, *16* , 14661-14664.

- What Molecular Features Govern the Mechanism of Supramolecular Polymerization?
  Kulkarni, C.; Balasubramanian, S.; George, S. J.
  ChemPhysChem **2013**, *14* , 661-673.

- Self-Assembly of Coronene Bisimides: Mechanistic Insight and Chiral Amplification
  Kulkarni, C.; Munirathinam, R; George, S. J.
  Chem. Eur. J. **2013**, *19* , 111270-11278.

- Cooperativity in the Stacking of Benzene-1,3,5-tricarboxamide: The role of dispersion.
  Kulkarni, C. H.; Reddy, S. K.; George, S. J.; Balasubramanian, S.
  Chem. Phys. Lett. **2011**, *515* , 226-230.

Miscellaneous

- Synthesis and self-assembly of a C_3-symmetric benzene-1,3,5-tricarboxamide (BTA) anchored naphthalene diimide disc
  Narayan, B.; Kulkarni, C.; George, S. J.
  J. Mater. Chem. C **2013**, *1*, 626-629

- Perylene Based Porous Polyimides: Tunable, High Surface Area with Tetrahedral and Pyramidal Monomers
  Rao, K. V.; Haldar, R.; Kulkarni, C.; Maji, T. K.; George, S. J.
  Chem. Mater. **2012**, *24* , 969-971.

- Fluorescent coronene monoimide gels via H-bonding induced frustrated dipolar assembly
  Jain, A.; Rao, K. V.; Kulkarni, C.; George, A.; George, S. J.
  Chem. Commun. **2012**, *48*, 1467-1469

- Vibrational Spectra of Linear Oligomers of Carbonic Acid: A Quantum Chemical Study.
  Reddy, S. K.; Kulkarni, C. H; Balasubramanian, S.
  J. Phys. Chem. A **2012**, *116* , 1638-1647.

- Extended phenylene based microporous organic polymers with selective carbon dioxide adsorption
  Rao, K.V.; Mohapatra, S.; Kulkarni, C.; Maji, T, K.; George, S. J.
  J. Mater. Chem. **2011**, *21* , 12958-12963.

- Observation of Pore-Switching Behavior in Porous Layered Carbon through a Mesoscale OrderDisorder Transformation
  Datta, K. K. R.; Jagadeesan, D.; Kulkarni, C.; Kamath, A.; Datta, R.; Eswaramoorthy, M.
  Angew. Chem. Int. Ed. **2011**, *123* , 4015-4019.

- Theoretical Investigations of Candidate Crystal Structures for β-Carbonic Acid
  Reddy, S. K.; Kulkarni, C. H; Balasubramanian, S.
  J. Chem. Phys. **2011**, *134* , 124511.

- Aminoclay: a permselective matrix to stabilize copper nanoparticles
  Datta, K. K. R.; Kulkarni, C.; Eswaramoorthy, M.
  Chem. Commun. **2010**, *46* , 616-618.